DEPARTMENT OF ELECTRONIC & ELECTRICAL ENGINEERING

University of Strathclyde Engineering

THE BEHAVIOUR OF CHARGE ON THE SURFACE OF POLYMERIC MATERIALS

A thesis presented in fulfilment of the requirement for the degree of

Doctor of Philosophy

Mohammad Burhan Tariq, B.Eng. (Hons)

Department of Electronic and Electrical Engineering

University of Strathclyde

Glasgow, UK

2019

Declaration of Authencity and Author's Rights

'This thesis is the result of the author's original research. It has been composed by the author and has not been previously submitted for examination which has led to the award of a degree.'

Signed:

Date:

Acknowledgements

First of all I would like to acknowledge Dr. Martin J Given for his incredible support and supervision. This project was very challenging and without Dr. Givens guidance it would have been very difficult to complete it.

I would like to thank all of my colleagues and especially my good friends Omer Panni and Dr. Sotiria Koutoula for their support during difficult times. I would also like to thank Sean, Frank, David and Andy from the mechanical workshop for their efforts in constructing the test geometries as requested.

My deepest gratitude goes to my family. My mom for her unconditional love and support and my brothers “Dr. Mohammed Sufyan Tariq” (RIP) and “Usman Tariq”. My cousins who are more like my brothers “Dr. Ahmad”, “Dr. Hassan”, “Dr. Ahsan”, “Hammy”, ”Raza”, ”Nadeem”, “Rafy” and “Dave” for keeping me motivated and encouraging me to stay strong when I needed a push. Also my uncles “Khalid Rashid”, “Ajaz Sher”, “Imtiaz Sher” and “Arfan Sher” for their support and looking after the family unconditionally.

Last but not the least, my most sincere and genuine thanks to “Allah (sbt)” for making it possible for me to complete this project. He has given me everything in life and without his permission nothing can happen. I would like to take this chance to thank my lord for all his blessings.

I would like to dedicate this project in the memory of my late father “Dr. Tariq Rashid” (RIP) who raised me to be the man I am today, my late brother “Dr. Mohammed Sufyan Tariq” (RIP) who sadly passed away this year and was my best friend. May “Allah (sbt)” grant both of you the highest place in “Jannah”. You are always with me and I will always love you.

During the course of this project both me and my supervisor lost loved ones. So, I would also like to dedicate this thesis in the memory of the parents of Dr. Martin J Given, “Patrick J Given” (RIP) and “Delia Given” (RIP).

Abstract

In the high voltage industry one of the factors limiting the performance of a pulse power system is the build-up of charge on the surface of the insulators. In these systems solid insulators are used to support the conductors. When operating pulse power systems in repetitive mode, the accumulation of charge on the insulators after each pulse can promote "surface flashover" and cannot be ignored as a limiting factor in the design of the system.

The aim of this project was to enhance knowledge of the effect of accumulated charge on the surface conductivity, the surface charging/discharging behaviour and the surface charge decay behaviour of polymeric insulators. The project was carried out in 2 stages.

Firstly surface charging/discharging transient currents were observed using a concentric cylindrical measurement system for uncharged PMMA and PMMA samples charged by exposure to corona. The charging/discharging transients were analysed to characterise possible conduction mechanisms and the DC steady state currents were used to calculate the surface conductivities. Charging the sample surfaces with corona led to an increase in the surface conductivities of the samples. The behaviour of the charging/discharging transients were complex and fitted well against 3 and 4 term exponential functions. Differences in behaviour were also observed due to sample thickness.

In the second stage of the project surface charge decay measurements were performed on PMMA samples that were subjected to corona charging. This was done to determine the relative importance of surface conductivity and charge neutralisation to the decay of surface charge. A novel charge probe based on varactors was developed and calibrated to perform these measurements. This system was novel in its use on measurements of surface charge on polymeric materials. The measured surface potentials from the varactor probe were used to calculate the surface charge density distributions. It was observed that most of the charge accumulates near the electrodes. Analysis of the total surface charge showed that the rate of charge decay was higher when the decay occurs through the surface conduction mechanism as compared to conduction through gas neutralisation, where no significant charge decay was observed. The rates of charge decay for thin and thick samples, which were corona charged at a grid voltage of 1 kV, were observed to be 0.027 μC/min and 0.048 μC/min, respectively, for neutralisation through the gas; while the corresponding rates of charge decay through surface conduction were observed to be 0.096 μC/min and 0.18 μC/min, respectively. Evidence of the crossover effect has been observed in certain geometries.

Correlations have been made between the charge decay measurements and the transient behaviours observed in the first part of the project. The charge decay behaviours were found to be in good correlation with the surface conductivities observed for corona treated samples where an external field was applied across the sample surface.

Contents

List of Symbols

Ti	Equilibrium melting point
E_{1n}	Normal field component
E_g	Electric field generated in a void
U	Applied voltage, Potential difference
ϵ_r	Relative permittivity of dielectric / spacer / material
d_1	Length of void, Diameter of probe sensor
d_2	Length of spacer or probe sensor, Thickness of dielectric
d_3	Diameter of outer conductor of the probe
ε	Permittivity of dielectric / polymer, Absolute permittivity of material
$\bar{E}$	Applied electric field
σ	Conductivity of material/ dielectric, Charge density
ρ	Bulk conductivity, Equilibrium density
N_s	Density of states
e	Electron charge
Φ_m	Work function of the metal
Φ_q	Work function of the polymer
J	Current density
A_o	Universal constant.
T	Absolute temperature, Dielectric thickness
Φ	Work function of dielectric
K	Line slope coefficient
E	Electron energy, Electric field, Electric field Strength
h	Planck's constant, Gap separation, Sample thickness
v	Frequency of incident light, Thermal velocity of electrons
ε_Φ	Work function of dielectric surface

ρ_s	Surface charge density, Surface resistivity of dielectric
t	Time, Thickness of insulator
τ	Time constant
ρ_{so}	Surface charge density under equilibrium
χ	Electron affinity
k	Dielectric constant, Boltzmann constant
ϕ	Energy barrier
A^*	Effective Richardson's constant
q	Electron charge
$q\Phi_B$	Schottky barrier height
C	Capacitance
Q	Charge
ε_o	Permittivity of free space
D	Separation, Outer conductor thickness
U_1	Probe and ground reference potential difference, Surface voltage
U_2	Potential difference between test surface and ground reference
I_{sensor}	Current across sensor
V	Flat surface potential, Applied voltage
q_s	Charge density for flat surface
d	Dielectric thickness, Width of the sample
n	Number of surface elements, number of electrons per unit volume
V_{ij}	Induced potential at probe tip
$\overline{V}$	Vector containing induced potentials
$\overline{\sigma}$	Vector containing charge densities
F	Average field, Force exerted on electron
F_{th}	Critical field
μ	Mobility of electrons/ carriers
θ	Ratio of number density

ϕ_{pf}	Lowering of the barrier
z	Charge at the centre
n_c	Number density of carriers
n_t	Number density of occupied trapping sites
N_D	Number density of donors
n_D	Number density of donors that have not offered their electrons
$F_{(r)}$	Coulombic force
$V_{(r)}$	Resultant potential energy
r	Separation
r_m	Point at which field is maximum
v_o	Frequency of electrons effort to escape
S	Cross sectional area where donors are captured
N_{eff}	Effective density of carriers in conduction band
σ_{th}	Thermally assisted hopping conductivity
ΔH	Average trap depth
R_1	Radius of central circular electrode, RC network series resistor
R_2	Radius of outer ring electrode, High value resistor
J_s	Surface current density
R'	Variable radius between outer ring and central electrode
I_s	Current across sample surface
E_s	Electric field along sample surface
$V_{R_1R_2}$	Voltage across sample surface between outer ring and central electrode
R_s	Resistance across sample surface
C_{sg}	Capacitance between sensor and ground
C_{sCs}	Capacitance between the sensor and the charged surface
C_{pCs}	Capacitance between the probe body and the charged surface
C_{pg}	Capacitance between the probe body and ground

U_1	Voltage across charged surface
R	Resistor
C_{sCs1}	Capacitance dependant on configuration of the sensor plate and the dielectric permittivity of the space between the probe and charged surface
C_{sCs2}	Variable capacitance
C_{v1}	Capacitance of first varactor
C_{v2}	Capacitance of second varactor
$C_{v1(t)}$	Change in the capacitance of varactor 1 with time
$C_{v2(t)}$	Change in the capacitance of varactor 2 with time
C_{sCs20}	Fixed part of C_{sCs2}
C_{sCs21}	Amplitude of variable part of C_{sCs2}
$U_{C_{sCs2}}$	Voltage across C_{sCs2}
i	Current
C_{Csg}	Capacitance between charged surface and ground
V_v	Voltage across varactor
V_t	Sinusoidal voltage from oscillator
V_p	Voltage at probe
C_v	Varactor capacitance
C_o	Constant part of C_v
C_A	Amplitude of variable part of C_v
q_v	Total charge stored in varactor couple
V_s	Potential on charged surface
C_c	Capacitive coupling
V_r	Reverse voltage
C_{jo}	Zero junction bias capacitance
V_j	Junction potential
G_c	Grading coefficient

R_G	Resistor to adjust gain
A	Effective area
C_1	Capacitance between sensor and sample
C_2	Capacitance between sensor and grounded back plate
P	Probe sensor thickness
X	Probe to sample gap,
M	Length of Probe
L	Length of charged surface
Z	Outer cylindrical electrode
Y	Lower central cylindrical electrode
X'	Upper central ring electrode
X''	Upper central electrode.
W	Grounded upper central tube
S_S	Sample surface
S_V	Sample bulk
l	Length of the sample
R_V	Volume resistance of the sample
I_V	Current across sample volume
ρ_V	Volume resistivity
X^{Sense}	Sensing electrode
I_{Peak}	Peak current
I_{Output}	Output current
I_o	Initial current at t = 0, DC steady state current
$I_{(t)}$	Current at time t
A_1	Pre-exponential term associated with the short time behaviour
A_2	Pre-exponential term associated with the mid time behaviour
A_3	Pre-exponential term associated with the long time behaviour
A_4	Pre-exponential term associated with the very long time behaviour

τ_1	Time constant term associated with the short time behaviour
τ_2	Time constant term associated with the mid time behaviour
τ_3	Time constant term associated with the long time behaviour
τ_4	Time constant term associated with the very long time behaviour
I_{3300}	Average current or Approximate DC steady state current
m	Gradient of curve
R^2	Coefficient of determination
Q_o	Charge offset
Q_t	Charge at time t
Q_1	Initial charge at t = 0

1. Introduction

1.1. Motivation

To improve the performance of pulse power in terms of operating voltage, energy density and pulse repetition rate will require electrical insulation systems to work at higher stresses. This is also a benefit for other electrical systems. An area of concern in both pulse power systems and gas insulated substation/switchgear (GIS) is the build-up and decay of surface charge on the solid insulators in these systems, which can lead to surface flashover, and ultimately to compromised system operation or failure.

The accumulation of charge can cause problems with other insulating surfaces such as those in cables and capacitors, where the large charge accumulation can lead to electrical breakdown which results in damage or destruction of the device. Research into the effect of surface charge on the decrease of the dielectric strength has been going on from the 1980s. Despite the amount of research that has been done in this area, there have been conflicting results.

To assess the significance of this problem, it is necessary to measure the surface conductivity associated with the insulation, as this will control both the build-up and decay of surface charge. It is also important to measure the charge distributions that develop under the expected operating conditions for the insulators to assess their effects on their breakdown strengths.

The aim of this project was to enhance knowledge of the effect of accumulated charge on the surface conductivity, the surface charging/discharging behaviour and the surface charge decay behaviour of polymeric insulators. The project matches the expertise available within the "High Voltage Technologies" group in the measurement of low currents (~ 10^{-13} A) in dielectric systems, and in charging of polymer surfaces.

1.2. Objectives

In order to further develop the knowledge base on the behaviour of charge on the surface of polymeric materials, the following project objectives were defined:

- Development of automated and calibrated systems for measuring surface transient currents and the surface charge for dielectric samples.
- Measurement and comparison of surface conductivities for samples under consideration.
- Measurement of the decay of surface charge.
- Establishment of the correlations between the measured behaviours, leading to enhanced understanding of the mechanisms.

1.3. Thesis Structure

This thesis is divided into 8 chapters:

- ***Chapter 1*** presents the motivation, aims and objectives of the research.
- ***Chapter 2*** provides a comprehensive literature review of the research topic. Starting from fundamental understanding of polymer properties to more technical details of the mechanisms responsible for surface breakdown, conduction, charging and decay. The surface conductivity and surface charge measurement techniques are also discussed along with the $\boldsymbol{\Phi}$-Matrix method employed in this project to evaluate surface charge density distributions.
- ***Chapter 3*** gives a detailed background of the varactor probe sensor which was developed and used in this project to perform surface charge measurements. The design and development of the probe circuitry is presented and simulations to observe probe output are also performed.
- ***Chapter 4*** initially discusses the basic construction and working principle of a capacitive probe. This is followed by a demonstration of the effect of different probe parameters on the output response of the probe by performing simulations in QuickField. The construction of the probe geometry used in this research is presented and the calibration of the complete surface charge measurement probe is also carried out experimentally.
- ***Chapter 5*** describes the development of the surface conductivity measurement system, the arrangement to conduct surface current measurements and the experiments conducted to observe leakage currents, noise and accuracy of the system.

  This chapter also presents the constructed grid system for depositing charge in a controlled manner on a sample surface. This is followed by performing an initial experiment for measuring surface charge on the sample using the varactor probe system developed in chapters 3 and 4. The results from this experiment are used in conjunction with the simulated $\boldsymbol{\Phi}$-Matrix to establish a procedure to obtain realistic set of values for the surface charge density distribution.

- ***Chapter 6*** is based on the experiments performed to observe surface charging/discharging transient currents using the surface conductivity measurement system developed in chapter 5. The first part of the chapter describes the type of samples used and their preparation for experiments. This is followed by presenting the experimental setup and the test conditions for the transient current measurements. The last part of the chapter presents the experimental results, their analysis and discussion.
- ***Chapter 7*** is based on the experiments conducted to measure surface charge decay using the varactor probe system developed in chapters 3 and 4. The chapter initially presents the experimental arrangement, its calibration and test conditions. This is followed by describing the results and analysis. Correlations are made between these results and the experiments conducted to observe the surface transient currents from chapter 6.
- ***Chapter 8*** summarises the achievements and conclusions from the project. It also outlines suggestions for future avenues of the research.

2. Literature Review

2.1. Polymers: Structure and Properties

Polymers are very popular in the high voltage industry for their use as insulation in high voltage appliances. Large band gap (> 6 eV) [1], high breakdown strength (~ 10^9 $V \cdot m^{-1}$), small dielectric losses (normally tan $\delta < 10^{-3}$), high DC resistivity (normally > 10^{16} $\Omega \cdot m$), high resistance to corrosion, ease of production and economic viability are all the properties that make them suitable for extensive use in the power industry [2]. One such example is the use of Epoxy resins in high voltage switch gears and electrical machine insulation. They are a class of thermoset polymers which are formed by mixing two components to form a glassy product at room temperature which has good electrical insulating properties and high permeability in water.

The basic structure of a solid polymer is based on an assembly of molecular chains. Each molecular chain contains additional individual molecules that are bound together by strong covalent bonds, however, ionic bonding has also been observed in a few cases. The polymeric chains are bound together with weak Van der Waals forces. Every unit of a polymeric chain can be considered as an individual molecule with electron states related with the molecular orbitals of other molecules. The orbitals of the molecules overlap each other and this leads to the creation of bonding and anti-bonding states which result in the development of the conduction and valence bands [3]. The presence of these energy bands shows that the energy band gap theory can be used to describe the electrical properties of these dielectric materials.

In simpler terms, the structure of a polymer can be described as one consisting of long chained macromolecules with repeating monomer units. Homo and hetero polymers are two polymers that contain different linkage in the polymeric chain. Figure 1 [2] shows the basic linkage in a homo-polymer chain.

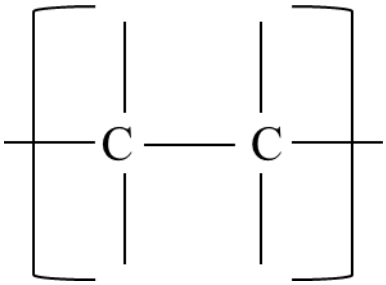

Figure 1: Basic Linkage in homo-polymers following [2].

In a hetero-polymer the linkage will contain some other element instead of carbon. Branching in the main chain of the polymer is very common. It lowers the potential for regular molecular packing hence reducing the density which results in the production of polymers like LDPE (low-density polyethylene). This scenario in polyethylene is shown in figure 2 [2].

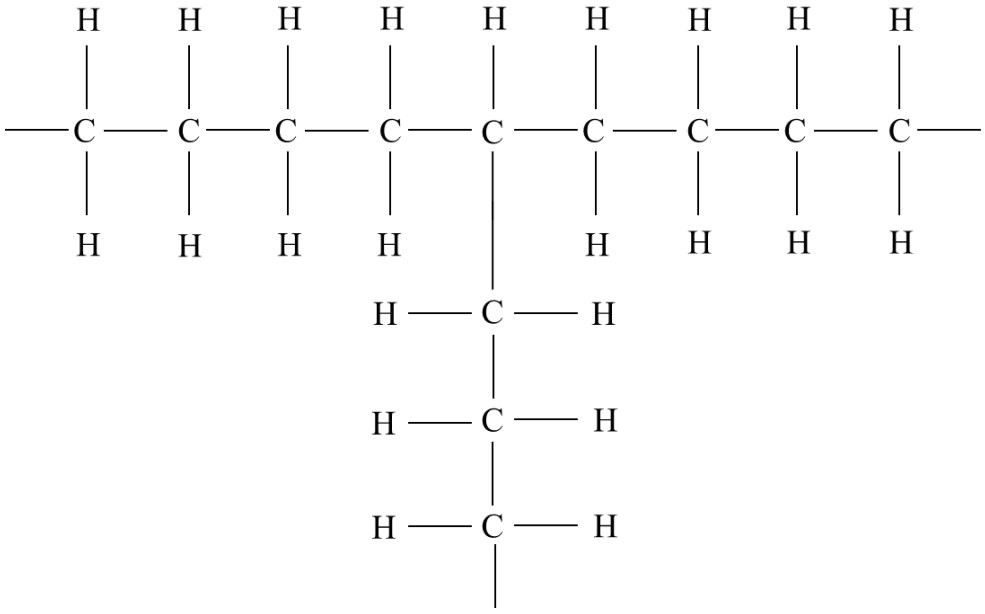

Figure 2: Branching in Polyethylene following [2].

Crystalline polymers contain both crystalline and amorphous regions. Amorphous polymers show different characteristics than crystalline polymers as they don't show any crystallinity. If an amorphous un-crosslinked polymer is cooled through its glass transition temperature then the polymer adopts a glass like state. Co-polymers and ter-polymers are examples of amorphous polymers as they do not have a regular structure. Alternatively, crystalline polymers have a simple and systematic arrangement. Crystallisation requires the molecules to have the ability to align them in a way to become a part of a growing crystal [2].

The electrical breakdown strength of these polymers is influenced by the structure of the crystalline region and the degree of crystallinity which describes the structural order of the polymer [4]. The crystallinity of the polymer will also depend on the impurities and structural defects introduced during manufacture, which can also influence the electrical strength. In the presence of cross links the polymer can be referred to as a gigantic molecule, sine the polymeric chains are now joined together by short, long or even polymeric molecules which effectively produce connecting branches.

The degree of crystallinity and the physical properties of a polymer can vary with temperature as molecular motion of the material varies with temperature. However, at a certain temperature known as the equilibrium melting point $\boldsymbol{T_i}$, the degree of crystallinity neither decreases nor increases. The behaviour of polymers can be characterized in three different ways depending on the amount of temperature rise.

As the temperature rises the polymer adopts a state similar to that of a glass. Further increase in temperature results in the material adopting a rubber like and finally plastic flow state. Figure 3 [4] represents the effect of raising temperature on the electric strength of a linear polymer and also shows the three different states that the polymer adopts with raising temperature. Region 1, 2 and 3 represent the glass, rubber and plastic flow states.

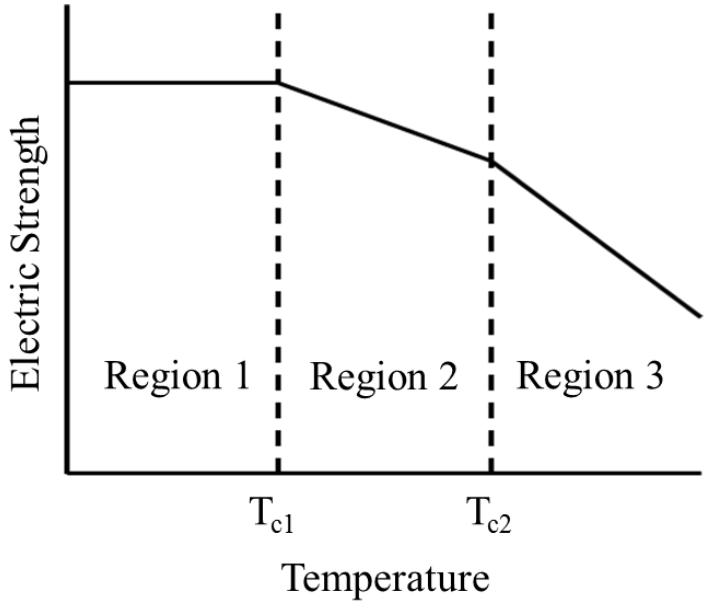

Figure 3: Effect of temperature on electric strength of a linear polymer [4].

Ieda [4] carried out experiments on the electrical strength of polymers by applying DC voltage to eliminate the edge effect, where a region of high electric fields exists due to the presence of the triple junction (section 2.3.1), which is described as the point of contact or

the boundary between metal, dielectric and gas. The triple junction and its effect on the breakdown of a high voltage system is described in more detail in section 2.3.1. It is recognised that the electric strength of polymers is generally in the range of (1 to 9 MV/cm at 20 °C) which is higher than ionic crystals (0.5 to 1 MV/cm at 20 °C) [4]. According to the experimental observations, it was proposed that the electric strength of the polymer can be divided into two different temperature regions. In the low temperature region, the electric strength was observed to rise minutely or could even be considered to be independent of the temperature. The maximum strength of the polymers was obtained in the low temperature region [4]. The reason for high electric strength in the low temperature region is thought to be the scattering of electrons due to dipoles which may result in an increase in molecular weight of the material. The mechanism responsible for the breakdown of the polymer at low temperature region is thought to be caused by an electron avalanche process. On the contrary, the electric strength is observed to decrease in the high temperature region. Due to the rigid skeleton structure of the polymers, they show exceptional thermal endurance at high temperatures.

It is almost impossible to manufacture polymers without impurities as these are added into the material during fabrication process. The added impurities decrease the electric strength and cause an increase in the electric conductivity of the material. Polymers contain intrinsic defects due to structural disorders [3]. Added impurities, free volume and inner stress can all be causes of the defects. In an insulating polymer the defects act like trapping regions and trap charge carriers. Figure 4 shows the two energy bands within a polymer and also shows the localised positions i.e. trapping sites where charge carriers are trapped.

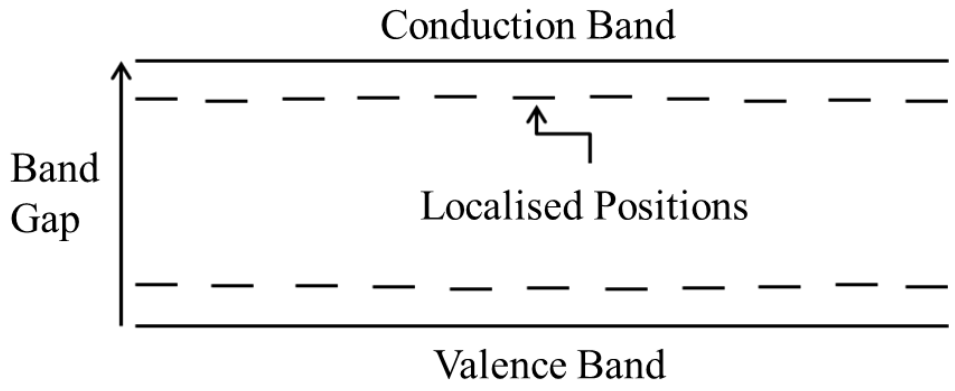

Figure 4: Energy Band diagram with trapping sites.

Intramolecular and intermolecular motions are two different mechanisms responsible for electron transport within the dielectric [3]. Intramolecular forces are responsible for holding the atoms together that produce the molecule and happen inside the molecule. In this phenomenon the transfer of electrons is dependent on the intramolecular bond and the bond of the individual monomer. The conduction band for these cases is expected to be narrow and the band width is expected to be wide. One such example is that of polyethylene where a strong covalent bond exists between the carbon atoms and the monomers are saturated preventing any molecular overlap with carbon atoms on the opposite molecule. In contrast, intermolecular forces are responsible for holding two or more molecules together. Intermolecular forces between large molecules can be an obstruction for electrical conduction. The macromolecules contain weak "Van der Waals" forces and can be considered as a blend of crystalline and amorphous domains. The boundary among these two territories can also act like a trapping region.

Insulating and conducting polymers are two separate classes of polymers:

2.1.1. Insulating Polymers

Insulating polymers have been used widely in high voltage appliances for many years. This is due to them being cheap, having excellent dielectric properties and reasonable polarization. Properties such as narrow band width, large carrier effective mass, wide energy band gap, numerous trapping sites in band gap and low electric conductivity at low electric fields all make them suitable for insulation purposes. They have a comparatively low relative permittivity which points to them being non-dipolar. Polytetrafluoroethylene (PTFE) or perhaps more commonly known as Teflon is widely used in making spacers which are used as mechanical support in compressed gas insulated systems (CGIS). Teflon is a fluorocarbon plastic with a relative permittivity of ~ 2.1 and has a resistivity of ~ $10^{16}\ \Omega/\mathrm{m}$ [5]. It exhibits excellent electrical insulating properties; however, it also contains the ability to store charge for long periods of time which can result in charge accumulation. Figure 5 [2] shows the chemical structure of this thermo plastic as it is obtained by the polymerisation process of tetrafluoroethylene.

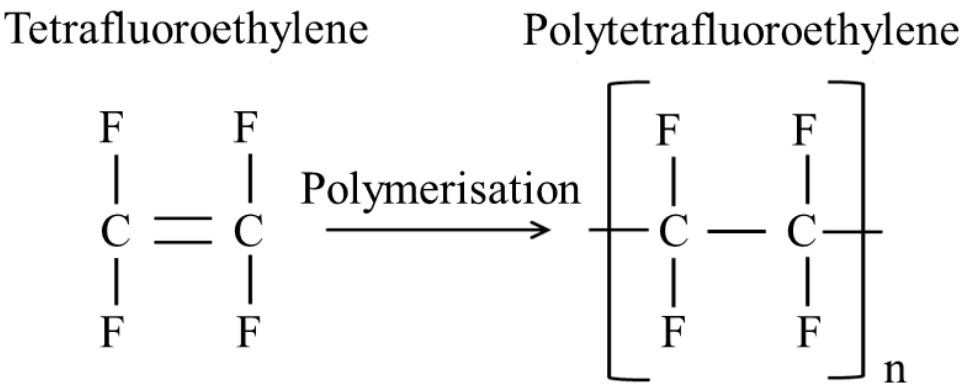

Figure 5: Polymerisation of Tetrafluoroethylene to obtain Teflon.

Some polymers like Polyethylene have a semi-crystalline structure which makes theoretical analysis more difficult. It is hard to find pure polymers as the dipole impurities like moisture and other particle contaminants may be added during manufacturing process. However, studies have shown that these impurities do not significantly affect the permittivity or the conductivity of the material. Under operational conditions, space charge forms near the edges of the electrodes due to the low mobility of the electrons within the insulating polymers. The region of the dielectric beyond the space charge can be considered free of space charge; in this region, the field is assumed to increase linearly with the applied field. It is common to find this type of behaviour in polymers like polypropylene and polyimide. Polyimides are used extensively in microelectronics and passivation. However, over the years there has been a growing amount of failures that have been reported in polymer insulated apparatus. As these systems operate at high stresses, the industry is particularly interested in electrical conduction at high fields and how this would affect the life time of the material [3].

Insulating polymers can further be divided into two different classes:

2.1.1.1. Saturated or Paraffin Polymers

Normally polymers that are used in everyday life are electrical insulators. This is because they are saturated (hard to break), and contain strong covalent bonds. Saturated polymers do not conduct due to the unavailability of free electrons and pi bonds. Polyethylene is a saturated polymer which is popular in the industry for its use as insulation in high voltage environments. Figure 6 shows the polymerisation of ethylene to obtain this thermo plastic.

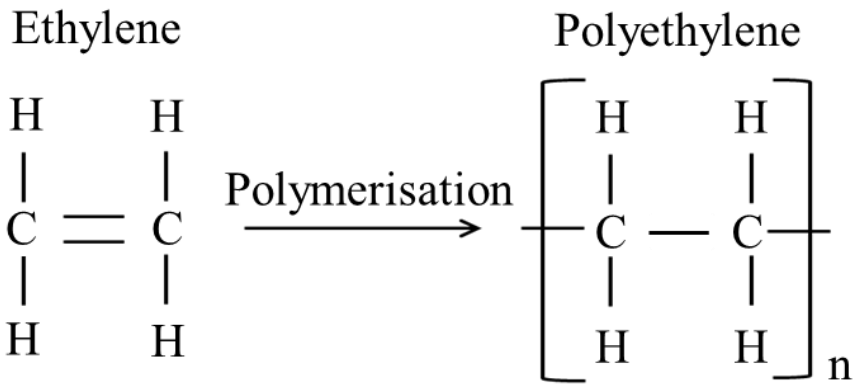

Figure 6: Polymerisation of ethylene to obtain Polyethylene [2].

Intramolecular attraction within the polymeric chains is strong as the molecules are bound together by strong covalent bonds and monomer units are arranged regularly. Semi-crystalline and amorphous parts are formed by the weak Van der Waals forces that keep the polymeric chains bound together. The overlap integral (~ 0.001 eV) between chains is widespread which prevents the valence band to attain an appreciable width. According to theoretical calculations [3], it is predicted that the width of the conduction band for polyethylene is very narrow and the mean free path of the electrons, described as the average distance travelled by carriers between successive collisions, is less than 100 Å [3]. The charge mobility of polyethylene is low (~ 10^{-3} to 10^{-10} cm/V·s) [6]. It is normally thought that the energy band gap of saturated hydrocarbons like polyethylene is large (≥ 8 eV) and that these materials have a narrow conduction band and large valence band.

2.1.1.2. Conjugated Polymers

In conjugated polymers the intermolecular bonding is weak and the conduction band is usually narrow. These polymers have an overall integral of (~ 0.01 eV) and contain conjugate chains where each carbon atom has alternating single or double bonds. The other form of polymer is the conducting and semiconducting polymers which are discussed briefly.

2.1.2. Conducting Polymers

Conducting and semiconducting materials are a new class of polymer. In order for conduction to take place there needs to be a presence of free ions or electrons which can be located in these polymers as they are unsaturated i.e. bonds are weak. Polymer films made from this material is useful in appliances like computers and communication equipment. However, these polymers have some disadvantages that include poor processibilty, majority

of dopants being toxic, lack of stability in open environment and tendency to fail in humid atmosphere. Polypyrrole is an example of this type of polymer and is obtained by the oxidative polymerisation of pyrrole. An example of the chemical structure of this polymeric material is shown in figure 7 [2].

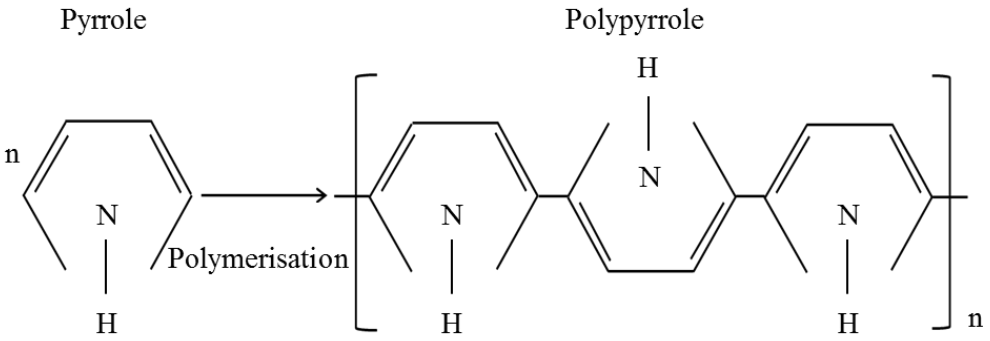

Figure 7: Oxidative polymerisation of Pyrrole.

Conducting polymers can be further divided into two classes:

2.1.2.1. Intrinsically Conducting Polymers

Intrinsically conducting polymers behave like conductors in their pure state as they are inherently conductive. In these polymers, unsaturated sites are common where the electron system will be found to make the polymer conducting. Polythiophene, which is obtained by oxidative polymerisation of thiophene, is a good example of an intrinsically conducting polymer. In this polymer the double or pi bonds support the conducting process. An example of the chemical structure of this unsaturated dielectric material is shown in figure 8 [2].

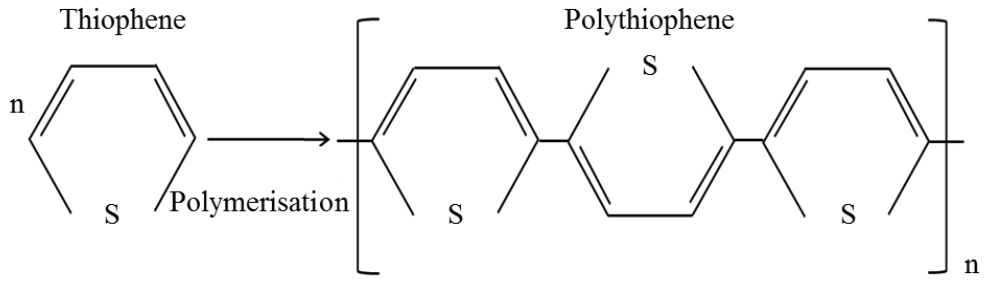

Figure 8: Oxidative polymerisation of Thiophene.

In intrinsic conducting polymers sometimes impurities are added to increase the electrical conductivity. These types of polymers are called “doped polymers”.

2.1.2.2. Extrinsically Conducting Polymers

Polymers in which some foreign substances are added to make them conduct forcibly are called extrinsically conducting polymers. The polymers are made into conductors possibly by blending with intrinsically conducting polymers or elements such as carbon black and metal oxides. The blending process increases the conductivity and enhances the mechanical strength of the material.

Conducting polymers are used in the preparation of antistatic fabric where their use prevents the build-up of static charge hence reducing the attraction of dirt on to the fabric. Other uses include the making of biosensors, button type batteries and photovoltaic cells.

The research in this project is solely based on insulating polymers.

2.2. Influence of Surface Charge on Flashover

In the high voltage industry one of the main culprits in limiting the performance of a pulse power or a gas insulated substation/switchgear (GIS) is the phenomenon of accumulated charge on the surface of the insulators. It is well known that a system that makes use of gas or vacuum for electrical insulation requires solid insulators to support the electrodes. The primary objective of the solid insulator in these systems is to provide separation between the high voltage and the ground electrode. In such cases the phenomena of accumulated charge on the surface of these insulators plays an important role as a limiting factor in the design of the apparatus. This is because any apparatus design would need to consider the practical implication of the “surface flashover” caused by these charges. Charge accumulation on a polymer surface can cause interfacial adhesion. It is also a cause of problems in other polymeric appliances such as cables and capacitors, where the large charge accumulation can lead to electrical breakdown which results in damage or destruction of the device. Another example [7] is that of charge storage devices where leakage causes problems like loss of sensitivity.

It is understood that surface charge is formed due to the interactions between electrons emitted at the cathode/dielectric junction between gas molecules and the solid dielectric itself. At this junction the electron emission takes place at a relatively low voltage. This is because of the energy-level distortion induced by the dielectric. A positive charge is left on the surface of the insulator if an electron with sufficient energy for the secondary field coefficient > 1 strikes it [8]. This initial electron can be emitted at the cathode by any likely mechanism e.g. thermionic emission. Each time an electron strikes the surface of the

insulator; there is a gain of positive charge and release of another electron from the surface. These secondary electrons are accelerated by the field in the gap and may cause the gas to ionise or they can keep colliding with the surface of the dielectric repeatedly causing further electron multiplication. There is a time when the surface charge becomes sufficient enough to attract the emitted electrons back to the surface and produce further positive charge and electron multiplication. The enhanced positive charge on the surface gives encouragement to an electric field at the cathode which adds to the field produced by the applied voltage across the gap. So, now the voltage required to initiate breakdown is lower than that which would be required in the absence of surface charge.

"Surface flashover" can be described as the development of an electrical discharge over or around the surface of an insulator [9]. The "weakest link" in a high voltage system is normally linked with the interactions at the boundaries and electric field [10]. This practice can lead to flashover or other non-desirable outcomes like; encouragement of partial discharge activity which can permanently damage the system as it will also eventually lead to flashover. Flashover is likely to occur at the interface between the solid dielectric and gas/vacuum. If another conductor is added to the equation, this will form a "triple junction" (Gas-Dielectric-Metal) which increases the probability of such incident. In HVDC (high voltage direct current) systems the accumulation of charge on solid dielectrics is considered as a major problem as this can result in field distortion and also reduction in the breakdown voltage of these insulators [11]. The presence of surface charges can alter the behaviour of developing surface discharges. One such observation is that if surface charge is present on the insulator surface, then it is possible to obtain long surface discharges at low voltages [10].

Research into the effect of surface charge on the decrease of the dielectric strength at a solid/gas interface, and the mechanism responsible for the charge accumulation has been going on from the 1980s [12]. The effect of this phenomenon on the flashover voltage is one that cannot be ignored and takes top priority while designing a GIS or CGIT (compressed gas insulated transmission) system. The main aspects being explored are:

- The origin of the charges,
- Defining the distribution of the charges on the surface of the dielectrics,
- The effect of these charge distributions on the flashover behaviour,
- The measures that can be taken in order to prevent the accumulation of such charges.

Despite the amount of research that has been done in this area, there have been conflicting results. Although much data has been collected to establish the factors responsible for

insulator flashover, progress still needs to be made in the development of an analytical model of this experience.

2.3. Surface Breakdown in HV Systems

From past research, it is a well-known fact that electrical insulation breaks down at a lower voltage for a gap that is bridged by an insulator as compared to an un-bridged gap [8]. At low fields, the factors believed to be responsible for surface breakdown are attributed to the non-uniformities in the system which may lead to high field sites, modifications in the developing discharge and the growth of charge on the insulator surface [13]. However, it has been shown that under the influence of high fields, it is the cathode/dielectric junction that plays a pivotal role in the breakdown of the dielectric. It is believed that the presence of surface charge leads to high field sites on the insulator causing field modification that results in the eventual flashover.

Under operating conditions, solid insulators are required to withstand elevated levels of electrical stresses. It is believed that the poor performance of the solid insulators can weaken the overall electrical strength of the high voltage system. This is better understood by observing the flashover at the surface of these dielectrics which occurs at a much lower voltage than that needed to cause a breakdown in the bulk of the insulator. In Vacuum insulated systems, the mechanism that is believed to be responsible for surface flashover of insulators is the charging of the surface of these insulators [13]. At high fields the cathode emits electrons that strike the surface of the insulators which causes charging of the surface. The polarity of the charge depends on the intensity by which the electrons strike the surface of the insulator which is a measure of the energy that the electron occupies. If the surface is struck by low energy electrons then this causes negative charging whereas if it is struck by high energy electrons then this causes positive charging. If high energy electrons repeatedly strike the surface of the insulator and cause sufficient positive charge growth then this will cause field enhancement at the cathode junction which will eventually lead to surface flashover. The breakdown will be caused along the surface of the insulator in the layer of the gas that is released by the surface due to the electron striking.

In compressed gas insulated systems, the solid insulators are usually in the form of spacers. Electrical insulation failure has been observed to occur mostly along the surface of the insulating spacers. In HVDC systems the initial electric field plays a vital role in charge accumulation as the charge reaches the spacer surface by the electric force applied by the field. It has been observed that the mechanism responsible for the charge accumulation is the

gas conduction by ions [11]. The ions travel onto the surface of the spacer by moving in the direction of the electric flux lines. Charge accumulation is more likely to take place on the spacer surface if the spacer has a high resistivity; this is because the trapped charge would propagate along the surface of the spacer if the surface conductivity encourages mobility. The accumulated charge acts against the initial field at the surface of the spacer. This results in the reduction of the normal field component $\boldsymbol{E_{1n}}$ at the gas side whereas there is an increase in the field $\boldsymbol{E_{2n}}$ at the spacer side [11]. A fixed condition is reached where, $(\boldsymbol{E_{1n}(i) = 0})$ and the spacer becomes fully charged when the normal component of the electric field becomes zero.

While designing a high voltage system it is important to consider the implication of high field sites on the insulation. The presence of these high field sites will deteriorate the insulation and is known to cause surface breakdown of the insulation. The breakdown of the insulation can be caused directly by corona discharge which is triggered by the presence of the high field sites or first by the phenomenon of surface charge accumulation of the insulator. Some of the other factors that can also be responsible or influence the breakdown process of an insulator in a high voltage system such as GIS are discussed below.

2.3.1. Effects of Triple Junction and Voids

The Triple Junction can be described as the point of contact or the boundary between metal, dielectric and gas. It is known to be the weakest point in the GIS and care is required when designing this part of the system. It is the zone where partial discharges are most likely to occur. This is because of the mismatch between the permittivity associated with the gas and the solid dielectric. The mismatch causes a field enhancement in the gas and partial discharge activity is initiated as the local field exceeds a critical threshold [14]. Once the partial discharge activity has started this can result in accelerated ageing of the solid insulators and the deposited charge on the surface of the insulators can cause electric field modifications which encourages further partial discharge activity [15]. Partial discharges can be experienced at very low voltages but this depends on other factors like the design of the insulator and presence of contaminants.

Experimental observations carried out in [16] showed that the maximum field existed in the triple junction region. It was observed that sufficient distance was not present for the discharge to develop in the triple junction zone and was formed 2mm-3mm from the triple junction. However, it was observed that, as the gas pressure was increased the discharge moved closer to the triple junction region.

The effect of voids at the triple junction region cannot be ignored. If voids are present in the system, particularly at the triple junction then this can result in the formation of highly stressed gas gaps which can promote corona, leading to surface flashover [13]. Voids are present generally due to imperfect contact between the spacer and electrode. Such problems can be eliminated by coating the surfaces with a layer of conducting material or by shielding the electrodes that are close to the triple junction [5]. For a cylindrical spacer placed within a uniform field, the electric field $\boldsymbol{E_g}$ in a small gas gap due to imperfect contact between the spacer and the electrode is given by equation 1 [17].

$$\boldsymbol{E_g} = \frac{\boldsymbol{\epsilon_r U}}{(\boldsymbol{\epsilon_r d_1 + d_2})} \tag{1}$$

Where,

$\boldsymbol{U}$= the applied voltage.

$\boldsymbol{\epsilon_r}$= the relative permittivity of the spacer material.

$\boldsymbol{d_1}$= the width of the gas gap..

$\boldsymbol{d_2}$= the length of the spacer.

2.3.2. Particle Contamination

In a high voltage system particle contaminants can play a vital role in causing high field sites. In [14] an experimental investigation was carried out on the effect of metal particles on the partial discharge behaviour in the triple junction region under alternating current (AC) voltage. It was found that the presence of such particles near the triple junction region altered the electric field distribution, thus encouraging further degradation of the system. If charged particles exist in a gas-gap then this can initiate breakdown as the particles travel towards the conductor of opposite charge. In case of longer and wire-type contaminants, corona is observed on its tip and this can further alter the breakdown mechanism [13].

In the case where a spacer is added to the gap containing the gas, the breakdown mechanism is not known however it was observed in [18] that the particles accumulate onto the spacer surface where they cause flashover by field modification. The magnitude of the effect of these contaminants on the flashover of the system is unknown and their influence can vary according to different properties of the system like the magnitude and polarity of the applied voltage and the type of insulation being used.

Particle contaminants are almost impossible to remove from the system. However, the influence of these particles can be minimised by the use of particle traps and some spacers

are designed in such a way that the electric field drives the metallic particles towards these traps [19]. Al-Bawy in [5] has suggested that the performance of the insulation can be improved by using a mixture of gases (50% air/SF_6) instead of 100% SF_6. The experimental arrangement and test results to support this claim have not been presented in [5].

2.3.3. Anomalies in the Spacer Surface

Anomalies in the surface of the spacer or poor insulator design are one of the common problems found in the high voltage industry. The irregularities are usually induced during the manufacturing process and are not prominent until after the installation due to contamination of the surface by conducting particles. The variances in the surface of the insulators are a cause of the generation of high field spots in the system, which contributes to the degradation of the insulation by promoting flashover.

The surface roughness of SF_6 insulated systems has a significant influence on the breakdown voltage, especially at high gas pressures [20]. Lederle and Kindersberger [20] carried out experiments to investigate the effect of surface roughness, with and without dielectric coating, on the breakdown voltage. The breakdown voltage of aluminium electrodes in a hemisphere-plane arrangement at an SF_6 pressure of 0.5MPa was investigated. It was observed that the breakdown voltage of the system decreased with an increase in the roughness of the electrode surface. It was also observed that coating of electrode surface with a thin dielectric material reduced the influence of the surface roughness on the breakdown strength.

Even though there is no solution to remove this problem entirely, the coating of the electrodes with a thin dielectric layer does provide a possible cure. This type of procedure can only be carried out on surfaces where surface charges are unlikely to accumulate [5].

2.4. Surface Discharge on Insulators

In a high voltage apparatus surface discharges normally take place at the triple junction. Such discharges deteriorate the surface of the insulator and the residual charge left by them plays a key role in the electric field distortion that eventually leads to flashover. Flashover that is usually a result of field enhancement may occur before the insulating material has deteriorated from the discharge [21]. In order for a surface discharge to be initiated there needs to be a presence of an electric field along the boundary between the solid insulator and a gas. At present the multiple physical process that take place at the head of the discharge, the solid dielectric and the gas are not fully understood [10]. However, it is known that the

mechanisms that are responsible for the initiation and propagation of the discharge are dependent on different factors that include: the type of gas being used, type of dielectric, the distribution of charge in the system and other features like the magnitude and polarity of the applied voltage.

Surface discharges cause the surface charge distributions on the insulators to vary. Even in the case where present charge distribution is known, the discharge that propagates across the surface causes an alteration in the electric field by modifying the charge distribution. As the discharge propagates along the insulator surface, the charge distribution is modified, resulting in further field modification, which leads to additional discharges. The propagation of surface discharge is influenced by existing surface charge on the solid insulator.

In [22], experiments were carried out to investigate the influence of residual charge on the propagation of the discharge by use of high-speed framing and streak cameras, and an electrostatic probe. The results of experiments carried out on insulators with their surfaces free of charge, and on the same insulators with residual charge left by a previous surface discharge of the same and different polarity were investigated. The results obtained from these experiments showed a clear influence of residual charge on the discharge behaviour. One such result is regarding the velocity of the discharge and the length it travels, when the residual charge on the surface is of opposite polarity to that of the impulse being applied to the system. It was observed that in this scenario the discharge travels faster and a longer length as compared with to a dielectric free of surface charge. This result evidently shows that the surface discharge is accelerated by residual charge of opposite polarity.

2.5. Surface Charging Mechanisms

There has been considerable work done on identifying the possible mechanisms by which charge accumulates on the surface of the insulators. However, it has not been possible to identify a single mechanism to be held accountable for this phenomena and it is believed that surface charging is a result of several different mechanisms rather than one dominant mechanism [23].

The phenomena of electrical charging takes place when electrical insulation is subjected to DC stressing. The charging mechanisms can vary with regards to different factors that include the polarity and magnitude of the applied stressing. Another key factor that can influence the charging time and the amount of charge deposited on the surface is the resistivity of the insulator. It is reported in [24] that reduction in the surface resistance causes less amount of charge to be deposited. In [23] investigations were carried out on the

accumulation of charge on Teflon and Polyethylene spacers due to DC stressing between 10 and 30 kV for a period of time. It was observed that charge accumulation took longer (5-6 hours) for a Teflon spacer compared to a Polyethylene spacer (3-4 hours). The difference in charging time was attributed to the variance in the resistivity of the two materials (10^{16} Ω·m for Teflon and 10^{18} Ω·m for Polyethylene). If the insulation does not contain any metallic particles then it is believed that the charging can be as a result of conduction across the surface, conduction through the bulk/volume, and the movement of electric charges caused by electric field emission [24].

As mentioned earlier, there are several different charging mechanisms that can be responsible for charging of an insulator surface. Depending on the different factors these mechanisms can range from micro corona discharge at the triple junction [25], charge from electrode, particle contaminants, ionisation of surrounding gas and field emission.

2.5.1. Charging through Surface and Bulk Conduction

Polymeric materials are well known for their charge retention properties. This property is established in studies as old as 1967 [26], where it was observed that polymeric surfaces retain charge for long periods of time due to the interactions of the charge with the active surface of the material, which results in the modification of surface potential. In some cases the charge on the surface takes a long time to decay and it becomes very difficult to distinguish whether the charging mechanism responsible was through the surface or the bulk [27]. It is believed that conduction through the surface and bulk of the material are two separate mechanisms and are likely to take place when the stressing voltage is too low to cause gas ionisation [23].

Surface charging through surface conduction is known to be influential under DC stressing. It is produced by gradients that create non-linear surface conduction [5]. The gradients are a result of the structure of the insulator surface and the field dependence of the surface conductivity. Charging in this mechanism is stopped after the gradients are cancelled. It is known that no two spacers have completely identical surfaces and slight differences arise during manufacturing process. So, due to the structure difference the surface gradients on each spacer are different and this is the reason why different charge distributions are observed when two spacers are stressed with the same stressing levels.

Charging of the surface through “bulk conduction” is known to be a slow process. If a high voltage is applied across a solid dielectric for a long period of time then some ions in the bulk of the insulator drift to the surface causing surface charging [5]. The distribution of the

normal field at the surface of the solid dielectric directs the conduction of the ions in the bulk. Charge patterns at the surface of the insulator are developed in such a way that the normal field is cancelled out. The phenomenon of surface charging due to bulk conduction is considered important for conditions where DC stressing is applied. It has been shown in [28] that bulk charge accumulation is developed in an insulator with a gradient in bulk conductivity in the same direction as the applied field. This is expressed in equation 2.

$$\rho = -\frac{\varepsilon \bar{E}.\nabla\sigma}{\sigma} \tag{2}$$

Where,

$\bar{E}$ = the applied electric field.

ε = the permittivity of the dielectric.

σ = the conductivity of the dielectric.

The gradient arises from the dependence of the conductivity on the electric field or due to the irregularities in the material. Charges from the volume of the insulator migrate to the surface of the insulator over an extended period of time and can have a big influence on the reduction of dielectric strength. Manglesdorf and Cooke [29] studied volume charging in post type spacers mounted between parallel plate electrodes. It was observed that, for short periods, the spacer could withstand DC voltages of up to 600kV. After stressing for several hours, it was observed that the flashover voltage had reduced to half of its initial value.

2.5.2. Charging by Gas Conduction

Gas ionisation is considered as one of the mechanisms responsible for surface charging of insulators when the voltage applied is high enough to produce gas ionisation. Under this mechanism the solid surface is charged by the conduction of gas ions to the surface [5]. The ions are generated through discharges that take place at the triple junction, insulator surface and at the electrodes due to inhomogeneity in the material. The distribution of the normal field at the surface of the gas side directs the configuration of the accumulated charge at the surface. Charge accumulation at the surface of the insulator continues until the normal field is cancelled out.

2.5.3. Frictional Charging

Frictional charging is considered important in this study as charge can be deposited onto the surface of the dielectric during handling of the test apparatus. Frictional charging occurs if an

insulator is brought into contact with another insulator or a metal and then separated or by rubbing two materials together. It is believed [13] that the material that is being rubbed, initially free from charge, charges positively whereas the rubbing material collects negative charge.

Charge density on the insulator surface can be significantly increased by repeated contact and separation of the two surfaces. If the field above the surface of the insulator reaches a high enough value to cause breakdown of the surrounding gas then this can limit the amount of charge that is generated from repeated contact and separation [13]. The expression for the charge density $\boldsymbol{\sigma}$, for an uncharged polymer surface brought once into contact with a metal is expressed as equation 3 [13].

$$\boldsymbol{\sigma = N_s x_s = \frac{2\varepsilon(\Phi_m - \Phi_q)}{e x_s}} \tag{3}$$

Where,

$\boldsymbol{N_s}$ = the density of the states ranging to the depth $\boldsymbol{x_s}$.

$\boldsymbol{\varepsilon}$ = the permittivity of the polymer.

$\boldsymbol{e}$ = the charge on an electron.

$\boldsymbol{\Phi_m}$ = the work function of the metal.

$\boldsymbol{\Phi_q}$ = the work function of the polymer.

2.5.4. Thermionic Emission Charging

When the temperature of the solid insulator surface is increased, this provides more energy to the electrons on the surface and they become more mobile. There is a time when the component of electron velocity that is normal to the surface of the material becomes sufficient enough to breach the attractive forces. As a result, electrons get emitted from the dielectric surface and positive charging occurs. In case of a conducting material some electrons may be ejected from the surface at room temperature. This is expected as the behaviour of electrons in a conducting material is similar to that of a gas. However, a small number of electrons per unit area per unit time are ejected from the surface. This can be increased substantially as the temperature of the surface of the dielectric is increased. Richardson's equation in [8] provides the relationship between absolute temperature and the charge per unit area per unit time (Current density $\boldsymbol{J}$). This is expressed in equation 4 [8].

$$\boldsymbol{J = A_o T^2 \exp\left(-\frac{e\Phi}{kT}\right)} \tag{4}$$

Where,

$\boldsymbol{A_o}$ = the universal constant.

$\boldsymbol{T}$ = the absolute temperature in kelvins.

$\boldsymbol{\Phi}$ = the work function of the dielectric.

$\boldsymbol{e}$ = the charge of an electron.

$\boldsymbol{k}$ = the Boltzmann constant.

2.5.5. Photo Electric Charging

The surface of a dielectric emits electrons when light falls on it. The photons transmit enough energy to the electrons in the surface to overcome the forces of attraction and positive charging of the surface takes place. In order for this phenomenon to take place, the Einstein criteria for photoelectric emission $(\boldsymbol{hv > \varepsilon_\Phi})$ should be met. The Einstein equation for photoelectric emission is given below [8]:

$$\boldsymbol{E = hv - \varepsilon_\Phi} \tag{5}$$

Where,

$\boldsymbol{E}$ = the energy of the ejected electron.

$\boldsymbol{h}$ = Planck's constant.

$\boldsymbol{v}$ = the frequency of incident light.

$\boldsymbol{\varepsilon_\Phi}$ = the work function of the surface of the dielectric.

2.5.6. Field Emission Charging

Charging by field emission is known to have a greater influence in vacuum insulated systems [5] as the electrons in these systems have a higher energy as compared to GIS. However, it is a very important mechanism where the electron collision with the surface of the insulator causes a secondary electron emission resulting in positive charging of the insulator.

When an electric field is applied across an uncharged insulator, this results in the polarisation of the insulator. The polarisation process can be described as charge migration within the material whereby there is an accumulation of positive charge at one end and negative charge on the other end of the material. The surface charge density $\boldsymbol{\rho_s}$ at any location for a material with electrical conductivity ($\neq 0$) at time $\boldsymbol{t}$ is related to the time constant $\boldsymbol{\tau}$ and expressed in equation 6 [8].

$$\rho_s = \rho_{so}\{1 - \exp(-t/\tau)\} \quad (6)$$

Where,

ρ_{so}= the value of surface charge density under equilibrium and the time constant τ is expressed as equation 7 [8].

$$\tau = \varepsilon/\sigma \quad (7)$$

Where,

σ = the conductivity of the material.

In a gaseous environment the charging of the insulator surface with field emission will depend on the availability of free electrons [13]. Generally it is very hard to attain sufficient field strength in order to cause field emission in gaseous environment. This is because the field strengths in the region of (~ 10^7 Vcm^{-1}) are required to eject electrons from the cathode or to cause an avalanche in the gas that may provide electrons to carry out this charging phenomena, but breakdown of the gas occurs before fields of this magnitude are reached. However, contradicting results have been attained in the past, like in [30], where electron emission at the cathode took place at fields as low as 60-70$kVcm^{-1}$.

2.5.7. Corona Charging

Corona discharge is described as a non-disruptive and self-sustaining discharge [31]. Amongst the different charging mechanisms it is corona charging that is widely used due to the fact that controlled charging can be achieved via this mechanism [32]. Modifications to the charging method were made in order to control the amount of charge deposited as initially there used to be no control over the amount of charge deposited as charging by corona was done by directly exposing the surface to a corona point. The method was later altered and it was established that insertion of a grid between the corona point and the material surface provided much better control over the charging process.

The surface of the material is charged by deposited gaseous molecular ions which are determined by the polarity of the corona applied. The ions charge the surface of the dielectric material in two ways: by remaining stable in the surface or by neutralising the incoming ions by ion migration in/out from the material surface. This behaviour charges the material to the same polarity as the incident ions. It is to be noted that in both cases the charges are located in trapping sites within the surface and sufficient amount of energy needs to be gained for the charges to become mobile [31].

In Gas insulated systems (GIS) one of the most important mechanisms that causes surface charging that eventually leads to flashover is the phenomena of micro corona discharges at the triple junction. It was found in [25] that for a plane spacer with plane electrodes under the application of DC stress the mechanism responsible for surface charging is the phenomenon of micro corona discharges. It was observed that positive carriers were produced when the anode junction was active and negative carriers were produced when the cathode junction was active.

Corona discharge takes place if sufficiently high potential difference exists between asymmetric electrodes. The point plane geometry is a perfect example where corona discharge is likely to take place. It has many applications and one of the most common is the usage of corona in electrical separation of particles from gases. Another popular application is the usage of corona for production of electrets which has had a big influence on manufacturing costs for a number of appliances ranging from microphones to motors [31].

2.6. Mechanism of Charge Transfer from Electrode to Insulator

The Fowler-Nordheim theorem and the Schottky effect are two mechanisms by which charge can be transported from a metal into the insulator. They both use the basic principle in which an energy barrier needs to be overcome by the charge carriers, to migrate from a metal into the insulator. In addition to the lowering of the energy barrier, the Fowler-Nordheim theorem also involves the tunnelling of the carriers through the barrier when the width of the barrier is narrow. In an ideal situation the electron affinity χ, which is described as the energy that is released as the electron becomes a negative ion, will cause the potential barrier to drop as the electrons are excited into the conduction band. If an electron has a greater energy than the electron affinity then it will be ejected from the metal automatically, so in the case where a polymer has negative electron affinity, this will result in an increase of barrier height [2]. However, in practice this is not possible as there are many different factors which will influence the injection phenomena. These factors include the structural defects in the insulator, moisture in the system and imperfect contact between insulator and electrode.

In the Fowler-Nordhiem injection theory charge carriers pass through thin potential barriers by a process known as tunnelling. This phenomenon takes place under the influence of very high electric fields (~ 10^9V/m). Electrons and photons which exhibit wave-particle duality exhibit behaviour opposite to the classic mechanics where it is known that an electron cannot

migrate into a region if it's total energy is less than the potential energy needed to make the transition [2]. So, the carriers that show behaviour of dual nature have a possibility to migrate into the region requiring more potential energy than these carriers might occupy at that time.

The Schottky effect can be explained by an example of electron flow from an n-type semiconductor to the metal. It describes the change in "electrostatics" at the interface between a metal and a semiconductor. As the charge carriers move from one region (metal) into another (semiconductor) or the opposite side, there is a formation of a depletion region, which can be described as the accumulation of positive charge at the boundary which is formed due to the electron donor atoms remaining unscreened. The positive space charge at the semiconductor end causes energy bands to bend and induces an image charge at the metal side of the boundary. The purpose of the image charge is to drop the height of the Schottky barrier, which is the difference between the Fermi level of the metal and the bottom of the conduction band of the n-type semiconductor. The positive space charge now attracts electrons from the metal side which do not have enough energy to flow back to the semiconductor, and there is an accumulation of electrons at the metal end of the boundary.

The level of the energy barrier plays a big role in determining the amount of carriers that may be injected. The height of the barrier $\boldsymbol{\phi}$ depends strongly on the difference between the work function of metal and insulator and also on the conditions surrounding it. The influence of the barrier on carrier injection can be acknowledged by changing the work function, which is described as the minimal energy required for ejecting an electron from the surface of a material. It is expected that the current flow is limited by space charge effects when the barrier height is low, and in the case when the barrier height is high, then the current is limited by the injecting contacts [33]. Wintle [34] has studied the effect of space charge on time dependence in different samples subjected to Schottky injection, where an existence of trapping was observed, but the distribution of trapping sites was not established. The Schottky emission can be expressed as equation 8 [35].

$$\boldsymbol{J = A^{*}T^{2}exp[-\frac{q}{KT}\left(\Phi_{B} - \sqrt{\frac{qE}{4\pi\epsilon_{r}\epsilon_{o}}}\right)]} \tag{8}$$

Where,

$\boldsymbol{J}$ = Current Density.

$\boldsymbol{A^{*}}$ = Effective Richardson constant.

$\boldsymbol{q}$ = Electronic charge.

$\boldsymbol{q\Phi_B}$ = Schottky barrier height.

$\boldsymbol{T}$ = Absolute temperature.

$\boldsymbol{E}$ = Electric field across the dielectric.

2.7. Surface Charge Decay

The study of surface charge decay on insulating polymers has been carried out theoretically and practically over decades. Surface charges can accumulate on the insulator as a result of local field enhancement on particles or protrusions [36], under normal operation of the system, and cause flashover [37, 38]. The charge accumulated can cause an undesirable influence on many different industrial applications, particularly in the high voltage industry, where the accumulation of these charges can potentially degrade the insulation properties of the dielectric e.g. on insulators in GIS apparatuses [39]. Dielectrics in high voltage applications [40, 41, 42, 43] are amongst the core foundation of numerous studies on surface potential decay signifying the importance of understanding the process of the build-up and decay of surface charge.

In order to understand this phenomenon it is important to grasp the knowledge of the charge transport mechanisms involved. Surface charge decay method is one of the more common methods used to investigate this behaviour. The objective of the technique is to deposit charge onto the surface of the dielectric using a DC corona source and measure the behaviour of the charge deposited by use of electrostatic probing. This method prevents any contact with the surface under test and reduces the risk of the charge distribution on the surface of the dielectric to be altered by contact. Although many investigations have been made using these techniques [44, 45, 46, 47, 48, 49, 50, 51, 52], the knowledge on the various parameters involved is not yet consistent.

Ieda in [53] observed the “crossover effect” in the surface potential decay curves analysed under different charging magnitudes. It was reported that the charge decay behaviour of the samples charged initially at a higher potential tend to cross those of the samples with lower initial potential. It is also reported that the decay rate of the samples with a higher initial potential is faster than those with lower initial potential. This observation has enhanced interest and many authors have reported similar effects [41, 54, 55, 56]. It is widely believed that the phenomenon provides evidence of partial injection of the surface charge into the

bulk of the sample. The amount of charge injected into the volume of the dielectric depends on the magnitude of the potential that the surface is exposed to [57].

For a dielectric sample under “open circuit conditions” where the charged surface is exposed to a gaseous environment and the opposite side of the surface lays flat on top of a grounded back plate, it is expected that the decay can occur due to three key mechanisms [58] which are named as, surface conduction [59, 60, 61, 62], bulk neutralization [27, 38, 45, 63] and neutralization due to the surrounding gaseous environment [25, 63, 64, 65]. While analysing the charge decay curves of the dielectric samples under observation, most of the reported studies ignore one or more the charge decay mechanisms. In [66] surface potential decay behaviour on corona charged low density polyethylene (LDPE) was experimentally observed and it was concluded that charge decay thorough bulk neutralisation was the dominant mechanism. It was also noted that the decay in thinner samples was much faster than thicker samples charged to the same initial potential. Whereas, in [40] it was concluded that decay through surface conduction and neutralisation through gas ions were not the dominant mechanisms. As for the former it was observed that the rate of the decay was independent of the surface leakage length and for the later there was a negligibly small decay observed on the thick sample. In [67] charge neutralisation through gas was identified as the dominant mechanism for charge decay on samples with a high resistivity being used in indoor applications such as GIS.

In [68] the influence of the three potential mechanisms mentioned was investigated where the dielectric was simulated as an insulating plate using finite element analysis software. It was concluded that a certain charge decay characteristic was formed as a result of each of the above mentioned mechanism. The impact of the three mechanisms is dependent on the height and the shape of the initial charge distribution, the parameters of the insulator and the properties of the surrounding gaseous environment. It was also reported that assuming only Ohmic and displacement currents contribute to the charge decay, the behaviour can be characterised by a time constant reliant on the properties of the dielectric. Whereas, a time constant dependent on dielectric properties cannot be provided for neutralisation through gaseous ions as this mechanism is strongly reliant upon the test geometry, the properties of the surrounding gas and the magnitude of the initial surface potential. For surface conduction a lateral spread of charges across the surface was observed that remained unchanged until the edge of the dielectric where they could flow to a grounded electrode. The three mechanisms are described briefly below.

2.7.1. Charge Decay through Surface Conduction

The mechanism refers to the decay of electrical charge on the dielectric due to migration of charge carriers along the surface of the insulator. In polymeric materials the charge migration along the surface can be due to the hopping of charge carriers from one localised surface state to another or/and through a thin moisture layer on the surface of the material [69]. The charge leakage is strongly dependent on the magnitude of electric field and takes place due to uneven spreading of surface charge that gives rise to a tangential electric field [70]. The mechanism is likely to dominate at the initial stage of surface charge decay [71] and can be quantified by surface conductivity of the material under observation. The process can be influenced by external factors such as air humidity and pollution as the surface conductivity of the dielectric is also dependent on these parameters. Decay through surface conduction is indicated in cases where an exponential potential decay is observed [72], however, there are cases reported of charge mapping experiments leading to lateral spreading of charge [59] which have not resulted in exponential charge decay.

2.7.2. Charge Decay through the Bulk/Volume

The mechanism refers to the decay of surface charges due to the migration of charge carriers into the volume of the dielectric. The mechanism takes place due to intrinsic conduction, charge injection and polarisation processes in the volume of the dielectric [70]. At low fields the dielectric intrinsic conduction can be considered to be 0. The rate of charge carrier trapping and recombination along with the mobility of these carriers within the volume of the material strongly influences the intrinsic conductivity. It is known to grow at higher electric fields through mechanisms such as the Poole-Frenkel effect and at higher temperatures through ionic conduction [71]. The transport of the charges through the material bulk or charge injection is strongly influenced by factors such as electric field drift, carrier trapping and recombination of opposite charges [70]. The process of charge injection is thought to be the dominant mechanism according to most theoretical models of surface charge decay [73, 74]. Dipolar polarization is another component of charge decay which can be described as a very slow relaxation process [71]. The mechanism is thought to be applicable for a polar material so has been neglected by past models.

Several mathematical models were developed to observe the relative contribution of the material bulk to the total charge decay and it was shown in [72] that the exponential decay type behaviour was attributed to intrinsic conduction whereas, a power law type response is observed for other mechanisms (charge injection and dipole polarization).

2.7.3. Charge Decay through the Surrounding Gas

The process of charge decay by gas neutralisation involves the neutralisation of the deposited surface charges as a result of free ions in the surrounding gaseous medium being attracted to the material surface due to the induced electric field [68]. The free ions in the gaseous medium occupy the free surface traps and screen out the present surface charges or recombine with them. As a result of this interaction a visible reduction in surface charge/potential can be observed. The energy depth of the surface states, strength of electric field, number of free gaseous ions and conditions of their diffusion and drift are all factors that the mechanism is dependent upon [70]. Quantification of this mechanism is complicated as some of the factors depend on the distribution of the electric field around the geometrical arrangement of the system and its surrounding environment. In [75] it is reported that at higher potential values induced by deposited surface charges, the mechanism of charge decay through gas neutralisation can play a significant role in decay of surface charges.

2.8. Surface Charge Measurement Techniques

When surface charge is deposited on a solid dielectric material, as a result an electric field is produced on the dielectric and the surrounding gas environment. Factors such as the voltage magnitude of the supply, dimensions of the material, gap between the source and dielectric, presence of nearby ground objects and the geometry of the experimental setup all influence the strength of the electric field being produced. One of the most known techniques for observing electric field distribution pattern was discovered in the late 17^{th} century by Lichtenburg [76] recognized as the Lichtenburg figures or the dust figures. The basic theory behind this technique is discussed below.

2.8.1. Lichtenburg/Dust Figures

The dust figure method was one of the earliest techniques employed to observe charge distribution patterns. The phenomenon was discovered in 1777 by Lichtenburg [76]. This technique involves the sprinkling of suitable powders on the surface of the insulator after an electrical discharge has occurred. As a result the powder sticks to the surface and can be seen as a characteristic pattern. This technique is simple and relatively inexpensive and the pattern of charge distribution can be visualised. This technique is mostly used in studying charge distributions developed on thin dielectric samples and it is rare to find the development of these figures on thick samples. Figure 9 shows an example of dust figures [76].

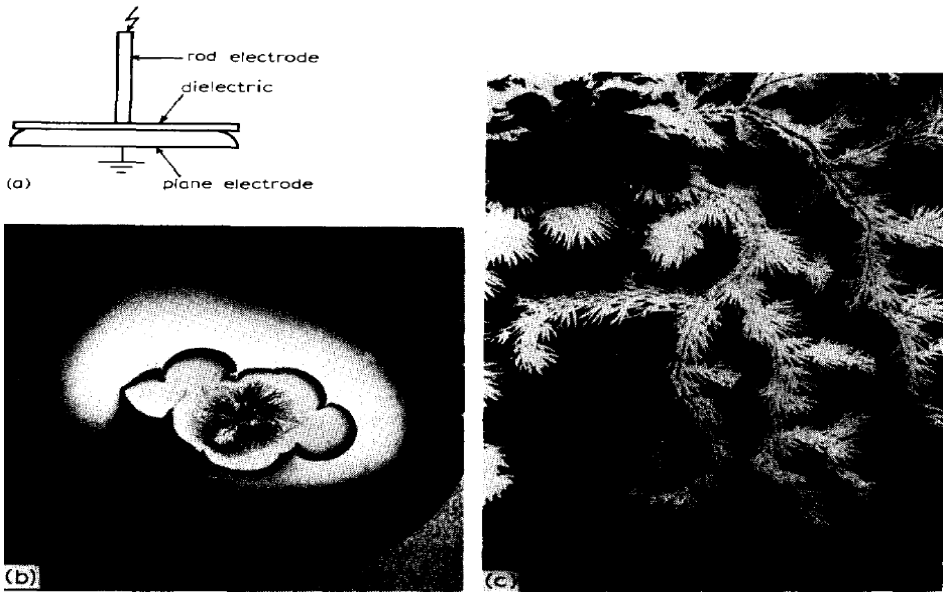

Figure 9: Dust figures in a mixture of 1% SF6 and 99% N2 gas at atmospheric pressure (a) Electrode arrangement; (b) negative figure (-25kV); (c) positive figure, enlarged (+20kV) [76].

Lichtenburg figures were employed in [13] to study the charge distributions on the material surface. To study positive charge, black photocopying powder was used as it does not attach to charge of negative polarity and in order to study charge distribution of varying polarity, sulphur powders and lead oxide can be employed. The surface of the material can be heated by use of an infrared source which makes sure that the powder has stuck to the surface completely.

A drawback of this method is that it is not possible to measure the overall amount of residual charge [77] and over time more popular techniques have been developed that can be classified as contacting and non-contacting methods. Both of these techniques make use of electrostatic probe scanning. In this literature the non-contacting techniques of surface charge measurement are being presented as they are widely used and are preferred over contacting methods of charge distribution measurement. This is because unlike contacting methods, it does not alter the physical state of the charged surface [78]. Although improved contacting methods are being manufactured; the use of non-contacting techniques are the preferred option in applications where a high input impedance of the sensing instrument is required.

2.8.2. Non-Contacting Electrostatic Probe Scanning

Indirect measurement instruments such as induction probes, field mills and electrostatic probes are commonly employed to measure the electric field and surface potential on

dielectrics which can be used to analyse the amount of charge on the surface of the dielectric and the rate of charge decay with time. The very first studies on charge density measurements at the surface of the insulating materials by use of electrostatic probes were reported in the 1960s [79].

These measurement techniques can be classified in two categories: dynamically induced current/voltage sensors and capacitive sensors. The dynamically induced current/voltage sensors require a change in the electric field to sense the field, an example being that of an antenna coupled to a voltage/current measuring system. They are non-useful in detection and quantification of static (DC) electric charge or field as they require variation in the actual field being measured.

The capacitive sensor is of interest in this project. The capacitive sensors not only depend on the variation of electric field but also a change in the capacitive coupling between the electric field and probe. The theory behind the operation of the capacitive sensor based measurement techniques is discussed below.

2.8.2.1. Capacitive Sensors and their Working Principle

Capacitive sensors allow non-destructive and contactless observation of the surface potential and charges. The principle of this technique originates from equation 9 which links the capacitance of a capacitor to charge and potential.

$$\boldsymbol{C} = \frac{\boldsymbol{Q}}{\boldsymbol{U}} \tag{9}$$

Where,

$\boldsymbol{C}$ = Capacitance of capacitor in Farads.

$\boldsymbol{U}$ = Potential difference between electrodes of the capacitor.

$\boldsymbol{Q}$ = Charge accumulated by the capacitor.

The capacitance of a simple capacitor model with two flat plane parallel plates depends on the area of the plates, the gap between the two parallel plates and the kind of medium present between the plates. The capacitance of this parallel plate capacitor can be given as equation 10 where it is assumed that the electric field between the parallel plates of the capacitor is homogeneous and uniform [80].

$$\boldsymbol{C} = \frac{\boldsymbol{\epsilon_o \epsilon_r A}}{\boldsymbol{d}} \tag{10}$$

Where,

$\boldsymbol{C}$ = Capacitance of parallel plate capacitor.

$\boldsymbol{\epsilon_o}$ = Permittivity of free space.

$\boldsymbol{\epsilon_r}$ = Relative permittivity of the medium between the parallel plates.

$\boldsymbol{d}$ = Separation between the plates.

Under this configuration if a voltage $\boldsymbol{U}$ is applied across the plates of the capacitor then the total amount of charge stored in the capacitor is proportional to the potential applied across the capacitor plates. The principle of the capacitive sensor is similar to that of the parallel plate capacitor model where the capacitance is formed between the surface under test and the probe sensor held parallel to each other. Figure 10 shows the basic configuration of a capacitive sensor.

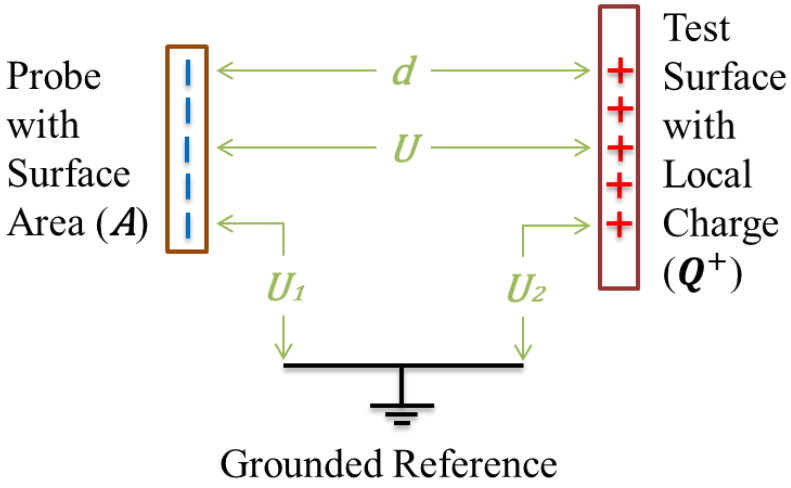

Figure 10: Model of a Parallel Plate Capacitor.

Where,

$\boldsymbol{d}$ = Separation between capacitor plates.

$\boldsymbol{U}$ = Potential difference between the two capacitor plates.

$\boldsymbol{U_1}$ = Potential difference between Probe surface and grounded reference.

$\boldsymbol{U_2}$ = Potential difference between the test surface and the grounded reference.

As the voltage $\boldsymbol{U}$ is the potential difference between the two capacitor plates, this can be expressed as $\left| \boldsymbol{U_1 - U_2} \right|$. Under the assumption that the probe is grounded, the probe to grounded reference potential $\boldsymbol{U_1}$ equals 0 and the potential $\boldsymbol{U}$ between the two capacitor plates equals directly to the potential between the test surface and the grounded reference

U_2. The charge across the capacitor plates can be calculated by using equation 9 and 10 and represented as equation 11 [80].

$$Q = U * \frac{\epsilon_o \epsilon_r A}{d} \tag{11}$$

Where,

$U = U_2$

Using this method the charge on a surface can be calculated providing the potential U and U_1 can be determined.

Under the condition where a fixed charge exists on the test surface, the potential U between the probe and the test surface is also constant. If the separation between the probe and the test surface changes this also causes the voltage U to change. However, to keep the potential U constant it is necessary to adjust the potential difference U_1 as the potential U_2 stays constant. This is possible by removing or adding charge onto the probe. Kelvin probe and induction probes are amongst the popular devices that make use of this method and the theory behind their operation is discussed below.

2.8.2.1.1. The Vibrating Kelvin Probe

The Kelvin probe consists of a vibrating sensor which is connected to a feedback loop. The feedback loop can be provided in the form of an electrostatic voltmeter, field meter or an AC-feedback voltmeter [81, 82, 83]. Figure 11 shows the geometry of the vibrating kelvin probe.

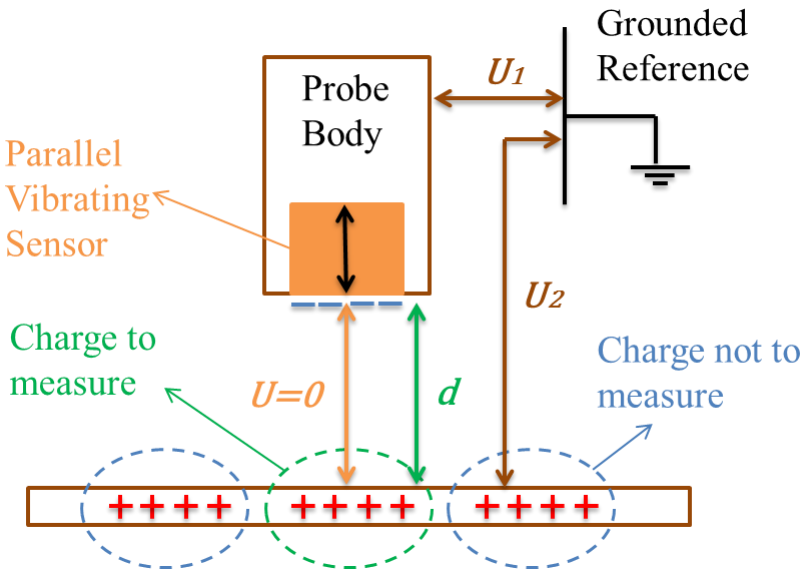

Figure 11: Vibrating Kelvin Probe suspended over a positively charged sample.

The vibrations of the sensor are perpendicular to the surface under test and the amount of current going into or coming out of the sensor plate is proportional to the frequency and amplitude of the vibrations. The Kelvin probe makes use of the field nullifying technique where by the voltage on the sensor to the voltage on the surface is adjusted in such a way that the field between the sensor and the surface is brought to 0 [80]. As the field becomes 0 there is no current flowing to or from the probe so, whenever this phenomena occurs, at that point the potential on the sensor is equal to the potential $\boldsymbol{U_2}$ of the tested surface.

T.Oda and K.Ueno [84] made use of Kelvin probe technique in which high frequency (30 kHz to 40 kHz) vibrations for quick response and high sensitivity are observed by the use of a ceramic piezo-electric element. In [85] a kelvin probe based sensor was utilised to study the surface charge distributions on cylindrical polymeric insulators consisting of a glass fibre reinforced epoxy core covered with a sheath of silicon rubber. Charge distributions were observed for surface charging through corona and DC stressing. Charging by negative corona yielded higher surface potentials than charging by positive corona. Homo charge near the electrodes was observed for pre-stressing with negative DC.

The technique has several advantages as the measurements are independent of the probe to test surface distance within a certain range, it also reduces the risk of discharge between the probe and test surface gap and there is a reduction in measurement errors due to capacitive couplings between both the (sensor and probe body) and the surface being absent. However, like every measurement instrument, kelvin probes have their limitations which are reviewed by Noras and Pandey in [83]. Some of the major flaws include the systems high sensitivity to noise which can cause errors in measurement as any mechanical or electromagnetic noise might cause offset in the measured current. Limitation also comes from the fact that in order to maintain a high resolution it is required that the system be used within the recommended surface to probe spacing that is usually within a few millimetres. This is because measuring beyond this distance will cause the probe to pick up unwanted signal from neighbouring charges.

2.8.2.1.2. Induction Type Probe

Induction or Scanning mode devices are capacitive sensors where the capacitance between the sensor and charged surface is varied by the mechanical motion of the sensor being parallel to the surface under test. Figure 12 shows a schematic diagram of this device [80].

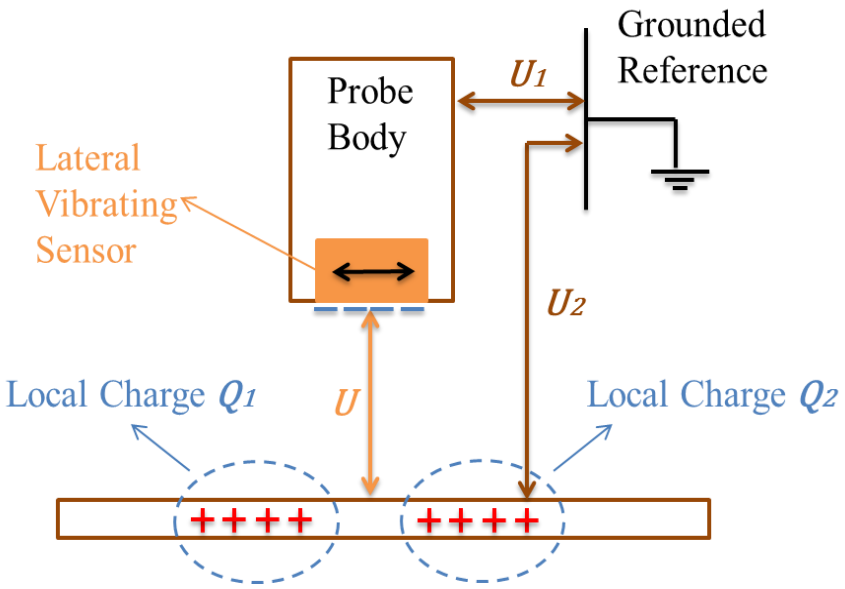

Figure 12: Induction type probe suspended above a charged sample.

If the separation $\boldsymbol{d}$ between the sensor and the test surface remains constant then the capacitive couplings between sensor and test surface also remains constant. However, as the sensor vibrates laterally to the test surface, the potential induced on the sensor will vary due to the non-uniformity of the charge distribution on the charged surface. The change in the electric potential $\boldsymbol{U}$ detected across the sensor can be used to calculate the current detected across the sensor and expressed as equation 12 [80].

$$\boldsymbol{I_{Sensor}} = \frac{\boldsymbol{d_U}}{\boldsymbol{d_t}} * \boldsymbol{C} \tag{12}$$

The amount of current detected through the sensor also varies with the speed of the vibrations of the sensor plate. The faster the vibrations the higher the current sensed by the sensor. This is also the case in the vibrating kelvin probe. The system however, has a drawback that as the sensor vibrates laterally it tends to average the surface potential beneath. This causes unwanted neighbouring charge to also get averaged in the actual signal being measured and causes measurement errors.

2.8.3. Proposed Varactor Technique

Other examples of capacitive sensors include field mills [86, 87, 88]and electrostatic voltmeters [81, 89]. Both techniques are effective however, lack of precision in the former and added complexity and relatively high cost of the latter increase the need for a more precise, simpler and cost effective measurement device. Limitation in these measurement

techniques predominantly originate from the fact that they use mechanical modulation of the capacitance between the probe and the electric field being sensed.

Voltage controlled variable capacitance diode (Varicap), Metal-insulator-semiconductor (MIS) and Metal-oxide-semiconductor (MOS) are a few devices whose capacitance can be varied electronically and provide a possible path to avoid mechanical modulation of the capacitance between probe and surface. The idea of using varactor diodes as an electronic way of modulating the capacitance instead of mechanical modulation employed by devices such as the vibrating capacitive probe is of interest in this project. The technique has not been applied in the non-contacting measurement of surface charges on solid dielectrics.

The proposition to use varactor diodes as a means to measure low currents was first made in 1979 by Herscovici [90].The technique can prove to be a cost effective alternative without the need to use mechanical modulation of probe to surface capacitance. This may also provide the user with a greater degree of freedom compared to some of the limitations that exist with traditional capacitive sensing techniques like the resolution problems with the kelvin probe. The charge measurement system based on the technique proposed by Noras [91, 92] is of interest in this project. The measurement system was used to detect quasi-electrostatic field of a bullet. The theory and development process behind the system is described in detail in chapter 3.

2.9. Surface Charge Density Calculation

The measurement of surface charge density on solid dielectrics has been of interest for more than 50 years [93]. Once the surface potential values have been obtained from the electrostatic probe scanning, the next step is to convert these potential values into meaningful surface charge distribution profiles. This process requires knowledge of the potential and charge densities that were present under the exact conditions when the measurements were made. Calculating electrostatic field is the general approach which can be used to evaluate this relationship. The complexity of the calculation depends on the geometrical configuration and the test object under consideration. It ranges from a simple analytical to a complex numerical problem, in which case, an electrostatic field solving software is employed.

For example a simple relationship between the potential $\boldsymbol{V}$ and the charge density $\boldsymbol{q_s}$ for a flat sample under open air configuration can be derived from figure 13 where a kelvin probe is being employed to scan the surface of a dielectric with thickness **d** and permittivity $\boldsymbol{\epsilon}$. It is

assumed that the sample surface is uniformly charged and that space charges in the bulk of the sample are insignificant.

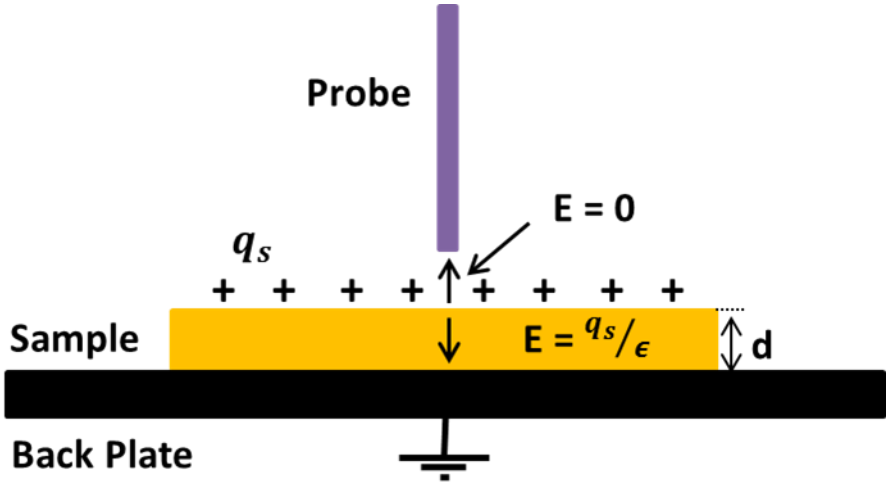

Figure 13: Electric Field as a result of Kelvin probe scanning of the system.

The surface charge is only coupled to the grounded back plate. This is because the potential of the probe is identical to that of the charged dielectric which results in the electric field between the probe tip and the surface of the material becoming 0. The resulting relationship between the potential $\boldsymbol{V}$ and the charge density $\boldsymbol{q_s}$ is given as equation 13.

$$\boldsymbol{V = \frac{d}{\epsilon} * q_s} \tag{13}$$

It is important to note that this relationship has been derived for a simple geometry and it becomes invalid for more complex geometries where both normal and tangential field components add complexity to the field structure. These cases require a more detailed evaluation.

2.9.1. Previous Methods

The effect on the response of the probe due to the influence of the neighbouring charges has to be considered. This has not always been the case, as in earlier studies [26, 94, 95] electrostatic probing was conducted without calibration on thin dielectric samples with a grounded back plate and the potential values were directly converted to surface charge density. An example being that of the very first study reporting the use of the capacitive probe by Davies [26] where, the probe response was linearly related to the surface charge density. The technique limits the accuracy of the system and does not account for the influence of the nearby charges on the total output response of the probe.

Al-Bawy [5] employed a similar approach to thicker dielectric samples and reported inaccuracies in the measurement of charge distributions due to their probe lacking resolution due to the influence of neighbouring charges. For thick dielectrics, multipoint measurement along with numerical field calculation was proposed by Takuma et al. [96] as the only accurate way to obtain true surface charge density**.**

Pederson's $\boldsymbol{\lambda}$ function [97] was employed by Rerup et al. [98, 99] to model the response of the probe to more distant charges. Their approach did not involve the use of a 3 dimensional (3D) field solver to evaluate the response function of the probe adding inaccuracy in the results. Ootera and Nakanishi [100] developed an analytical method based on 3D surface charge method to solve the problems associated with capacitive probing and used it on cone type spacers in ±500kV GIS. Sudhakar and Srivastava [101] also employed a surface charge simulation technique [102] to obtain charge distribution on a spacer and found that the matrix equations resulting from the electrostatic field analysis exhibit similar degree of complexity to that experienced by Ootera and Nakanishi [100].

An improved technique based on the refinement of Pederson's $\boldsymbol{\lambda}$ function [97] proposed by Faircloth and Allen [103, 104] is of interest in this project, the technique is more flexible as it can be applied to a wide range of dielectric profiles. It also addresses the problems of the $\boldsymbol{\lambda}$ function and the probe geometry.

2.9.2. $\boldsymbol{\Phi}$-Matrix Technique

In this technique the surface of the dielectric is divided into a number of different elements dependent upon the geometry of the test object and the scanning procedure. The elements do not have to be square in geometry and an equal number of vertical and horizontal elements is not necessary [103]. The notion behind this technique is to account for the contribution that charges at different locations on the surface of the sample make to the overall response of the probe above a fixed position over the sample [104]. The technique requires the potential due to the charge distribution to be measured at a number of positions equal to the number of elements. Frequently these measurements are performed directly above each element but this is not required.

For a surface divided into $\boldsymbol{n}$ elements, the potential $\boldsymbol{V_{ij}}$ induced on the probe tip at the position of the $\boldsymbol{i_{th}}$ element due to a unit charge being present at the $\boldsymbol{j_{th}}$ element can be represented by:

$$\boldsymbol{V_{i,j} = \Phi_{i,j}} \tag{14}$$

The overall potential induced on the probe tip above a fixed position on the sample is illustrated by figure 14, where the probe is suspended above the first of the measurement positions for the surface.

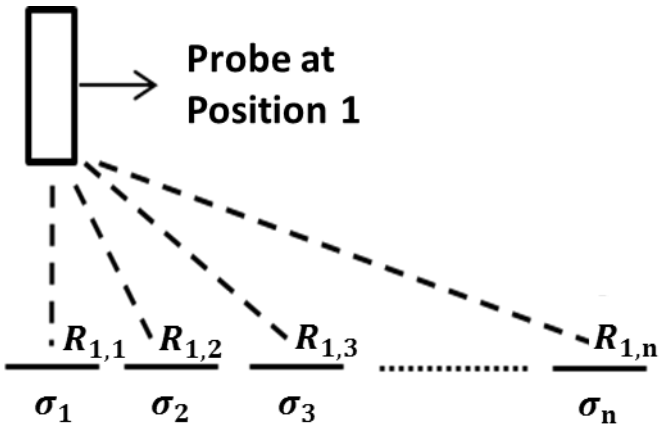

Figure 14: Probe above position 1 of n positions above sample surface.

At this position the total potential $\boldsymbol{V_1}$ on the probe is the sum of contributions from all measurement positions with reference to the probe position. This can be expressed as:

$$\boldsymbol{V_1 = \frac{\sigma_1}{4\pi\varepsilon_o R_{1,1}} + \frac{\sigma_2}{4\pi\varepsilon_o R_{1,2}} + \frac{\sigma_3}{4\pi\varepsilon_o R_{1,3}} + \cdots \frac{\sigma_n}{4\pi\varepsilon_o R_{1,n}}} \tag{15}$$

After obtaining the overall potential value for position 1, the calculations are made for the probe being positioned above position 2 shown in figure 15.

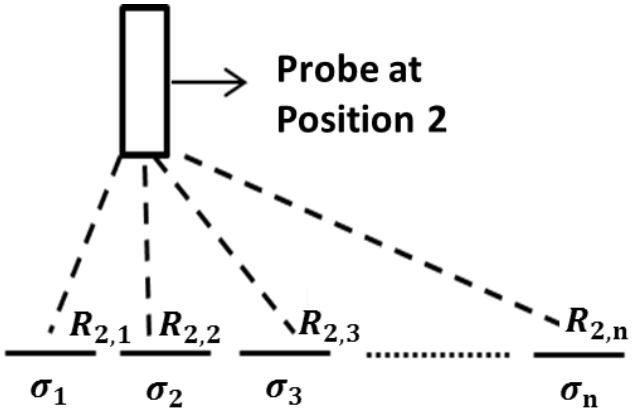

Figure 15: Probe above position 2 of n positions above sample surface.

The total potential $\boldsymbol{V_2}$ can be expressed as:

$$\boldsymbol{V_2 = \frac{\sigma_1}{4\pi\varepsilon_o R_{2,1}} + \frac{\sigma_2}{4\pi\varepsilon_o R_{2,2}} + \frac{\sigma_3}{4\pi\varepsilon_o R_{2,3}} + \cdots \frac{\sigma_n}{4\pi\varepsilon_o R_{2,n}}} \tag{16}$$

A general expression for the total potential at the probe tip at position $\boldsymbol{i}$ can therefore be given as:

$$\boldsymbol{V_i = \Sigma_{j=1}^{n} \Phi_{i,j} \sigma_j} \quad \text{[85](17)}$$

Where,

$\boldsymbol{\Phi_{ij}}$ = Potential at $\boldsymbol{i_{th}}$ measurement position due to a unit charge density at the $\boldsymbol{j_{th}}$ element.

$\boldsymbol{\sigma_j}$ = Surface charge density at $\boldsymbol{j_{th}}$ element.

There are a total of $\boldsymbol{n}$ measured potential values and it is to be noted that each value is a function of $\boldsymbol{n}$ surface charge densities. The measured potentials and the unknown charge densities can therefore be grouped into two vectors $\overline{\boldsymbol{V}}$ and $\overline{\boldsymbol{\sigma}}$ and can be related through a matrix of $\boldsymbol{\Phi}$ values shown as the expression in equation 18.

$$\boldsymbol{[V]_{n,1} = [\Phi]_{n,n}[\sigma]_{n,1}} \quad \text{[85](18)}$$

This process is repeated until the potential values for $\boldsymbol{n}$ number of probe positions is obtained. The resulting matrix equation can be expressed as equation 19.

$$\begin{bmatrix} V_1 \\ V_2 \\ \vdots \\ V_n \end{bmatrix} = \left[\frac{1}{4\pi\varepsilon_0}\right] * \begin{bmatrix} \frac{1}{R_{1,1}} & \frac{1}{R_{1,2}} \cdots & \frac{1}{R_{1,n}} \\ \frac{1}{R_{2,1}} & \frac{1}{R_{2,2}} \cdots & \frac{1}{R_{2,n}} \\ \vdots & \vdots & \vdots \\ \frac{1}{R_{n,1}} & \frac{1}{R_{n,2}} \cdots & \frac{1}{R_{n,n}} \end{bmatrix} * \begin{bmatrix} \sigma_1 \\ \sigma_2 \\ \vdots \\ \sigma_n \end{bmatrix} \quad (19)$$

Rearranging this equation gives an expression which can be used to evaluate the surface charge densities.

$$\boldsymbol{[\sigma] = [\Phi]^{-1}[V]} \quad \text{[85](20)}$$

The process of solving these equations can get complicated, so numerical calculation tools are employed. The method used to employ the $\boldsymbol{\Phi}$-Matrix is described in chapter 5.

2.10. Mechanisms of Conduction in Polymers

Polymeric insulators have many great properties that make them suitable for insulation in the high voltage systems. One such property is the ability of these materials to store charge for long periods of time. This has led to them being used in the manufacture of a wide range of appliances such as electrets and xerographic photo-receptors [105]. It is important to gain a better appreciation of the different properties such as electrical conduction and breakdown of polymeric materials so that advancements in the different applications can be made and the performance of these insulators can be improved.

In order for electrical conduction to take place, carrier's must be injected into the material via electrical contact which leads to trapping and recombination of the carrier species [3]. Energy is evolved when a carrier moves from a high energy state to a low energy state. The energy dissipated is equal to the potential difference between the two states and results in the breaking of polymer bonds that leads to further traps in the material. This process leads to degradation of the polymeric material as it causes the electrical aging of the material. The electrical conductivity $\boldsymbol{\sigma}$ can be expressed in terms of charge carrier Mobility $\boldsymbol{\mu}$ and density $\boldsymbol{n}$ [6]. Equation 21 shows this expression.

$$\boldsymbol{\sigma = \Sigma q_i n_i \mu_i} \qquad \text{[6](21)}$$

Where,

$\boldsymbol{q_i}$= the charge on $\boldsymbol{i_{th}}$carrier species.

Electrical conduction in solid dielectrics is influenced by various different factors. The chemical and physical structures and additives all affect the conduction process in the dielectric material. In [105], the effect of polarity of charge carriers on the electrical conductivity of different polymers was studied and it was found that, injecting carriers from a corona electrode introduced more carriers into the material than were introduced through an evaporated metal (Aluminium) electrode. The currents induced on the Polyethylene sample by the corona electrode were observed to be at least two to three orders of magnitude above that of the evaporated metal electrode. It was also observed that, negative carriers had a greater influence on the current than positive carriers in polyethylene. It was suggested that, using the corona electrode, some carriers reach the surface of the specimen with some kinetic energy, which assists the carriers to penetrate into the bulk of the specimen. It was also proposed that excited molecules and/or corona light would also assist carriers to be injected from the surface. These were possible reasons why the corona electrode was able to inject carriers more easily than the evaporated metal electrode.

It is known that, polymeric insulators exhibit low conductivity at low applied fields as they contain many localised states in the band gap. Electrical conduction at high electric fields is a subject of great interest in industry and a lot of work has been done on the electrical conduction and breakdown of polymers [3]. The subject of electrical conductivity and breakdown of polymers is not fully understood as until now a consensus has not been established and further work in this area is ongoing. The section below is a review of different conduction mechanisms that are involved at low and high fields.

2.10.1. Low-Field Conduction (~ 10^4 V.cm^{-1})

At low electric fields polymers are known to exhibit low electrical conductivity through ionic and Ohmic processes. The conduction at low fields tends to follow an Arrhenius type relationship [2]. Equation 22 shows this expression.

$$\boldsymbol{\sigma(T) = \sigma_o exp[^{-\phi}/_{k_B T}]} \quad [2](22)$$

Where,

$\boldsymbol{\phi}$ and $\boldsymbol{\sigma_o}$= Constants that are determined experimentally.

The low field can be described as the average field $\boldsymbol{F}$, which is smaller than the critical field $\boldsymbol{F_{th}}$ required to initiate mass injection of carrier species into the material through the electrical contacts [3]. The average electric field $\boldsymbol{F}$ can be expressed as equation 23.

$$\boldsymbol{F = \frac{E}{d}} \quad [3](23)$$

Where,

$\boldsymbol{E}$ = the applied electric field.

$\boldsymbol{d}$ = the thickness of the dielectric material.

2.10.1.1. Ionic Conduction

Ionic conduction follows an Arrhenius type relationship for both high and low fields. The structure of a polymer doesn't contain a regular polar lattice this suggests that the theory of ionic conduction which requires mobility of ions within the material does not directly apply to polymeric materials. However, in this case the theory follows the hopping phenomena which are widely appreciated in polymers. The carrier species hop over the potential barriers that are modified in the presence of an electric field giving the hopping process a greater probability of happening in the direction of the field [2]. The process of conduction depends on the production of ions and the ability of these ions to move freely. The ions may arise from electrolytic action at the boundaries between electrodes and insulator or by the breakdown/decay of the electrodes or insulator. Intrinsic and extrinsic conduction are the two types of ionic conduction mechanisms.

Intrinsic conduction is possible in polymers that contain ions and also polymers that contain groups to cause ionisation. The side groups or main chains of the structure of the material are dissociated and this process is followed by carrier transfer through the hydrogen bonded linkages. Intrinsic conduction is expected to increase with temperature. An example of this

behaviour is provided by polyimide at high temperatures (120 °C) [2]. Sulphonated polystyrene is an example of a polymer which exhibits extrinsic conduction. In this mechanism, ions that are not part of the chemical structure of the material remain as additives or contaminants in the material and filter through the structure.

The knowledge of electrical conduction in polymers is incomplete and in some cases it becomes difficult to identify the charge carriers responsible for transportation of charge in the material. However, various studies point to the electrical conduction at low fields being ionic in nature. The dependence of the conductivity on pressure, free volume, degree of crystallinity all support the theory that ionic conduction can be identified as one of the low field mechanisms. From past experiments the observation of faradays law in a gas evolution experiment provides further evidence in support of this theory [106].

2.10.1.2. Ohmic Conduction

At low fields it is believed that the relationship between voltage and current is identical to "Ohm's law". However, when low electric fields are applied to solid insulators it becomes difficult to establish the conduction process. This is because low currents and large transients may be observed due the relaxation effects in the insulator.

In "Ohmic conduction" the carrier species obtain an average velocity in the direction of the applied field. The carrier species are predicted to have high mobility in the Ohmic conduction model however this is not the case in insulators. If the conduction model is modified by including traps into the band gap of the material then this results in lowering of the conductivity due to lack of mobility. The Ohmic conduction model can be divided into two models which include: "Trap free" and "Trap-limited" conduction models [2].

In the trap free model the electrons move freely before an electric field $\bar{\boldsymbol{E}}$ is applied. After the application of the electric field the electrons experience a force in the opposite direction to the electric field. This is due to the fact that electrons contain a negative charge $-\boldsymbol{e}$. The force $\boldsymbol{F}$ exerted on the electrons can be expressed as equation 24 [2].

$$\boldsymbol{F} = -\boldsymbol{e} * \bar{\boldsymbol{E}} \qquad [2](24)$$

The trajectory of the electrons between collisions changes from straight lines to a parabola. There is a resultant drift velocity that is experienced by the electrons and this is opposite to the electric field due to the opposing force. The drift velocity induces a current $\boldsymbol{I}$ that can be expressed in terms of mobility $\boldsymbol{\mu}$ which can be described as the drift velocity per unit electric field $\boldsymbol{E}$ [2]. This is shown in equation 25.

$$\boldsymbol{I = n.e.\mu.E} \qquad [2](25)$$

Where,

$\boldsymbol{n}$ = the number of electrons per unit volume.

$\boldsymbol{e}$ = the charge of an electron.

In the trap free model the drift velocity is of very small magnitude so the influence of this on the average velocity of the electron is minimum and the effect on the mean free path and mean free time between collisions is insignificant. In the trap-limited Ohmic conduction model, traps are introduced in the band gap of the material. This has an adverse effect on the mobility of the charge carriers. It now takes the carriers a longer time to drift the same distance that was travelled faster when no traps were present. This has effectively reduced the mobility of the charge carriers and decreases the conduction.

2.10.2. High-Field Conduction (> 10^6 V.cm^{-1})

Until now the mechanisms of electrical conduction at high fields have not been fully understood. One of the reasons for this ambiguity is because of the irregularities in the structure of polymeric insulators. A lot of work has been done in this area and different theories have been presented to describe the behaviour of voltage-current characteristic under high fields. In [107] work is carried out on the voltage-current characteristic of polyethylene films at different temperatures and the behaviour of current was observed to be strongly dependant on temperature. However, at high voltages a non-linear behaviour was observed and a phonon assisted tunnelling model was proposed to be responsible. Adamec and Calderwood [108] proposed that the "Poole-Frenkel" mechanism was responsible for the creation of carrier species which carry out the conduction process at high fields. On the contrary, "Schottky emission" is proposed as the likely conduction phenomena in Polyethylene films in [109]. However, Bahri and Singh [110] have studied the conduction phenomena in thin polyvinylchloride films at high and low temperatures with high applied electric fields, and according to their observations, the two mechanisms mentioned above cannot be held responsible as potential conduction mechanisms at high temperatures. Conduction at high fields can be divided into three categories [111]:

- The Space Charge Limited Type Conduction (SCLC)
- Bulk Limited Type Conduction (Poole-Frenkel and Hopping Mechanisms)
- Electrode Limited Type Conduction (Schottky Emission and Fowler-Nordheim)

The electrode type mechanisms have been described in section 2.6. The main features of the SCLC and bulk limited type conduction mechanisms are discussed below.

2.10.2.1. Space Charge Limited Type Conduction (SCLC)

The accumulation of space charge in the volume of insulators is a major problem in high voltage insulation as it leads to uncompromised insulation failure. Space charge can be described as "uncompensated" real charge which is generated in the volume of the material due to mechanisms such as: charge injection from the electrodes, charge decay into the bulk and thermal ionisation of contaminants in the volume [112]. Under the influence of high electric field (≥ 10kV/mm), space charge forms in a dielectric due to charge injection from the electrodes. The electric field may cause the thermal ionisation of contaminants in the volume of the material which leads to space charge formation. Other mechanisms include the application of mechanical or thermal stress to a polarisable material. In some cases space charge in the volume of the material is initiated without the above mentioned mechanisms. At particular points in the bulk of the material the breakdown voltage is exceeded by the local field enhancement that is caused by the field modification due to space charge accumulation and this causes breakdown of the material. Space charge in the bulk of the material with equilibrium density $\boldsymbol{\rho}$ can be expressed as equation 26 [112].

$$\boldsymbol{\rho} = \boldsymbol{J}.\boldsymbol{\nabla}\left(\frac{\boldsymbol{\varepsilon}}{\boldsymbol{\sigma}}\right) \qquad \text{[112](26)}$$

Where,

$\boldsymbol{J}$ = the steady state bulk current density.

$\boldsymbol{\varepsilon} = (\boldsymbol{\varepsilon_r}\boldsymbol{\varepsilon_o})$, the absolute permittivity of the material.

$\boldsymbol{\sigma}$ = the conductivity of material.

A lot of work has been done on the influence of space charge on high field conduction and breakdown in polymeric materials. Several different techniques have been used to measure space charge in insulators so that a better understanding of this problem can be gained. In [113] a review has been carried out on the different techniques to measure space charge and space charge distributions in polyethylene films. It is observed that the distribution of space charge in polyethylene depends on various factors including the electrode material and additives like antioxidants that increase the hetro-charge in low density polyethylene (LDPE) film. In [114] an air gap structure was employed using a modified pulse electro acoustic (PEA) technique in order to study the influence of space charge on the current in LDPE. It

was observed that the dominant conduction mechanism was the space charge limited current (SCLC). The dominance of this mechanism depends on various factors that include: polarity of charge, its concentration, distribution of trapping sites in the material, mobility of charge and the state of the injecting contacts [2].

For SCLC mechanism to take place a large amount of carriers need to be injected into the material. This way the charge from the thermal carriers can be neglected [114]. The thickness of the dielectric material has a big influence on the SCLC mechanism as the injection of excess charges requires high electric fields. The mechanism is generally found in thin insulating films. This is because in a thin film with high dielectric constant although initially there will be a small amount of charge carriers, more carriers can be added by the injecting contacts which can lead to charge build-up in the bulk of the material. This suggests that at the start, the amount of carriers entering the material will be more than the amount leaving it [2]. However, the influence of the structure of these polymeric films cannot be ignored. A polymeric material has structural disorders and trapping sites that are distributed in the bulk of the material. These trapping sites prevent SCLC from appearing, though this deterrent is overcome by applying a higher electric field. The trapping sites decrease the current and the conversion of the mechanism from Ohmic region into the SCL region is strongly dependent on the distribution of these trapping levels in energy [114].

For a trap free dielectric the current density $\boldsymbol{J}$ can be expressed as a sum of Ohmic ($\boldsymbol{n_o e\mu\frac{V}{s}}$) and SCL $\left(\frac{\boldsymbol{9\varepsilon_o\varepsilon_r\mu V^2}}{\boldsymbol{8s^3}}\right)$ currents [2]. Equation 27 shows this relationship.

$$\boldsymbol{J = n_o e\mu\frac{V}{s} + \frac{9\varepsilon_o\varepsilon_r\mu V^2}{8s^3}} \quad \text{[2](27)}$$

Where,

$\boldsymbol{e}$ = charge of an electron.

$\boldsymbol{\mu}$ = carrier mobility.

$\boldsymbol{V}$ = applied voltage.

For a dielectric with trapping sites, in this case shallow traps, the current density is expressed as equation 28 [2].

$$\boldsymbol{J = \theta\frac{9\varepsilon_o\varepsilon_r\mu V^2}{8s^3}} \quad \text{[2](28)}$$

Where,

$\boldsymbol{\theta}$ = the ratio of number density of conduction band electrons $\boldsymbol{n_c}$ to the number density of occupied trapping sites $\boldsymbol{n_t}$.

2.10.2.2. Poole-Frenkel Mechanism

The Poole-Frenkel effect is similar to the Schottky effect; however it is more likely to take place in the bulk of the dielectric. Frenkel [115] proposed the concept of this mechanism where it was shown that the increase in probability of ionisation in an electric field can be expressed as equation 29.

$$\frac{\boldsymbol{e(E)}}{\boldsymbol{e(0)}} \propto \boldsymbol{exp}\left(\frac{\boldsymbol{\phi_{pf}}}{\boldsymbol{k_B T}}\right) \quad \text{[115](29)}$$

Where,

$\boldsymbol{\phi_{pf}}$ = the lowering of the barrier and can be expressed as equation 30 [115].

$$\boldsymbol{\varepsilon_{pf} = 2\sqrt{\frac{zq^3E}{k}}} \quad \text{[115](30)}$$

Where,

$\boldsymbol{z}$ = the charge at the centre.

$\boldsymbol{E}$ = the strength of electric field.

$\boldsymbol{q}$ = the charge on an electron.

$\boldsymbol{k}$ = the dielectric constant.

The Poole-Frenkel conduction mechanism takes place for charged impurities only [115]. In this mechanism, the applied electric field lowers the energy barrier that restricts the charged carriers within the material. In order for this mechanism to take place, an insulator with a wide band gap is required along with a large number of acceptors and donors. In this case, large energy is required to ionise the acceptor or donors. So, there is little to no migration of electrons to the conduction band or from the valence band at room temperature.

For a dielectric with only donor states the number density $\boldsymbol{n_c}$ can be expressed as equation 31 [2].

$$\boldsymbol{n_c = N_D - n_D} \quad \text{[2](31)}$$

Where,

$\boldsymbol{N_D}$ = the number density of donors.

$\boldsymbol{n_D}$ = the number density of the donors which have not offered their electrons.

When a donor donates an electron, this results in a coulombic force $\boldsymbol{F_{(r)}}$ to appear between the donated electron and the charged ion and a resultant potential energy $\boldsymbol{V(r)}$. The coulombic force $\boldsymbol{F_{(r)}}$ can be expressed as equation 32 [2].

$$\boldsymbol{F_{(r)} = \frac{-e^2}{4\pi\varepsilon_o\varepsilon_r r^2}} \quad [2](32)$$

The resultant potential energy $\boldsymbol{V(r)}$ can be expressed as equation 33 [2].

$$\boldsymbol{V(r) = \frac{-e^2}{4\pi\varepsilon_o\varepsilon_r r}} \quad [2](33)$$

Where,

$\boldsymbol{r}$ = the separation.

$\boldsymbol{\varepsilon_o}$ = permittivity of free space.

$\boldsymbol{\varepsilon_r}$ = the relative permittivity of material.

$\boldsymbol{e}$ = the charge of an electron.

The presence of an external electric field $\boldsymbol{E}$ changes the potential energy. Derivation of this expression and equating it to 0 provides an expression for the point $\boldsymbol{r_m}$ at which the field is at its maximum. This is shown as equation 34 [2].

$$\boldsymbol{r_m = \left(\frac{e}{4\pi\varepsilon_o\varepsilon_r E}\right)^{\frac{1}{2}}} \quad [2](34)$$

The maximum height of the barrier is altered by $\boldsymbol{\Delta V_m}$ in the direction of the field and can be expressed as equation 35.

$$\boldsymbol{\Delta V_m = -2\left(\frac{e^3 E}{4\pi\varepsilon_o\varepsilon_r}\right)^{\frac{1}{2}}} \quad [2](35)$$

In order to meet the condition of dynamic equilibrium, the rate of migration of electrons from donor to conduction band is equal to the rate of capture. The expression of the electrons that are thermally excited from the donor to conduction band can be given as equation 36 [2].

$$\boldsymbol{n_D v_o \, exp\left\{-\frac{\phi_{eff}}{k_B T}\right\}} \quad [2](36)$$

Where,

$\boldsymbol{v_o}$ = the frequency of electrons effort to escape.

$\boldsymbol{\phi_{eff} = \Delta E_d + \Delta V_m}$, lowering of the level of the barrier.

The expression for the rate of acceptance of electrons can be expressed in terms of the cross sectional area where donors are captured $\boldsymbol{S}$ and the thermal velocity $\boldsymbol{v}$ of electrons in the conduction band and is shown as equation 37 [2].

$$\boldsymbol{n_c = (N_D - n_D)vS = n_c^2 vS} \quad \text{[2](37)}$$

The number density of carriers that are free in the conduction band can be expressed as equation 38 [2].

$$\boldsymbol{n_c = N_{eff}^{1/2} N_D^{1/2}\, exp\left\{-\frac{\phi_{eff}}{2k_B T}\right\}} \quad \text{[2](38)}$$

Where,

$\boldsymbol{N_D = N_D + n_c;}$ for deep donors.

$\boldsymbol{N_{eff}}$ = the effective density of the carriers in the conduction band of the material.

Now the expression for the "Poole-Frenkel" mechanism $\boldsymbol{\sigma}$ can be given as equation 39 [2].

$$\boldsymbol{\sigma = n_c e\mu = N_{eff}^{1/2} N_D^{1/2} e\mu\, exp\left\{-\frac{\Delta E_d}{2k_B T}\right\} exp\left\{\frac{e^{3/2}E^{1/2}}{(4\pi\varepsilon_o\varepsilon_r)^{1/2}k_B T}\right\}} \quad \text{[2](39)}$$

Equation 39 shows the expression for conduction due to the Poole-Frenkel mechanism for an insulator containing only donor states. In the case where an insulator contains acceptors or both donors and acceptors, the analysis is similar. The conduction due to Poole-Frenkel mechanism under each case can be characterised by a straight line plot between $\ln(I/V)$ against $V^{1/2}$.

2.10.2.3. Hopping Conduction

In this mechanism the conduction takes place by migration of charge carriers from one localised state to another. This process can take place by tunnelling through a barrier, excitation of charge carriers over the barrier or the combination of both processes. In this mechanism the electrons in an occupied state are thermally excited and gain enough energy and migrate to an unoccupied state which has an identical energy level. This happens at an applied temperature of (T > 0K). According to Lewis [116] the mechanism requires the presence of localised trapping sites with a distribution of energies.

The expression for thermally assisted hopping conductivity ($\boldsymbol{\sigma_{TAH}}$) with average trap depth $\boldsymbol{\Delta H}$ can be expressed as equation 40.

$$\boldsymbol{\sigma_{TAH} = \frac{\alpha}{E} * \exp\left\{-\frac{\Delta H}{K_B T}\right\} * sinh\left(\frac{qaE}{2K_B T}\right)} \quad \text{[117](40)}$$

2.11. Measurement of Surface/ Bulk Conductivity of Dielectric Materials

The resistivity or the conductivity of a dielectric material can indirectly measure moisture content, deterioration of various properties, and the mechanical strength of the material. The surface resistivity can be defined as the electrical resistance of a material surface whereas the bulk/volume resistivity can be defined as the resistance through a cube of the dielectric material [118]. Once the data has been gathered the usefulness of this indirect measurement method depends on the correlations established compared to other supporting work. The surface conductivity of an insulator can have an effect on the development and lifetime of surface charges on the material. It can also have a detrimental impact on the flashover strength of the material [119] as the accumulated surface charges may influence the initiation of surface discharges on an insulator [21]. A decrease in surface resistance may result either in an increase of the dielectric breakdown voltage because the electric field intensity is reduced, or a decrease of the dielectric breakdown voltage because the area under stress is increased [120]. In order to assess the significance of the problem it is important to measure the surface and bulk conductivity associated with material as this will control the build-up and decay of surface charge.

2.11.1. Concentric Ring Geometry (ASTM D257-78)

The concentric ring electrode geometry is a common measurement method for surface conductivity measurements of insulating films and is adopted as a standard (ASTM D257-78). It is to be noted that when testing for surface resistivity/ conductivity it is assumed that the flow of current only flows between the electrodes on the surface of the material and no current penetrates into the volume of the material [121].

Figure 16 shows the electrode arrangement of the ASTM-D257 measurement system with an outer ring electrode radius of $\boldsymbol{R_2}$ and a central circular electrode radius of $\boldsymbol{R_1}$.

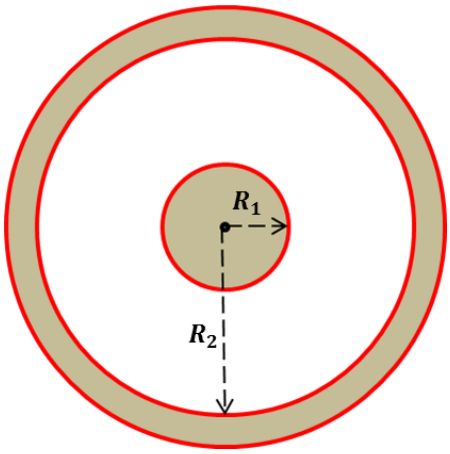

Figure 16: Concentric Ring Geometry: Electrode arrangement.

The surface current density $\boldsymbol{J_s}$ for the arrangement where the radius $\boldsymbol{R'}$ varies between outer electrode radius $\boldsymbol{R_1}$ and inner central electrode radius $\boldsymbol{R_2}$ can be expressed as:

$$\boldsymbol{J_s = \frac{I_s}{2\pi R'}} \tag{41}$$

Where,

$\boldsymbol{I_s}$ = Current along the surface of the sample between outer ring electrode and central inner electrode.

Electric field $\boldsymbol{E_s}$ along the surface of the sample with surface resistivity $\boldsymbol{\rho_s}$ is expressed as:

$$\boldsymbol{E_s = \rho_s * J_s} \tag{42}$$

Substituting equation 41 into equation 42 further simplifies expression of electric field $\boldsymbol{E_s}$.

$$\boldsymbol{E_s = \frac{\rho_s I_s}{2\pi R'}} \tag{43}$$

The voltage $\boldsymbol{V_{R_1R_2}}$ along the surface of the dielectric between electrodes of radius $\boldsymbol{R_1}$ and $\boldsymbol{R_2}$ can be calculated by integrating the electric field $\boldsymbol{E_s}$ from the outer ring electrode radius $\boldsymbol{R_2}$ to the central electrode radius $\boldsymbol{R_1}$. Equation 44 shows this expression.

$$\boldsymbol{V_{R_1R_2} = \frac{\rho_s I_s}{2\pi} ln(\frac{R_2}{R_1})} \tag{44}$$

By substituting equation 44 into Ohm's law the resistance $\boldsymbol{R_s}$ along the surface of the insulator can be expressed as:

$$\boldsymbol{R_s = \frac{\rho_s}{2\pi} ln(\frac{R_2}{R_1})} \tag{45}$$

The expression for the surface resistivity can be obtained by rearranging equation 45.

$$\rho_s = R_s * 2\pi * \frac{1}{ln\frac{R_2}{R_1}} \tag{46}$$

Several measurement methods have been applied based on the standard ASTM-D257 approach [118, 122, 123]. Although this technique is effective and widely used, it has been reported in [124] that the geometry suffers from some draw backs as the electric field depends on the sample thickness and electrode size which can result in high field regions at the edges of the electrodes. Using this geometry for surface conductivity measurements can therefore provide measurement errors due to the currents in the bulk of the sample contributing to the actual surface currents being measured when highly insulating materials are being investigated. Figure 17 illustrates this problem.

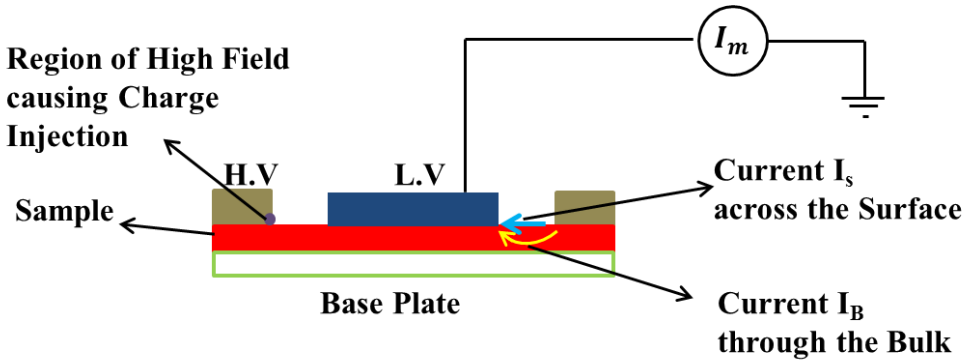

Figure 17: Concentric ring geometry (ASTM D-257) for Surface/ Bulk resistivity measurement of dielectric materials.

2.11.2. Concentric Cylindrical Geometry

In [124] a method to eradicate some of the drawbacks of the concentric ring geometry was proposed. The method involves the use of a concentric cylindrical arrangement whereby the plane of the insulator is perpendicular to the axis of the cylinder which removes the high field region. The arrangement of this geometry can be seen in figure 18.

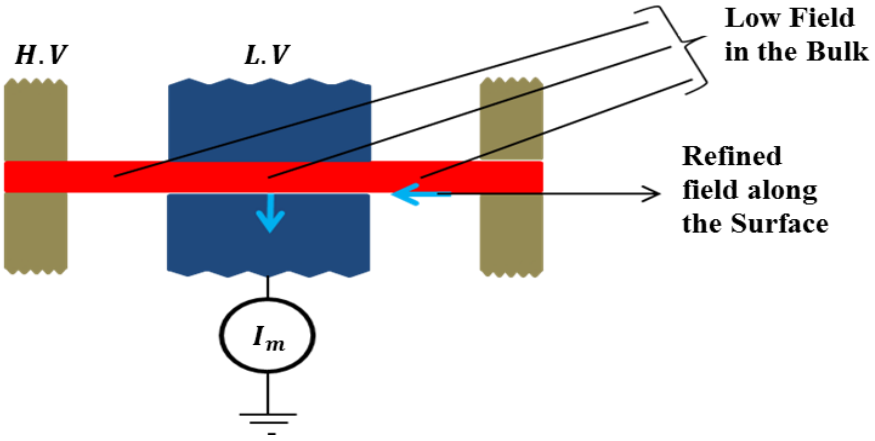

Figure 18: Concentric cylindrical geometry proposed in [123].

Numerical field calculation based on [125] was applied to a standard concentric ring arrangement and the concentric cylindrical arrangement. It was observed that the latter had a reduced high field region as compared to the former geometry and the field distribution across the surface of the sample was more evenly distributed. This observation is further supported by the findings in [126], where the voltage distributions developed under both measurement methods were investigated and it was concluded that the concentric cylindrical arrangement was a better alternative to the traditional ASTM-D257.

In [127] experimental observations on 100μm thin acetate sheets were performed to compare surface resistance measured by both measurement systems. It was observed that carrying out the measurements with the concentric ring geometry was comparatively difficult and took a longer time as the initial transient current response lasted much longer before a steady state current behaviour was achieved. Whereas, shorter initial transients were observed for concentric cylindrical arrangement and the experiments were comparatively easier to perform. It was also observed that the concentric ring geometry produced currents that were at least three orders of magnitude greater than the proposed concentric cylindrical arrangement. This was attributed to field enhancement at the outer electrode that leads to charge injection. The proposed geometry reduces the effect of polarisation in the bulk of the material and the currents produced in the bulk are so small that they can effectively be ignored.

Another advantage of using this geometry is that it is possible to operate in a voltage divider mode with the lower arm of the divider constructed of a parallel combination of resistance and capacitance. Due to the well-defined capacitance of the concentric cylindrical geometry

it is possible to eliminate the capacitive transient effects in the measurement system by careful selection of the resistance and capacitance in the lower arm [127].

Given et al [128] developed a measurement system that was a modification of the concentric cylindrical technique proposed in [124]. The technique was employed on a curved insulator as the sample being used was a part cut out of a PMMA cylindrical moulding. One of the modifications of interest was the sensing electrode geometry, whereby in order to measure the current along the surface of the sample the grounded central electrode was cut to incorporate a sensing electrode. The central electrode was cut in a way that the main body of the grounded electrode acts as a guard ring. This modification along with the concentric cylindrical geometry forms the basis of the measurement system developed in this project for the surface and bulk conductivity measurement of flat circular insulators. The developed measurement system and its working principle are discussed in more detail in chapter 5.

3. Varactor Probe Geometry: Design and Construction of the System

3.1. Theoretical Background

Noras in [91] proposed a method based on voltage controlled variable capacitance for non-contacting measurement of electric fields. The idea is to replace the mechanical modulation of the capacitance between sensor and field with electronic modulation. Following Noras [91] the proposition can be explained by considering the basic circuit of a standard electrostatic voltmeter (ESVM) probe held above a conductive surface. The probe is cylindrical in shape with a circular sensor. Figure 19 shows the capacitive coupling between the probe, sensor, ground and the conductive surface.

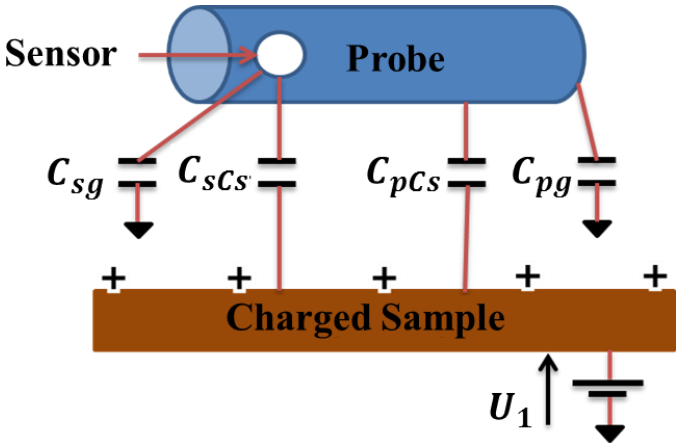

Figure 19: ESVM with coupling capacitances between probe, sample, ground and sensor.

Where,

C_{sg} = the capacitance between the sensor and ground

C_{sCs} = the capacitance between the sensor and the charged surface

C_{pCs} = the capacitance between the probe body and the charged surface

C_{pg} = the capacitance between the probe body and ground

U_1 = the voltage across the charged surface

A circuit representation of figure 19 is shown below**.** A resistor $\boldsymbol{R}$ is added to the circuit in order to measure the output current.

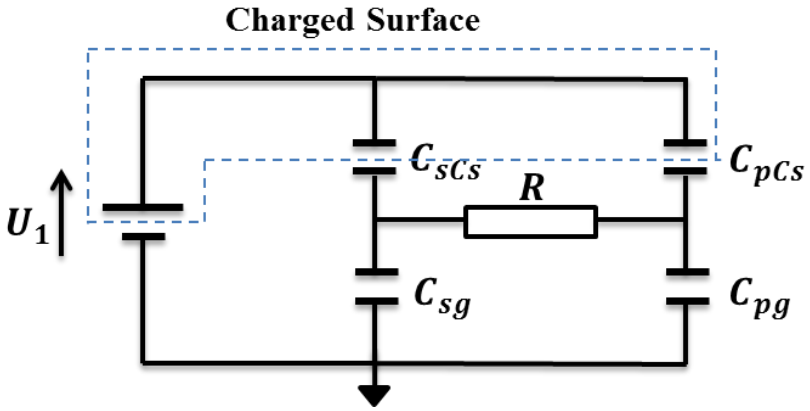

Figure 20: ESVM circuit diagram.

To measure electric field between the sensor and the charged surface, the ESVM would require mechanical modulation of the coupling capacitance $\boldsymbol{C_{sCs}}$ however; this can now be achieved electronically by the use of varactor diodes. The capacitance $\boldsymbol{C_{sCs}}$ can now be split into two capacitances $\boldsymbol{C_{sCs1}}$ and $\boldsymbol{C_{sCs2}}$ in series. Figure 21 shows the modified version of figure 20.

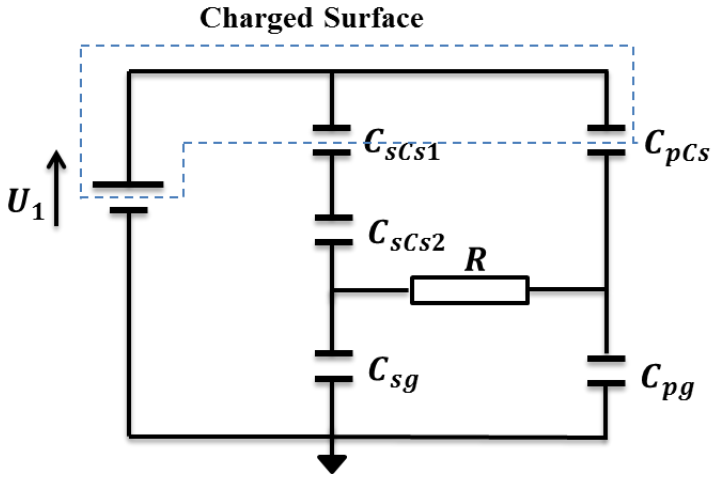

Figure 21: Modified circuit with C_{sCs} divided into C_{sCs1} and C_{sCs2}.

Where,

$\boldsymbol{C_{sCs1}}$ = the capacitance dependant on the configuration of the sensor plate and the relative permittivity of the space between the probe and the charged object being measured. During surface potential measurements the probe is held at a fixed position, thus, $\boldsymbol{C_{sCs1}}$ has a fixed value under these conditions.

$\boldsymbol{C_{sCs2}}$ = the capacitance that changes with time i.e. variable capacitance.

The variable capacitance $\boldsymbol{C_{sCs2}}$ is obtained by the employing a matched pair of varactor diodes that is discussed in more detail in the following section. The voltage-capacitance behaviour of a matched pair of varactor diodes can be considered identical. So, when a bias voltage is applied across the varicaps, it can be assumed that the capacitance $\boldsymbol{C_{v1}}$ of the first varactor equals the capacitance $\boldsymbol{C_{v2}}$ of the second varactor i.e. $\boldsymbol{C_{v1(t)} = C_{v2(t)}}$.

Where,

$\boldsymbol{C_{v1(t)}}$ = Change in the capacitance of varactor 1 with time.

$\boldsymbol{C_{v2(t)}}$= Change in the capacitance of varactor 2 with time.

It is assumed that for a certain period of time the voltage-capacitance behaviour of the matched varactor pair is linear. Under this instance when a sinusoidal voltage is applied across the varactor couple then the variable capacitance $\boldsymbol{C_{sCs2}}$ modulates sinusoidaly with the applied voltage and can be represented by equation 47.

$$\boldsymbol{C_{sCs2} = C_{sCs20} + C_{sCs21} * \sin(\omega t)} \quad (47)$$

Where,

$\boldsymbol{C_{sCs20}}$ = the part of the capacitance $\boldsymbol{C_{sCs2}}$ that remains fixed.

$\boldsymbol{C_{sCs21}}$ = the amplitude of the part of $\boldsymbol{C_{sCs2}}$ that varies.

The voltage $\boldsymbol{U_{C_{sCs2}}}$ is dependent on the voltage $\boldsymbol{U_1}$ across the charged surface. If the voltage $\boldsymbol{U_1}$ is fixed then $\boldsymbol{U_{C_{sCs2}}}$ across the capacitance $\boldsymbol{C_{sCs2}}$ remains constant. The modulating capacitance $\boldsymbol{C_{sCs2}}$ becomes a current source where current $\boldsymbol{i}$ can be represented as equation 48.

$$\boldsymbol{i = \frac{dC_{sCs2}}{dt} * U_{C_{sCs2}} + \frac{dU_{C_{sCs2}}}{dt} * C_{sCs2}} \quad (48)$$

As the voltage across the charged surface is fixed and the resulting voltage across the varactor couple is also fixed, the current $\boldsymbol{i}$ can be represented as equation 49.

$$\boldsymbol{i = \frac{dC_{sCs2}}{dt} * U_{C_{sCs2}}} \quad (49)$$

Substituting, equation 47 into equation 49 yields equation 50.

$$\boldsymbol{i = U_{C_{sCs2}} C_{sCs21} * \omega * \cos(\omega t)} \quad (50)$$

By detecting and measuring the current $\boldsymbol{i}$ the potential $\boldsymbol{U_1}$ of the charged surface can also be measured.

3.2. Sensing Technique Implementation

In this sub-section the basic implementation of the sensing technique is discussed. Following Noras [129] the theoretical background and its implementation can be described in more detail. Figure 22 shows the sensing end circuit diagram for the varactor probe geometry.

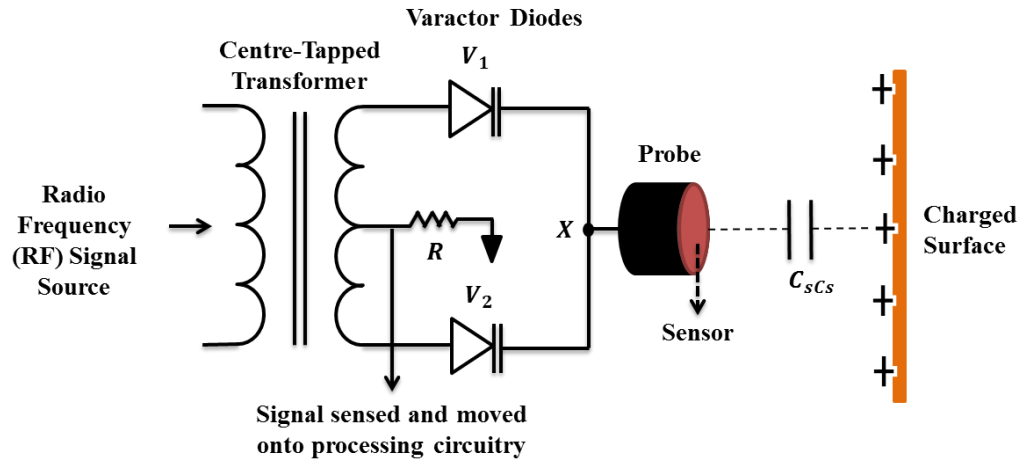

Figure 22: Sensing end circuitry for varactor probe geometry.

This part of the system is responsible for sensing the electric field signal which is then moved onto the next stages of the circuit where the signal is processed. The varactor pair to be used is identical and the junction $\boldsymbol{X}$ between the probe and the charged surface acts as a common node for the varactor couple. This junction is floating at the average value of the carrier signal which is nominally close to 0.

The probe sensor is capacitively coupled to the charged surface through a capacitance $\boldsymbol{C_{sCs}}$ which is dependent on various parameters discussed in section 3.1. The capacitance of the varactors is being modulated by a high frequency carrier signal supplied by a centre tapped transformer which is powered up by a radio frequency (RF) source. In this way it is ensured that the high frequency power source and the sensing end circuitry are separated galvanically i.e. stray currents are minimised.

Figure 22 can be remodelled as figure 23. Where, the centre-tapped transformer has been replaced by two separate voltage sources which would mimic its behaviour. Thus, the voltage sources would now have the same magnitude but will be 180 degree out of phase as is the case with the centre-tapped transformer. Additionally, the capacitive couplings of the probe sensor to ground $\boldsymbol{C_{sg}}$ and the charged surface to ground $\boldsymbol{C_{Csg}}$ are also shown.

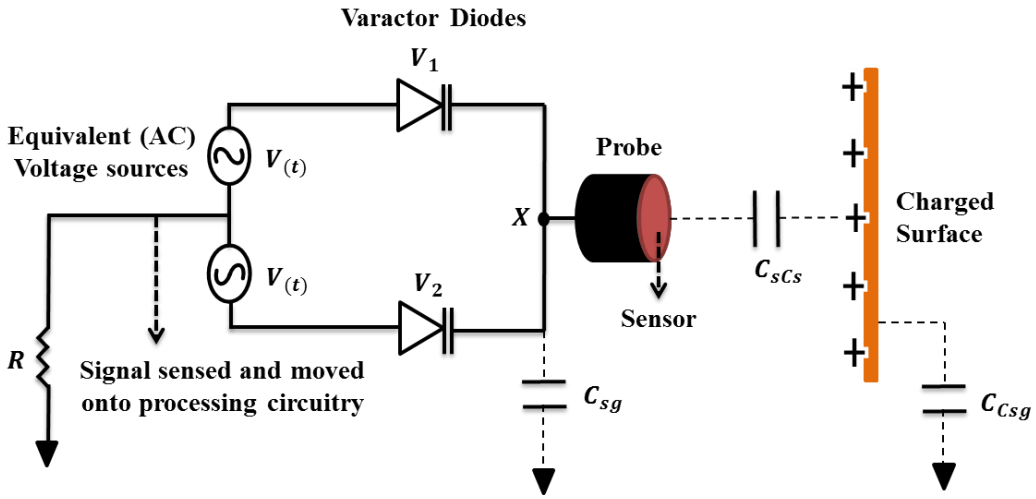

Figure 23: Remodelled sensing end circuitry for varactor probe geometry.

The concept of this measurement system can be further described by analysing figure 23 in more detail. Dividing figure 23 into two subfigures (24 & 25) and analysing them provides much needed clarity on the mechanism involved and factors that influence the output of the system. In Figure 24 the varactors are combined to form a combined variable voltage dependent capacitor, in series with $\boldsymbol{C_{sCs}}$.

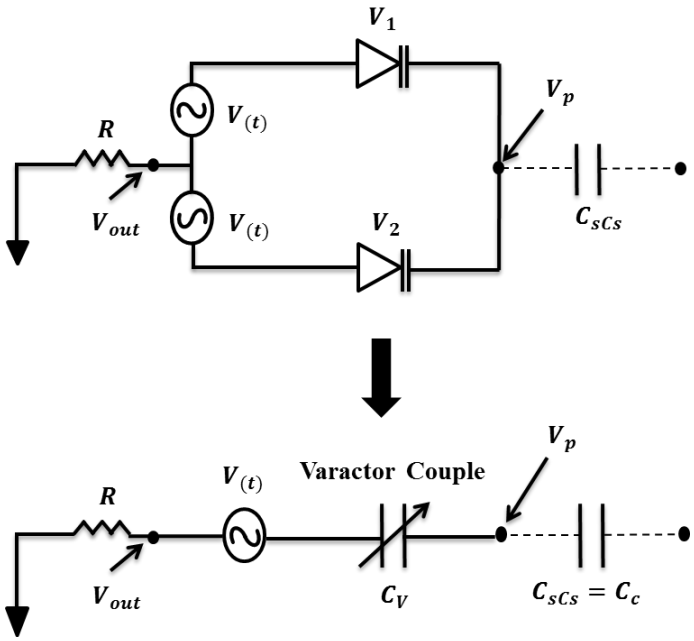

Figure 24: Subfigure 1 representing equivalent of figure 23 without the surface under test.

As in [91], it is assumed that, within a certain range, the voltage-capacitance dependence of a varactor couple is linear i.e. the varactor can be seen as a time varying capacitor. From figure 24 the voltage $\boldsymbol{V_v}$ across the varactor couple can be expressed as equation 51.

$$\boldsymbol{V_v = Vsin\,(\omega t) - V_p} \tag{51}$$

Where,

$\boldsymbol{Vsin\,(\omega t)}$ = the time varying sinusoidal voltage $\boldsymbol{V_{(t)}}$ from the high frequency oscillator, and

$\boldsymbol{V_p}$ = voltage at the probe sensor.

As $\boldsymbol{V_p}$ is regarded as a constant and $\boldsymbol{V_{(t)}}$ is varying sinusoidaly, the capacitance $\boldsymbol{C_v}$ of the varactor can be given by equation 52.

$$\boldsymbol{C_v = C_o + C_A sin(\omega t)} \tag{52}$$

Where,

$\boldsymbol{C_o}$ = constant portion of varactor capacitance $\boldsymbol{C_v}$.

$\boldsymbol{C_A}$ = amplitude of the variable portion of capacitance $\boldsymbol{C_v}$.

As the total capacitance cannot be less than 0 therefore, $\boldsymbol{C_A < C_o}$ the total charge $\boldsymbol{q_v}$ stored in the varactor couple is given by equation 53.

$$\boldsymbol{q_v = V_v * C_v} \tag{53}$$

The output voltage signal across the sensing resistor depends on the current flowing in the circuit. This current comes from the time varying voltage across the varactor which controls its capacitance. Current in the system depends on the rate of change of electric charge. The current in the system can now be expressed as equation 54.

$$\boldsymbol{i_t = {d_q}/{d_t} = \frac{d}{d_t}(V_v * C_v) = V_v \frac{dC_v}{d_t} + C_v \frac{dV_v}{d_t}} \tag{54}$$

The voltage across the varactor couple is the difference between the sinusoidal carrier being supplied by the high frequency oscillator and the voltage at the tip of the sensor. As the amplitude of the sinusoidal carrier voltage is constant, an assumption is made that the voltage at the sensor plate is also constant. So, equation 54 can be expressed as:

$$\boldsymbol{i_t = V_v \frac{dC_v}{d_t} = V_v \frac{d(C_o + C_A sin(\omega t))}{d_t}} \tag{55}$$

The final expression for the current through the system can be obtained by further evaluation of equation 55. This is expressed as equation 56.

$$\boldsymbol{i_t = V_v * \omega * C_A cos(\omega t)} \tag{56}$$

As the voltage from the transformer is of constant amplitude and if the voltage on the charged object is considered to change then the current across the system is dependent on the potential $\boldsymbol{V_p}$ on the sensor plate and can be expressed as:

$$i_t = V_p * \omega * C_A cos(\omega t) \tag{57}$$

Following this, the voltage according to Ohm's law $(V = IR)$ depends on the amount of current and the value of the resistor where the current is being measured. So, if the amount of charge across the varactor couple changes, this results in a change in the time varying current which results in a change in the output voltage. The time varying voltage output can now be calculated using Ohm's law and can be expressed as:

$$V_{out} = R * i_t = R * V_p * \omega * C_A cos(\omega t) \tag{58}$$

The amount of charge across the varactor couple is strongly dependent on the value of the varactor capacitance and the magnitude of the coupling capacitance between the sensor plate and the surface under test. This is better explained by considering the second subfigure that figure 23 has been divided into i.e. figure 25, where the potential drops across the two capacitors are analysed with respect to capacitance.

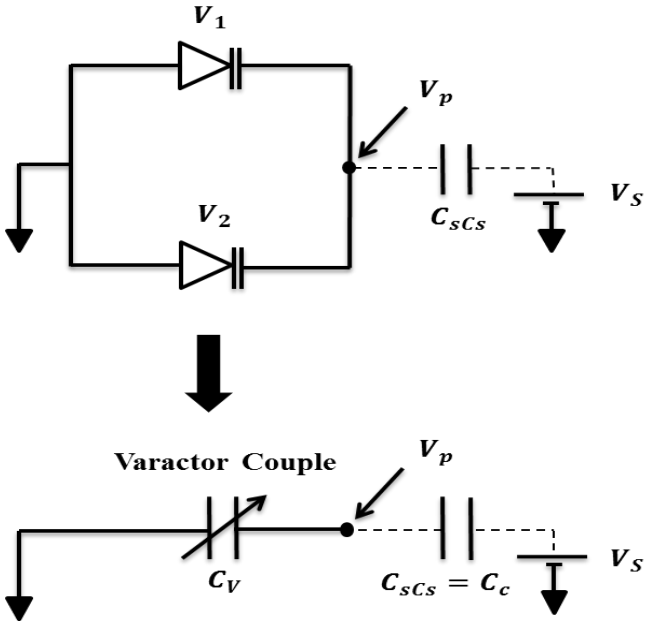

Figure 25: Subfigure 2 representing equivalent of figure 23 including the surface voltage.

The voltage V_p at the tip of the sensor is dependent on both the coupling capacitance and the capacitance of the varactor couple. As the varactor couple and the coupling capacitance are in series, the potential at the tip of the sensor can be derived by voltage division and expressed as:

$$V_p = V_s * \frac{C_c}{C_v + C_c} \tag{59}$$

Where,

$\boldsymbol{V_s}$ = the potential on the charged surface.

From equation 59 the effect of varactor capacitance $\boldsymbol{C_v}$ and the coupling capacitance $\boldsymbol{C_c}$ on the sensor potential $\boldsymbol{V_p}$ can be analysed for two separate cases. Each case considers the voltage $\boldsymbol{V_s}$ from the charged surface to be constant.

- **Case 1: $\boldsymbol{C_c >> C_v}$**

In the first case it is considered that the coupling capacitance $\boldsymbol{C_c}$ is much larger than the capacitance of the varactor couple $\boldsymbol{C_v}$. Under this condition the expression in equation 59 can be written as equation 60.

$$\boldsymbol{V_p = V_s} \tag{60}$$

The potential across the sensor plate is equal to the potential on the charged surface. For best sensitivity it is ideal to use a varactor pair that can match the capacitance of the coupling capacitor. However, in the case of measuring very high voltage values it is wise to have a coupling capacitance smaller than the varactor capacitance, as this would aid the design process that involves electronic components and their limitations, such as the measurement limits of the Arduino analogue pins which could be damaged in the event of measuring a large signal. This is managed through the various gain stages incorporated in the measurement circuitry, which can be adjusted to keep the measured signal within the limits of the microcontroller.

- **Case 2: $\boldsymbol{C_c << C_v}$**

In the second case it is considered that the coupling capacitance $\boldsymbol{C_c}$ is much smaller than the capacitance of the varactor couple $\boldsymbol{C_v}$. Under this condition the expression in equation 59 can be written as equation 61.

$$\boldsymbol{V_p = {C_c}/{C_v} * V_s} \tag{61}$$

The potential across the sensor surface is a product of the ratio of the coupling capacitance $\boldsymbol{C_c}$ to varactor couple capacitance $\boldsymbol{C_v}$ and the potential on the charged surface $\boldsymbol{V_s}$. This relationship also shows that a bigger coupling capacitance will lead to a greater potential $\boldsymbol{V_p}$ on the probe sensor hence, leading to a larger voltage output being measured, as the current in the system increases. The coupling capacitance in the experiments being carried out in this thesis is much smaller than the capacitance of the varactors but the effect of the capacitance ratio will be compensated by the much higher voltages that are expected to be measured on the charged surface.

3.3. PSpice Model

Figure 23 represents the circuit that is constructed in PSpice simulation software to further exhibit the practical working of the system. A transient analysis of the circuit is carried out with the charged object being mimicked by an alternating source at an arbitrary frequency. It is to be noted that the change in potential due to the probe moving across the charge distribution in the practical experiment will be much slower and that this simulation is only being performed as a basis of demonstrating the working system behaviour over a reasonable simulation time. In this simulation it can be considered that the surface potential is varying sinusoidaly at a frequency of 5kHz. The high frequency sinusoidal signal that is being applied to the varactors from the centre-tapped transformer is being modulated by the much slower signal coming in from the alternating source. Figure 26 shows the PSpice circuit for this configuration.

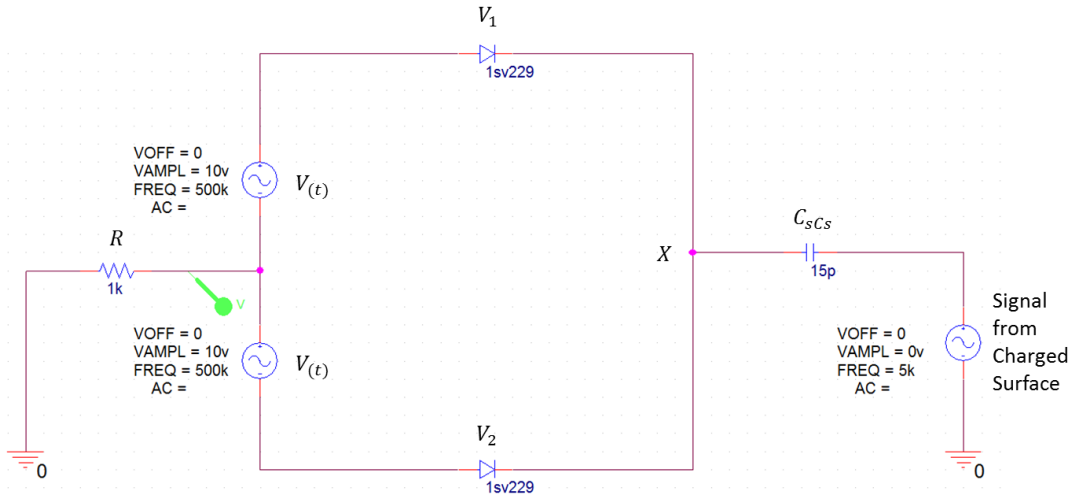

Figure 26: PSpice sensing end circuit diagram.

The frequency of 500kHz supplied by the centre-tapped transformer is carefully selected keeping in mind the real-world component limitations that will be used in the circuitry that will process the signal being sensed. The magnitude of the peak to peak (pk-pk) voltage driving the varactors is an arbitrary value within the range specified for this particular varactor type (1sv229) and a suitable value will be selected based on the limitations of the components available for processing circuitry. A 1kΩ resistor is inserted at the centre-tap of the transformer where the output current through this resistor is being monitored. The information of the voltage signal representing the charging surface potential is carried on the envelope of the current signal through the resistor.

3.3.1. The Influence of the Varactor Voltage and Coupling Capacitance on the Measured Output

In this section the effect of coupling capacitance and voltage magnitude driving the varactors was observed in more detail. A PSpice simulation was performed using the circuit in figure 26 and the magnitude of the voltage running the varactors was varied to observe its effect on the sensed output signal. The coupling capacitance between the sensor and the perceived charged object was kept constant during this simulation.

After the simulation concluded, the magnitude of the coupling capacitance was changed to a different fixed value and the magnitude of the voltage driving the varactors was adjusted to the same value that it was in the previous case. The results are compared to see the influence of these parameters on the sensed output of the charge measurement system.

Figures 27 and 28 illustrate the observed output voltage waveforms where a coupling capacitance $\boldsymbol{C_c}$ of 15pF and 5pF exists between the sensor and charged surface. This coupling capacitance is much larger than would be expected in the practical system however; the expected surface potential values will also be much higher leading to similar values of potential at the probe. The values of coupling capacitance and surface potential are chosen to prevent resolution/convergence problems within PSpice. In this case the varactors are driven with a 500kHz/ 10V(pk-pk) input signal from the RF source. Whereas, figures 29 and 30 show the behaviour under similar conditions but with an input signal of 500kHz/ 20V(pk-pk) driving the varactors. In each experiment the potential of the perceived charged object is increased from 0V to 30V(pk-pk) in three increments of 10V(pk-pk).

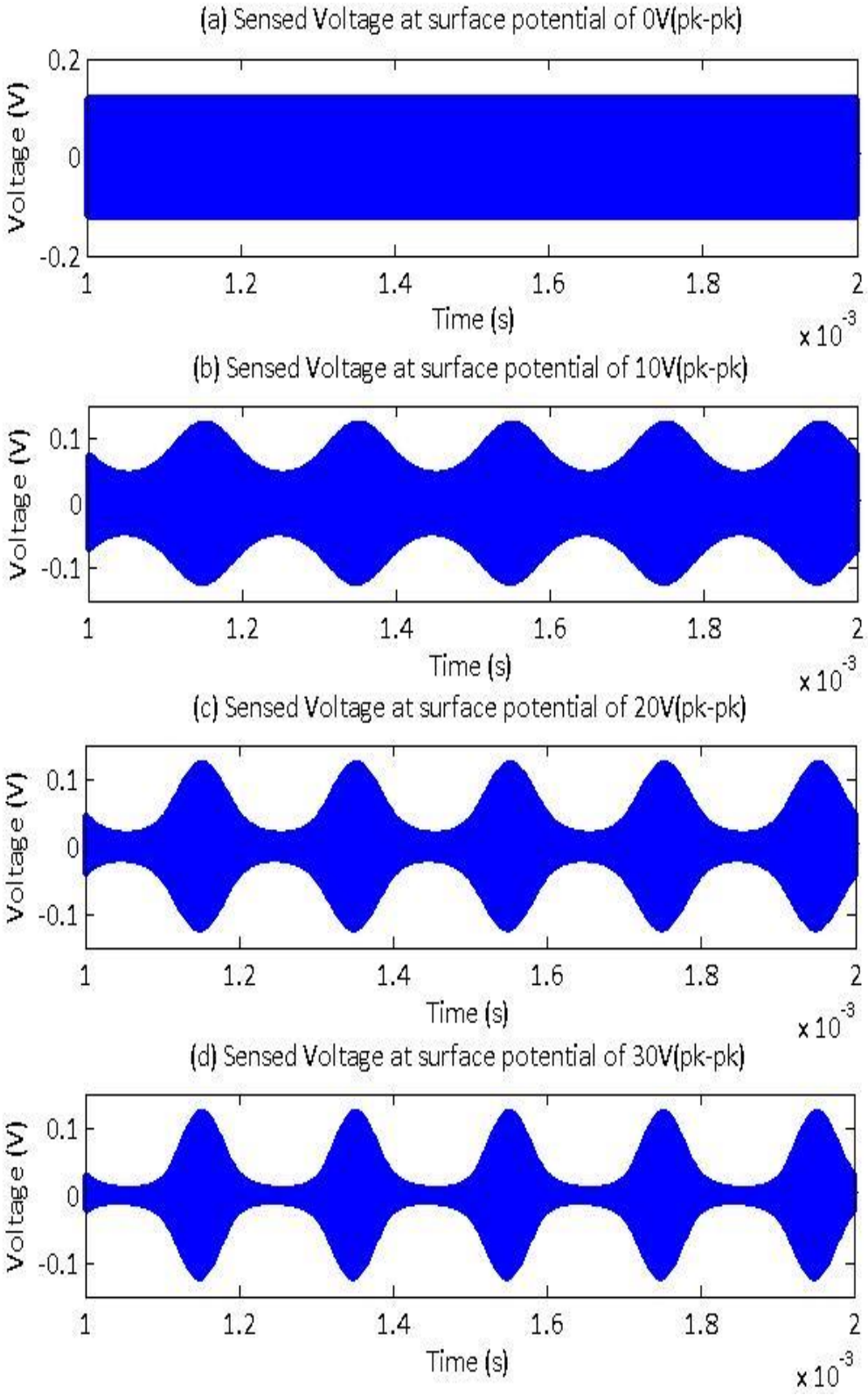

Figure 27: Sensed voltage waveforms with a 15pF coupling capacitance between sensor and charged surface and 10V(pk-pk) input to varactors.

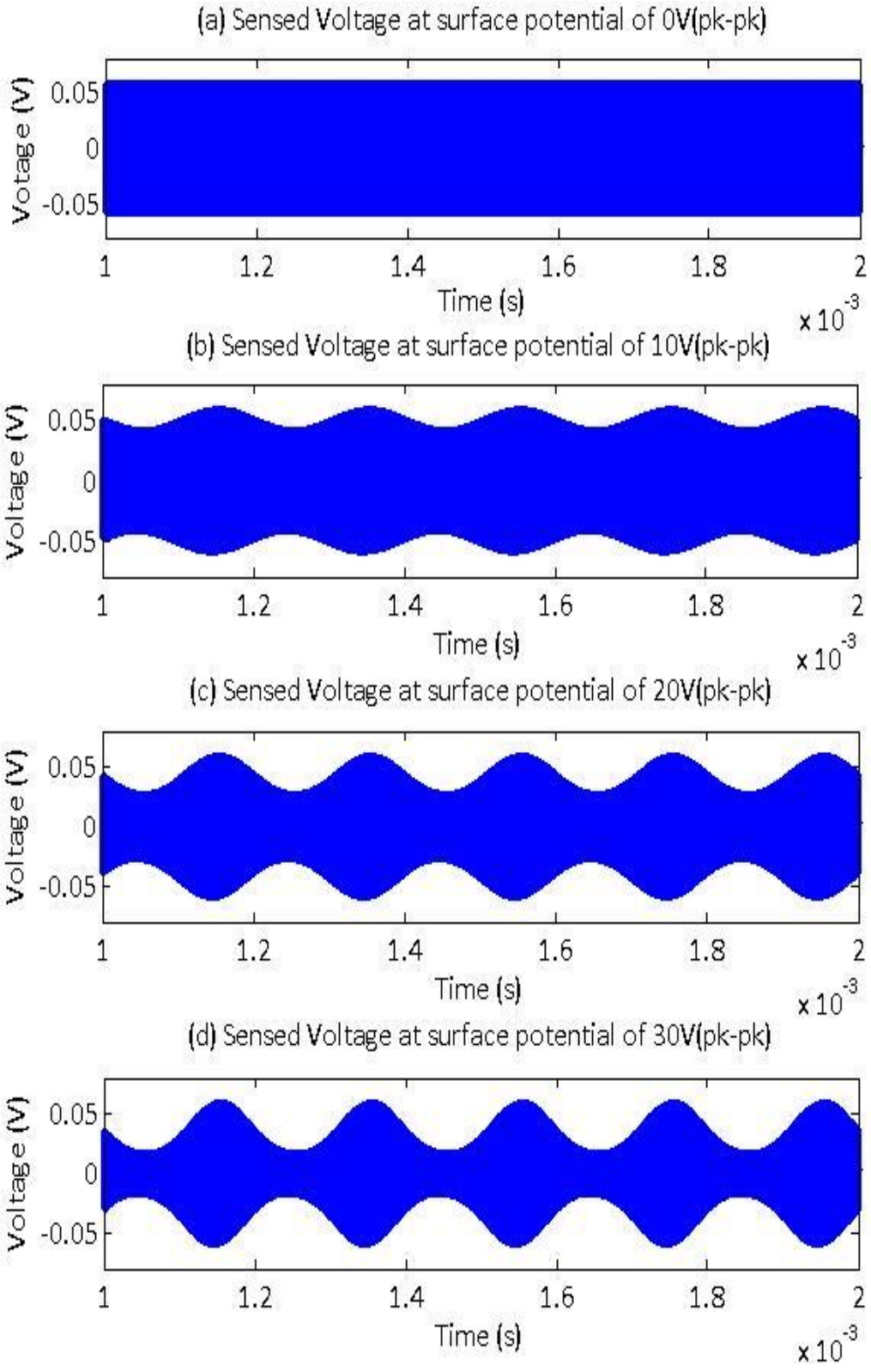

Figure 28: Sensed voltage waveforms with a 5pF coupling capacitance between sensor and charged surface and 10V(pk-pk) input to varactors.

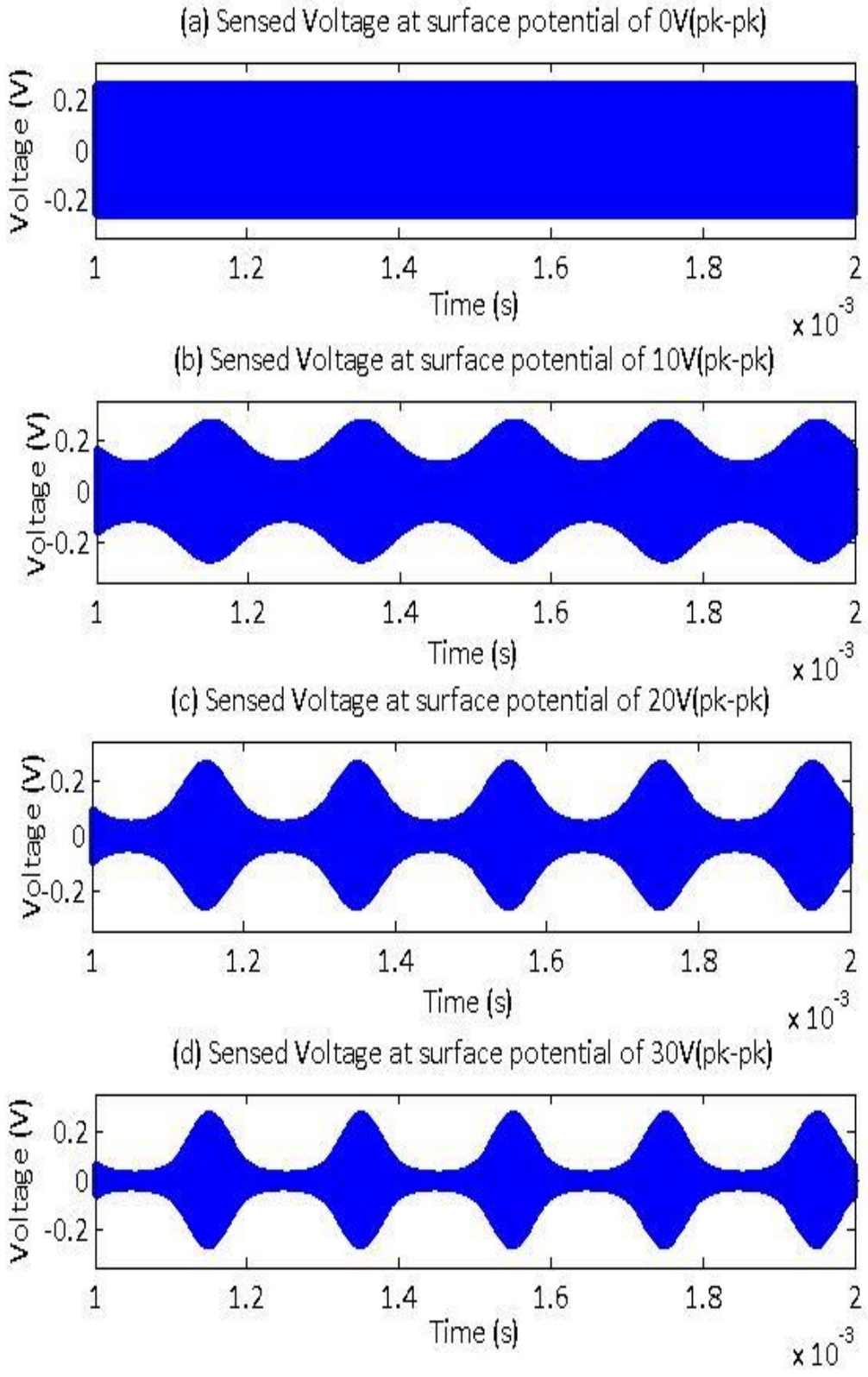

Figure 29: Sensed voltage waveforms with a 15pF coupling capacitance between sensor and charged surface and 20V(pk-pk) input to varactors.

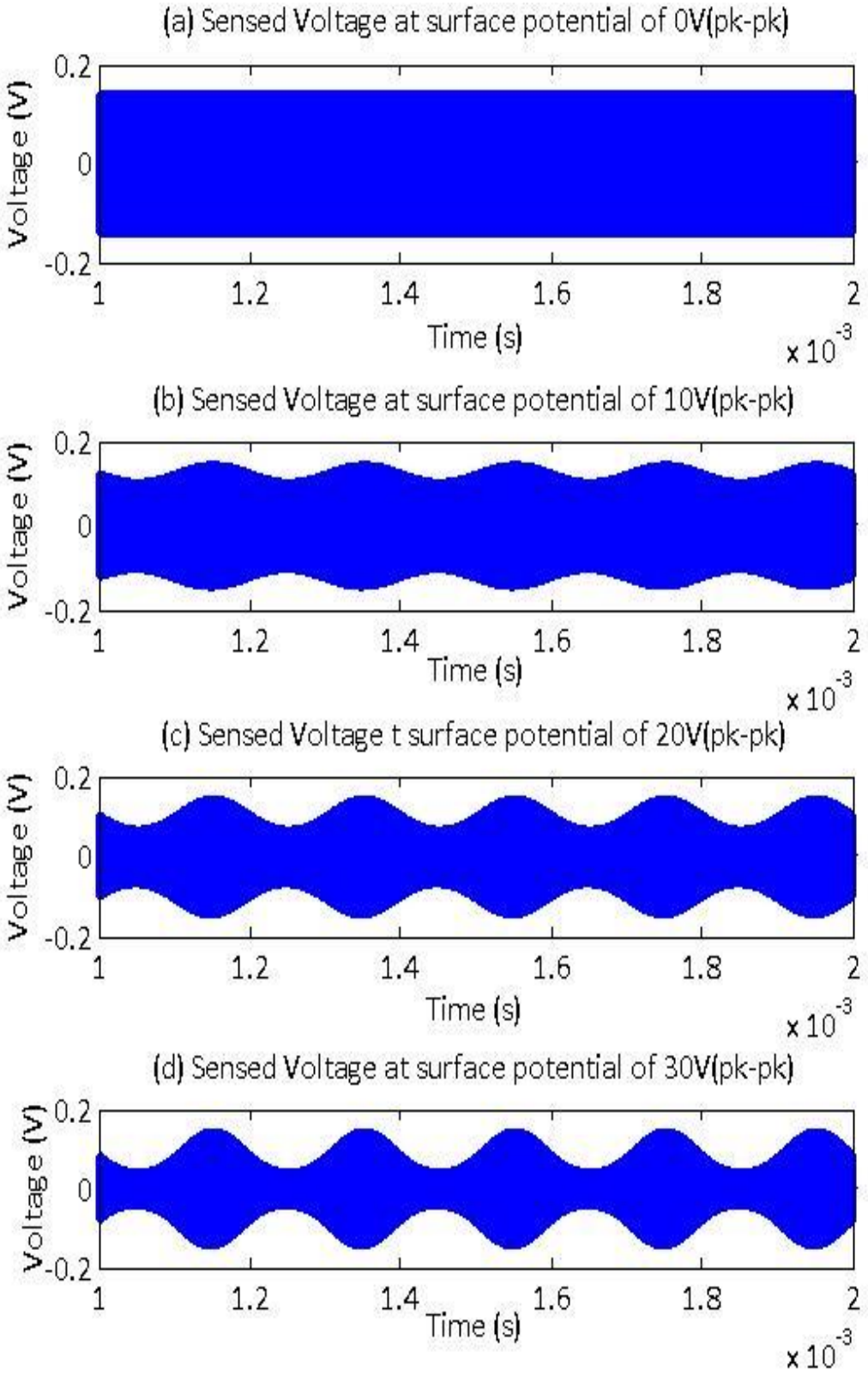

Figure 30: Sensed voltage waveforms with a 5pF coupling capacitance between sensor and charged surface and 20V(pk-pk) input to varactors.

Figures 27-30 show that, when the surface under test is at 0 potential, there is no modulation of the output signal. Amplitude modulation is evident when the surface is charged. The amount of modulation increases with an increase of potential on the surface. It can also be seen that for higher values of potential the modulation tends to reach a saturating point. Figure 31 and 32 demonstrate this behaviour for a wider range of coupling capacitance.

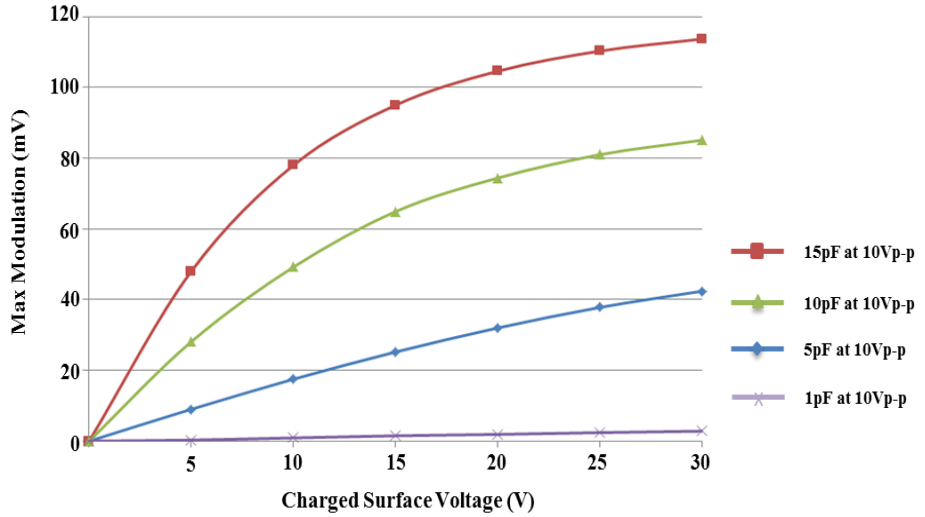

Figure 31: Max modulation vs charged surface voltage at supply voltage of 10V(pk-pk).

Figure 31 shows that for higher values of coupling capacitance, the maximum modulation of the output signal is greater. The amount of modulation with respect to the potential of the charged surface is not linear but tends to follow a path to saturation which will become evident if the simulation is run for higher values of charged surface potential. The effect of driving the varactors at a higher supply voltage of 20V(pk-pk) is shown in figure 32.

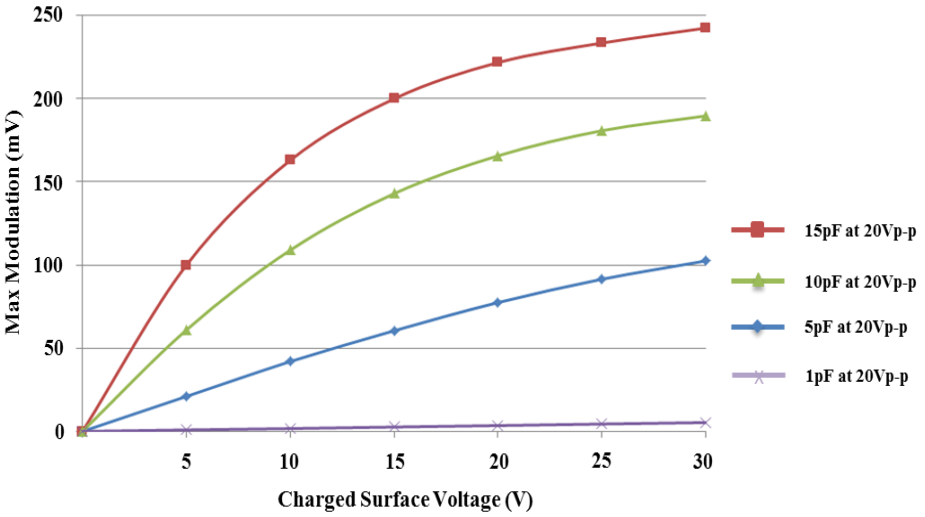

Figure 32: Max Modulation vs charged surface voltage at supply voltage of 20V(pk-pk).

When compared to figure 31 it can be seen that the output waveform of figure 32 seems to follow the same trend. However, as the voltage driving the varactors has doubled it has also caused the output voltage across the sensing resistor to increase significantly. This can be shown by comparing the data of figures 31 and 32 and plotting the max modulation of the output waveform against surface potential at specific coupling capacitances. In this case the coupling capacitance considered are 5pF, 10pF and 15pF. Figure 33 shows this behaviour.

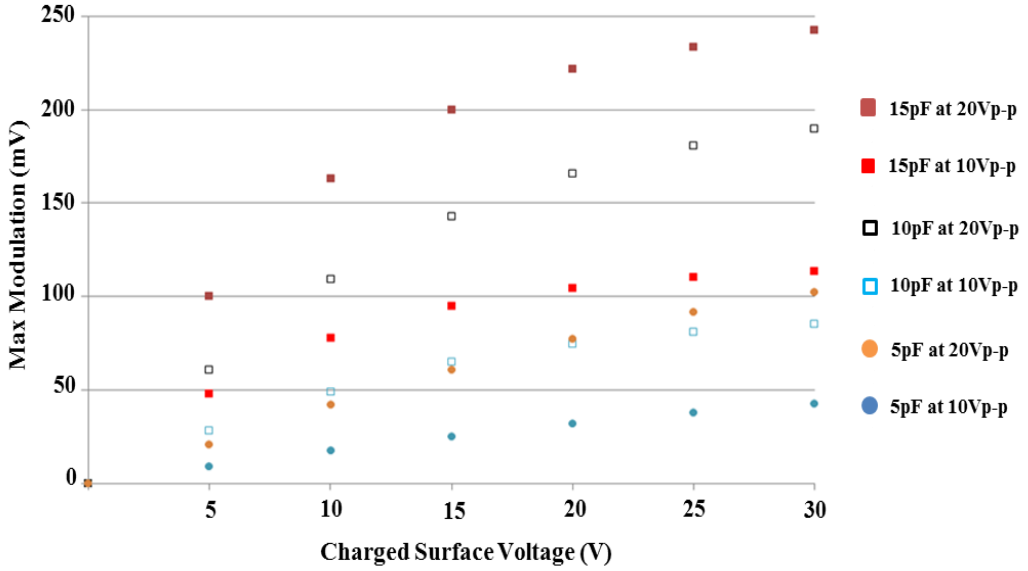

Figure 33: Comparison of max modulation vs charged surface potential with coupling capacitance of 5pF, 10pF and 15pF for varactor running at 10V(pk-pk) and 20V(pk-pk).

3.3.2. Reason for Saturation

From figure 33 it is evident that as a result of driving the varactor at a higher voltage level the modulation of the output signal increases significantly. It is also evident that the behaviour of the increase in modulation is not linear and tends to saturate at higher values of surface potential. This saturation can be explained by considering the capacitance-voltage (C-V) curve of the varactor diodes. It needs to be noted that the capacitance $\boldsymbol{C_v}$ of a varactor is a non-linear function of the reverse voltage $\boldsymbol{V_r}$ established across the varactor. This relationship is shown in equation 62.

$$\boldsymbol{C_v = \frac{C_{j0}}{\left(1 + \frac{V_r}{V_j}\right)^{G_c}}} \tag{62}$$

Where,

$\boldsymbol{C_{j0}}$ = Zero junction bias capacitance.

$\boldsymbol{V_j}$ = Junction potential.

$\boldsymbol{G_c}$ = Grading coefficient.

Noras in [129] uses an example of a pair of 1sv277 varactors and shows that for low reverse voltage values the C-V relationship of the varactors can be considered linear. In this instance the relationship can be represented by equation 63.

$$\boldsymbol{C_v = K * V_R + C_{j0}} \quad (63)$$

Where,

$\boldsymbol{K}$ = the line slope coefficient.

It is also shown that the modulation depth of the output signal is also dependent on the line slope coefficient $\boldsymbol{K}$ of the C-V characteristic of the varactor being used [129]. This behaviour was illustrated by use of the analogue behavioural model (ABM) function in PSpice and implementing a mathematical model of the output of the linearized voltage-dependent capacitor model. It was observed that for the 1sv277 varactor pair the C-V characteristic followed a linear path for a reverse voltage of 0 to 2 V. The value of the actual slope coefficient at this point was calculated to be -1.8. By increasing the slope coefficient in their model to -4 it was shown that the depth of modulation increased. It was also concluded that the depth of the modulation or the modulation index was proportional to the gain associated with the slope coefficient $\boldsymbol{K}$ [129].

Equation 63 can also be applied to the varactors being used in this system. The non-linearity in the modulation depth can be attributed to the voltage at which the varactor pair is being driven at. This is clearly shown from figure 34 where the C-V characteristic can be assumed to follow a linear path up to a reverse voltage of 2 V and after that the curve can no longer be considered linear. It is also to be noted that the limitations of the electronic components also limit the range of the modulation depth that can be measured effectively. The C-V characteristic of the 1SV229 varactor is shown in figure 34.

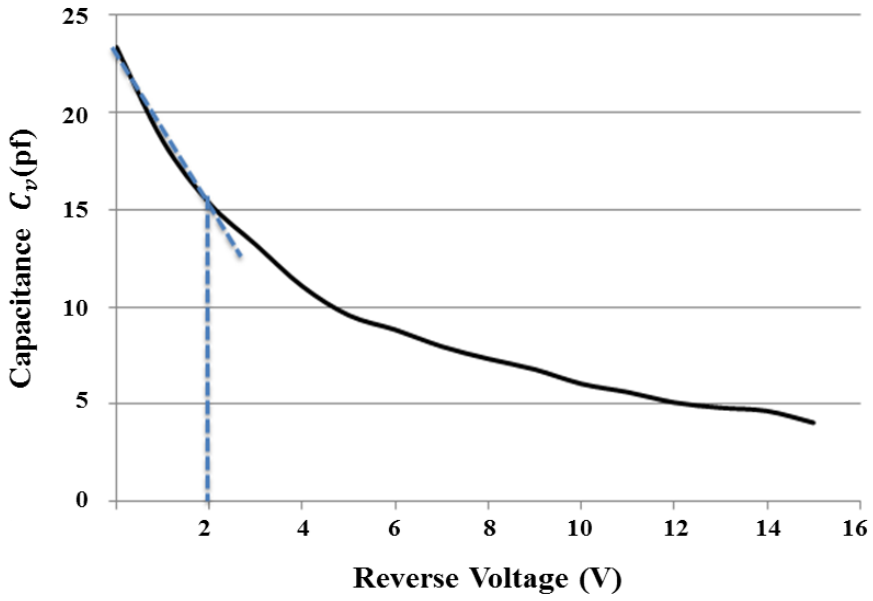

Figure 34: C-V characteristic of 1sv229 varactor following [130].

Figure 35 shows the modulation index against charged surface voltage behaviour of some of the data from figure 33. Only coupling capacitances of 15 pF and 10 pF are considered for the varactors driven at 10 Vpk-pk. The behaviour of the output waveform demonstrates the amount of amplitude modulation as a fraction of the unmodulated carrier signal. The magnitude of modulation depends on the coupling capacitance, the potential on the charged surface and the voltage driving the varactors. The modulation index increases for a larger coupling capacitance.

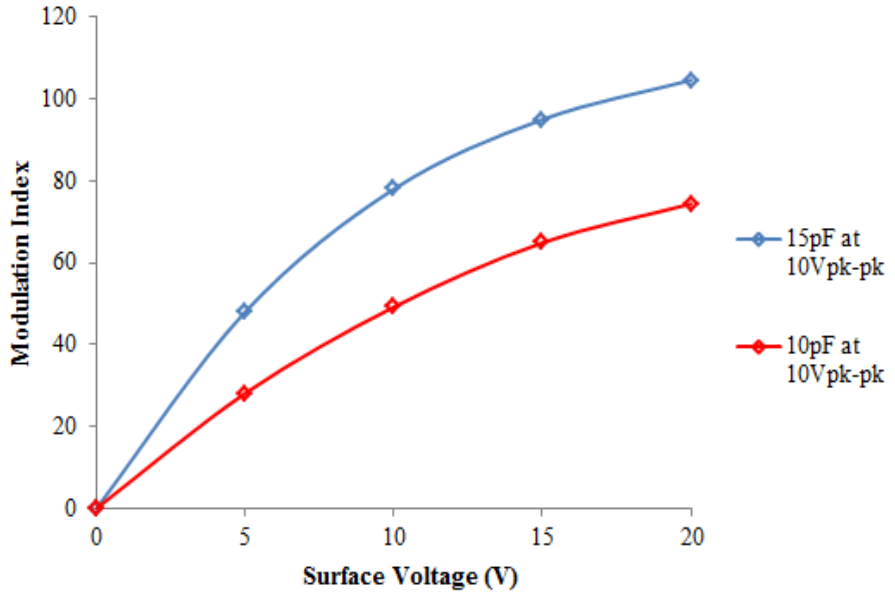

Figure 35: Modulation index vs Surface voltage (V) for 10 pF and 15 pF coupling capacitance.

3.4. Construction of the Measurement System

The measurement system was constructed in different stages. All electronic components were mounted onto separate PCB boards and joined together at the end to make one complete charge measurement circuit. The various stages are illustrated below.

- High Frequency Sinusoidal Oscillator
- High Frequency Transformer
- Varactor detector circuit
- Pre-Amplifier
- Demodulator
- Instrumentation Amplifier
- Data acquisition

A block diagram of the measurement system is shown below.

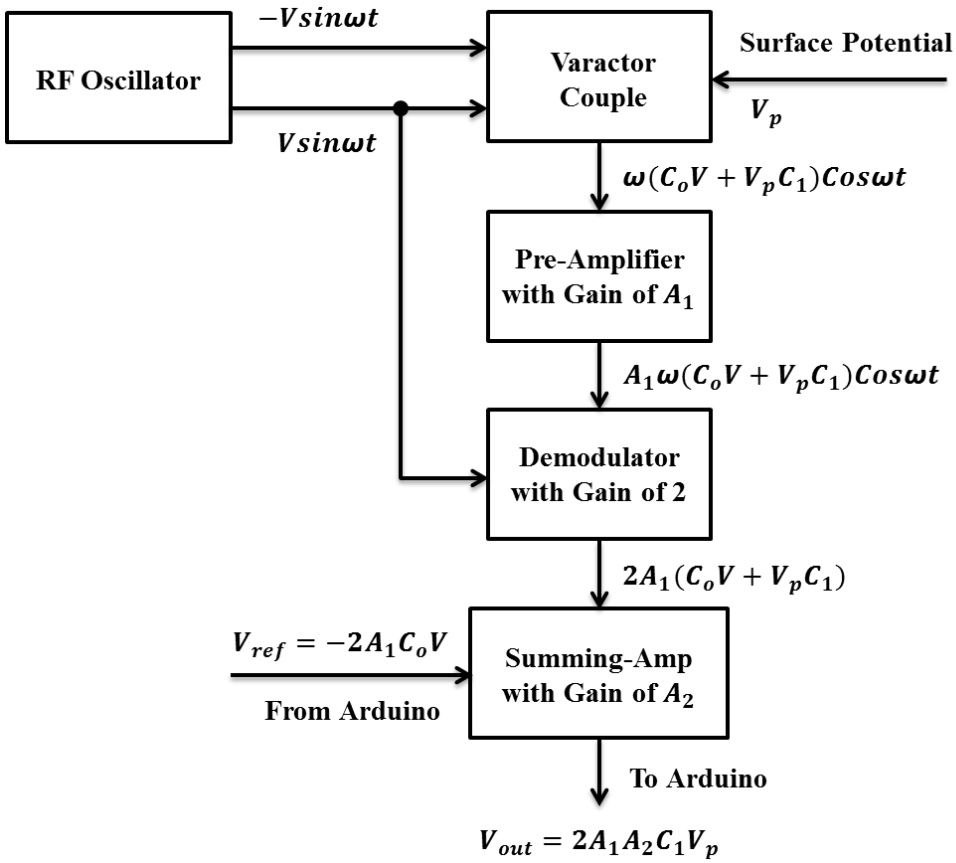

Figure 36: Overview of the charge measurement circuitry.

3.4.1. High Frequency Sinusoidal Oscillator

The high frequency signal was attained through the construction of a Wien bridge oscillator. It was designed to produce a sinusoidal signal having a frequency of ~ 500 kHz. The frequency of the oscillator was chosen so that it would also meet the maximum range of the demodulator circuitry. The function of the oscillator was to power up the centre-tapped transformer which would provide an oscillating signal to each of the two varactors in the varactor detector circuit as described in figure 22. The magnitude of the signal being provided by the transformer was controlled by adjusting the gain of the Wien bridge circuit. This was achieved by using a potentiometer to set the gain of the Wien bridge circuit as desired. As well as providing the ac voltage for the varactor pair the Wien Bridge also provides a carrier reference signal used in the demodulation stage. The amplifier used in the construction of this circuit was the (AD842). It was chosen as it provided more than ample gain bandwidth product (80 MHz) and slew rate (375 V/μs) which made it suitable for use in this circuit design. Figure 37 shows the circuit representation of the Wien Bridge.

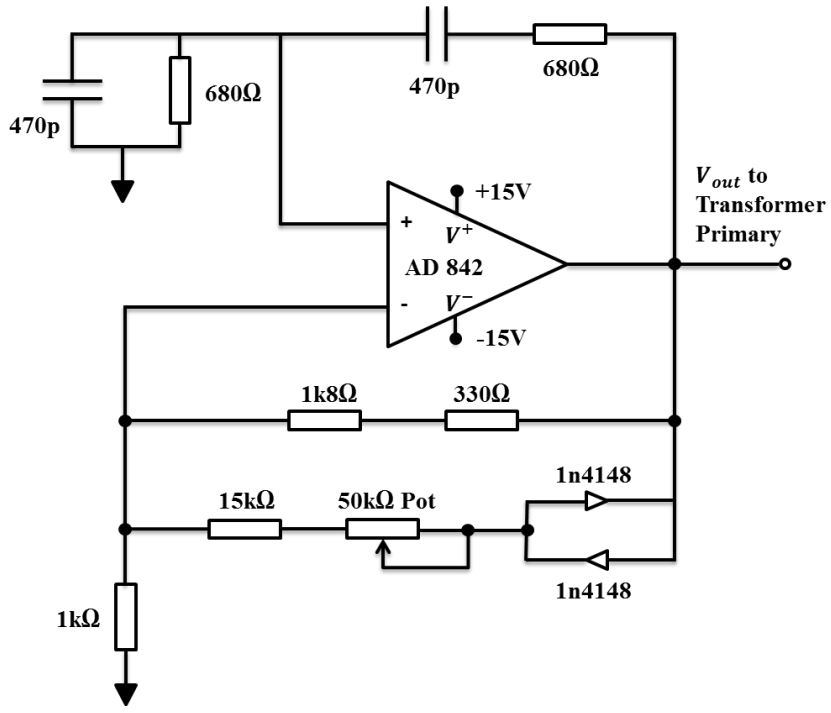

Figure 37: Wein bridge oscillator to provide ~ 500 kHz sinusoidal signal.

3.4.2. High Frequency Transformer

A centre tapped transformer was required to supply the two 180° out of phase sinusoidal voltages for the varactor pair from the single output of the Wein bridge oscillator. The

current flowing from the centre tap through the sensing resistor provides the modulated output from the varactor detector circuit. The transformer was hand constructed by using a ferrite toroid core. The ratio between the primary winding and each end of the secondary windings was 2:1. A tertiary winding with 8 turns was also present to provide the carrier reference for the demodulator. Figure 38 shows the diagram of the centre tapped transformer.

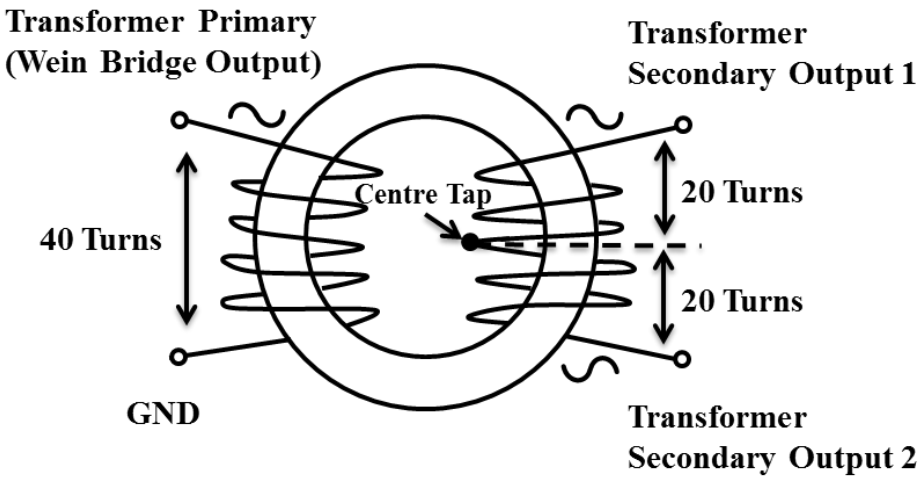

Figure 38: Centre tapped transformer powered up by the Wien Bridge oscillator.

3.4.3. Varactor Detector Circuit

The varactor detector circuit was constructed as described in section 3.2. It was assembled on a separate PCB board placed in close proximity to the probe to minimise interference. A separate circuit board was used to allow the varactor pairs to be easily changed to adjust the sensitivity of the circuit. The following varactor pairs were available: MA46H070-1056 (0.7 pF), SMV2201-040LF (0.855 pF), MA144769-287T (1.2 pF), 1SV277 (4 pF), 1SV229 (14 pF) and 1SV232 (28 pF). Figure 39 shows the circuit diagram.

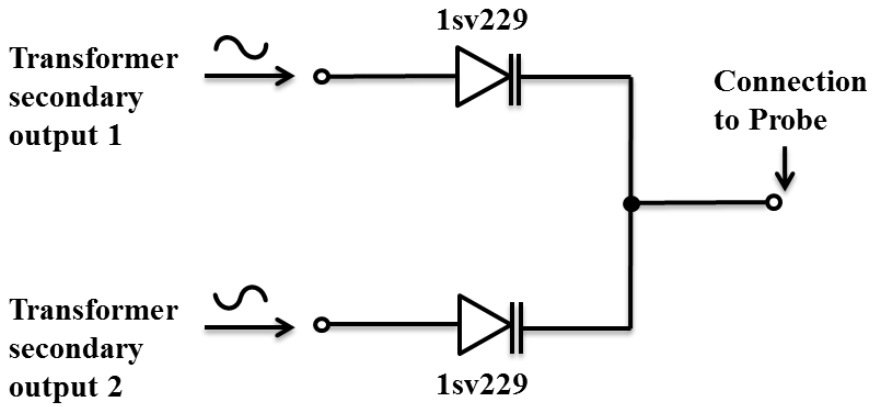

Figure 39: Varactor detector circuit.

3.4.4. Pre-Amplifier

After the signal has been produced by the varactor detector circuit it is necessary to amplify the magnitude of the detected signal. This is done so that the requirements of the rest of the circuitry are met. A non-inverting amplifier with a variable gain was constructed to carry out this process. The amplifier used was again the AD842 as its gain bandwidth product and slew rate were more than adequate for this circuit. Initially a gain of 20 was intended but available resistor values were used providing a gain of 23. The circuitry for the amplifier is shown in figure 40.

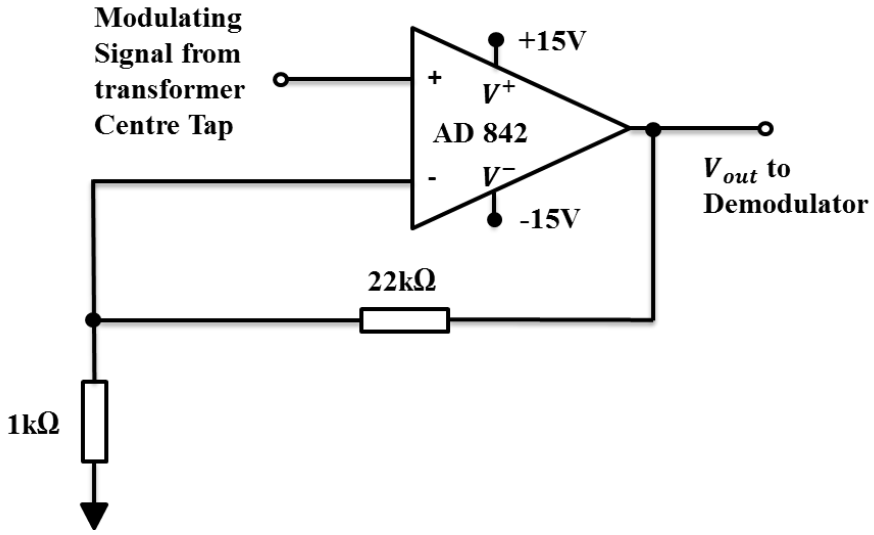

Figure 40: Non-Inverting pre-amplifier circuit.

3.4.5. Demodulator

The purpose of the demodulator circuit is to extract the sensed voltage signal from the modulated carrier signal**.** This can be achieved simply by a use of a diode however; there are other more efficient ways to achieve demodulation of a signal**.** In order to demodulate an amplitude modulated signal it is important to understand the format of the modulated signal. Amplitude modulation consists of a carrier reference signal and any modulation appears as sidebands on each side of the carrier reference. These side bands are a mirror image of each other. An amplitude modulated signal is dominated by the carrier reference signal and it is reported that in a 100 % modulated signal the sidebands consists of 25 % of the full signal [131].

In amplitude demodulation one of the most important elements is to create a base band signal. Although this process can be achieved by simple use of a diode and rectifying the

signal. This method leaves elements of the original carrier reference. Therefore, in this measurement system, demodulation of the signal was achieved through a custom made synchronous demodulator which was expected to provide a much higher level of performance than simple use of a diode. Figure 41 shows the overview of the demodulator circuit.

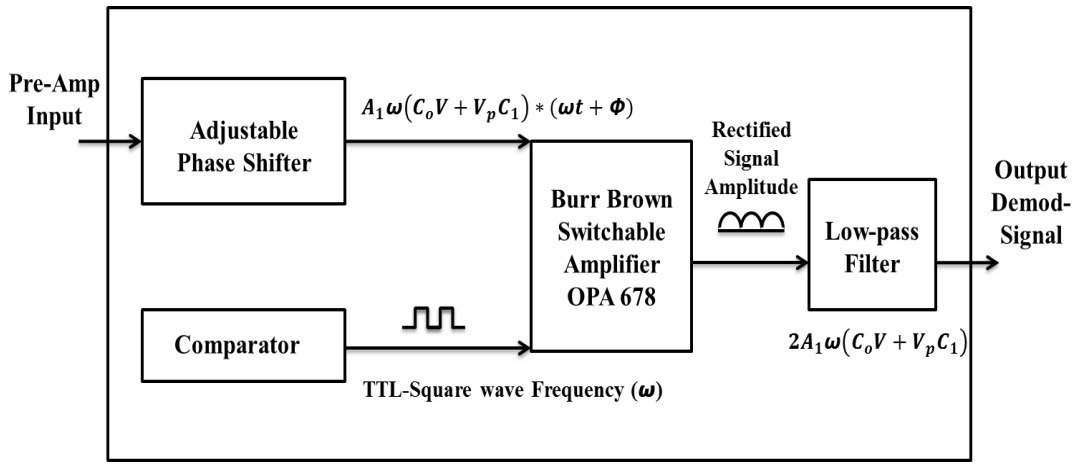

Figure 41: Demodulator circuit overview.

The demodulator circuit consists of four stages.

- Phase Shifter
- Comparator
- Switching Device
- Low Pass Filter

All four stages were constructed and tested on separate PCB boards and combined together to make one full working demodulator with high performance capability. The details of each stage are described below:

3.4.5.1. Phase Shifter

The phase shifting circuit was constructed so that the phase of the carrier reference going into the switching device could be adjusted to have the same phase as that of the modulated signal coming from the pre-amplifier. An additional output was taken from the Wien Bridge that was passed through the transformer tertiary winding. The winding was configured to step down the voltage to an acceptable level for the comparator circuit. Phase matching was achieved by the use of a potentiometer that could be adjusted to provide a phase shift of up to 90 degrees. The phase shifter circuit is an all-pass filter which provides frequency

dependent phase shift with unity gain. It was constructed to work at the frequency of the carrier signal. The phase shifter circuit is shown in figure 42.

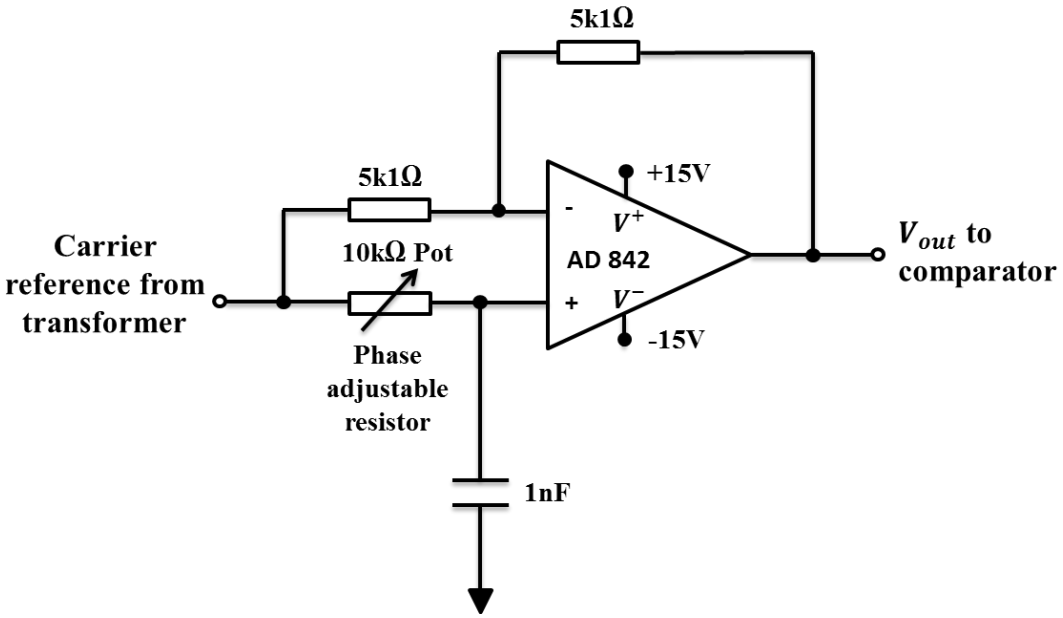

Figure 42: Phase shifter circuit to adjust phase of the carrier reference to equal that of the modulated signal.

3.4.5.2. Comparator

The comparator circuit converts the carrier sinusoidal signal into a ± 5 V TTL signal at the same frequency as that of the carrier wave. This stage was added to the circuitry as the switching device (OPA678) in the following stage required a TTL input as it's carrier reference. In this circuit the LT 1016 ultra-fast (10 ns) comparator IC was used. The circuit was constructed following the data sheet [132] of the LT 1016 comparator. Figure 43 shows the circuit diagram of the comparator.

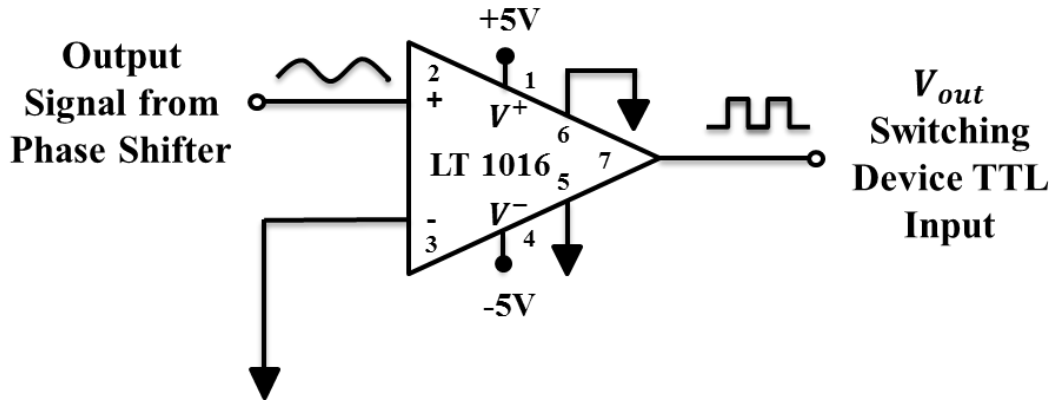

Figure 43: Comparator circuit to convert sinusoidal carrier into TTL output.

The phase of the TTL waveform was adjusted through the phase shifter. As the phase shifter output was the input reference to the comparator, any phase adjustment to the phase shifter output consequently changed the phase of the comparator output in equal amount.

3.4.5.3. Switching Device

The switching device used for this part of the circuitry was the OPA678 wide band switched-input operational amplifier. The circuit of the switching device was constructed following the data sheet [133] of the OPA678 IC. The circuit was constructed to provide an output waveform with a gain of 2. Figure 44 shows the circuit diagram of the switching device.

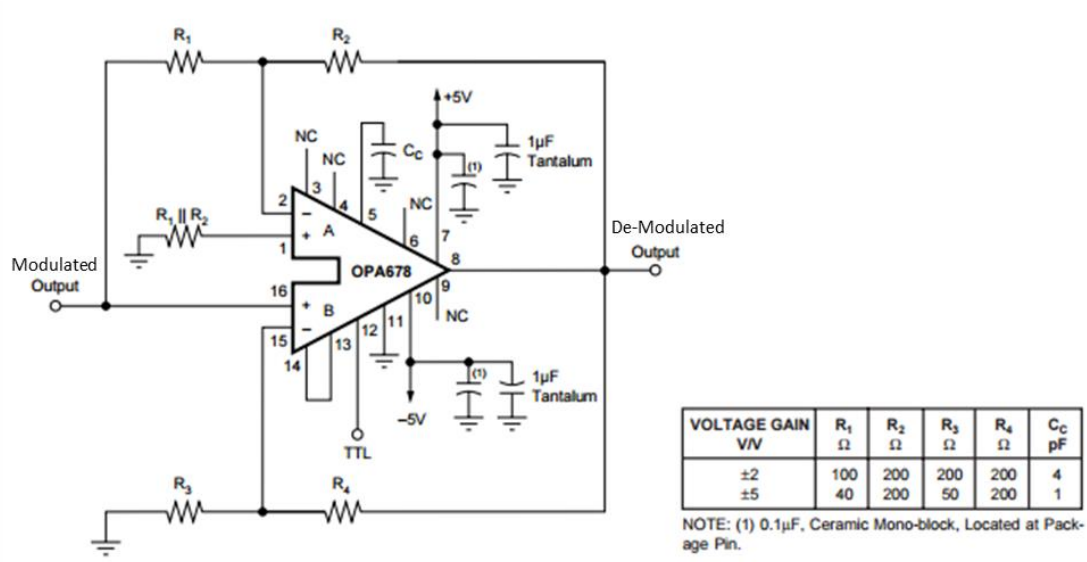

Figure 44: Circuit diagram for switching device with gain [133]

As the phase between the two input signals is the same, the device rectifies the signal at the zero crossing point. If there is a difference in phase or frequency between the carrier reference and the input signal, rectification does not occur and the output will be rejected by the integration that occurs in the low pass filter stage. This way a more precise and sensitive demodulation of the signal is achieved. The technique is very useful in obtaining small signals from high noise levels and providing a signal with significantly less distortion.

3.4.5.4. Low-Pass Filter

As the modulation signal being retrieved from the rectified amplitude modulated signal was at much lower frequencies than the carrier signal, it was possible to obtain the modulation signal by passing the rectified signal from the switching device through a low-pass filter. The low-pass filter allows all frequencies below a specific cut-off to pass through (modulation

signal) and block frequencies of higher magnitude than this point (carrier signal). This stage would remove unwanted high frequency components from the output signal leaving the modulated signal with residual interference from the high frequency components of the carrier signal. In this study a low pass filter with a cut-off frequency of ~ 3.3 kHz was chosen. This would certainly block the carrier signal coming in at ~ 500 kHz and would allow the much slower modulating signal to pass through. The circuit diagram for the low-pass filter is shown in figure 45.

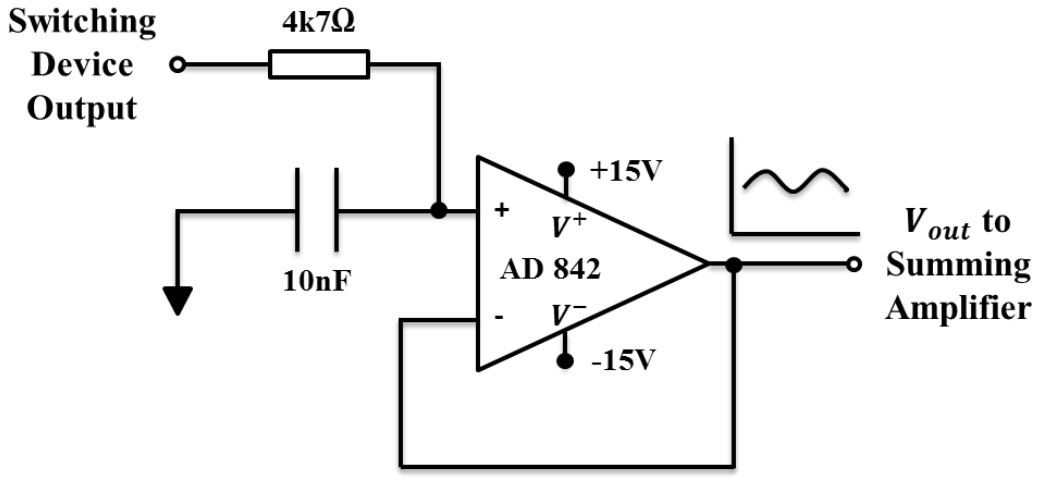

Figure 45: Low-pass filter with a cut-off frequency of 3.3 kHz.

3.4.6. Instrumentation Amplifier

After the demodulation, the output signal contains a DC value depending on the constant component of the varactor capacitance plus a component depending on the probe voltage and the varying element of the varactor capacitance. To optimise detection of the varying element of the signal an instrumentation amplifier (ina128p [134]) was used to eliminate the DC component using a reference signal provided by the Arduino Uno microcontroller. Although the microcontroller does not have an analogue output pin, it is achievable by using DAC (digital to analogue conversion card), which in this instance was the MCP4725 from Adafruit. The instrumentation amplifier was designed to provide four different gain values in case the signal detected needed amplification. Gains of ~ 1, 2, 5 and 10 were achievable by using a rotary switch and switching between fixed resistors i.e. $\boldsymbol{R_G}$ that would adjust the gain accordingly. The gain $\boldsymbol{G}$ of the system was given by equation 64.

$$\boldsymbol{G = 1 + \frac{50\ k\Omega}{R_G}} \tag{64}$$

Where,

R_G = any of the four fixed resistor values that can be selected by adjusting the rotary switch. Figure 46 shows the circuit diagram of the instrumentation amplifier.

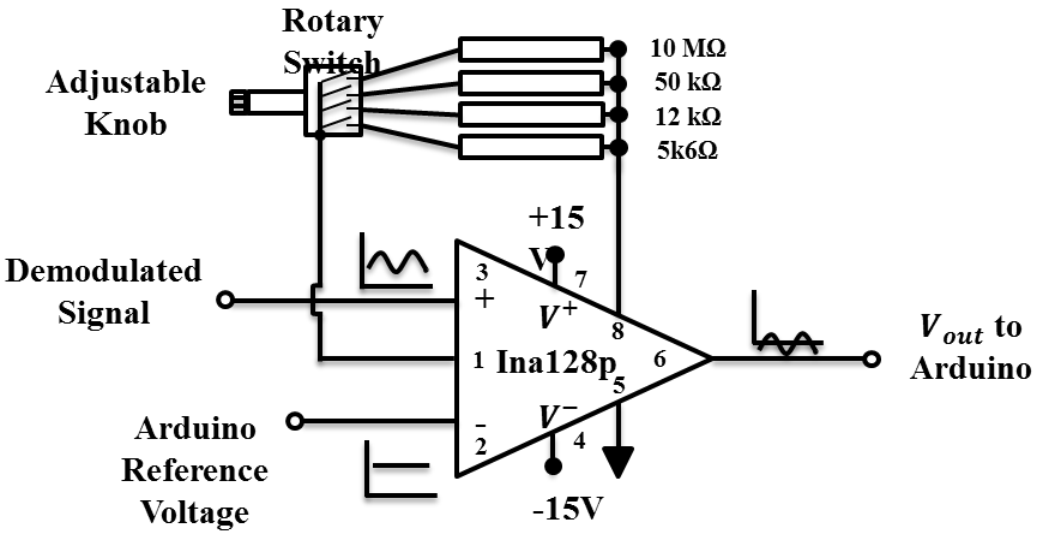

Figure 46: Instrumentation amplifier with a range of gain selection.

3.4.7. Data Acquisition

Data was acquired using the Arduino Uno microcontroller. The analogue input pins of the microcontroller only measure in the positive domain and have a maximum range of + 5 V. The gain of the instrumentation amplifier was set so that the maximum range of the microcontroller analogue input pin is not exceeded, as this would result in damaging the device. A program was written in the Arduino software (IDE) to record the data and this was latter sent to excel as a comma separated value (CSV) for processing. The Arduino program was also used to control the amount of voltage being provided to the non-inverting input of the instrumentation amplifier so that the demodulated signal could be brought to the zero reference point.

3.4.8. Full Circuit Simulation

Simulation of the full circuit was carried out in PSpice simulation software. The values chosen for the voltage driving the varactor pair, coupling capacitance and charged surface potential are all arbitrary and are chosen just to provide a better understanding of the expected behaviour of the circuit as the signal passes through each stage of the circuitry. Figure 47 shows the circuit diagram for the complete measurement system.

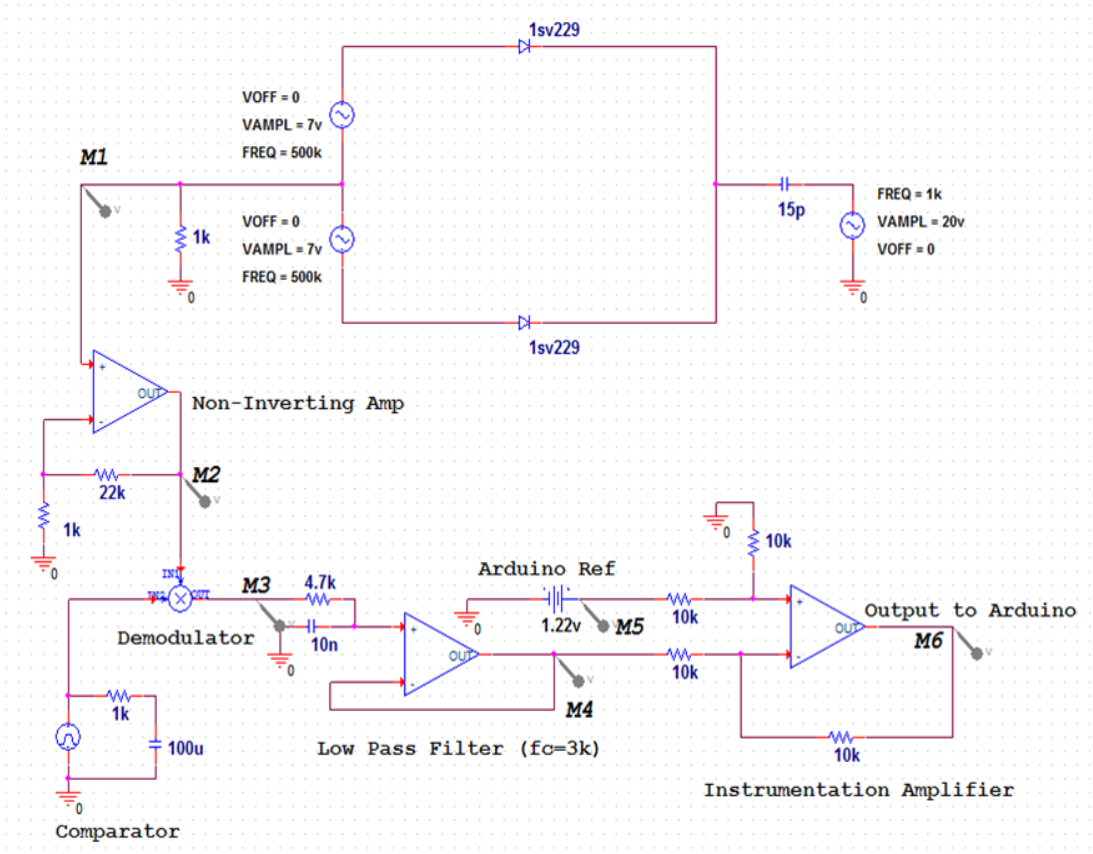

Figure 47: Complete measurement circuit for PSpice simulation

Figure 47 shows a circuit representation of all the stages of the complete measurement circuit. These stages were constructed in PSpice to mimic the behaviour of the actual system. Although this function is achieved, it is to be noted that some stages (comparator and demodulator) are chosen as a square wave source and a multiplier that would effectively rectify the signal as expected of the demodulator. These simple circuits were chosen from the PSpice library for simplicity, as the actual circuit of the demodulator was complex and would have caused convergence problems when running the full circuit.

Figure 48 shows the simulated outputs from PSpice at each stage of the measurement circuit. The expected outputs are marked at the output nodes (**M1**, **M2**, **M3**, **M4**, **M5**, and **M6**) of each stage in figure 47. Where, **M1** is the output of the varactor detector circuit, **M2** is the output of the non-inverting pre-amplifier, **M3** is the output of the demodulator, **M4** is the output of the Low-pass Filter, **M5** is the reference voltage from the Arduino Uno microcontroller and **M6** is the sensed output from the instrumentation amplifier going into the Arduino Uno analogue input.

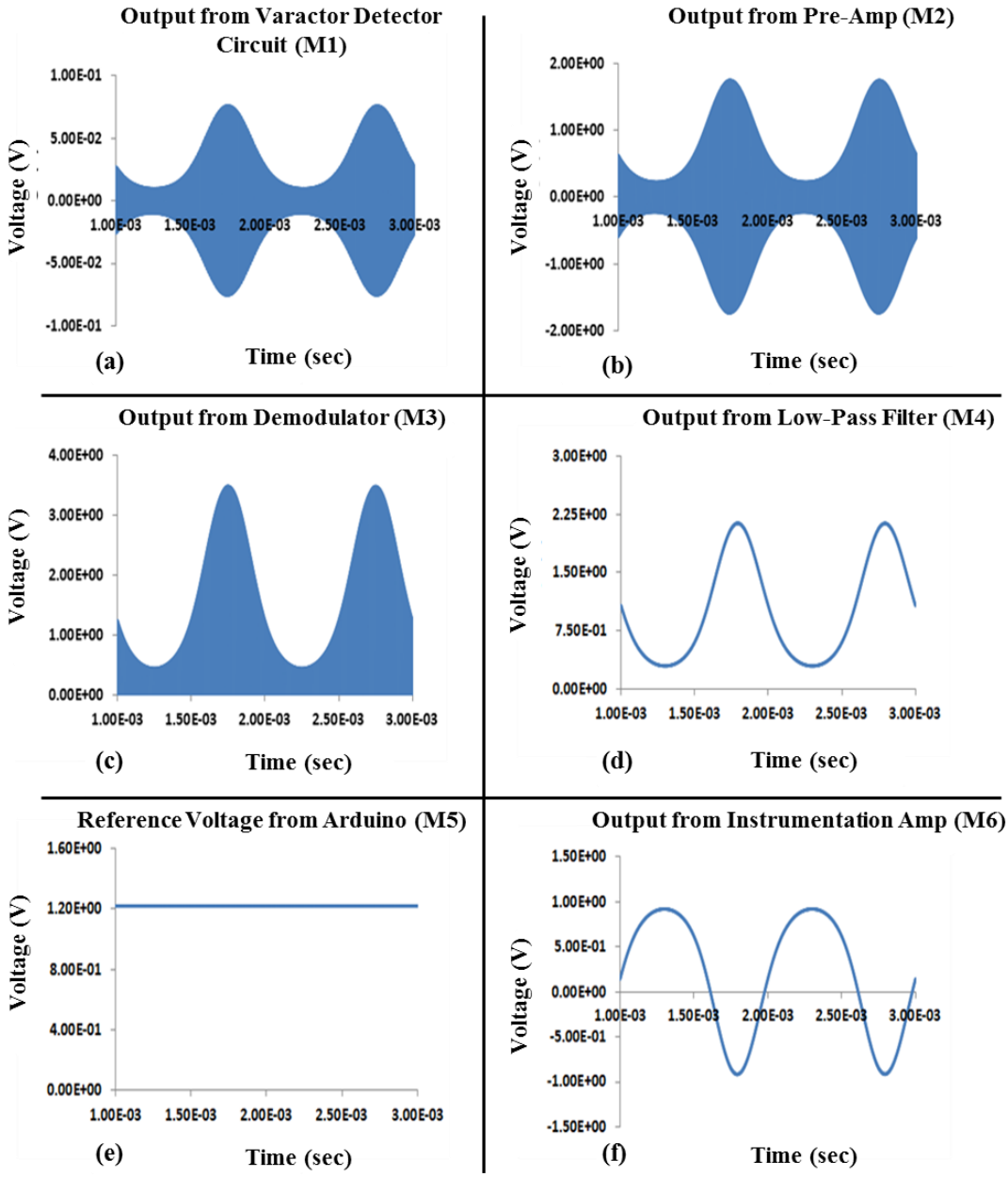

Figure 48: Full circuit simulation where, (a) M1, (b) M2, (c) M3, (d) M4, (e) M5 and (f) M6.

Figure 49 shows an image of the actual constructed circuitry, which was assembled into a grounded metal box to minimise unnecessary noise interference.

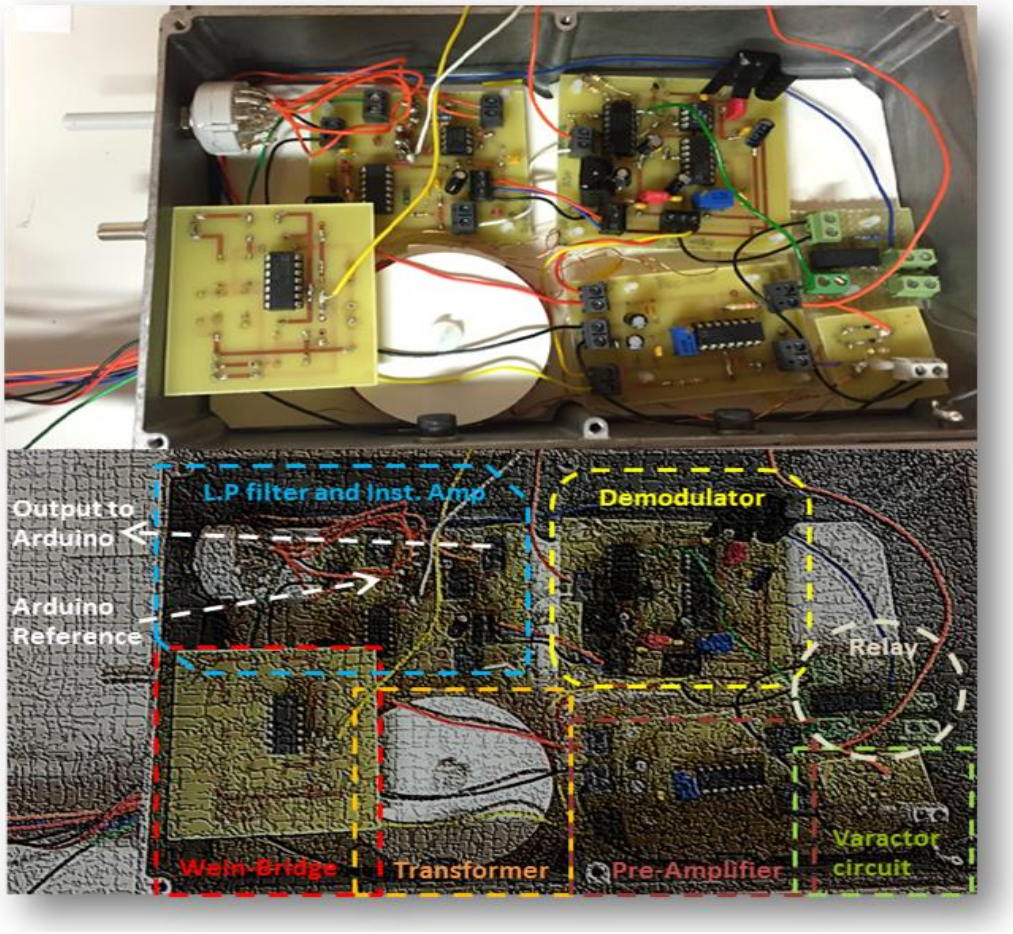

Figure 49: Complete charge measurement circuit.

3.5. Chapter 3: Summary

In this chapter a detailed background study of the varactor probe sensor was presented. PSpice modelling to demonstrate the effect of the magnitude of coupling capacitance between probe sensor and test surface and the effect of the magnitude of the potential of the test surface on the detected signal was performed. It was observed that the modulation of the detected signal increases with an increase in the coupling capacitance. The design and development of the probe circuitry is presented and simulations to observe the probe output were also performed.

4. Construction of the Capacitive Probe and Calibration of the Measurement System

4.1. Capacitive Probe- Construction and Theory

The use of the shielded capacitive probe was first employed by Davies in [26]. Following Al-Bawy [5] the basic construction of the capacitive probe geometry and its expected output can be explained. Figure 50 shows the basic structure of a capacitive probe and its equivalent circuit.

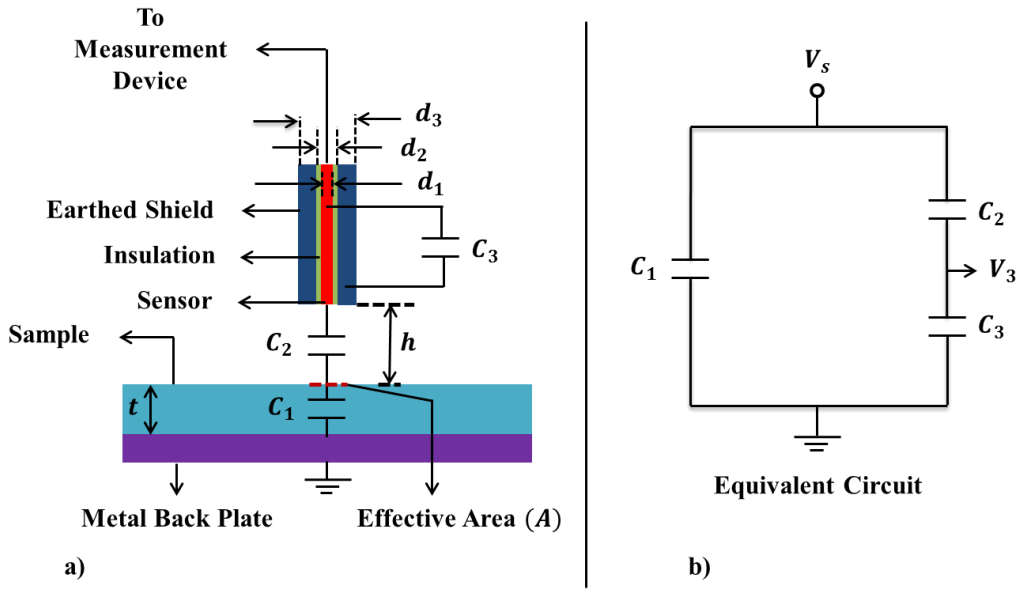

Figure 50: (a) Basic construction of capacitive probe, (b) Equivalent circuit

The charge that is induced on the probe sensor tip is determined by the effective area $\boldsymbol{A}$ which is defined as the area that the probe tip is exposed to. The size of the effective area along the surface of the sample is dependent on the gap $\boldsymbol{h}$ between the probe and the sample under observation, diameter of the probe sensor $\boldsymbol{d_1}$, the thickness of the dielectric $\boldsymbol{d_2}$, and the diameter of the outer conductor of the probe $\boldsymbol{d_3}$ [13]. The effective area is always larger than the probe sensor diameter $\boldsymbol{d_1}$. This is because some of the flux lines from the gap between $\boldsymbol{d_1}$ and $\boldsymbol{d_2}$ terminate at the outer conductor of the probe and also at the probe sensor tip. The amount of charge induced on the probe is dependent on the effective area. For a

good spatial resolution it is important that the area be kept minimal. The grounded outer conductor plays a key role in restricting this effective area.

Measurements are performed with the probe being held parallel to the insulator surface. This enables a uniform field to be established between the probe sensor tip and the insulator surface. The surface of the probe is also carefully ground flat so that any non-uniformity in the field between the probe and the insulator surface due to excessive protrusions on the probe can be minimised. The measurement system under the condition that a uniform field has been established between the probe and insulator surface of thickness $\boldsymbol{t}$ backed by a grounded back plate can be characterised by the equivalent circuit in figure 50b, where the probe is modelled as a capacitive divider.

In figure 50b: the capacitance $\boldsymbol{C_1}$ represents the capacitance between the insulator sample and the grounded back plate, $\boldsymbol{C_2}$ the capacitance between the probe sensor and the test sample and $\boldsymbol{C_3}$ the combined capacitance of the probe to ground which includes the input capacitance of the measuring device and the capacitance of the connecting lead from the probe to the measuring device.

The potential $\boldsymbol{V_3}$ measured at the probe sensor can be expressed as equation 65 [5, 26].

$$\boldsymbol{V_3 = \frac{\sigma * A}{C_1 + C_3(1 + {C_1}/{C_2})}} \tag{65}$$

Where,

$\boldsymbol{A}$ = Effective Area

$\boldsymbol{\sigma}$ = Surface Charge Density on the Insulator

As the field between the probe and insulator is assumed to be uniform, under this condition the capacitance $\boldsymbol{C_1}$ can be expressed as:

$$\boldsymbol{C_1 = \frac{A * \epsilon_o \epsilon_r}{t}} \tag{66}$$

Where,

$\boldsymbol{\epsilon_o}$ = Permittivity of free space.

$\boldsymbol{\epsilon_r}$ = Relative permittivity of the dielectric.

$\boldsymbol{t}$ = Thickness of the dielectric material.

The capacitance $\boldsymbol{C_2}$ can be expressed as:

$$\boldsymbol{C_2 = \frac{A * \epsilon_o}{h}} \tag{67}$$

Where,

$\boldsymbol{h}$ = the gap between the probe and the dielectric material.

The expression in equation 65 can be further simplified as the capacitance $\boldsymbol{C_1} << \boldsymbol{C_3}$ and can be expressed as:

$$\boldsymbol{V_3} = \frac{\boldsymbol{\sigma} * \boldsymbol{A}}{\boldsymbol{C_3}(\mathbf{1} + {}^{\boldsymbol{C_1}}/_{\boldsymbol{C_2}})} \tag{68}$$

Substituting the expressions for $\boldsymbol{C_1}$ and $\boldsymbol{C_2}$ in equation 68 further simplifies the expression for the output potential $\boldsymbol{V_3}$ and can be expressed as:

$$\boldsymbol{V_3} = \frac{\boldsymbol{\sigma} * \boldsymbol{A}}{\boldsymbol{C_3}(\mathbf{1} + \boldsymbol{\epsilon_r} * {}^{\boldsymbol{h}}/_{\boldsymbol{t}})} \tag{69}$$

The height $\boldsymbol{h}$ of the probe above the insulator surface will strongly influence the output potential induced across the probe sensor as this will affect the different capacitances associated with the system. As $\boldsymbol{h}$ decreases the output potential will increase for a given value of $\boldsymbol{\sigma}$. However, it is to be noted that the reduction of height below a certain value might cause discharges on the surface of the probe and result in damage to the measurement circuitry [13]. As the height of the probe above the surface of the insulator is varied, the existing field strength on the charged dielectric material is changed. Due to the very high resistivity of the dielectric surface and low mobility of the charges, the charge distribution on the surface is not significantly changed which enables the measurement of surface charge. It is therefore important to calibrate the system with regards to the height $\boldsymbol{h}$ along with other parameters that might influence the output signal being sensed by the probe.

4.2. Initial Simulations on Probe Parameters

In order to observe the effect of different parameters of the probe structure on the sensed output signal, a two dimensional axisymmetric model was constructed using Tera Analysis QuickField simulation software. The sample being used was a metal plate of known potential. The simulations were carried out with atmospheric air as the surrounding medium. Figure 51 shows the geometry constructed in QuickField and the field distribution across the system.

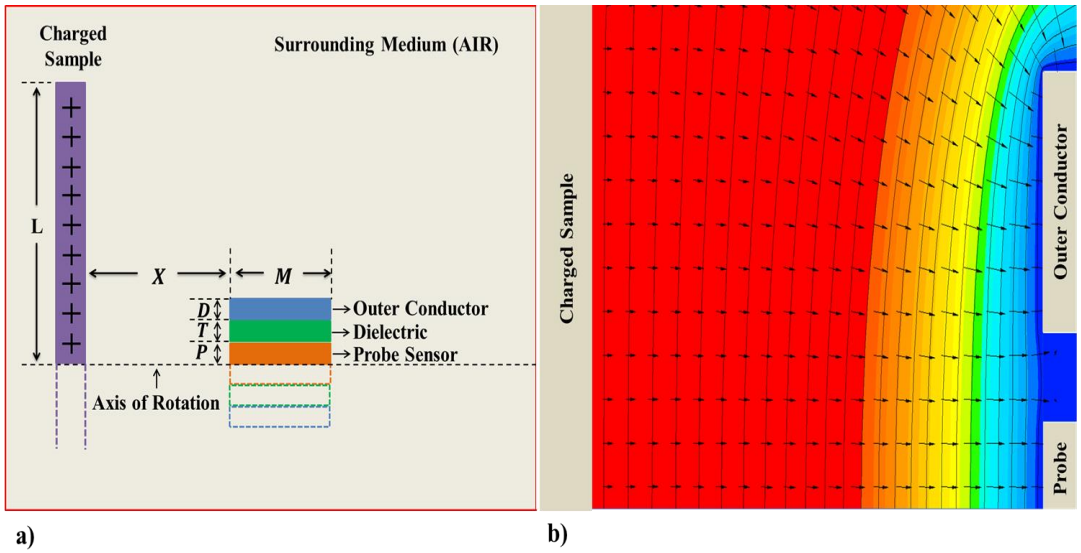

Figure 51: a) The modelled two dimensional probe geometry in QuickField, b) Field distribution across the geometry with high field region denoted by the red coloured zone and blue region denotes the lower field zone in the vicinity of the probe.

After constructing the model above, simulations were run to obtain the surface potential measured by the probe sensor by varying different parameters of the model. Four different observations were made and during each observation, all the other parameters were kept constant including the surface potential on the sample under investigation. The observations were made in the order below:

- Effect of probe sensor thickness ***P***.
- Effect of dielectric thickness ***T***.
- Effect of probe outer conductor thickness ***D***.
- Effects of gap separation ***X***.

The dimensions of the parameters of the geometry in figure 51 can be seen in table 1:

Table 1: Initial parameters of the simulated geometry.

Probe Length ***M***	Sample Length ***L***	Probe Sensor Thickness ***P***	Dielectric Thickness ***T***	Outer Conductor Thickness ***D***	Probe to Sample Gap ***X***
5 mm	20 mm	0.5 mm	0.5 mm	0.5 mm	5 mm

The length ***M*** of the probe and the charged surface ***L*** had a fixed value throughout the simulations. The potential allocated to the charged surface was also kept constant while the thickness of the parameters ***P***, ***T*** and ***D*** of the probe sensor, dielectric and the probe outer

conductor were changed along with the gap separation $\boldsymbol{X}$ and observations were made on the output across the probe sensor. The results obtained are discussed below.

4.2.1. Effect of Probe Sensor Thickness $\boldsymbol{P}$

The output response was observed for three different probe sensor thickness P, having the radii of 0.5 mm, 1 mm and 1.5 mm. During the simulation all other dimensions of the probe were kept constant. The values of these parameters are shown in table 1. The simulations were repeated with changing the potential on the sample surface from 0 to 3 kV with 6 increments of 500 V. It was observed that the potential at the probe sensor increased with an increase in the probe sensor thickness P. This trend was observed throughout the simulation. Figure 52 shows the results obtained for this observation.

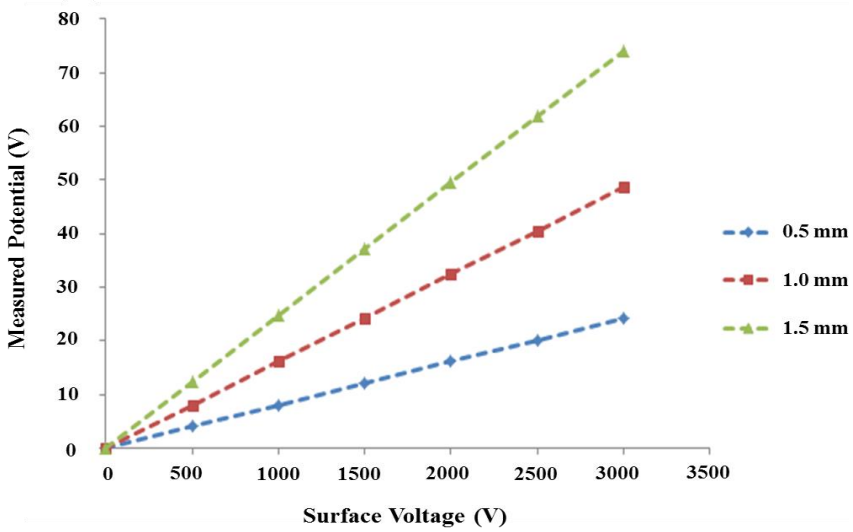

Figure 52: Simulated output response with changing probe sensor thickness.

As the probe model constructed is similar to that of a coaxial cable the capacitance $\boldsymbol{C_3}$ can be represented as equation 70 which represents the expression for the capacitance per unit length between the outer and the inner conductor of a coaxial cable.

$$\boldsymbol{C_3 = \frac{2\pi\epsilon_o}{ln\left[B'/A'\right]}} \tag{70}$$

Where,

$\boldsymbol{B'}$ = the inner radius of the outer conductor which in terms of figure 51a is the sum of the radius $\boldsymbol{P}$ of the sensor and the thickness $\boldsymbol{T}$ of the dielectric.

$\boldsymbol{A'}$ = the radius $\boldsymbol{P}$ of the inner conductor i.e. the probe sensor.

Hence, the capacitance C_3 can be expressed as:

$$C_3 = \frac{1}{ln\left[\frac{P+T}{P}\right]} \tag{71}$$

The equivalent circuit for figure 51a can be represented as figure 53.

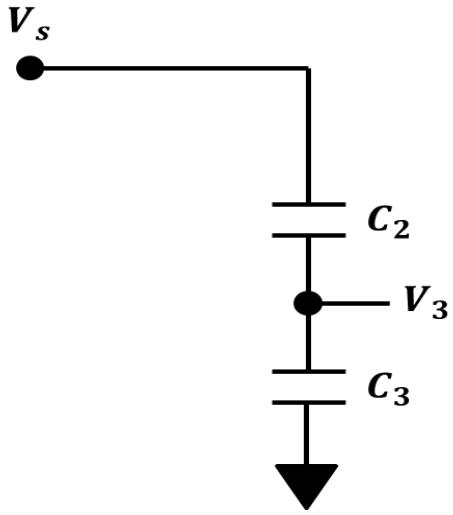

Figure 53: Equivalent circuit of figure 51a.

The output voltage V_3 can be expressed as equation 72.

$$V_3 = \frac{C_2}{C_2 + C_3} * V_S \tag{72}$$

Where,

V_s = Voltage of the sample surface.

The magnitude of the capacitance C_2 between the probe sensor and the charged sample is dependent on the surface area of the probe sensor tip and can be expressed as equation 73.

$$C_2 \propto \pi R^2 \tag{73}$$

Where,

R = radius P of the probe sensor.

As the radius P of the probe sensor increases, this results in an increase in the capacitance C_2 and C_3. The capacitance C_2 increases at a higher rate than C_3 resulting in an increase in the output potential V_3. The increase observed in the measured potential across the sensor of the probe follows the theoretical explanation.

4.2.2. Effect of Dielectric Thickness T

The output response was observed for three different dielectric thickness $\boldsymbol{T}$ of 0.5 mm, 1 mm and 1.5 mm. During the simulation all other dimensions of the probe were kept constant. The values of these parameters are shown in table 1. The simulations were repeated with changing the potential on the sample surface from 0 to 3 kV with 6 increments of 500 V. It was observed that the potential at the probe sensor increased with increase in the dielectric thickness. This trend was observed throughout the experiment. Figure 54 shows the results obtained for this observation.

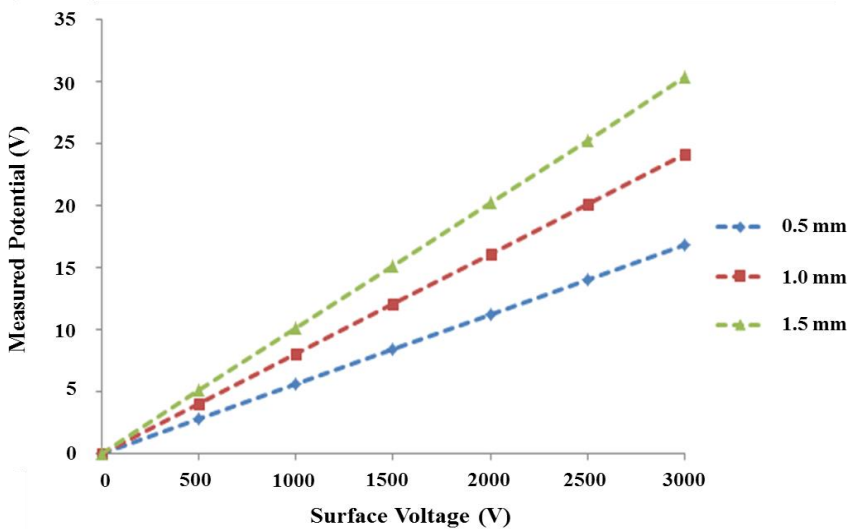

Figure 54: Output response across probe sensor for changing dielectric thickness.

The output potential response observed across the probe sensor follows the theory as the increase in the dielectric thickness $\boldsymbol{T}$ results in a decrease in the capacitance $\boldsymbol{C_3}$. According to equation 72, as $\boldsymbol{C_3}$ decreases this results in an increase in the measured output potential.

4.2.3. Effect of Outer Conductor Thickness D

The output response was observed for three different outer conductor thickness $\boldsymbol{D}$ of 0.5 mm, 1 mm and 1.5 mm. During the simulation all other dimensions of the probe were kept constant. The values of these parameters are shown in table 1. The simulations were repeated with changing the potential on the sample surface from 0 to 3 kV with 6 increments of 500 V. It was observed that the potential at the probe sensor decreased with an increase in the thickness of the probe outer conductor. This trend was observed throughout the experiment. Figure 55 shows the results obtained for this observation.

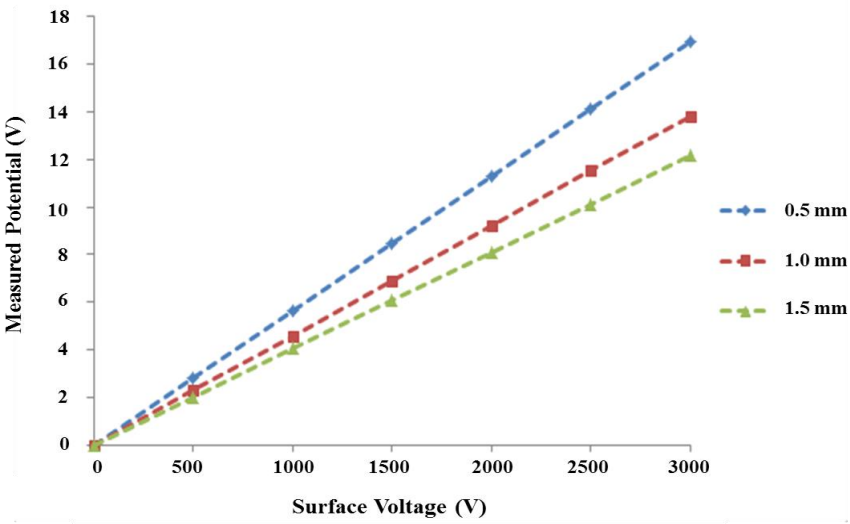

Figure 55: Output response across probe sensor for changing outer conductor thickness.

The effective area ***A*** that induces the charge on the probe sensor tends to become smaller and closer to the area of the probe sensor tip as fringing fields are eliminated. Hence, the amount of charge induced on the probe sensor and therefore the measured potential is reduced.

4.2.4. Effect of Gap Separation *X*

The output response was observed for three different probe to charged sample gap separations of 5 mm, 10 mm and 15 mm. During the simulation all dimensions of the probe were kept constant. The values of these dimensions are shown in table 1. The simulations were repeated by changing the potential on the sample surface from 0 to 3 kV with 6 increments of 500 V. A decrease in potential across probe sensor was observed.

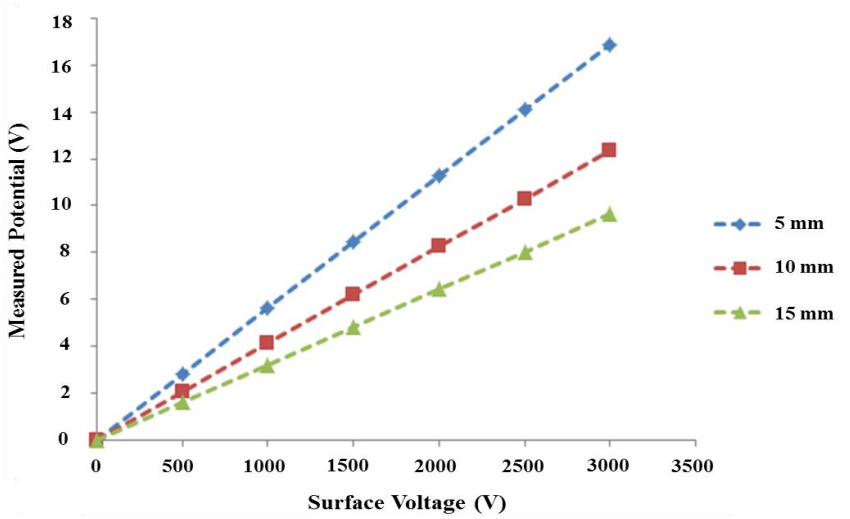

Figure 56: Output response across probe sensor for changing gap separation.

The observed output potential response follows the theory as according to equation 67 the relationship between the capacitance $\boldsymbol{C_2}$ and the gap separation $\boldsymbol{h}$ can be expressed as equation 74.

$$\boldsymbol{C_2} \propto \frac{\boldsymbol{1}}{\boldsymbol{h}} \tag{74}$$

Capacitance $\boldsymbol{C_2}$ decreases with an increase in the gap separation $\boldsymbol{h}$. According to equation 72, a decrease in capacitance $\boldsymbol{C_2}$ leads to a decrease in the measured potential $\boldsymbol{V_3}$.

4.3. Modifications to the Original Capacitive Probe Design

The initial design of the electrostatic probe in this project was similar to that in [5] and [13]. The probe body was constructed from brass. The outer conductor of the probe had an outer diameter of 12 mm and inner diameter of 9 mm. The dielectric material used to insulate the outer conductor from the inner sensor plate of the probe was a cylindrical nylon spacer of 3.5 mm thickness. The inner sensor of the probe had a diameter of ~ 2 mm and the length of the probe was 70 mm. The probe sensor and the outer conductor were flush to maintain field uniformity.

The sensor of the probe was built in such a way that the backend of the sensor, which was opposite to the end that was exposed to the charged object, was protruding by 5 mm. This was done so that a connection could be made between the measurement circuitry and the probe sensor. It was also thought that any inconsistencies while performing measurements due to this exposed part of the sensor will be negligible as this side of the sensor would reside inside a shielded metal box, hence acting like a Faraday cage and minimising induced potential and noise effects. Furthermore, the connection to the sensor was made through a crocodile clip which was covered with a layer of insulation and was soldered onto a wire which connected to the measurement circuitry.

One of the modifications in the probe geometry compared to the original proposal by Davies in [26] was that the insulation around the tip of the probe sensor was removed and the length of the dielectric was shortened so that it resides inside the outer conductor of the probe. This modification was first employed by Bektas and Farish in [135] and provides two advantages. The first advantage is that the insulation is protected from contamination which would lower the input resistance of the combined circuit leading to a reduction in the probe time constant. The second advantage is that the insulation is no longer in the vicinity of the probe sensor

tip, so it is difficult for the insulation to pick up charge from the sample which might result in variation in the field distribution between the probe and the charged surface.

4.3.1. Shutter Plate and Base Plate

A grounded shutter plate was designed and constructed in order to calibrate the measurement system. The plate provided a surface at ground potential that could be moved into close proximity to the probe which would reduce the measured probe voltage to zero. The thickness of the plate was 1.5 mm. The shutter plate was built with a through hole of 5 mm drilled in it to allow the probe sensor exposure to the charged insulator surface while taking a measurement. Another smaller hole was drilled into the shutter so that a threaded screw could be used to attach it onto a metal rod that was used to hold the shutter plate parallel to the insulator surface. The metal rod with a flange had a threaded hole drilled into the base which allowed the shutter to be screwed onto it. The metal rod was then screwed onto a servo motor which would provide precise control of angular and linear position of the shutter plate. Figure 57 shows a schematic diagram of the top view of the shutter plate.

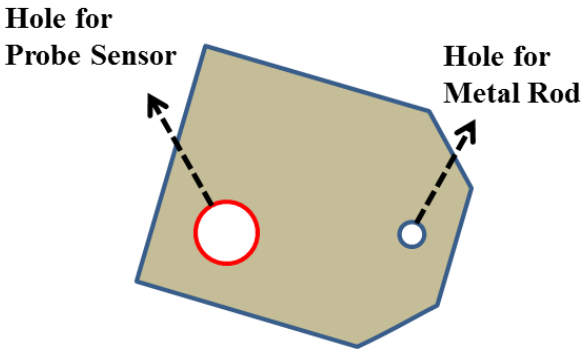

Figure 57: Shutter plate top view.

In addition to the shutter plate, a metal base plate was also designed and constructed that was large enough so that the shutter plate and the screwed metal rod reside beneath it and do not protrude outside the area of the base plate. A suitable diameter of 40 mm was selected for the base plate. The thickness of the base plate was 2 mm. The base plate was constructed with a hole in the middle having a diameter ~ 12 mm. This diameter was slightly larger than the initial probe and allowed a friction fit to be established as the initial probe was fitted through it. A through hole was drilled into one side of the base plate along the central line to allow access to the screwed metal rod. The base plate was constructed in such a way that it was flush with the probe outer conductor and metal grub screws were used to keep the plate in position and establish a solid contact with the probe outer conductor. The purpose of the base

plate was to maintain a uniform electric field between the probe and the charged insulator surface. This should increase the spatial resolution at the cost of a slightly lower measured potential. Figure 58 shows a schematic diagram of the top view of the base plate.

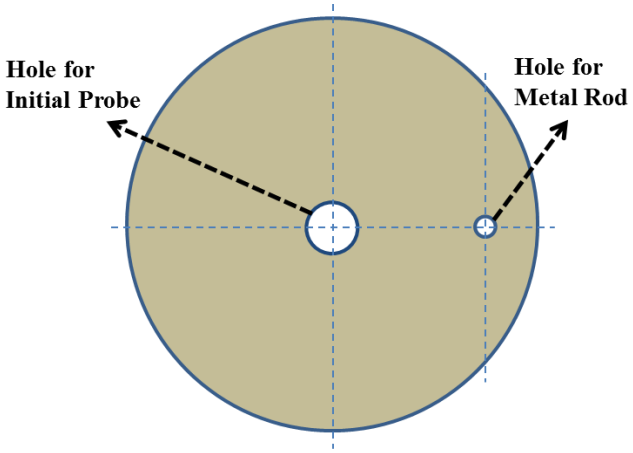

Figure 58: Base plate top view.

In order to maintain uniformity in the electric field distribution, the gap between the shutter and the base plate that allowed the shutter to rotate was kept minimal, which in this design was 0.5 mm. The flange on the metal rod rested against the hole at the side of the base plate. This helped in maintaining position throughout the period of operation of the shutter. It was evident after connecting all three parts (servo, shutter and base plate) together that the shutter does not protrude outside the area of the base plate for the conditions where the probe sensor is exposed to the charged sample or if the sensor is completely covered by the base plate. Figure 59 shows the schematic bottom view of the position of the shutter and base plate under the two conditions mentioned above.

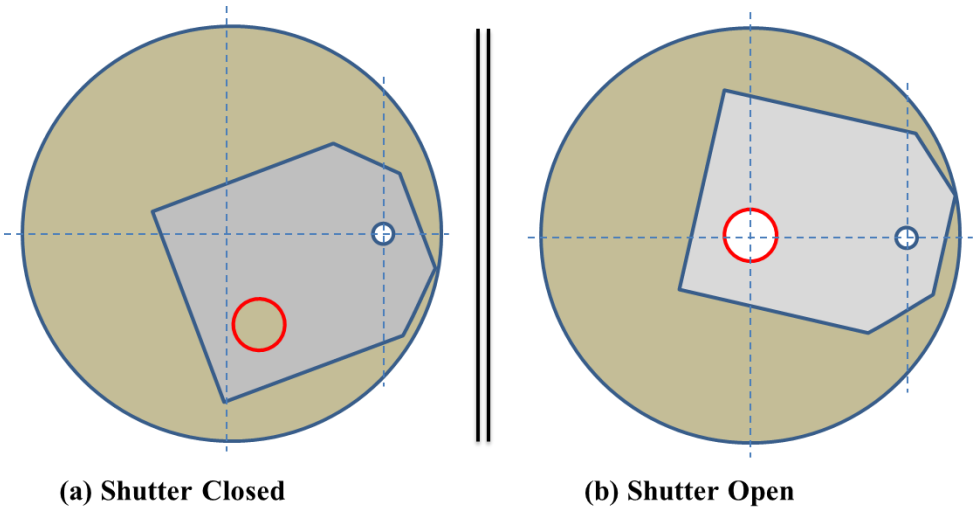

Figure 59: The position of the shutter plate in (a) closed and (b) open state.

Once the construction was completed, a wire was used to secure the contact between the probe outer conductor and the shutter so that all three components of the modified probe design i.e. the initial probe, shutter plate and the base plate could be regarded as one complete probe. Figure 60 shows the different stages of the probe design leading to the complete probe geometry.

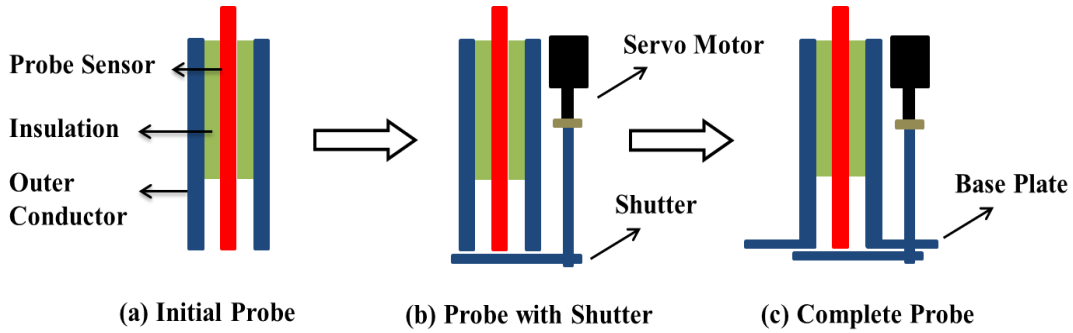

Figure 60: Different stages of probe design.

4.3.2. Probe Resolution Comparison

A comparison of the effect of introducing the modifications-i.e. shutter and base plate-to the initial probe design were carried out using COMSOL Multiphysics simulation software. Using the electrostatics model in the software package, two separate three dimensional models of the probe geometries were constructed. Figure 61 shows the two geometries assembled in COMSOL: (a) the initial probe and (b) the complete probe containing the shutter and the base plate.

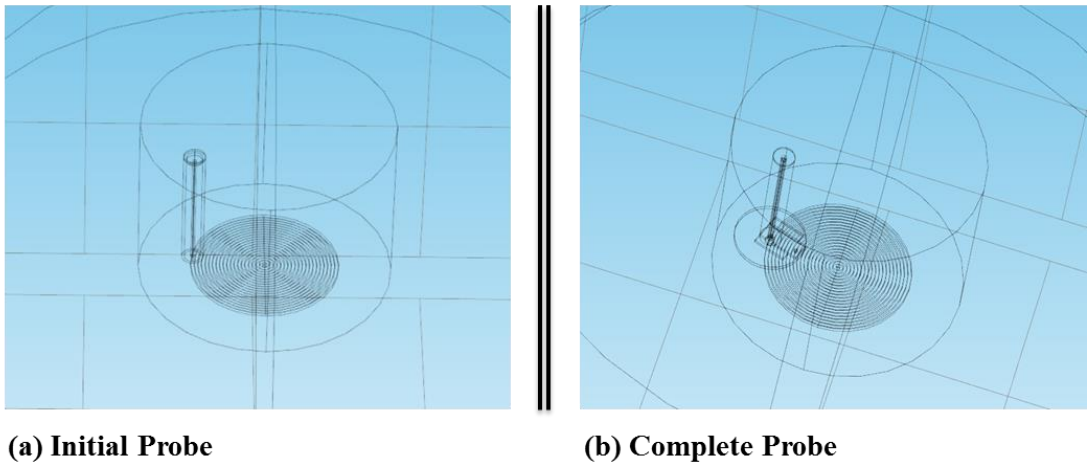

Figure 61: (a) COMSOL geometry of initial probe, (b) COMSOL geometry of complete probe

Simulations were carried out with atmospheric air as the surrounding gas medium against a circular acrylic sample of 80 mm diameter. The sample was divided into 20 rings and the

centre of the insulator was a circular disk of 2 mm diameter. Each of the rings had a thickness of 2 mm and the outer diameter increased in equal increments of 4 mm from the first ring up to the 20th ring so that the whole sample diameter has been covered. The thickness of 2 mm was chosen to be similar in diameter to the diameter of the probe sensor tip. The simulation was carried out primarily to investigate the effect that the modified probe geometry had on the resolution of the measurement system.

Two separate investigations were made. Firstly the resolution of the initial probe was compared to that of the modified complete probe geometry, at a probe sensor to insulator gap separation of 5 mm. The second observation was to investigate the effect of gap separation on the resolution of the modified complete probe geometry. This simulation was carried out at a probe sensor tip to insulator gap separation of 5 mm and 10 mm. For each of the simulations the central circular disk element of the insulator was given a surface charge density of 1 μC/m^2 and all the other ring elements were kept grounded. A parametric sweep was setup so that a scan along the centre of the insulator could be run and measurements of surface potentials at the centre of each of the elements of the insulator could be made. The parametric sweep was setup so that during each measurement the centre of the probe sensor tip aligns up precisely with the centre of each of the elements of the insulator. Figure 62 shows the observed output response for the first simulation.

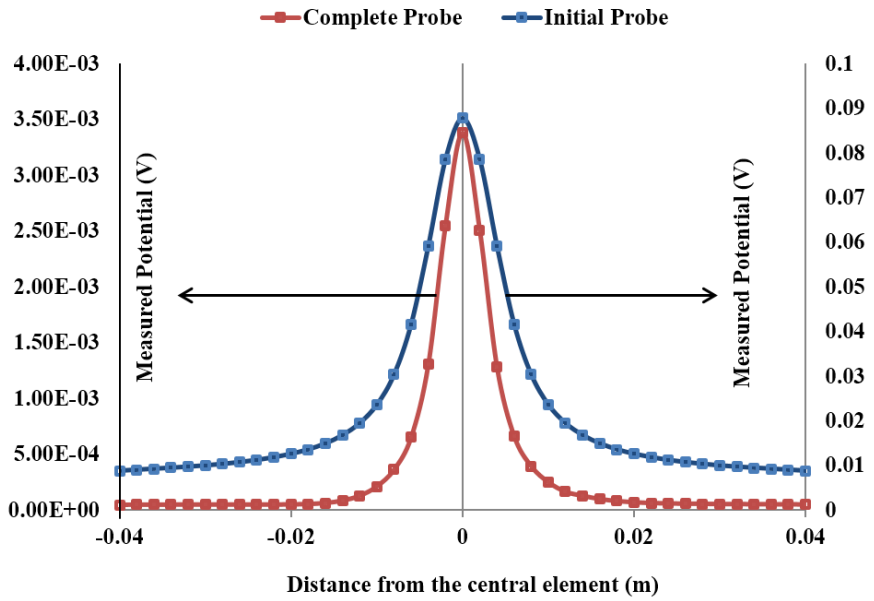

Figure 62: Potential response of initial and completed probe at a gap separation of 5mm.

When comparing the simulated output response of the initial probe to the modified probe, it is evident that the potential induced on the complete probe is smaller in magnitude but the

overall spatial resolution has increased. As the probe moves away from the test charge location the field lines will tend to terminate on the base plate above the charge rather than on the probe sensor. It is this increased spatial resolution that would help in measuring the charge that is directly below the sensor of the probe to a greater accuracy. Figure 63 shows the observed output response for the second simulation.

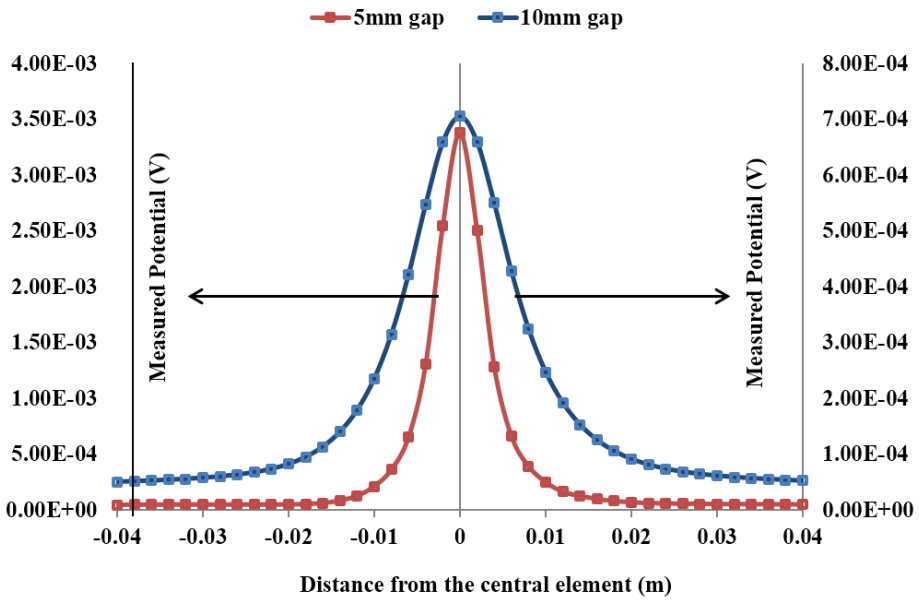

Figure 63: Effect of gap separation on the response of the modified probe geometry.

When comparing the simulated output response of the modified probe in terms of gap separation, it is evident that the spatial resolution of the probe increases as the gap separation between the probe and the insulator sample is reduced from 10 mm to 5 mm. It can also be seen that the induced potential on the probe sensor also increases with a decrease in the gap separation. In practical experiments a safe gap separation will be established where measurements of surface potentials can be made without causing discharges between the charged insulator and the grounded probe which may damage the measurement circuitry.

4.4. Calibration of the Measurement System

This section illustrates the experimental setup and procedure for calibration of the measurement system.

4.4.1. Experimental Setup

Calibration of the measurement system was performed by using a charged metal plate of known surface potential as the test object. The metal plate was made of aluminium and had a

diameter of 60 mm. The plate was charged by a positive 0 to 20 kV DC power supply. The probe was held vertically above the centre of the charged metal plate by sliding through a hole in the horizontal arm of the metallic fixture and a friction fit was established providing firm contact between the probe and the metallic fixture. The metallic fixture consisted of two stepper motors that were powered by a +12 V DC bench top power supply. This enabled positional control of the horizontal arm of the fixture in both the x-axis and y-axis hence the ability to adjust the position of the probe across the surface of the sample under test and the gap separation of the probe to insulator was also established.

The shielded metal box with the measurement circuity was positioned flat on top of the horizontal arm of the metallic fixture. A hole was drilled into the shielded box and it was aligned with the hole in the horizontal arm of the metallic fixture. This provided access to the unexposed side of the probe sensor into the shielded box and a wired contact was established between the measurement circuitry and the probe sensor. The shielded box was flush against the metallic fixture and held in position by threaded metal screws. Inputs and outputs from the measurement circuitry were established through wires which were allowed access via a small hole that was drilled on the side of the box and insulation was used to cover any gaps so that noise effects can be minimised.

The servo motor holding the shutter in place was connected to the horizontal arm of the metallic fixture through threaded metal screws. The motor was energised by a +5 V DC battery. As a firm connection was established between the probe and the metallic fixture through the friction fit, it was easy to ground the whole system by grounding the base of the metallic fixture by use of a grounding wire. In this way all parts of the system i.e. shielding box, metallic fixture, probe outer conductor, shutter and base plate were held at a common ground further reducing potential grounding problems. The control of the movement of the horizontal metallic arm of the fixture along with the position of shutter plate and the acquisition of data was performed using an Arduino microcontroller which was powered by the +5 V USB output of the PC, responsible for recording the output data that was sent from the microcontroller. The experimental setup for the calibration of the measurement system is shown in figure 64.

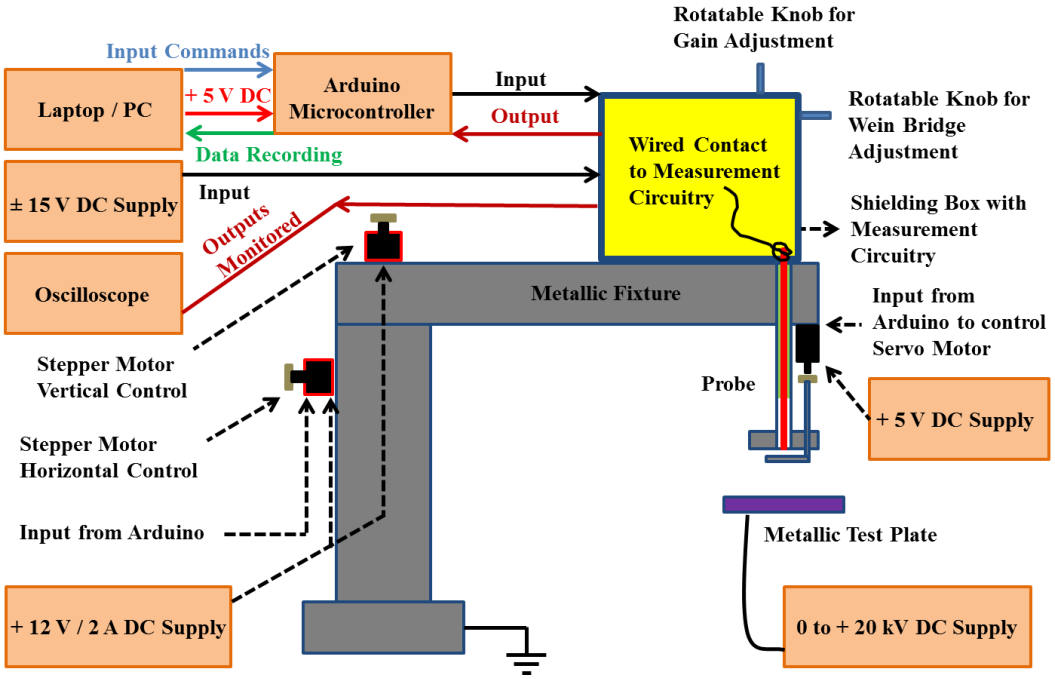

Figure 64: Experimental setup for measurement system calibration.

4.4.2. Measurement Procedure

The first step of the measurement procedure was to use the Arduino microcontroller to set the position of the probe above the centre of the metallic sample with a gap separation between the probe sensor and the test sample of 12 mm. At this gap separation, preliminary testing showed that there was no breakdown between the probe and the sample for charging voltages up to 10 kV. The measurement circuitry was now powered up by a ± 15 V DC bench top power supply. This was followed by adjusting the output voltage of the Wein Bridge to the required value. During initial measurements using the measurement system it was observed that the output of the Wein Bridge required some time to become stable. An initial warm up time of 2 hours was set so that stability in the measurement circuitry could be achieved and a constant noise level could also be established across the system.

Preliminary testing of the system also showed that the output potential decayed slowly and reached a constant DC level equal to that of a grounded sample. This was assumed to have occurred due to charge leakage across the varactor capacitance. The time constant associated with this decay was of the order of 30 seconds. This was the reason for introducing the grounded shutter plate. When the shutter is opened the surface potential induces charge on the varactors which then starts to decay. However the initial value can be measured. When the shutter is closed any remaining charge leaves the varactors allowing the zero value to be

established. The difference in the measurement with the shutter open and the shutter closed provides the actual value for the potential across the probe sensor.

Before taking any measurements the microcontroller was used to set the output DC level to ground. The gain on the instrumentation amplifier was set so that the measured output does not exceed + 5 V as this was the upper limit of measurements that the Arduino could read. Measuring values exceeding this limit could damage the microcontroller. The microcontroller was configured to use a sampling rate of 5000 samples per second and the output was measured for one second. As the time constant for decay of charge in the measuring system was much greater it was assumed that the voltage measured was representative of the surface potential. To remove noise the 5000 samples were then averaged. The sampling rate and time were selected based on preliminary testing where it was observed that it provided a high number of samples to average with negligible effect of the decay on the output potential. The output of the probe is defined as the difference between the averaged voltage with the shutter open and the averaged voltage with the shutter closed. Experimental data for all the calibration experiments was gathered for > 500 measurements of the difference between the two voltages.

The calibration of the measurement system was performed to observe the effect of four different parameters on the output signal. The parameters included:

- The effect of the Wein Bridge output voltage on the measured output response.
- The effect of the time delay between the shutter being open and measurement being taken i.e. effect of open shutter delay on the measured output response.
- The effect of the time for which the shutter was closed to neutralise remaining charge before a the next surface potential measurement was conducted.
- The effect of the gap separation between the probe sensor to test surface on the output response.

4.4.3. The Effect of Wein Bridge Voltage

In this observation the effect of the Wein Bridge sinusoidal output voltage driving the rest of the measurement circuitry was observed. The Wein Bridge was set to produce output voltages of ± 10 V(pk-pk), ± 11 V(pk-pk) and ± 12 V(pk-pk), as at these values the output and input limits of the measurement circuitry were not exceeded. The open shutter delay was ~ 0 seconds and the closed shutter delay was 5 seconds. Measurements were performed with the voltage on the metal test plate ranging between 0 to 10 kV in increments of 2 kV. The

behaviour of the output potential was observed to establish a suitable working range for practical experiments with a charged insulator. Figure 65 shows the results.

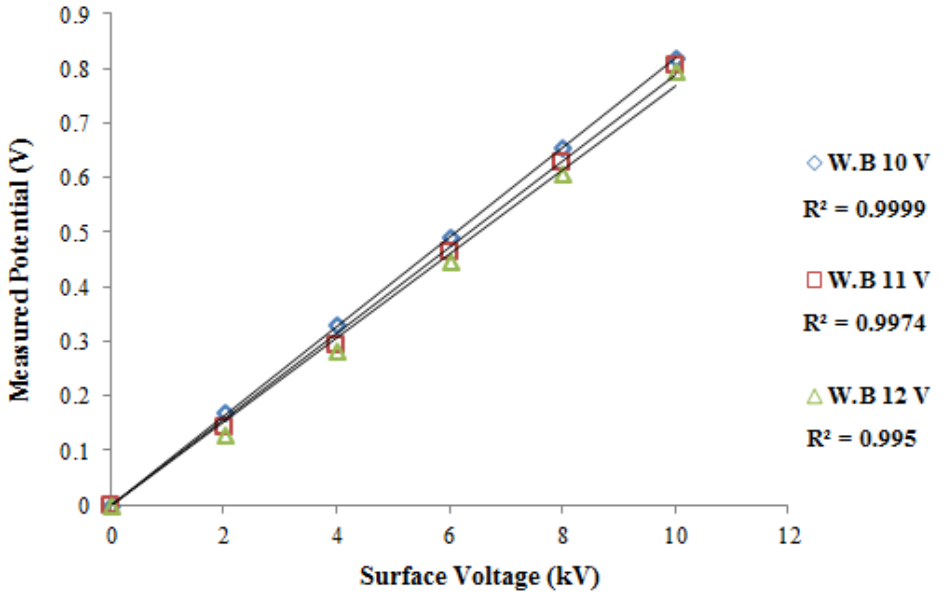

Figure 65: The effect of Wein Bridge sinusoidal output voltage on the output response.

Figure 65 shows that the response of the measured output is linear over the Wein Bridge operation range of ± 10 V(pk-pk) to ± 12 V(pk-pk). The best linearity and largest output is achieved at ± 10 V(pk-pk) and this is the value that will be used to conduct practical experiments on the charged insulator samples.

4.4.4. Effect of Open Shutter Delay

In this experiment the effect of the charge decay in the system during the delay that occurs between the opening of the shutter to expose the sensor to the charged sample and the start of the measurement was observed. The probe response for three different open shutter delay times of ~ 0 second, 0.5 second and 1 second were examined. The closed shutter delay was set at 5 seconds.

It was observed that an increase in the delay time between the shutter opening and the start of potential measurement resulted in a decrease in the measured output potential due to the charge leakage in the measurement system. The behaviour of the system with an open shutter delay of ~ 0 second shows a linear behaviour which becomes more non-linear as the open shutter delay increases. This observation shows that an open shutter delay of ~ 0 second is best suited to perform measurements. Figure 66 shows the output results.

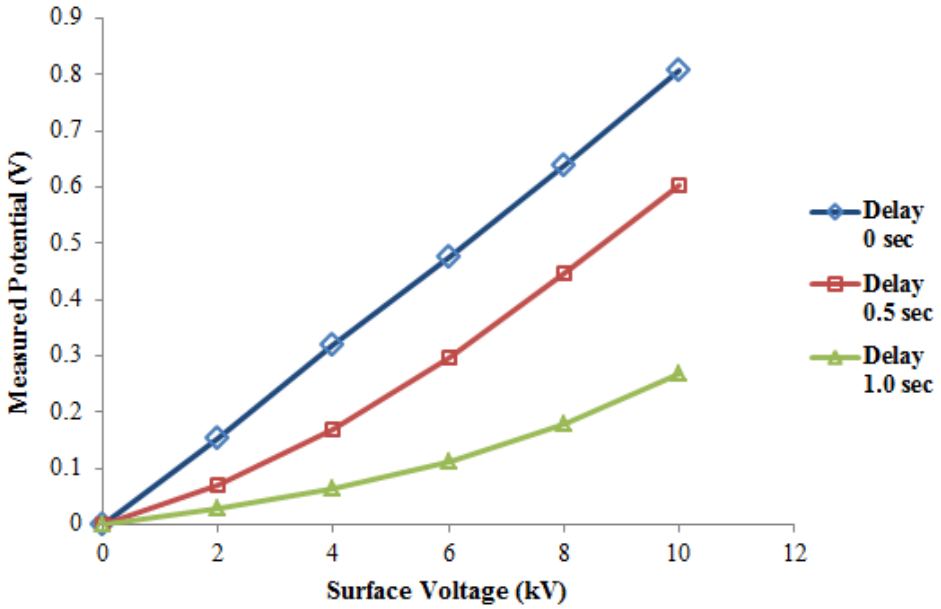

Figure 66: The effect of open shutter delay on the output response.

4.4.5. Effect of Close Shutter Delay

In this experiment the measured output potential was observed for the amount of time that the grounded shutter was closed to bring the sensor potential to zero value before opening the shutter. The probe output response for three different shutter closed delay times of 1 second, 5 second and 10 second were examined. Figure 67 shows the output results for this observation.

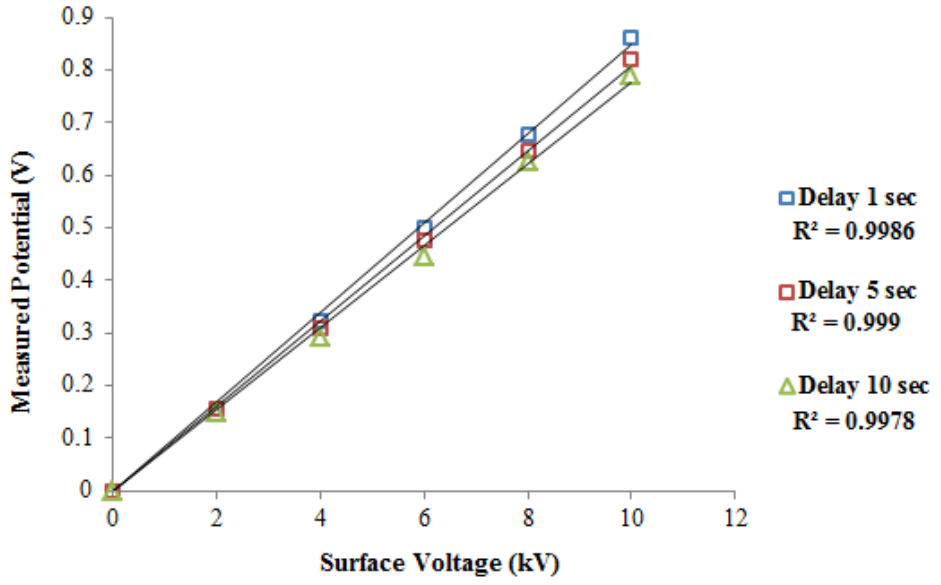

Figure 67: The effect of close shutter delay on the measured output response.

It can be seen be seen from figure 67 that the response of the measured output was strongly linear over all three shutter close times. A shutter close delay time of 1 second was chosen for the practical measurements. This value was chosen as no significant change in the linear response of the probe is observed for longer delay times. It would also help in reducing the time between measurements which would speed up the measurement process.

4.4.6. Effect of Gap Separation

In this experiment the effect of gap separation between the probe sensor and the test sample on the observed output response was observed. Five different gap separations were chosen ranging from 12 mm to 20 mm with increments of 2 mm. The gap separation was chosen so that breakdown between the probe and the charged metal plate could be avoided as the metal plate was charged up to 10 kV. Figure 68 shows the measured output potentials.

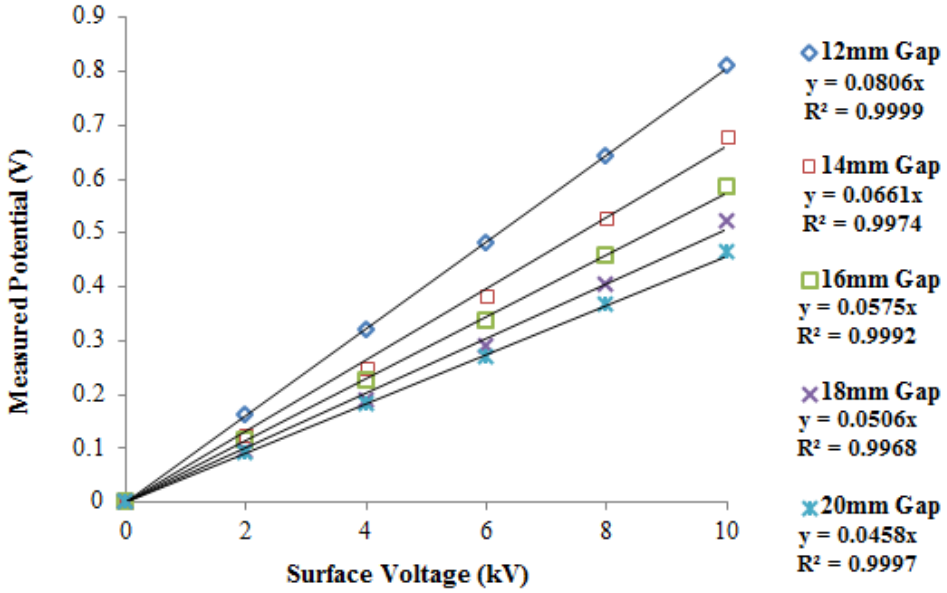

Figure 68: Measured output potentials for a range of surface voltages at fixed gap separations.

From figure 68 it can be seen that for all the gap separations there is a linear dependence on the surface voltage. It is also evident that the measured potential decreases with an increase in gap separation. Figure 69 shows the output potential plotted against equally spaced gap separations at fixed sample voltages.

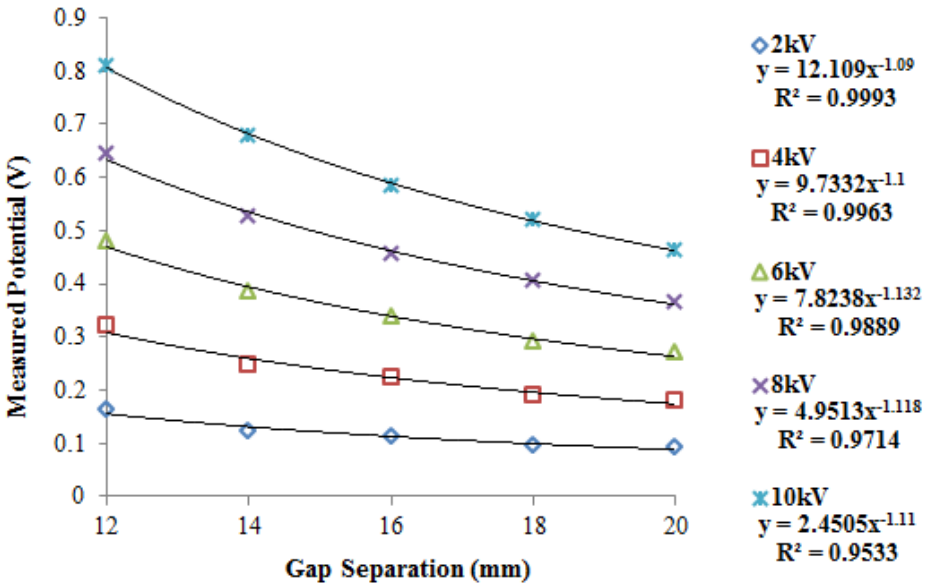

Figure 69: Response of measured potential against a range of equally spaced gap separations.

The response of figure 69 suggests that the system follows a power law relationship taking the form of equation 75.

$$y = mx^{-n} \tag{75}$$

Where, n is close to 1.

For a parallel plate capacitor the capacitance would be expected to be inversely proportional to the gap (n = -1). The equation can be used to estimate the actual potential on the surface of the sample for a particular gap separation by calibrating with respect to the output potential measured by the system.

4.5. Chapter 4: Summary

In this chapter initially the basic construction and working principle of a capacitive probe was presented. This was followed by a demonstration of the effect of different probe parameters on the output response of a basic capacitive probe by performing simulations in QuickField against an arbitrary test surface. The physical construction of the modified probe used in this project was described and simulations were performed to compare the probe response to that of a basic capacitive probe. It was observed that the modified probe had a better spatial resolution at the expense of the magnitude of the output signal.

An experiment was set up to calibrate the probe system for practical measurements on insulator samples. It was established that the time delay between opening the shutter to

expose the probe sensor to the charged sample and the start of measurements had an effect on the output response due to charge leakage within the system. The time constant for this charge leakage was ~ 30 seconds and it was established that the best response was observed when the time delay was set at ~ 0 seconds as the response of the output potential was linear at this delay. A time of 1 second was observed to be appropriate for neutralising the charge on the system by closing the grounded shutter plate. It was also established that the Wein Bridge would be set up to produce an output sinusoidal voltage of 10 V for all experiments in the project. The response of the probe to various gap separations was also observed.

5. Development of Surface Conductivity Test cell and the Method for Surface Charge Distribution Measurement

5.1. Surface Conductivity Measurement System

As discussed in section 2.11.2, the surface conductivity measurement system being used in this project is a combination of the concentric cylindrical system employed in [124] and a variation of this system developed in [128]. The following subsections (5.1.1 to 5.1.3) will provide details of the developmental stages of the measurement system along with the tests conducted to verify the accuracy and performance of this system.

5.1.1. Modifications to the Concentric Cylindrical Geometry

The measurement system being employed is based on the concentric cylindrical system in [124]. Therefore the dimensions of the system were also kept similar to those of the measurement system of [124]. The modification to the sensing electrode employed in [128] was also made use of in this system whereby, the central measurement electrode $\boldsymbol{X}$ was divided into an outer ring electrode $\boldsymbol{X'}$, a cylindrical electrode $\boldsymbol{X''}$ and another larger grounded cylindrical electrode $\boldsymbol{W}$**.** At any measurement time the electrodes $\boldsymbol{X'}$, $\boldsymbol{X''}$ and $\boldsymbol{W}$ sit at a similar potential of ~ 0 V, so the introduction of the modified electrode geometry has a similar principle to that of the concentric cylindrical geometry in [124] but at the same time is intended to provide some distinct advantages.

The purpose of the grounded electrode $\boldsymbol{W}$ was to maintain field uniformity between the outer cylindrical electrode $\boldsymbol{Z}$ and the central electrode. It permitted the length of the measurement electrodes to be shorter hence minimising the effect of high fields on the measured current transients. The grounded electrode $\boldsymbol{W}$ was isolated from the measurement electrodes $\boldsymbol{X'}$ and $\boldsymbol{X''}$ by a 2 mm layer of PTFE insulation. The relatively high volume resistivity (> 10^{18} Ω.cm) [136] of the PTFE insulation would minimise current leakage from $\boldsymbol{X'}$ and $\boldsymbol{X''}$ to $\boldsymbol{W}$. Figure 70 shows the modified geometry.

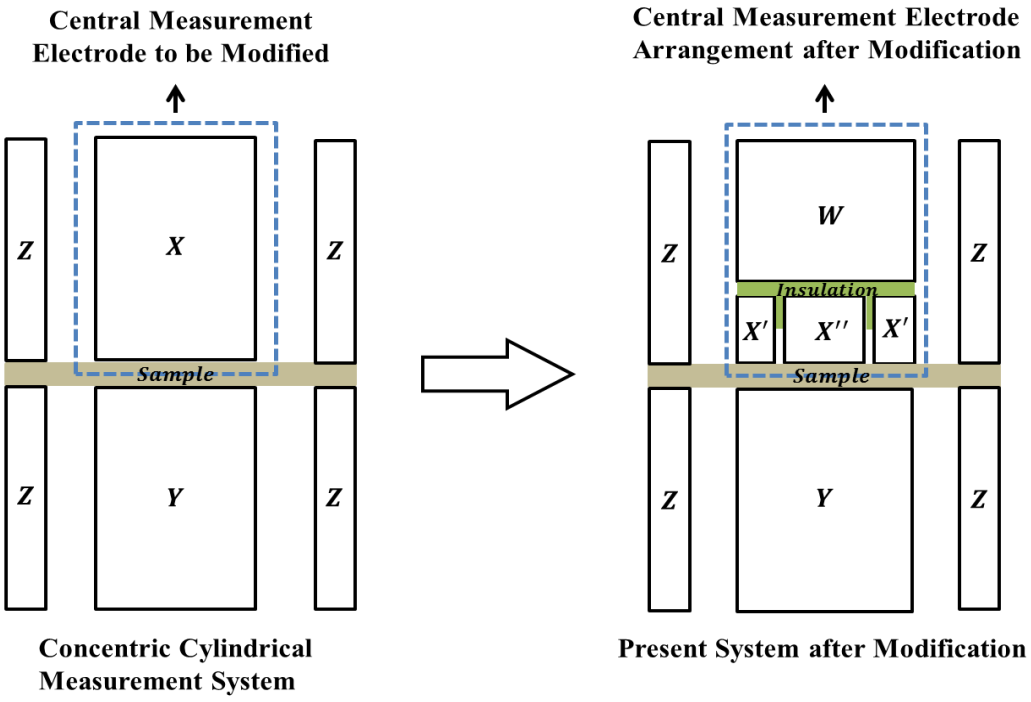

Figure 70: Modified geometry of the concentric cylindrical measurement system.

The geometry has also got the advantage that it can be used to conduct both surface and bulk conductivity measurements without the need to dismantle the system. The electrodes $\boldsymbol{X'}$ and $\boldsymbol{X''}$ have a gap separation of 0.2 mm and are isolated by PTFE insulation which helps in maintaining high impedance between the two electrodes. The electrodes are held in place through a friction fit with the PTFE insulation. All electrodes of the system are made so that their surfaces sit perpendicular and flush against the surface of the sample.

In the case where the system is intended to measure the surface conductivity of the sample, the central cylindrical electrode $\boldsymbol{X''}$ acts as a guard and the ring electrode $\boldsymbol{X'}$ is used to measure the current. The flush arrangement of the measurement electrode $\boldsymbol{X'}$ and the somewhat small gap (0.2 mm) between $\boldsymbol{X'}$ and the guard electrode $\boldsymbol{X''}$ minimises any distortions of the electric field between the high voltage electrodes $\boldsymbol{Z}$ and earth electrodes $\boldsymbol{X'}$and $\boldsymbol{X''}$. The sensing electrode only detects currents arising from the well-defined field region on the surface of the polymer between the electrodes. In addition, the area of the sensing electrode in contact with the surface of the polymer is much smaller than that of $\boldsymbol{X''}$ therefore, any currents flowing through the bulk are expected to have a minimal effect on the current detected by $\boldsymbol{X'}$. The total gap between the high voltage electrode $\boldsymbol{Z}$ and the sensing electrode $\boldsymbol{X'}$ is 41 mm and it is across this gap that the surface current is measured.

Figure 71 shows the connection diagram of the system for conducting surface conductivity measurement of insulating materials.

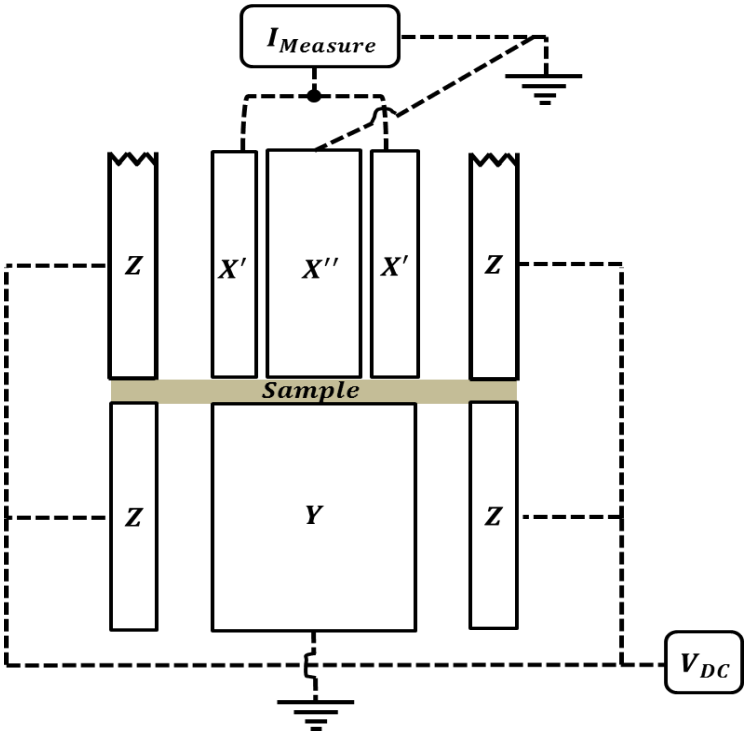

Figure 71: Connection diagram for surface conductivity measurement.

Where,

$\boldsymbol{Z}$ = Electrodes that are connected to high voltage supply.

$\boldsymbol{Y}$ = Lower grounded central cylindrical electrode.

$\boldsymbol{X''}$ = Upper central guard electrode connected to ground.

$\boldsymbol{X'}$ = Sensing ring electrode.

In the case of measuring volume conductivity of the insulation samples, the connections to each electrode can be easily rearranged to measure currents through the bulk of the material. In this case the outer electrodes $\boldsymbol{Z}$ are connected to ground to maintain field uniformity. The central lower cylindrical electrode $\boldsymbol{Y}$ is connected to the high voltage supply. In this geometry the ring electrodes $\boldsymbol{X'}$ are grounded and act as a guard to minimise distortions at the edge of the electrodes. The previously grounded electrode $\boldsymbol{X''}$ is used to make measurements as it is connected to the electrometer and acts as a virtual ground. Figure 72 shows the connection of the geometry when measuring volume conductivity.

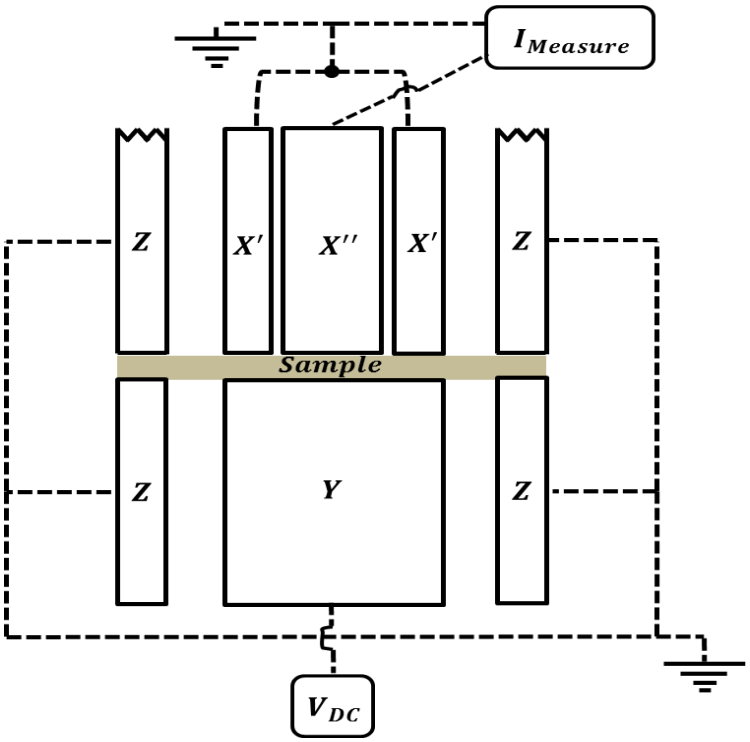

Figure 72: Connection diagram for volume conductivity measurement.

Where,

$\boldsymbol{Z}$ = Outer cylindrical electrodes connected to ground.

$\boldsymbol{Y}$ **=** Lower central cylindrical electrode connected to voltage supply.

$\boldsymbol{X''}$ = Upper central electrode used to perform measurements and connected to electrometer.

$\boldsymbol{X'}$ **=** Ring electrode acting as guard and connected to ground.

The material used to construct the electrode geometry was aluminium. In order to maintain the gap separation between the outer and inner electrodes of the system, PVC discs of 20 mm thickness were constructed to fit the gap between the inner and outer electrodes and the fitting was established as a result of a friction fit. As the grounded upper central tube $\boldsymbol{W}$ was much larger than $\boldsymbol{X'}$ and $\boldsymbol{X''}$**,** the spacers were placed between $\boldsymbol{W}$ and $\boldsymbol{Z}$**,** therefore isolating the sensing electrodes from detecting any currents flowing through these spacers.

The system was further reinforced by constructing end caps from PVC for the top and bottom electrode arrangements of the system. The top half of the system was used to make measurements as it contained the measurement electrodes. Contacts to the measurement electrodes $\boldsymbol{X'}$ and $\boldsymbol{X''}$ were made by using screwed metallic rods and these contacts extended beyond the polymer end caps into a grounded metal box. The sensing electrodes were held into position by a tightly screwed nut against the end cap. To prevent the influence of any

leakage currents flowing through the PVC end caps on the measured output currents, the PVC cap at the sensing half of the geometry was constructed as a ring with the inner radius slightly larger than the radius of the grounded central tube $\boldsymbol{W}$. This allowed $\boldsymbol{W}$ to pass through the end cap and a friction fit between the PVC end cap and $\boldsymbol{W}$ was established resulting in a flush arrangement.

A cylindrical block of PTFE with a thickness similar to the PVC end cap was cut and a friction fit was established between the PTFE circular block and the hollow tube $\boldsymbol{W}$. Two through holes were drilled into this PTFE block which allowed excess for the screwed metal rods connected to $\boldsymbol{X'}$ and $\boldsymbol{X''}$. The higher resistivity of PTFE compared to PVC provided better isolation between $\boldsymbol{W}$, $\boldsymbol{X'}$ and $\boldsymbol{X''}$. Contact between $\boldsymbol{W}$ and the shielded metal box was made by using M4 metal screws. The Die cast box contained two BNC connectors that made connection with the measurement electrodes $\boldsymbol{X'}$ and $\boldsymbol{X''}$ through insulated copper wire. Figure 73 shows this arrangement specifically constructed to avoid leakage currents through the polymer end caps.

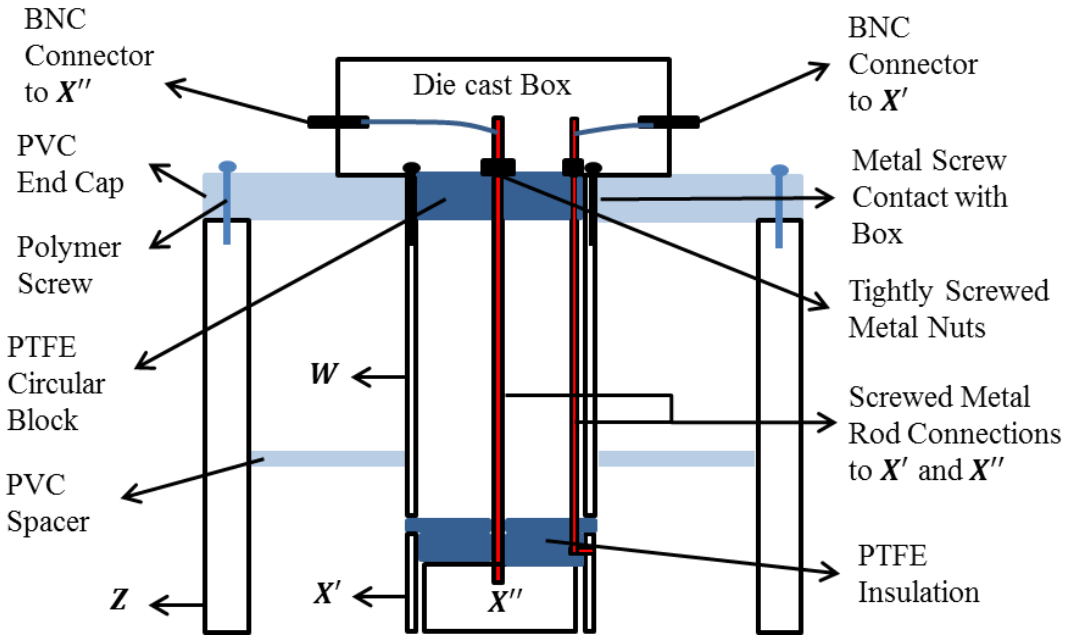

Figure 73: Sensing end geometry labelled.

The central tube $\boldsymbol{W}$ and the Die cast box were grounded through the BNC connectors when connection was made to these connectors with the electrometer to take measurements. This also had the advantage of reducing noise in the measured output current as once the box is grounded, the effect of the noise caused by the external interference is greatly reduced. Under operating conditions once the central tube $\boldsymbol{W}$ was connected to ground any current

flowing through the PVC end cap between the high voltage outer electrode ***Z*** and the central tube ***W*** was neutralised. The bottom half of the geometry was also reinforced by holding the outer and inner electrodes in place by the use of PVC end cap and PVC spacers similar to the one constructed for the top half of the geometry.

The top half of the system had a flange on the outside of the outer tube ***Z*** within which the outer electrode ***Z*** of the bottom half of the geometry could fit with precision when the two halves of the system were placed on top of each other under operating conditions. The system was placed on top of a PVC stand that was made to fit the bottom geometry of the system. Figure 74a shows the top and bottom half of the constructed measurement system and figure 74b shows the measurement system once the two halves of the system are aligned and rest on the PVC stand before measurements.

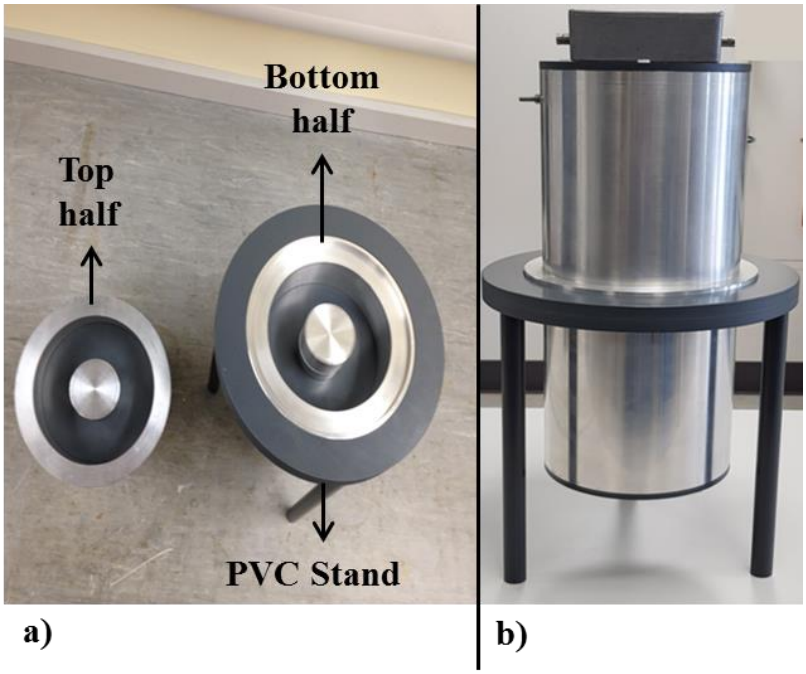

Figure 74: Constructed measurement system. a) the top and bottom part of the system and b) the system arrangement under measurement conditions.

A labelled diagram of the different parts of the measurement system is shown in figure 75.

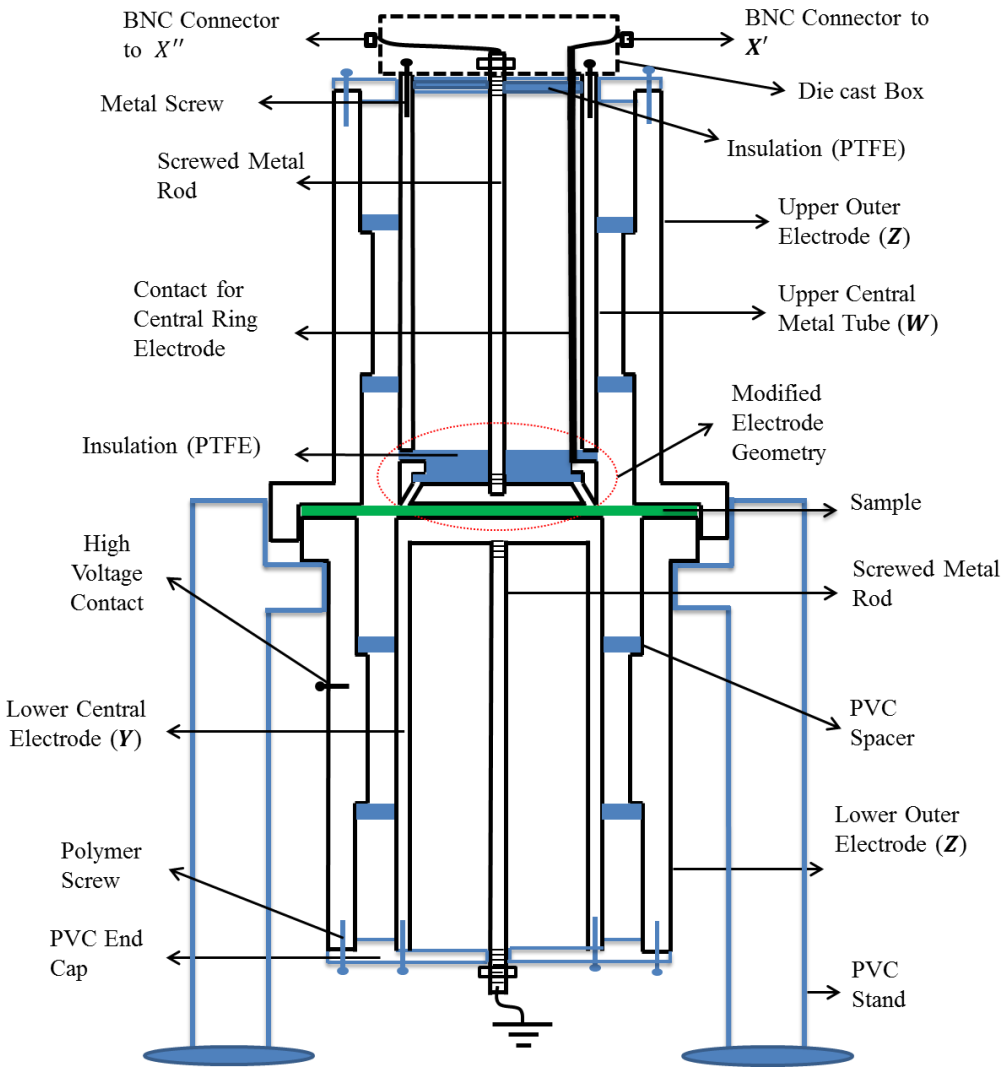

Figure 75: Labelled diagram of the conductivity measurement system.

5.1.2. Simulated behaviour of the Modified Geometry

Before conducting practical experiments using the modified conductivity measurement system, the effect of the modified system on the measured surface current was compared to the surface currents observed using the concentric cylindrical system [124]. To compare the surface currents measured from the two systems, simulations were carried out with QuickField simulation software using the DC conductivity model.

A 2D (Two Dimensional) model of the measurement system was constructed with the simulations to be performed on a thin (0.25 mm) and a thick (2 mm) insulating sample. This way the effect of the modified measurement geometry on the surface currents of both thick and thin samples can be observed. One of the parameters required by QuickField to perform

simulations is a value for the bulk conductivity of the sample as it does not have the capability to use a surface conductivity value.

As the simulations are performed by using a bulk conductivity value rather than a surface conductivity value, the QuickField model of the sample was constructed in two layers; surface and bulk, whereby a much thinner layer ~ 0.02 mm was used to represent the surface layer of the sample. It is across this surface layer where the currents are observed. Figure 76 shows the sample divided into two parts.

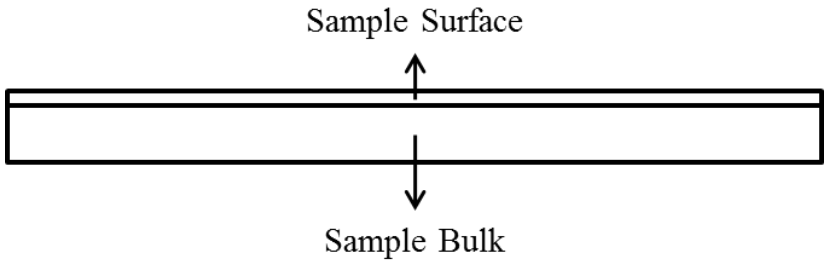

Figure 76: Sample divided into two parts.

Dividing the sample into two layers allows the possibility to calculate an equivalent value of the bulk resistivity for the thin surface layer for a given value of the surface resistivity of the sample. This surface resistivity value was taken from the sample data sheet [137]. In this case the sample that is being investigated is a PMMA (Poly(methyl-methacrylate)) sheet which has a quoted surface resistivity of 10^{14} Ω/sq. In order to convert this surface resistivity into equivalent bulk resistivity, appropriate formulae were derived. Using figure 77 where, figure 77a shows the sample surface $\boldsymbol{S_S}$ and figure 77b shows the sample volume $\boldsymbol{S_V}$, the appropriate formulae can be derived.

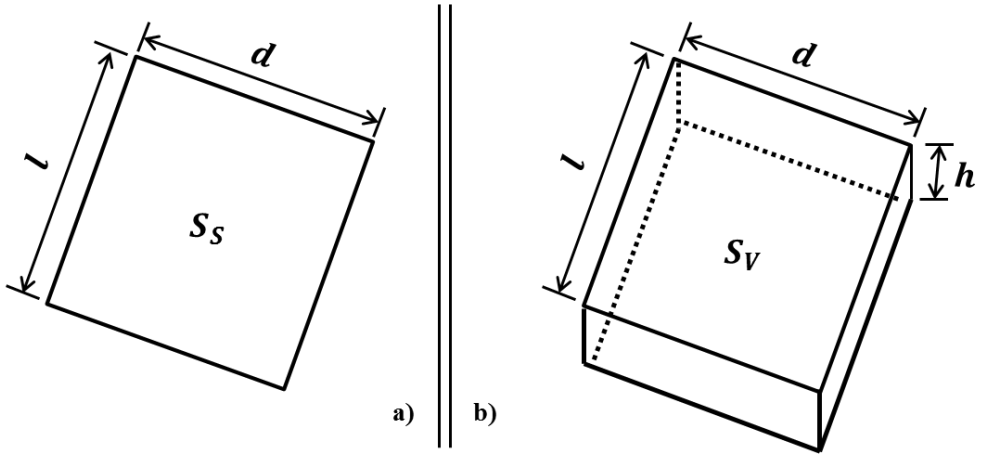

Figure 77: Figure 77a) shows sample surface S_S and figure 77b) shows sample with volume S_V.

In the case where a voltage $\boldsymbol{U}$ is applied across a sample with a surface resistance $\boldsymbol{R_s}$, the current $\boldsymbol{I_s}$ across the sample surface $\boldsymbol{S_S}$ from figure 77a can be expressed as equation 76.

$$\boldsymbol{I_s = \frac{1}{R_s} * U} \tag{76}$$

The resistance $\boldsymbol{R_s}$ of the sample surface $\boldsymbol{S_S}$ can be expressed as equation 77.

$$\boldsymbol{R_s = \rho_S * \frac{l}{d}} \tag{77}$$

Where,

$\boldsymbol{\rho_S}$ = Surface resistivity of the sample.

$\boldsymbol{l}$ = Length of the sample.

$\boldsymbol{d}$ = Width of the sample.

In the case where an equivalent voltage $\boldsymbol{U}$ is applied across a sample with a volume resistance $\boldsymbol{R_V}$, the current $\boldsymbol{I_V}$ across the sample volume $\boldsymbol{S_V}$ from figure 77b can be expressed as equation 78.

$$\boldsymbol{I_V = \frac{1}{R_V} * U} \tag{78}$$

The resistance $\boldsymbol{R_V}$ of the sample volume $\boldsymbol{S_V}$ with a thickness $\boldsymbol{h}$ and volume resistivity $\boldsymbol{\rho_V}$ can be expressed as equation 79.

$$\boldsymbol{R_V = \rho_V * \frac{l}{d * h}} \tag{79}$$

An expression linking the surface resistivity $\boldsymbol{\rho_S}$ and volume resistivity $\boldsymbol{\rho_V}$ of the sample can be obtained when equating equations 77 and 79 whereby, the actual surface resistance $\boldsymbol{R_s}$ of the entire sample and volume resistance $\boldsymbol{R_V}$ of the thin layer at the surface of the QuickField model of the sample which simulates the surface conductivity are assumed to be equal as the voltage $\boldsymbol{U}$ across the sample surface $\boldsymbol{S_S}$ and volume $\boldsymbol{S_V}$ is equal. The resulting expression can be expressed as equation 80.

$$\boldsymbol{\rho_V = \rho_S * h} \tag{80}$$

The surface resistivity $\boldsymbol{\rho_S}$ and volume resistivity $\boldsymbol{\rho_V}$ of a sample is inversely proportional to the surface conductivity $\boldsymbol{\sigma_S}$ and volume conductivity $\boldsymbol{\sigma_V}$. The expression in equation 80 can also be expressed as a relationship between the surface conductivity $\boldsymbol{\sigma_S}$ and volume conductivity $\boldsymbol{\sigma_V}$. This expression is shown in equation 81.

$$\boldsymbol{\sigma_S = \sigma_V * h} \tag{81}$$

The quoted value of the surface resistivity was converted to equivalent surface conductivity of $1e-14\,S$. By substituting this value of the surface conductance and the thickness $\boldsymbol{h}$ in equation 81, an equivalent value for the bulk conductivity for the surface layer was calculated. This calculation is as follows.

- **Calculation for the Surface Layer**:

$$\boldsymbol{\sigma_V = \frac{10^{-14}}{2 \times 10^{-5}} = 5 \times 10^{-10}\ (S \cdot m^{-1})}$$

The value for the sample bulk resistivity was quoted to be $2 \times 10^{15}\ \Omega \cdot cm$ [137] which was used to calculate the bulk conductivity in $S \cdot m^{-1}$ for the sample volume layer. The calculated value for the bulk conductivity was $5 \times 10^{-14}\ S \cdot m^{-1}$. The two calculated values whereby, an equivalent bulk conductivity value for a quoted surface resistivity value for the surface layer and the bulk conductivity value calculated from a quoted bulk resistivity value for the sample volume were used to perform simulations to observe the surface currents. Figure 78 shows the constructed 2D geometry in QuickField for both the concentric cylindrical system and the modified measurement system.

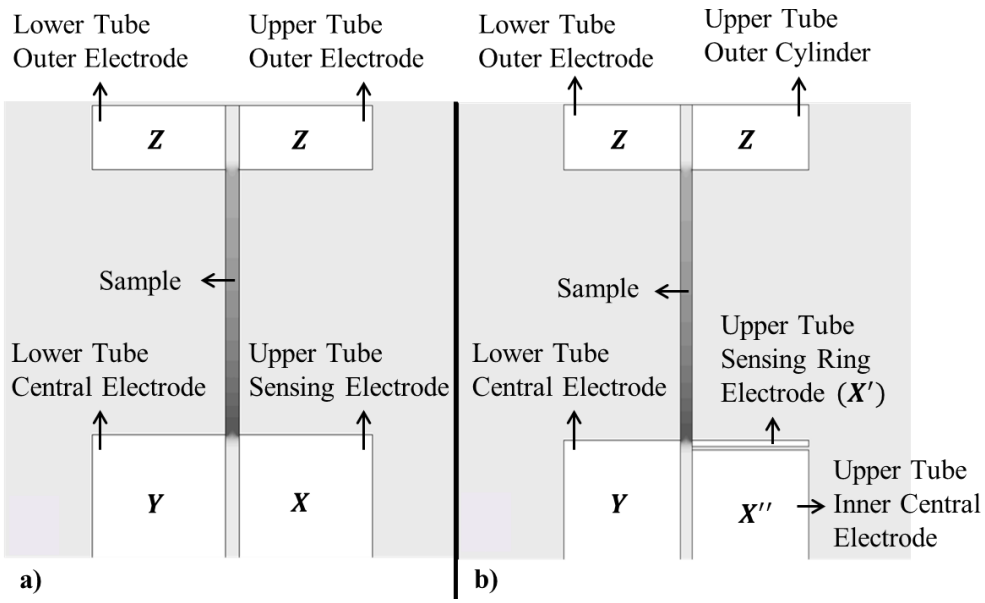

Figure 78: The two geometries built in QuickField. Figure 78a) shows the concentric cylindrical geometry and figure 78b) shows the modified measurement geometry.

The upper and lower outer electrodes $\boldsymbol{Z}$ were set at a potential of 2 kV whereas, the lower tube central electrodes $\boldsymbol{Y}$ were set to ground potential and the sensing electrodes ($\boldsymbol{X}$ and $\boldsymbol{X'}$) were held close to ground. This results in the current flowing from the outer electrodes

towards the inner grounded / sensing electrodes. In order to measure the currents flowing along the surface layer, a contour is placed along the interface between the sample surface and the sensing electrode. Figure 79 shows the simulation.

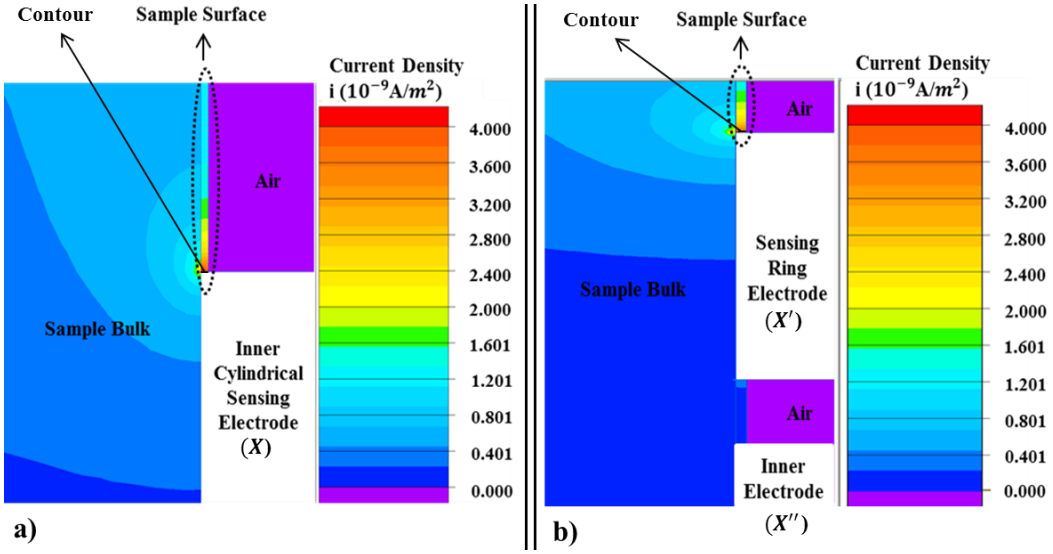

Figure 79: Electric field strength along sample surface. Where, figure 78a) shows the concentric cylindrical system and figure 78b) shows the modified geometry.

Table 2 shows the simulated currents along the surface of the thin and thick samples.

Table 2: Simulated surface and bulk currents from QuickField.

	Thin Sample	**Thick Sample**	
Concentric Cylindrical System	1.4e-10	1.4e-10	**Surface Current (A)**
Modified Measurement System	1.4e-10	1.4e-10	

The results from the simulations showed that there was no visible change in the surface currents measured for the thick sample when compared to the thin sample. It was also evident that no difference between the surface currents was observed between the two measurement systems. Although the introduction of the modified conductivity measurement system does not appear to have an influence on the measured surface currents in this case, however, it offers the advantage of being able to conduct bulk current measurements that are unreliable when using the concentric cylindrical arrangement due to no guard electrode.

As the calculated surface currents do not show visible changes, it was decided to connect the sensing ring electrodes $\boldsymbol{X'}$ and the central guard electrode $\boldsymbol{X''}$ together, forming a single sensing electrode $\boldsymbol{X^{Sense}}$. This effectively was reverting back to the concentric cylindrical system when making surface current measurements. This also made it easier to align the

samples within the measurement system and simplified the process of evaporated aluminium coating of the polymer samples for practical experiments later in the project. Figure 80 shows the new arrangement.

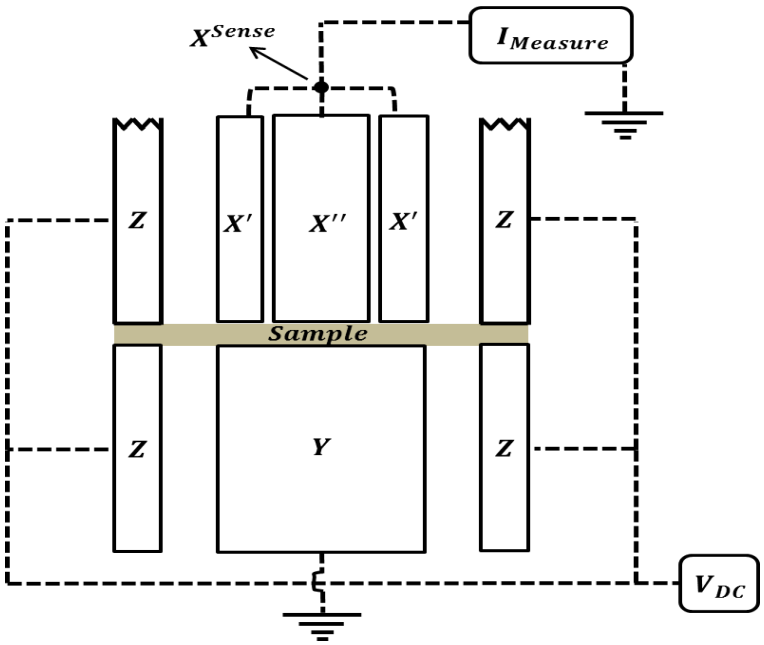

Figure 80: Surface current measurement test cell arrangement.

5.1.3. Measurement System Accuracy and Noise Test

In order to conduct practical experiments using the constructed measurement system, it was important to observe the accuracy and behaviour of the measurement system. This was a significant step to establish confidence in the measurement system as it was expected that the measured currents would be in the pico-amp (pA) region due to the high (> 10^{12} Ω) resistance of the samples and the effect of noise on the measured currents was not yet recognised. The system accuracy tests are discussed in three stages.

The first stage discusses the measurement system setup for current measurements. The second stage discusses the measurements conducted to observe the leakage currents which gives an appreciation of the noise levels. The last stage provides details of the tests conducted to determine the accuracy of the measurement system.

5.1.3.1. Stage 1: System Setup for Current Measurement

The electrical resistivity of a dielectric material can be influenced by external factors such as temperature and humidity [121]. So, before any current measurements were performed it was important to measure the temperature and humidity within the room where the experiments

were conducted. A 6100-Hygrometer was used to conduct measurements for the temperature in ºC and the percentage of relative humidity (%rh). The Hygrometer was able to measure temperatures in the range of -20 ºC and +70 ºC with a resolution of 0.1 ºC and %rh over a range of 0 to 100 %rh with a resolution of 0.1 %rh [138]. The measurements were conducted within a grounded screened metal room. This screened room was specifically constructed within the High Voltage Laboratory at the Technology and Innovation Centre of the University of Strathclyde to conduct high sensitivity measurements and acts as a Faraday cage. Figure 81 shows the screened room.

(a) Shielded Room Outside (b) Shielded Room Inside

Figure 81: Shielded grounded metal room acting as a Faraday cage.

The overall current measurement system is divided into different components:

- **High Voltage Power Supply:**

The outer electrodes $\boldsymbol{Z}$ of the measurement system were connected to a high voltage power supply. The power supply used was a GLASSMAN Series-EW high voltage supply [139] and was able to operate within a voltage range of 0 to 20 kV and could provide currents of up to 30 mA. In this project the supply was set up to generate voltages with positive polarity only. The connection to the test cell outer electrodes $\boldsymbol{Z}$ was made through a high voltage cable. The ground terminal of the voltage source was connected to a common ground point within the grounded screened metal room.

- **Test Cell:**

The test cell is set up to measure surface currents. The configuration of the system for these measurements and the geometry of the measurement system are discussed in detail in sub

sections 5.1.1. and 5.1.2. The details of the dimensions of the electrode arrangement of the test cell can be found in Appendix A.

- **Electrometer:**

A Keithley 617 programmable electrometer was used to measure currents in this project [140]. The electrometer can measure currents as low as 1 fA and currents as high as 20 mA in 11 ranges. This electrometer was considered suitable for current measurements in this project due to its capability of measuring very low currents (down to 1 fA). For a current range of 2 pA to 200 pA the quoted reading error is 1.6 % and for a current range of 2 nA to 200 nA the quoted reading error is 0.25 % [140].

Although measurements can be taken immediately after start up, it is advised to let the electrometer warm up for 2 hours before making high sensitivity measurements. In this project all measurements were made after giving the electrometer at least 2 hours of warm-up time. Before the start of each measurement process the electrometer was calibrated and rescaled by using the zero check and zero correct functions which removed offsets in the instrument. The electrometer sensing end circuitry was connected to the sensing electrode $\boldsymbol{X^{Sense}}$ of the measurement system through a BNC connector on the shielded metal box and acts as a virtual ground.

- **Data Recording:**

The Keithley 617 electrometer uses a standard IEEE-488 interface so it is possible to control the instrument through a GPIB (General Purpose Interface Bus). A Prologix GPIB-USB controller was used. It converts any computer with a USB port into a GPIB controller or device. GPIB enabled devices can be remotely controlled by the Prologix GPIB-USB when used in controller mode and whereas, data logging and screen shots can be obtained from the instrument front panel by using the controller in the device mode which converts the PC into a GPIB peripheral [141].

To pass commands to control the electrometer measurement rate, interval between measurements and number of measurements, the electrometer was used in a single shot trigger mode. To perform these operations, programs were developed in LabView. Data received from the electrometer was saved as a comma separated value (csv) on the hard drive of the PC. Although this electrometer was able to record up to 3 measurements per second, to achieve reliable data logging and avoid missing any measurements, it was established through initial experimentation that the minimum time interval between two successive

measurements would not be less than 1.5 seconds. Figure 82 shows the process of data logging.

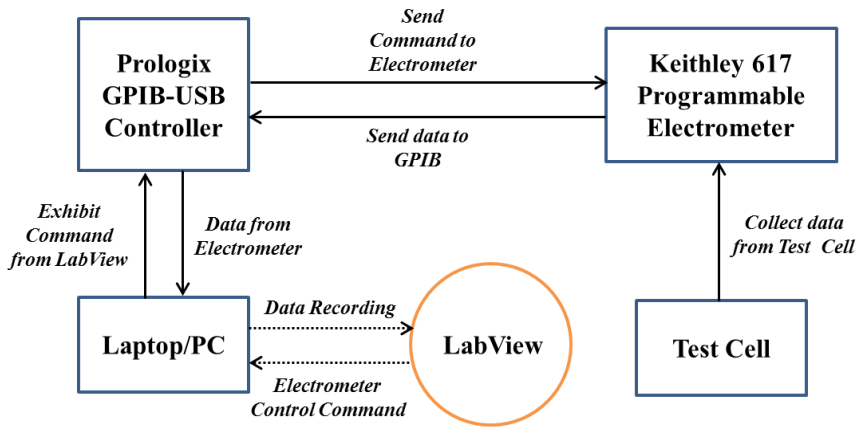

Figure 82: Process of data logging.

The overall setup for measurements of surface currents is shown in figure 83.

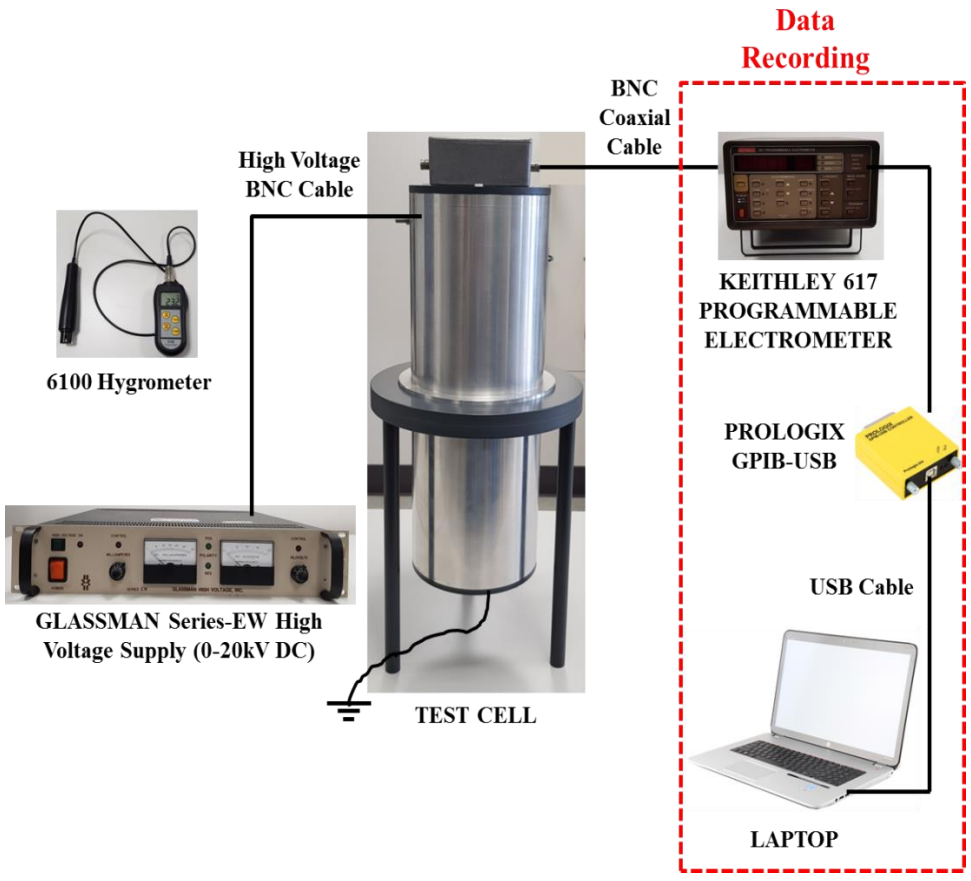

Figure 83: Experimental setup of the measurement system for surface current measurement.

5.1.3.2. Stage 2: Leakage Current and Noise Observation

To observe the leakage current and noise levels within the system, current measurements were made without any sample being placed in the system. It was important to isolate the sensing electrode $\boldsymbol{X^{Sense}}$ from any conducting path within the system. It was also crucial to avoid any contact between the bottom grounded electrode $\boldsymbol{Y}$ and the measurement electrode $\boldsymbol{X^{Sense}}$ to prevent ground loops as $\boldsymbol{X^{Sense}}$ was held at a virtual ground through the electrometer and not directly connected to the ground. This way any currents being measured would be due to establishment of electric field between the high voltage electrode $\boldsymbol{Z}$ and $\boldsymbol{X^{Sense}}$. The electrodes $\boldsymbol{X^{Sense}}$ and $\boldsymbol{Y}$ were isolated from each other by using 2 mm thick and 20 mm diameter Teflon spacers. To maintain symmetry within the system, spacers were also placed between the upper and lower high voltage electrodes $\boldsymbol{Z}$. However, to keep these electrodes at the same potential an external connection was made between them through a copper wire. Figure 84 shows the arrangement for these tests.

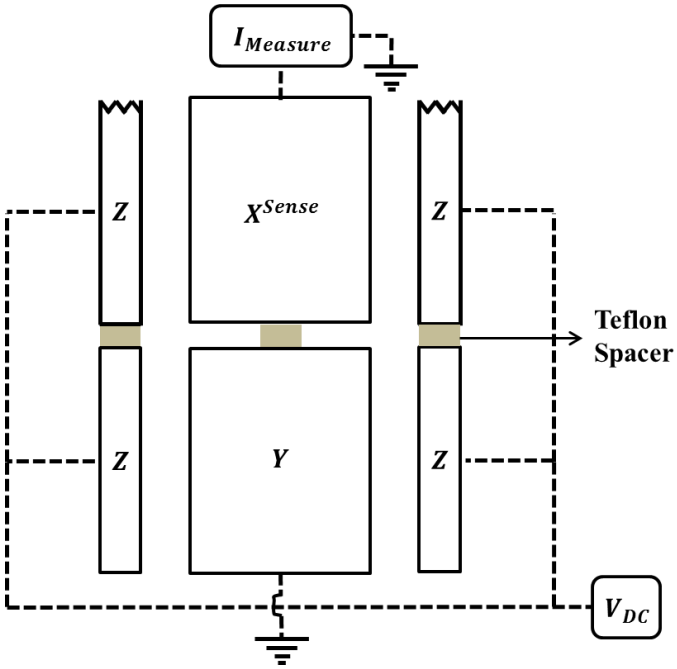

Figure 84: Arrangement for leakage current and noise observation.

The leakage current measurements were made at a minimum applied voltage of 2 kV and a maximum applied voltage of 10 kV. These voltage levels were selected as practical experiments for the surface conductivity measurements were planned to be conducted between supply voltage range of 2 kV up to 10 kV. The leakage current results from this test can be used to verify that the leakage currents are significantly smaller than the sample currents being measured when using an insulator.

The measurements were taken for up to 15 mins after voltage application. The LabView program was setup to take measurements every 1.5 seconds and take a total of 600 measurements. Figure 85 shows the resulting waveforms at DC voltages of 2 kV and 10 kV.

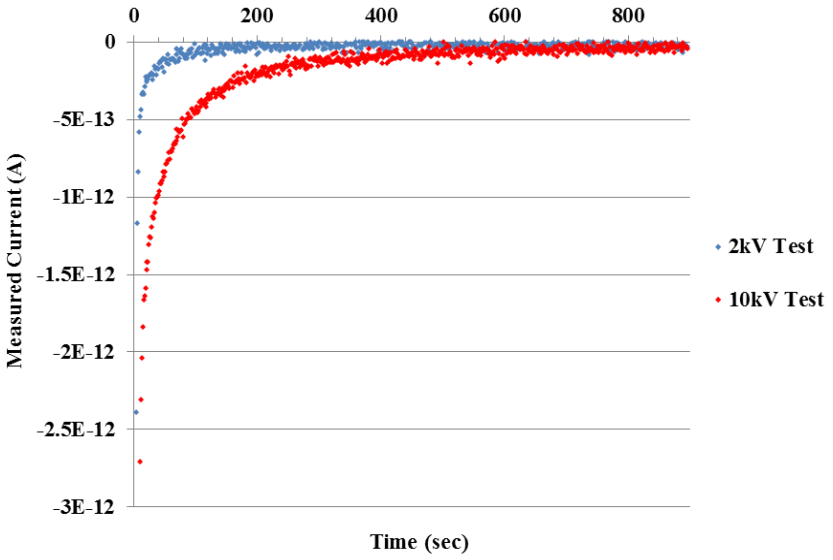

Figure 85: Leakage current waveforms for 2 kV and 10 kV DC voltages.

It was observed that the initial transient for the 10 kV test as expected had a greater magnitude than the 2 kV test, due to the higher electric field generated by the higher voltage application. The results show that the initial transients lie within the pico-Amp region. The transient response for DC voltage of 2 kV approaches steady state at ~ 200 seconds, whereas, the transient response for DC voltage of 10 kV approaches steady state at ~ 600 seconds. The currents at this point were below ~ 60 fA.

To get a better observation of the actual leakage currents, the data in the last 100 seconds was analysed, as in this region the leakage currents for both observed transients were in steady state. The mean of the leakage currents along with the upper and lower deviation from the mean value for the data were calculated and compared. This comparison provides an appreciation of the noise in the system at the lower and higher voltage levels and also shows the effect of the voltage magnitude on the amount of leakage current within the system. Table 3 shows these results.

Table 3: Mean, lower deviation and upper deviation of the last 100 seconds.

Test Voltage (kV)	Mean Current (A)	Upper Deviation (A)	Lower Deviation (A)
2.0	2.09e-14	4.03e-14	1.55e-15
10.0	3.58e-14	5.81e-14	1.35e-14

From the results it was observed that for an applied voltage of 2 kV the mean leakage current was ~ 21 fA with an upper deviation of ~ 40 fA and a lower deviation of ~ 1.5 fA. This shows that the leakage currents at 2 kV applied voltage were significantly smaller than a pico-Amp which was acceptable as the measured currents with the sample were expected to be higher in magnitude as per the quoted value of the surface resistivity of the sample from the manufacturers [137]. Figure 86 shows the raw data of the last 100 seconds of the measured leakage current at 2 kV applied DC voltage along with a representation of the mean, upper deviation and lower deviation.

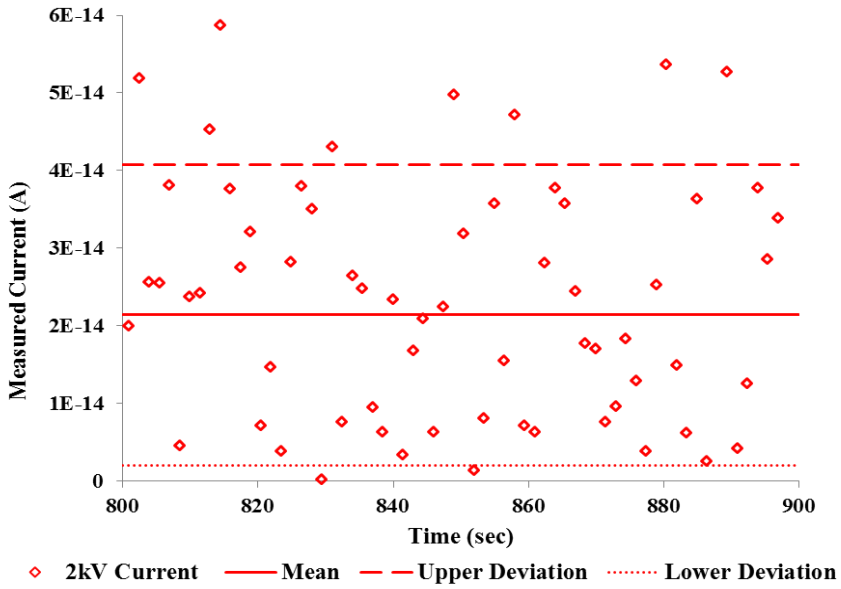

Figure 86: Raw data of leakage current with 2 kV applied voltage and the mean, upper deviation and lower deviation.

Table 3 shows that for an applied voltage of 10 kV the mean leakage current was ~ 36 fA with an upper deviation of ~ 58 fA and a lower deviation of ~ 14 fA. This suggests that the leakage currents at 10 kV applied voltage were again significantly lower than 1 pico-Amp which is acceptable. Figure 87 shows the raw data of the last 100 seconds of the measured leakage current at 10 kV applied DC voltage along with a representation of the mean, upper deviation and lower deviation.

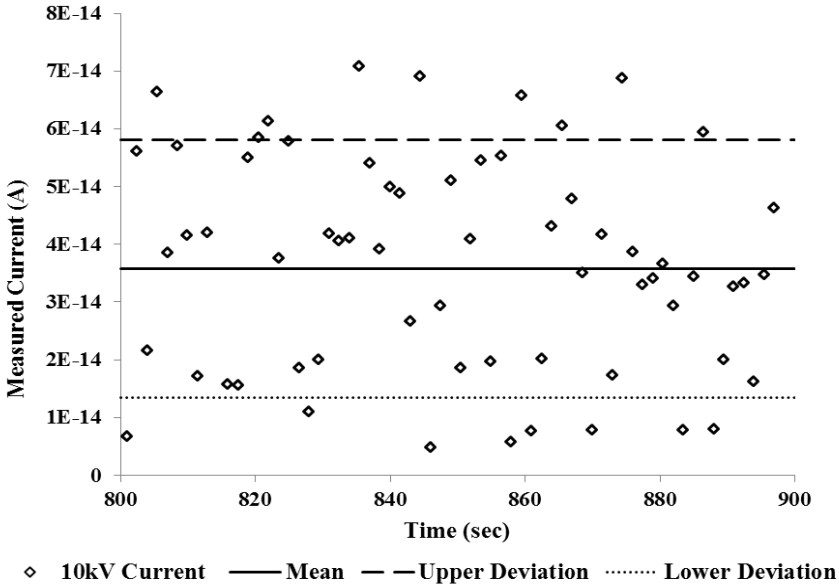

Figure 87: Leakage current, mean, upper deviation and lower deviation at 10 kV.

The total increase in the leakage current was ~ 15 fA and the standard deviation increases by 2.9 fA for measurements made at 10 kV compared to 2 kV applied voltage, suggesting that the increase in leakage current and noise was not sufficient enough to affect the measurements that would be made in the future with the sample in the system. Figure 88 shows the comparison of the mean, upper deviation and lower deviation at the two voltage levels.

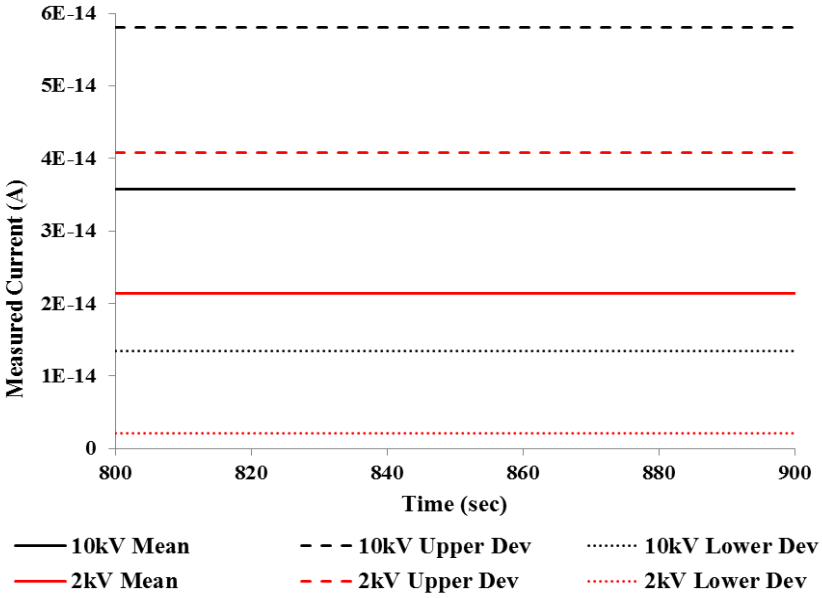

Figure 88: Comparison of mean, upper deviation and lower deviation at 10 kV and 2 kV.

5.1.3.3. Stage 3: Measurement System Accuracy Test

After conducting the leakage current and noise tests, a test was carried out to observe the response of the system to a known transient current. In order to carry out this test, a dummy sample configured to emulate an RC circuit was used. The peak current $\boldsymbol{I_{Peak}}$, output current $\boldsymbol{I_{Output}}$ and the time constant $\boldsymbol{\tau}$ were predefined and the response of the system would confirm its accuracy in measuring currents in the expected range.

The dummy samples used were PCB boards of epoxy glass fibre laminate (FR4) material with double sided copper coating. The PCB boards had a thickness of 1.6 mm and were cut into circular samples of 150 mm radius. Part of the copper coating on each side of the board was etched off forming a central electrode of 29 mm radius and an outer ring with an inner radius of 140 mm, matching the geometry of the measuring system. The coated parts of the PCB samples would provide good contact with the electrodes $\boldsymbol{X_{Sense}}$,$\boldsymbol{Y}$and $\boldsymbol{Z}$ of the system. The radius of the PCB sample central electrode is similar to the radius of $\boldsymbol{X_{Sense}}$ and $\boldsymbol{Y}$ of the system. Whereas, the inner radius of the ring electrode on the PCB sample surface is similar to the inner radius of the high voltage electrodes $\boldsymbol{Z}$. Furthermore, through hole pads were also etched on each electrode of the sample so that electronic components could be soldered onto them. Figure 89 shows the PCB board cut into a circular sample and etched to form the two electrodes on the sample surface.

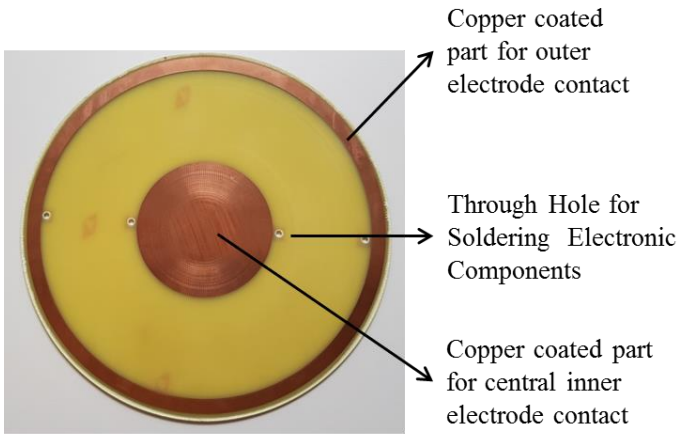

Figure 89: PCB after etching and cutting into circular sample.

One of the most important factors in selecting the component values for the RC network was the need to emulate the output behaviour of practical experiments. This would provide a more accurate observation of the system under operating conditions, where the surface currents along an insulating sample will be observed. In this case a key factor to consider

was the magnitude of the steady state current output $\boldsymbol{I_{Output}}$ after the capacitor had fully charged. Figure 90 shows a circuit diagram of a simple series RC network.

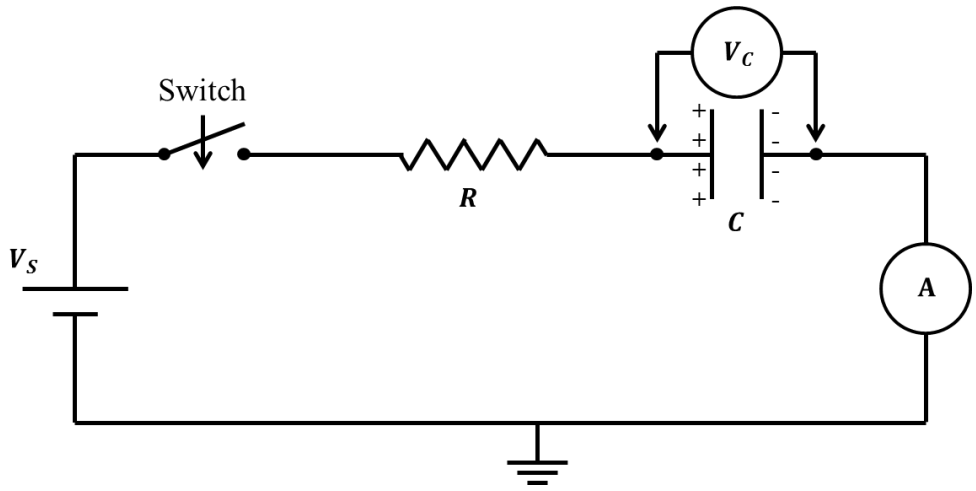

Figure 90: Simple RC circuit.

The current output $\boldsymbol{I_{Output}}$ at any time $\boldsymbol{t}$ can be expressed as:

$$\boldsymbol{I_{Output} = I_{(t)} = I_o \exp(\frac{-t}{R \times C})} \quad (82)$$

Where,

$\boldsymbol{I_o}$= The initial current at time (t=0).

The initial current $\boldsymbol{I_o}$ can be called the peak current $\boldsymbol{I_{Peak}}$ as this will be the maximum current that will flow through the circuit. At this moment $\boldsymbol{I_{Peak}}$ can be represented as equation 83.

$$\boldsymbol{I_{Peak} = I_o = {V_S}/{R}} \quad (83)$$

The rate of charging the capacitor depends on the time constant $\boldsymbol{\tau}$. This can be defined as the time associated with the capacitor to charge up to 63% of its total value. The expression to calculate the time constant is expressed as:

$$\boldsymbol{\tau = R \times C} \quad (84)$$

It was expected that the currents observed from the practical experiments later in the project would be in the pico-Amp region so, to get a more accurate observation of the system at these low current levels, $\boldsymbol{I_{Output}}$ for this test was configured to have a pico-Amp value depending on the maximum value of resistor available. This was achieved by placing a high value resistor $\boldsymbol{R_2}$ in parallel with the RC network. The system was configured as the circuit diagram represented by figure 91.

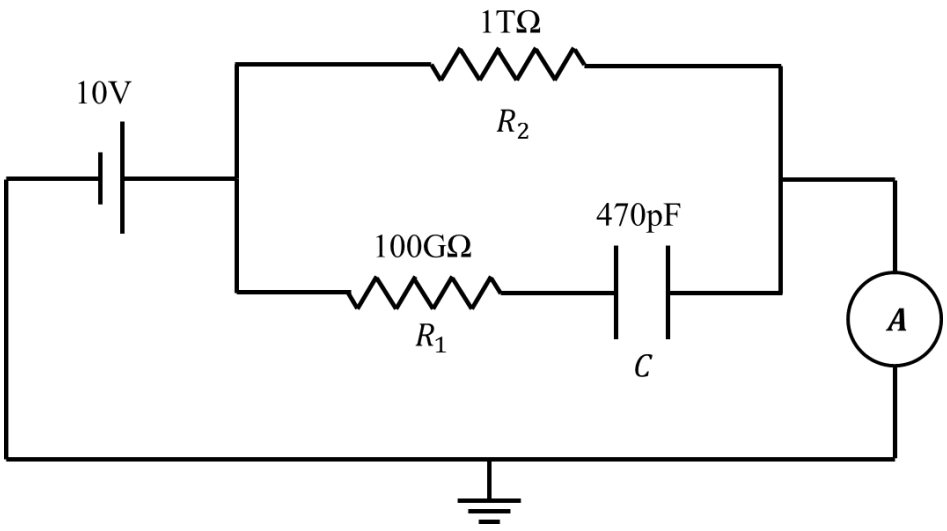

Figure 91: Configuration of the system for transient test observation.

The output current $\boldsymbol{I_{Output}}$ at any time $\boldsymbol{t}$ can be expressed as equation 85.

$$\boldsymbol{I_{Output} = I_{(t)} = I_o \exp\left(\frac{-t}{R_1 \times C}\right) * \frac{V_S}{R_2}} \quad (85)$$

In this experiment the circuit was driven by a supply voltage $\boldsymbol{V_S}$ of 10 V. The calculation for the expected output current at longer times (i.e. $\boldsymbol{t} = \infty$) is as follows:

$$\boldsymbol{I_{Output} = \frac{V_S}{R_2} = \frac{10}{10^{12}} = 10\ pA}$$

The time constant was set to 47 seconds and this was achieved by using a combination of a 470 pF ± 10 % capacitor in series with a 100 GΩ ± 5 % resistor $\boldsymbol{R_1}$. The calculation of the time constant is as follows:

$$\boldsymbol{\tau = R_1 * C = \left(100 \times 10^9\right) * \left(470 \times 10^{12}\right) = 47\ sec}$$

The resulting expected initial peak current at time ($\boldsymbol{t} = 0$) was calculated as follows:

$$\boldsymbol{I_{Peak} = \frac{V_S}{R_1 || R_2} = \left(\frac{10}{\left(\frac{1}{\left(\frac{1}{100 \times 10^9} + \frac{1}{10^{12}} \right)} \right)} \right) = \frac{10}{1.1 \times 10^{12}} = 110\ pA}$$

Figure 92 shows the PCB sample after the components had been soldered onto the surface electrodes.

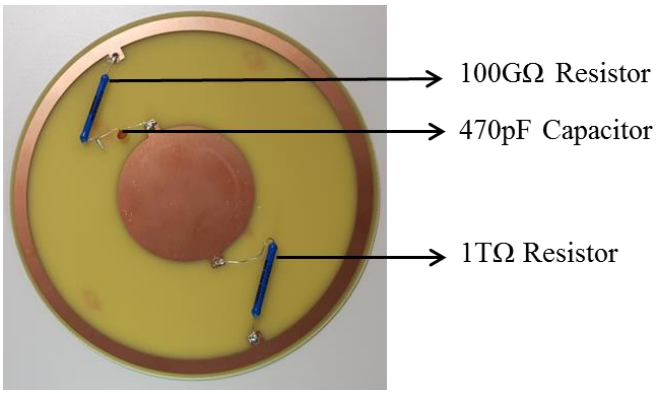

Figure 92: PCB sample after soldering the components.

It is to be noted that the calculated values of I_{Peak}, I_{Output} and τ are for ideal conditions where, it is assumed that there is no current leakage within the system and that the components have zero tolerance. To compare the results of the measured data to the calculated data under ideal conditions, the circuit was constructed and simulated in PSpice simulation software. Figure 93 shows the circuit configuration in PSpice where I_{Output} was being measured across a 1 Ω sensing resistor.

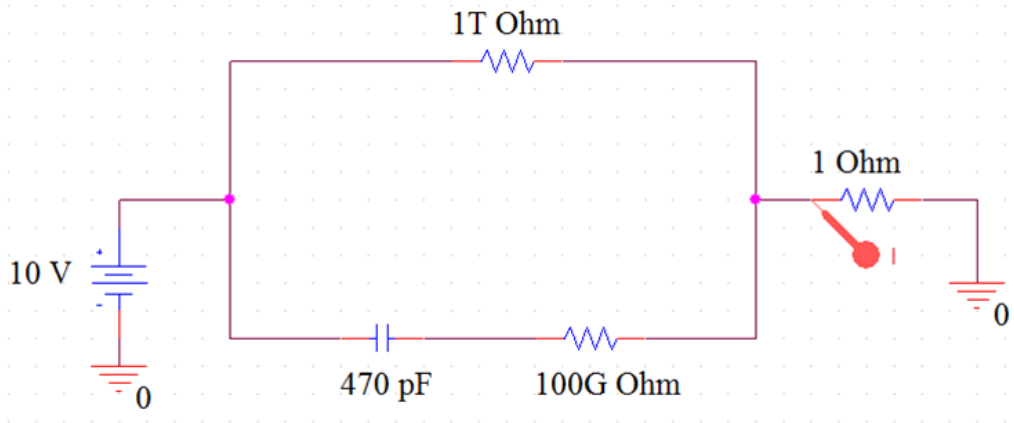

Figure 93: The transient test circuit configured in PSpice.

The results obtained from PSpice were compared to the results obtained from the practical experiment. It was observed that the system follows the expected behaviour of the ideal scenario however, at shorter times of up to 50 seconds the measured results show a slight deviation from the results under ideal conditions. It is also notable that the initial peak current I_{Peak} for the measured data is lower than the simulated value. These differences can be attributed to the tolerances of the components, leakage currents within the system and largely due to the time lapse between the triggering of the electrometer which was set to take a measurement after every 1.5 seconds. The overall results for these tests were satisfying and

showed that the system was capable of conducting transient measurements at lower current levels with a good level of accuracy and precision. The results for the measured data against simulated data from PSpice are plotted and shown in figure 94.

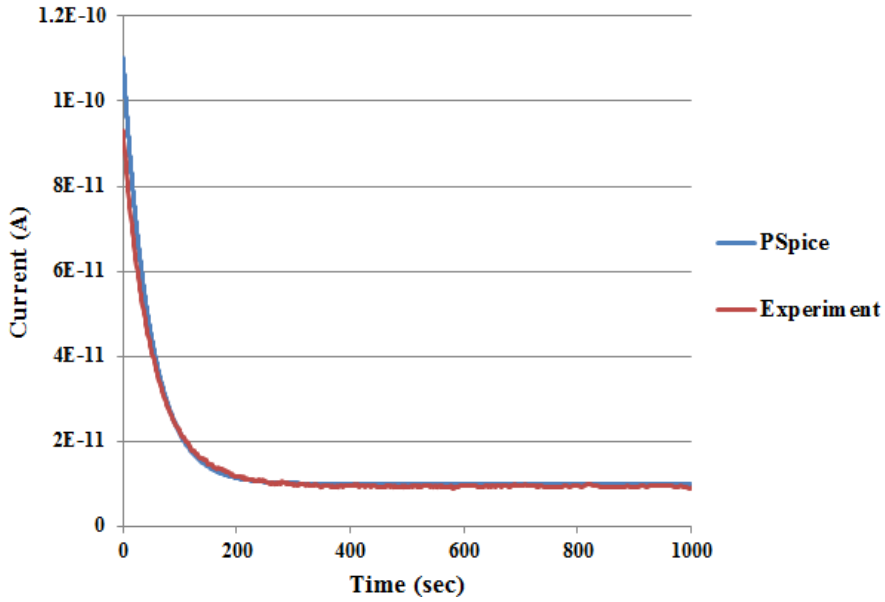

Figure 94: Practical measurements for RC test vs PSpice simulation.

5.2. Surface Charge Distribution Measurement

This section describes the procedure developed to calculate the charge distribution across the surface of a polymeric insulator. The procedure to deposit and measure a charge distribution across an insulator surface is divided into four parts. The first part (subsection 5.2.1) provides details about the system developed to deposit corona charge onto the surface of the insulator. The second part (subsection 5.2.2) describes the test setup and results from the initial tests for the surface potential measurement by using the charge measurement system described in chapters 3 and 4. The third part (subsection 5.2.3.) explains the procedure of computing the $\boldsymbol{\Phi}$-Matrix which is required to calculate the surface charge distribution. The fourth part (subsection 5.2.4.) provides details of the procedure established to calculate a realistic surface charge distribution.

5.2.1. System Design for Corona Deposition

There are several methods of charging the surface of an insulator. In this project corona discharge from an array of needle electrodes was used to charge the surface of the polymer samples. The mechanism of corona charging is described in more detail in subsection 2.5.7. In order to control the amount of corona deposition and to deposit charge uniformly on the

surface of the polymer samples, a grid system was employed as described in [31]. In this approach the grid is maintained at a constant potential, and it is assumed that charge will pass through the grid until the surface potential of the sample is equal to that of the grid. The samples under examination were cylindrical PMMA (Poly(methyl methacrylate))/Acrylic polymeric insulators with a radius of 75 mm. The samples were placed centrally on top of the surface conductivity test cell, with both the central and outer electrodes of the test cell grounded. The area between the central and outer electrodes of the surface conductivity test cell was the region where the surface potential would be scanned. Figure 95 shows the position of the sample, placed on top of the bottom half of the surface conductivity test cell and shows the effective area where the scanning of the surface potential would take place.

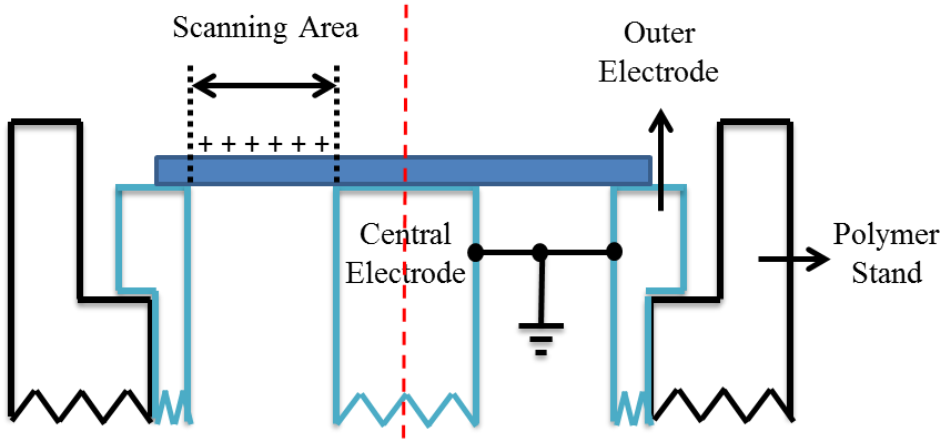

Figure 95: Sample positioned centrally on top of the bottom half of the surface conductivity test cell with scanning area clearly defined.

To deposit corona charge uniformly on the sample surface, an aluminium ring of 110 mm outer and 86 mm inner radius was constructed with eight equally spaced needle electrodes lying on a radius half way between the outer and inner radius of the test cell electrodes. The needle electrodes had a radius of 0.05 mm and were held in place by brass holders that were screwed into a metal ring. The metal ring was supported by a PVC fixture which also supported the grid electrode. This provided insulation between the needle array, the grid and the grounded electrodes of the test cell. The gap between the needle electrodes and the grid was 40 mm and the gap between the grid and the surface of the measuring system electrodes was 15 mm. The system was designed to be located in the outer electrode of the test cell so that the needle array was located in the middle of the scanning area.

Figure 96 shows an image of the complete corona system and the aluminium ring containing the needle electrodes.

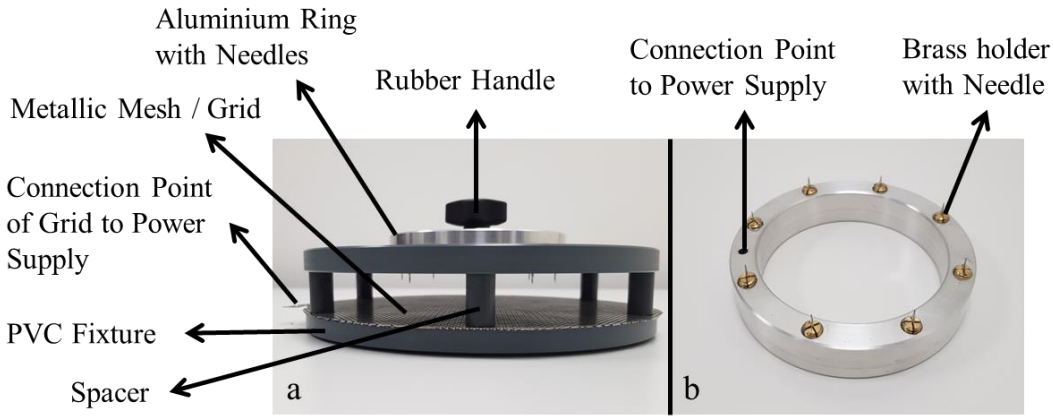

Figure 96: (a) Complete corona system and (b) Aluminium ring.

A schematic diagram of the arrangement prior to corona deposition is shown in figure 97.

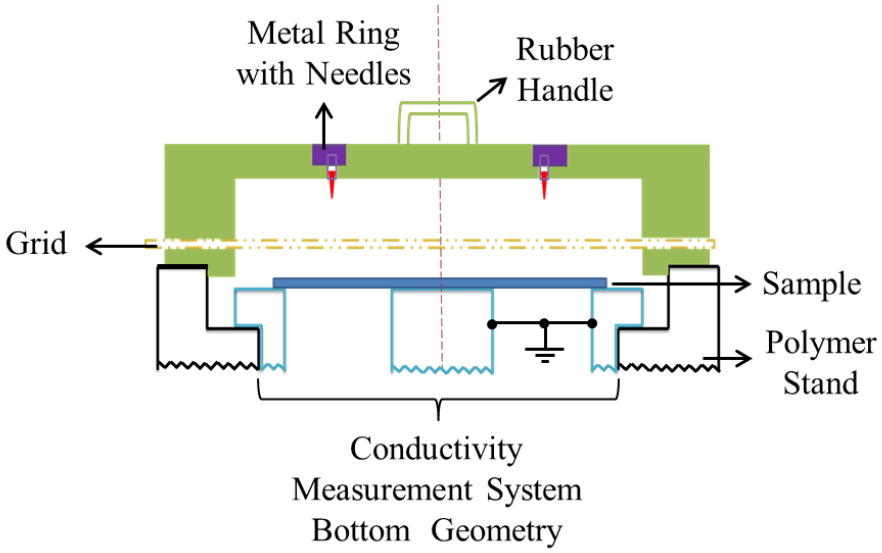

Figure 97: Corona system placed on top of the sample and electrode geometry before charging.

A detailed diagram of the size of all elements of the corona deposition system is provided in Appendix B.

5.2.2. Initial Practical Test on the Surface Potential Measurement

In this section, an initial test was carried out to measure surface potentials across an uncoated PMMA sample of 75 mm radius and a thickness of 2 mm. This initial test was a part of the complete procedure that was developed to calculate and verify the surface charge

distribution measurement process. Results for the potentials across the surface of the PMMA sample will be used in section 5.2.4 to calculate the surface charge distribution.

The first stage of the test involved the charging of the sample with positive corona. The array of needle electrodes were connected with a Matsusada AU-Series power supply capable of supplying DC voltages between 0 and 60 kV. The grid was connected to a Brandenburg Photo-Multiplier power supply capable of providing voltages in the range of 10 V to 2 kV. The needle electrodes were set at a voltage of 15 kV and the grid was set at a voltage of 2 kV. A charging time of 5 minutes was fixed for the entire duration of all surface potential measurements throughout this project. A stopwatch was used to keep a track of the charging time and the time to run a scan across the surface of the sample. The setup of charging the sample with positive corona is shown in figure 98.

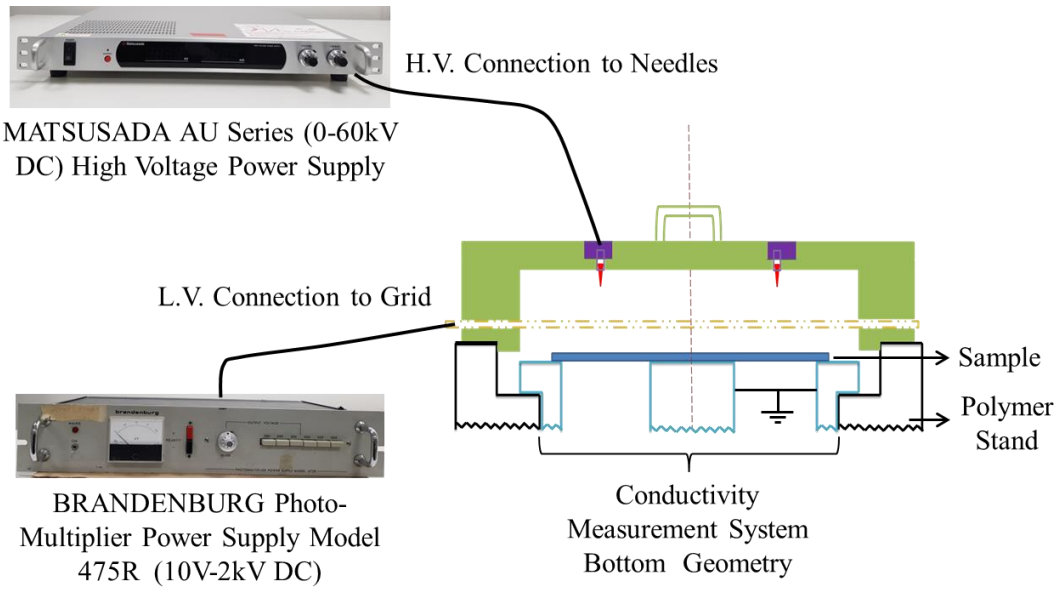

Figure 98: Setup to charge the sample with positive corona.

Once the sample was charged the corona deposition fixture was removed and the needle electrodes and the grid were grounded. The probe was then brought into an initial position, whereby the probe inner edge was directly in line with the edge of the inner central electrode of the conductivity measuring system. The height between the probe sensor and the surface of the sample was set to 10 mm. The total scanning area of 41 mm was divided into 20 measurement points of 2.05 mm length as this value was equal to the probe sensor thickness of 2.05 mm. The Arduino microcontroller was programmed to move the probe 19 times in increments of 2.05 mm, starting from the initial position and finishing with the probe sensor outer edge directly in line with the inner edge of the outer electrode of the surface

conductivity system. Hence, scanning the entire area between the inner and outer electrodes of the surface conductivity measurement system.

After scanning across the surface, the probe would return to its original starting position so that the next scan can be taken precisely over the same measurement points as before. While scanning over the surface of the sample, a total of 10 measurements above each measurement point were made before moving onto the next measurement point. These values were averaged to calculate the potential above each measurement point. Therefore a 20 by 1 vector of measured potential values was obtained. It took ~ 3 minutes to start the scanning process after charging of the sample had been completed. It took ~ 9 minutes to complete one scan of the surface. Figure 99 shows a schematic image of the system setup for measuring surface potential values.

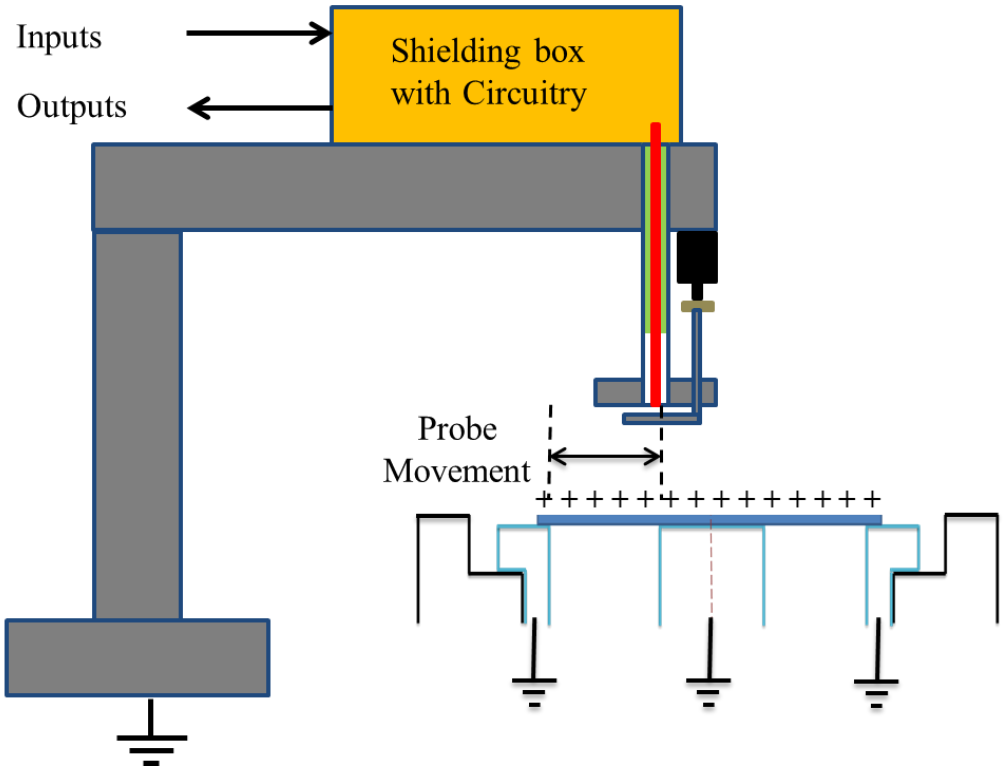

Figure 99: Schematic of the setup to measure surface potential values.

The actual image of the surface potential measurement system setup is shown in figure 100.

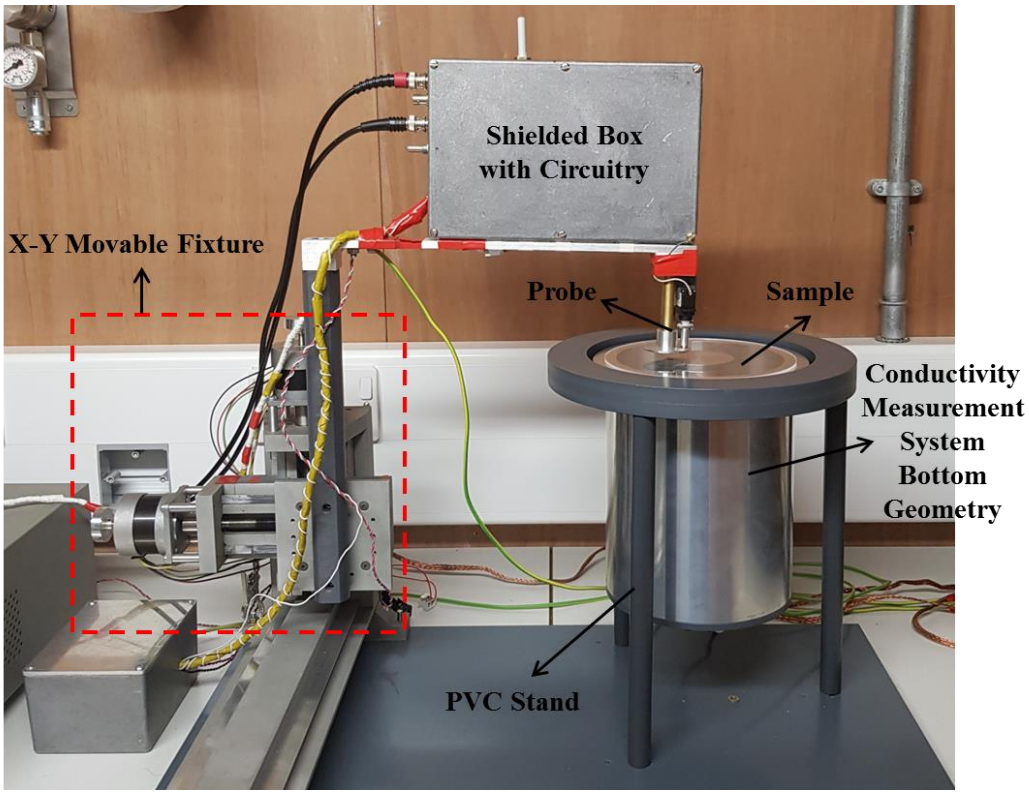

Figure 100: Practical setup of the surface potential measurement setup.

After charging the samples, initial measurements were made at time intervals of 3 minutes, 20 minutes, 40 minutes and 1 hour. For this initial test, a typical measured potential curve at 20 minutes after charging of the sample is shown in figure 101.

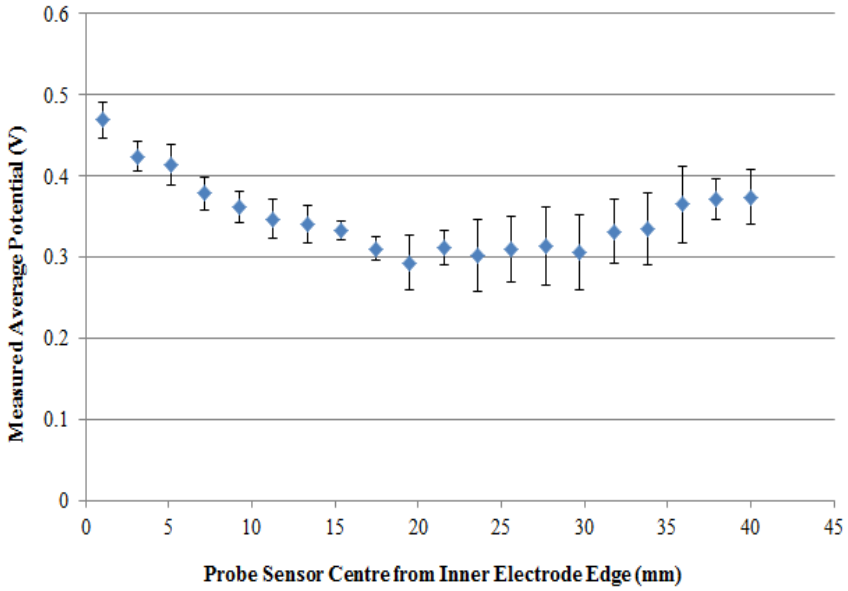

Figure 101: Averaged surface potential values after 20 minutes of charging.

5.2.3. Φ-Matrix for Measurement System

After obtaining the vector containing the surface potential values, the next step was to calculate the Φ-Matrix for the present geometry. The technique is described in detail in subsection 2.9.2. The calculations for the coefficients of the Φ-Matrix were carried out in COMSOL Multiphysics simulation software.

To compute the desired matrix, the geometry of the experimental system including the probe geometry, measurement system electrodes and the PMMA insulator were constructed with similar dimensions to the initial practical experiment and solved under Electrostatics model as a 3D geometry. Due to the circular design of the corona deposition system where the needles are mounted on an aluminium ring, and due to the circular geometry of the samples, it is assumed that the surface charging of the sample will be radially symmetric. So, the scanning area of the sample was divided into 20 ring elements of equal width of 2.05 mm. In this way the whole scanning area (~ 41 mm) was able to be scanned by the probe, as was the case in the practical experiment. The centre of the sample was a circular disc of 29 mm radius. The outer and inner central electrodes of the measurement system on which the sample rested were fixed at a potential of 0 V. The whole geometry was enclosed within a grounded metal box with the surrounding gas medium being air. The probe body was fixed at a potential of 0 V and, whereas, the probe sensor was designed to have an initial potential value of 0 V, it was set as a floating point conductor. The gap between the probe sensor and the surface of the test sample was fixed at 10 mm.

To calculate an element of the Φ-Matrix, a defined charge density was assigned to one of the ring elements while keeping all other elements at 0 charge density. The sample central disk element and the outer part of the sample that lay outside the scanning area were set to a 0 charge density throughout the scanning process. The probe was then placed directly above the other ring elements, corresponding to the probe positions used when scanning the surface, and the induced potentials at the probe sensor from the defined charge density were simulated at these positions. To carry out the scan, a parametric sweep was set up whereby, the probe edge was positioned vertically in line with the edge of the inner central electrode and the probe was set to move across the scanning area in increments of 2.05 mm measuring the induced potentials across all the ring elements for a defined charge density present at one of the elements

The defined charge density allocated to each ring element was +1 μC/m^2. After running the parametric sweep once, a 20 by 1 vector of the potential values was obtained for a charge

present at a specific ring element. This process was carried out 20 times with the defined charge density being assigned to successive ring elements resulting in a 20 by 20 $\boldsymbol{\Phi}$-Matrix. The 3D geometry of the system along with an illustration of the sample surface divided into different ring elements is shown in figure 102.

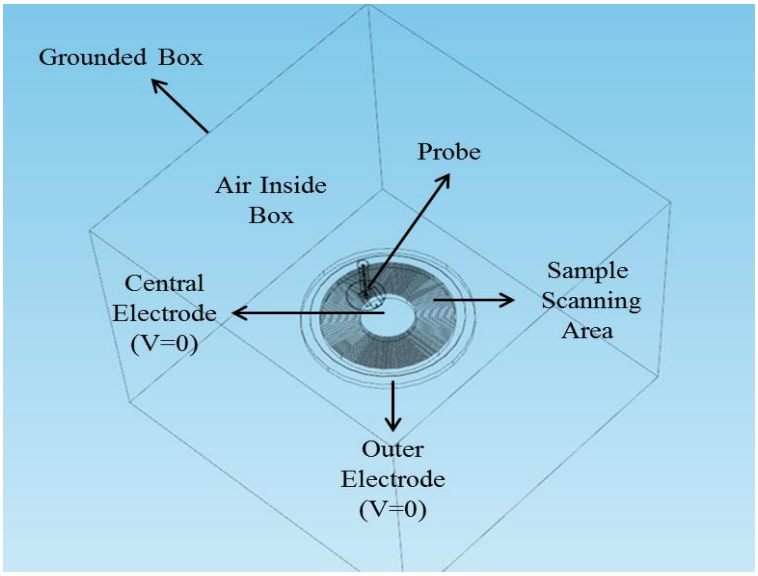

Figure 102: Constructed geometry in COMSOL to calculate the $\boldsymbol{\Phi}$-Matrix.

The calculated $\boldsymbol{\Phi}$-Matrix from COMSOL as a result of a defined charge density allocated to a specific ring element repeated 20 times to obtain a 20 by 20 matrix of $\boldsymbol{\Phi}$ values is shown in figure 103 where, Q_n represents the results when the defined charge density is present on ring n of the sample.

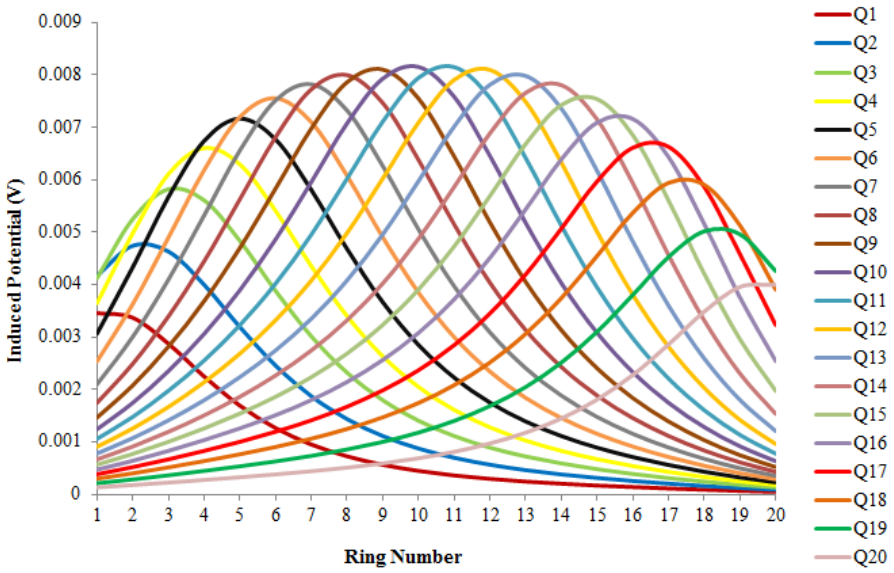

Figure 103: $\boldsymbol{\Phi}$-Matrix calculated from COMSOL at probe to surface gap of 10 mm.

5.2.4. Process to Obtain an Accurate Surface Charge Distribution

Using the measured surface potential values from the practical tests and the calculated $\boldsymbol{\Phi}$-Matrix from COMSOL, the method to calculate charge distribution was followed as described in section 2.9.2. Equation 20 was used to calculate the charge distributions across the surface of the sample by multiplying the inverse of the 20 by 20 $\boldsymbol{\Phi}$-Matrix by the 20 by 1 vector of the measured surface potentials acquired from the practical experiment for measurements conducted 20 minutes after corona charging the sample. MATLAB, a numerical computing software package was used to perform these calculations. Figure 104 shows the initial calculated charge densities from MATLAB.

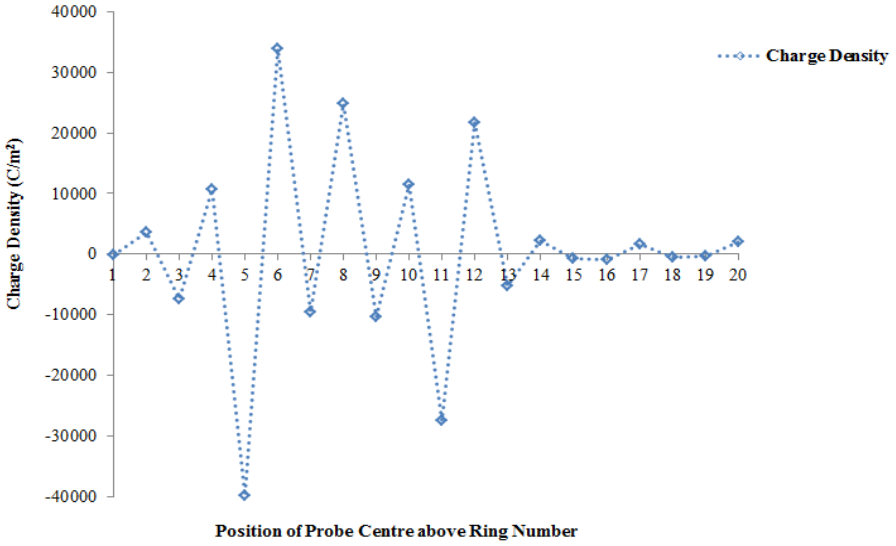

Figure 104: Initial charge densities calculated from MATLAB.

The calculated charge densities in figure 104 show regions of positive and negative charge densities which are unrealistic as it was assumed that the original charge distribution was positive and uniform. The migration of charge across the surface from this initial condition to produce regions where negative charge densities are immediately adjacent to positive charge densities is not physically realistic. Therefore it is expected that the charge densities on the surface of the sample will be positive.

At this stage the influence of the charge from the central disk and the outer part of the sample (out-with the scanning area) on the measured surface potentials was considered as a factor that might be causing these unrealistic results. To allow this to be tested without the requirements of completely recalculating the $\boldsymbol{\Phi}$-Matrix in COMSOL which would be

extremely time consuming, two new vectors of $\boldsymbol{\Phi}$ values were calculated for the existing probe positions for defined charge densities on the central disk element and the area out-with the scanning region. This effectively produced a 20 by 22 $\boldsymbol{\Phi}$-Matrix. As the behaviour of the calculated potential as a function of position in each column of the matrix was smoothly varying, it was possible to extrapolate each column to a 22 element vector effectively reducing the separation between the measured points. This gave a 22 by 22 matrix. As the 20 element measured potential vector was also smoothly varying it was possible to extrapolate a 22 element vector of potential values for positions corresponding to those in the recalculated 22 by 22 $\boldsymbol{\Phi}$-Matrix. The additional vectors derived for the defined charge density present at the sample central disk and sample outer elements are shown in figure 105.

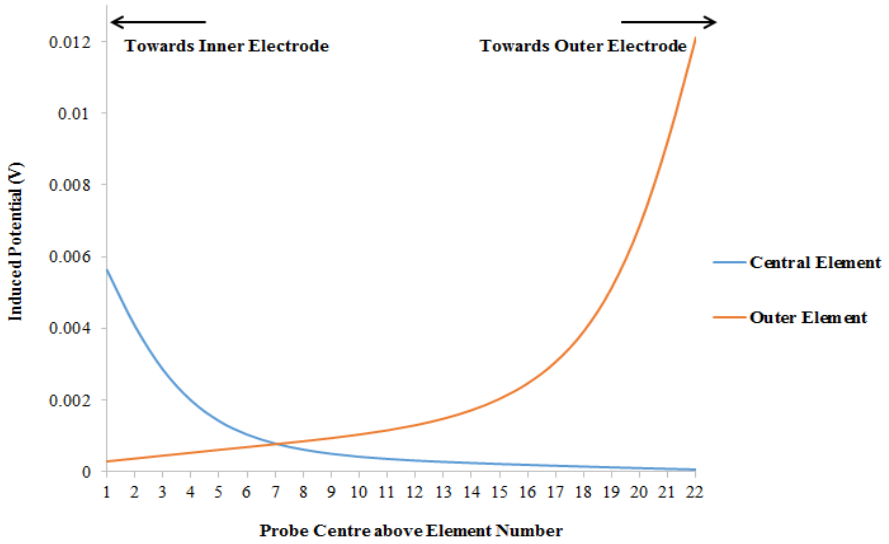

Figure 105: Additional potential values across the sample surface for a unit charge density present at the sample central disk element (1) and the sample outer element (22).

However, when MATLAB was used with these extrapolated arrays to calculate a solution which would include charge being present in the central region and the region outside the scanning area, the same problem of having calculated negative and positive charge density values in adjacent regions on the surface of the sample was observed.

To check if it was possible to derive a physically realistic surface charge distribution that would approximate the measured potentials using the calculated values of the existing $\boldsymbol{\Phi}$-Matrix, a spreadsheet in Microsoft Excel was created. This used equation 18 from subsection 2.9.2 to calculate the expected potential, by multiplying the elements of the $\boldsymbol{\Phi}$-Matrix with manually entered values of surface charge densities. The resulting expected potential was compared with the measured potential from experimental measurements. It was shown that

the calculated $\boldsymbol{\Phi}$-Matrix could provide a physically realistic solution. Figure 106 shows a plot of the measured voltage from experiment compared against the voltage derived from the spreadsheet.

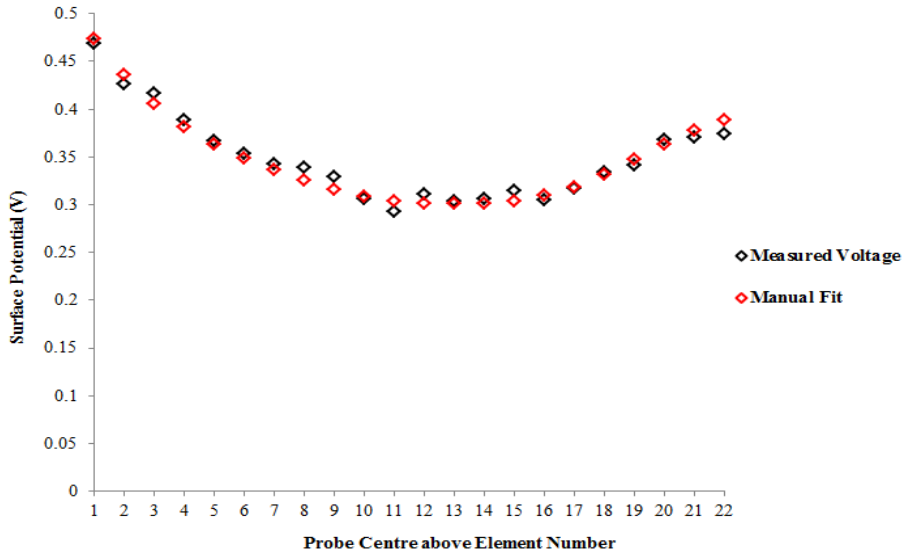

Figure 106: Measured potential compared to Manually calculated potential.

The resulting manually calculated charge densities are shown in figure 107.

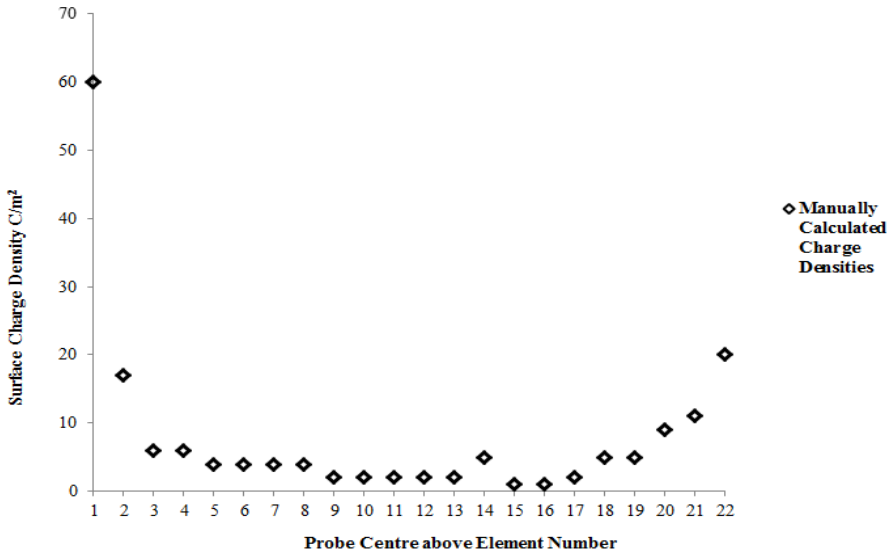

Figure 107: Manually calculated surface charge densities.

Having shown that realistic fits were possible based on the $\boldsymbol{\Phi}$-Matrix through this manual approach. It was assumed that the failure of MATLAB to converge to a physically realistic result may be due to noise in the potential measurements. The rapid variation in potential between successive measurement points could cause the calculated charge for specific

elements to be increased above its actual value and to be decreased in other regions in attempt to exactly match the measured profile containing noise. This could prevent MATLAB from converging to a solution for the true surface charge distribution. To reduce the noise in the measured potential values, a digital filtering process was employed.

The digital filter employed was the "SAVITSKY-GOLAY" filter. The filter uses a local least-squares polynomial approximation to smooth the data [142], whereby a low degree polynomial is fitted to a set of adjacent data points through the process of convolution. The filter smooth's the data while keeping a good signal to noise ratio. The filter comes as a in-built function within MATLAB. The expression to smooth the data is given by equation 86.

$$\boldsymbol{Y = sgolayfilt(X, O, F)} \tag{86}$$

Where,

$\boldsymbol{Y}$ = Filtered Data,

$\boldsymbol{sgolayfilt}$ = Function to carry out the filtering,

$\boldsymbol{X}$ = Data to be filtered,

$\boldsymbol{O}$ = Order of the polynomial and

$\boldsymbol{F}$ = The frame length which should be odd and larger than the polynomial order.

The set of measured potential data was put through the "SAVITSKY-GOLAY" filtering process with an order ($\boldsymbol{O}$) of 3 and a frame length ($\boldsymbol{F}$) of 11. For these values of $\boldsymbol{O}$ and $\boldsymbol{F}$ a balanced smoothing effect without distorting the signal was achieved. A plot of the filtered data and the original measured potential is shown in figure 108.

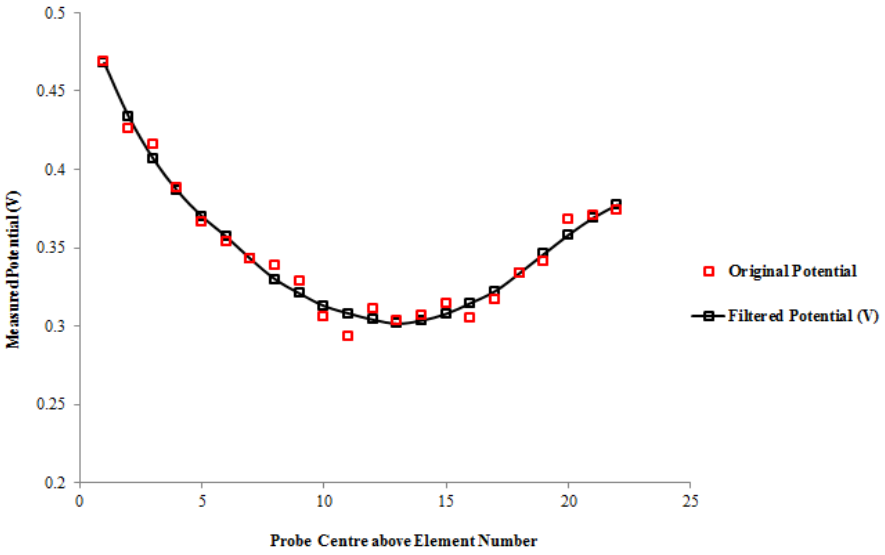

Figure 108: Filtered potential vs Original measured potential.

The filtered data and the $\boldsymbol{\Phi}$-Matrix were solved in MATLAB and a solution was found that was physically realistic and shape of charge densities was similar to the manually calculated charge densities calculated through the spreadsheet. This verified the $\boldsymbol{\Phi}$-Matrix approach to solve for charge densities along the sample surface. The charge densities computed through MATLAB are shown in figure 109.

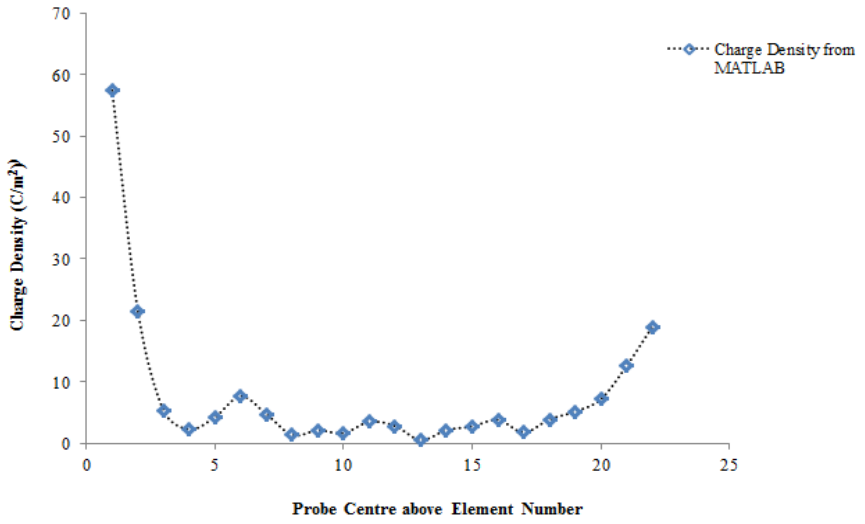

Figure 109: Surface charge densities from filtered data.

5.3. Chapter 5: Summary

In this chapter the development of the surface conductivity measurement system was presented. The arrangement to conduct surface current measurements and the experiments conducted to observe leakage currents, noise and accuracy of the system were discussed. It was established that the idea of the modified concentric cylindrical geometry did not significantly influence the output.

This chapter also presented the constructed grid system for depositing charge in a controlled manner on a sample surface. This was followed by performing an initial experiment for measuring surface charge on the sample using the varactor probe system developed in chapters 3 and 4. The results from this experiment were used in conjunction with the simulated $\boldsymbol{\Phi}$-Matrix to establish a procedure to obtain a realistic set of values for the surface charge density distribution.

6. Surface Conductivity behaviour of Polymeric Insulators

6.1. Chapter 6: Overview

The surface conductivity tests in this project were carried out under two conditions. The first condition where, no pre-charging of the sample surface was performed and the second where, charge was deposited on the sample surface prior to performing surface conductivity tests. In this chapter the results for the surface conductivity tests under these two conditions are presented. The tests were performed to observe and analyse the transient behaviour for both charging and discharging of the insulators. The tests were carried out on PMMA samples as in pulsed power systems such as the Z-Machine at Sandia National Laboratories in Albuquerque, New Mexico [128], PMMA is widely used in the housings of the Laser Triggered Gas Switches. The tests were conducted on thick (2 mm) and thin (0.25 mm) Poly(methyl-methacrylate) (PMMA) samples as this provides interesting observations of the behaviours of the transient currents in terms of material thickness.

The initial part of the chapter contains details on the type of samples used and their coating. The preparation of the samples to get them test ready is also discussed. This is followed by details of the test setup and results for charging and discharging transients under the two conditions. The results from the experiments are compared to see the impact of pre-existing charge on the transient behaviour of the samples. These results will help to provide important knowledge which will aid in better understanding the charging and discharging behaviour of thin and thick polymeric insulators under these conditions.

6.2. Sample Selection and Coating

Acrylic plastic or Poly(methyl-methacrylate) (PMMA) is one of the most versatile polymeric materials. It offers low cost, processibilty and possibility of functionalization. Low dielectric constant and dielectric loss over a wide range of frequencies are some of the reasons why this material is widely used as a gate dielectric in micro electric and electro-optic areas [143]. It is also useful within the high voltage industry where it has wide applications in pulsed power systems specifically in pulsed power vacuum interfaces [144].

The properties of PMMA have been characterised by many researchers however, the focus of these characterisations has mainly been in terms of its thermal, mechanical and optical properties. Little has been reported on the study of surface conductivity and charge decay behaviour of this dielectric material [145]. The study conducted in this project will provide additional knowledge to better understand the surface charging/discharging behaviour and the surface charge decay properties of thick and thin PMMA samples. The PMMA samples used in this project were ordered from a global materials supplier (Goodfellow) and came in the form of 300 mm by 600 mm rectangular sheets. The sheets were cut to form individual circular PMMA samples of 150 mm diameter. The material had a quoted surface resistivity of $10^{14}\,\Omega$/sq and a quoted bulk/volume resistivity of $2\text{-}14\times10^{15}\,\Omega\cdot$cm [137].

Before any surface conductivity or charge decay experiments were conducted the samples were coated with a thin (500 nm) metallic layer of aluminium in the region where the electrodes of the conductivity test cell would make contact with the sample. Metallic masks were constructed to allow the deposition of the aluminium metal only in the desired areas of the sample. This resulted in the samples being coated on both sides with a ring electrode having an inner diameter of 140 mm and an outer diameter of 150 mm and also a central circular electrode of 41 mm diameter. The process of evaporated aluminium electrodes was important so that a more consistent contact between the sample surface and the test system was established thus helping to maintain the uniformity of the system design. The sample coating would also aid in design and implementation of the surface charge decay experiments that were conducted after completing the conductivity experiments.

During the coating process the sample first underwent a stage of plasma surface cleaning whereby the surface of the sample is cleaned of any impurities/contaminants and once this stage was completed, the process of aluminium coating is carried out. The samples were handled with care and rubber gloves were used to avoid any unnecessary contaminant or charge transfer on to the sample surface. Figure 110 shows a coated sample.

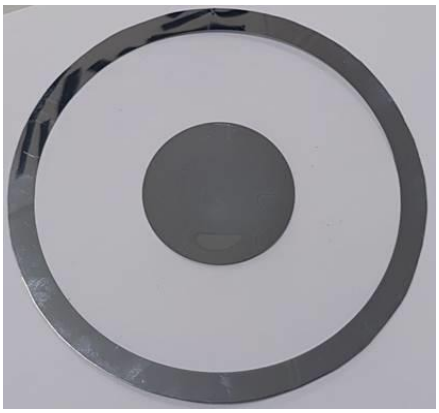

Figure 110: PMMA sample coated with 500 nm evaporated aluminium electrodes.

6.3. Sample Preparation before Experiments

Before any test on a sample was conducted, actions were taken to rid the surface of the insulator from any charge that might have been deposited on the sample surface while transferring the samples from the coating plant to the test system.

To remove charge from the sample surface, the samples were wrapped in aluminium foil, then placed on a flat surface followed by placing a flat weight on the samples so that the aluminium foil made good contact with the surface of the sample. The aluminium foil was connected to a common ground through a copper wire within the screened metal room where the experiments were conducted. The samples were kept in this arrangement for at least 12 hours. By doing this it was intended to neutralise any unwanted charge present on the sample surface. This method was also employed later in the project to remove unwanted charge from the surface of the samples when conducting repeated charge decay tests. Figure 111 shows this arrangement in different steps.

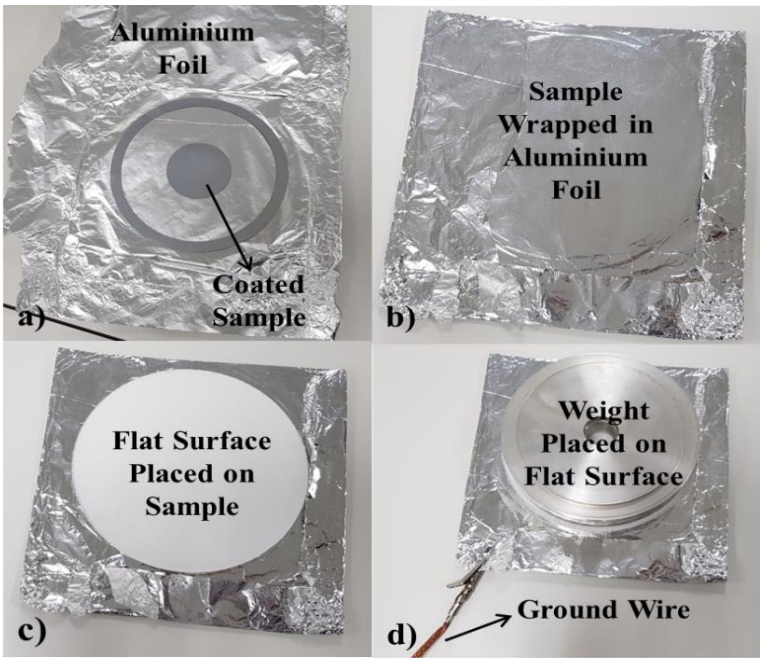

Figure 111: a) Sample placed on aluminium foil, b) Sample wrapped in aluminium foil, c) Flat surface placed on top of sample wrapped in aluminium foil and d) Weight placed on flat surface and aluminium foil connected to ground.

After discharging the sample using the method discussed above, the sample was placed inside the measurement system and was left for 12 hours with all the electrodes of the measuring system connected to a common ground. This was done to remove any potential surface charge that might have resulted from handling the sample during transfer to the measurement system. This arrangement is shown in figure 112.

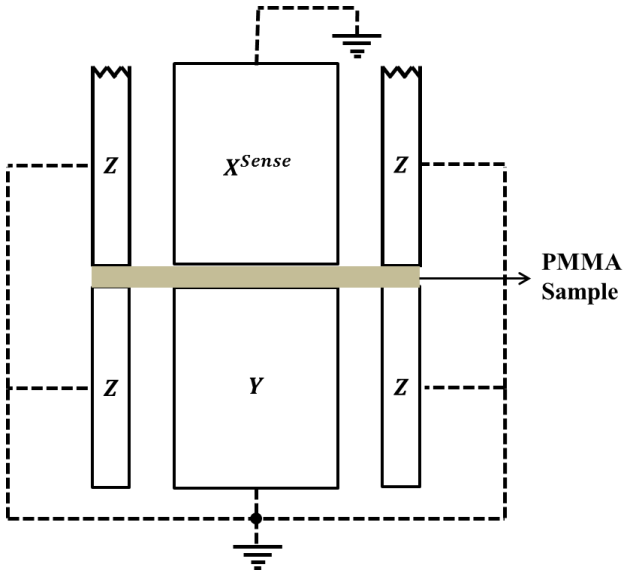

Figure 112: Discharging the sample prior to conducting surface conductivity tests.

6.4. Experimental Setup and Test Conditions

In this section, the test setup and the process used to perform surface transient measurements on thick and thin PMMA samples under the conditions where the samples were not subjected to any prior corona deposition and also for the condition where they were pre-charged with corona are described.

6.4.1. Samples with No Corona Treatment

The experimental arrangement for conducting measurements of the surface conductivity of polymeric insulators is explained in section 5.1.3.1, where figure 83 shows the arrangement of the test system for conducting surface current measurements.

The surface charging transient measurements were carried out using applied voltages ranging from 2 kV to 10 kV in increments of 2 kV. The programs developed in LabView to measure the transient currents collected a total of ~ 1030 measurements. Initially as the transient response was expected to be changing rapidly the first 710 measurements were taken at intervals of 1.5 seconds. This was followed by taking 200 measurements at 5 second intervals, 100 measurements at 10 second intervals and the last 20 measurements at 30 second intervals. The overall measurement time period was ~ 1 hour. This pattern of measurements was employed based on the behaviour of the charging current transients observed in initial trials where little change in current was observed after the first hour.

Once the data for a particular charging transient current had been collected the discharging transient was measured for a period of 2 hours as this time period allowed for the discharging transient currents to reach the noise level of the measurement system. This was an indication that most of the charge introduced during the charging transient had left the surface of the insulator through the grounded electrodes of the measurement system. Initially 1420 measurements were made at the smallest time gap of 1.5 second per measurement, followed by taking 400 measurements at 5 second intervals, 200 measurements at 10 second intervals and the last 40 measurements at 30 second intervals.

The set up for measuring the discharging current transient is comparable to that of figure 112, where the sample is setup to discharge any potential charge on its surface. The only difference in the configuration to measure the discharging current is that the measurement electrode ($\boldsymbol{X^{Sense}}$) is grounded through the electrometer rather than a direct connection to ground through a copper wire. Figure 113 shows this configuration.

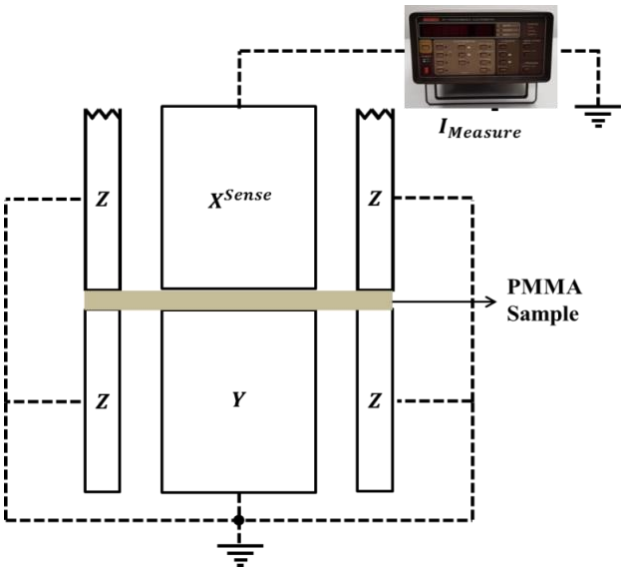

Figure 113: System setup to measure transient discharging current.

Measurements of the percentage of relative humidity (%rh) and the temperature (ºC) within the screened room were taken before each experiment was conducted. It was established that the range of the percentage of relative humidity for all the surface conductivity tests in this project lay between 30 %rh to 50 %rh and the range of temperature lay between 21 ºC to 24 ºC. Once a charging and discharging measurement had been completed the sample was left inside the measurement system with all the electrodes grounded for at least 12 hours. This was done to remove any remaining charge on the sample surface before the next test was conducted.

Figure 114 shows a schematic diagram of ideal charging and discharging transient currents. The charging current transient shows an initial peak that is a result of vacuum polarisation, and rapid dipole alignment associated with establishing the electric field across the sample surface. This is followed by a transient decay process associated with establishing a steady state charge distribution across the surface. Once this has occurred a DC current exists which is dependent on the magnitude of the supply voltage and the resistivity of the sample. The discharging current shows an initial negative peak associated with the change in charge distribution to bring the voltage across the electrodes to zero. The transient decay process which follows this initial peak current does not stop at a DC steady state value but continues to decay until the current becomes zero, as the charge leaves the surface of the sample through the grounded electrodes.

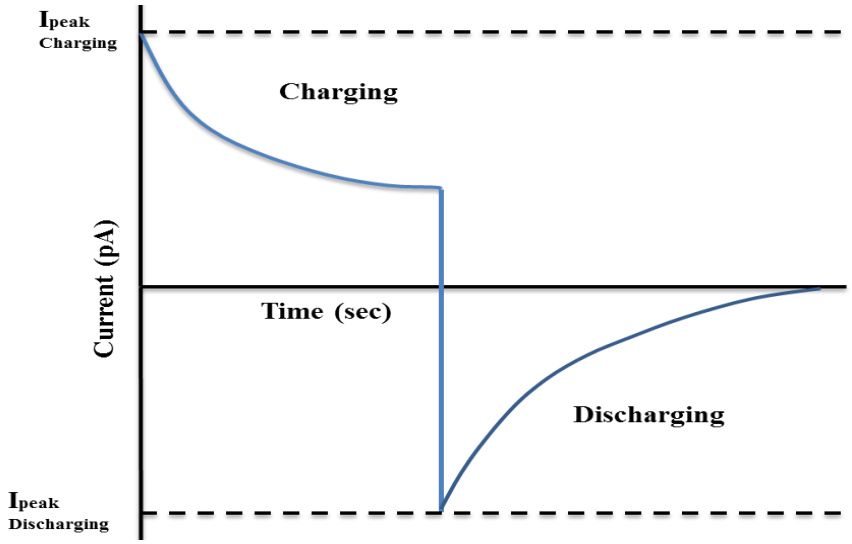

Figure 114: Transient response for surface currents under ideal conditions.

A minimum of 5 tests were conducted at each voltage level and the results are presented as an average of all 5 tests. Good repeatability was established between repeated measurements. The standard deviation between the measurements at any time was at least 1 order of magnitude below the average current being measured at that time. For measurements conducted on corona treated thick samples, the average current being measured at 60 seconds after DC stressing was 4.86×10^{-11} A, with a standard deviation of 3.13×10^{-12} A. At 1000 seconds, the average current being measured was 3.75×10^{-11} A, with a standard deviation of 3.77×10^{-12} A, whereas, the average current being measured at 3600 seconds was 3.08×10^{-11} A, with a standard deviation of 2.78×10^{-12} A. After each test had been completed, the system was grounded and left to completely discharge the sample for at least 12 hours and the test was repeated the next day until a full set of data had been collected for one applied voltage. The supply voltage was then increased to the next value and the test procedure repeated.

6.4.2. Samples Treated with Corona Charging

The experimental setup was divided into two stages: Stage 1: Depositing charge on the sample surface and Stage 2: Conducting surface transient measurements. The two stages involved a combination of the experimental arrangement used in section 5.2.2 to deposit charge on the sample surface, where figure 98 shows the arrangement for depositing charge, and the arrangement used in section 5.1.3.1, where figure 83 shows the arrangement of the test system for conducting surface transient measurements. The combined image of the two arrangements can be seen in figure 115.

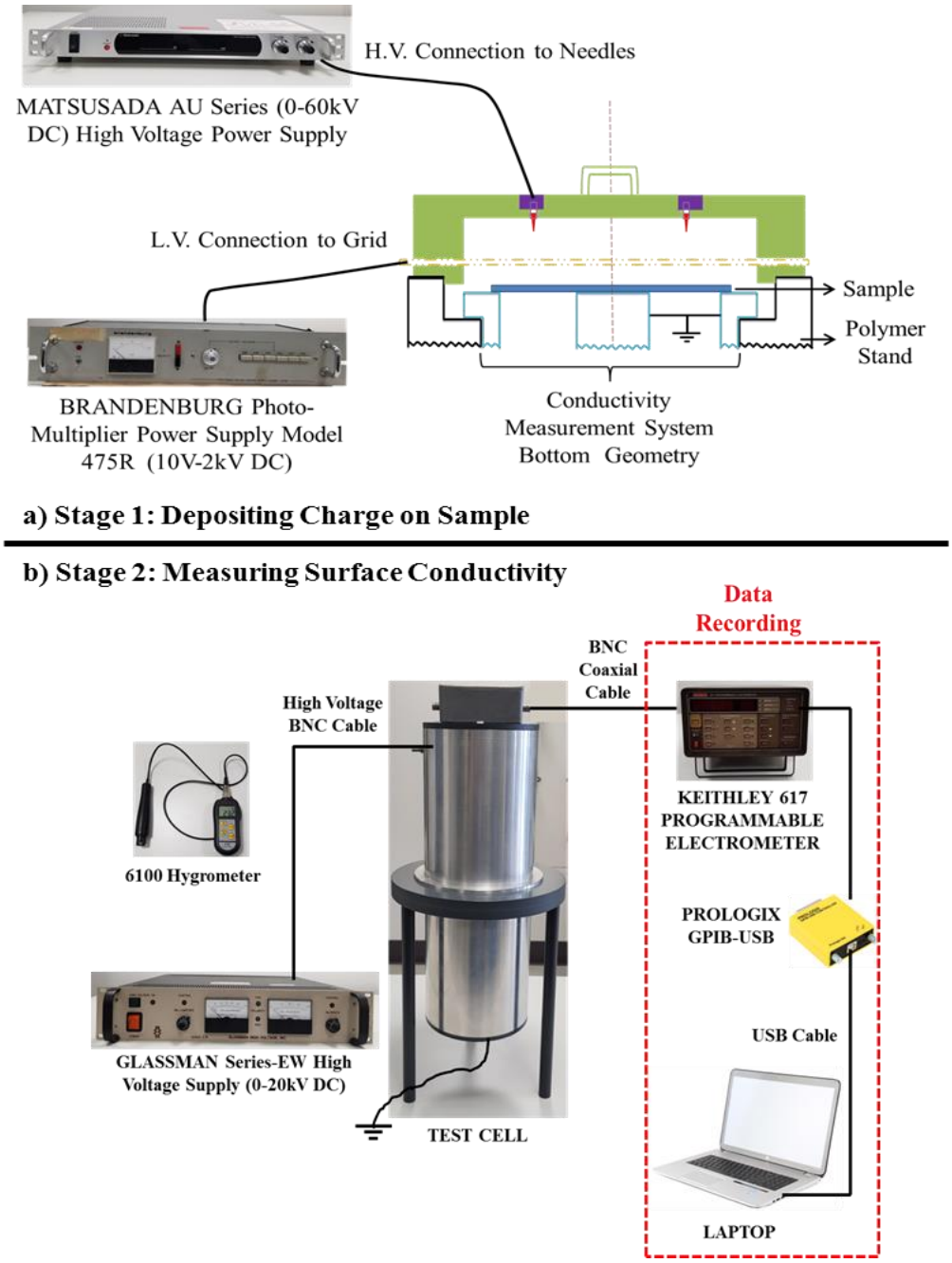

Figure 115: The combined image of the two stages where stage 1 shows the arrangement for depositing charge on the sample surface and stage 2 shows the arrangement for conducting surface conductivity experiments.

Before any experiments were conducted the samples were prepared for the tests as explained in section 6.3. To deposit corona charge on the sample surface the supply voltage to the needle electrodes was set at 13.5 kV and the grid voltage was set at 500 V. A charging time of 5 mins was set for surface charging via corona for all experiments in this project. Once the samples were charged with corona, the arrangement to conduct surface conductivity

measurements was set-up. The time taken to start conducting surface transient measurements after completing the process of corona deposition was ~ 50 secs.

The surface conductivity tests were conducted primarily over a range of 2 kV to 10 kV in increments of 2 kV. For a given measurement voltage, the sample was corona charged and then the charging transient was measured for a period of one hour followed by a 2 hour discharging transient measurement. The sample was then left in the measurement system to discharge overnight. This process was repeated for a minimum of 3 times for each supply voltage.

After completing these tests, further surface transient charging tests were conducted on the thick and thin samples with a higher grid voltage. In this case the aim was to deposit greater charge on the sample surface, so the needle electrodes were connected to a supply voltage of 14 kV and the grid voltage was set at 1 kV. After charging the sample, surface charging measurements were taken in the same way for supply voltages of 4 kV and 8 kV only. This way the effect of excessive pre-existing charge on the DC current can be realised.

6.5. Experimental Results and Analysis

In this section the results for the charging and discharging transients under the two experimental conditions and the fittings established across the transients are presented.

6.5.1. Charging Transient: Results and Analysis

The charging transient test results and the analysis of the charging behaviour for tests conducted under both experimental conditions are presented below.

6.5.1.1. Untreated Thick PMMA: Charging Transients

Figure 116 shows the averaged charging surface transient currents observed across the thick PMMA samples which were not subjected to any corona charging.

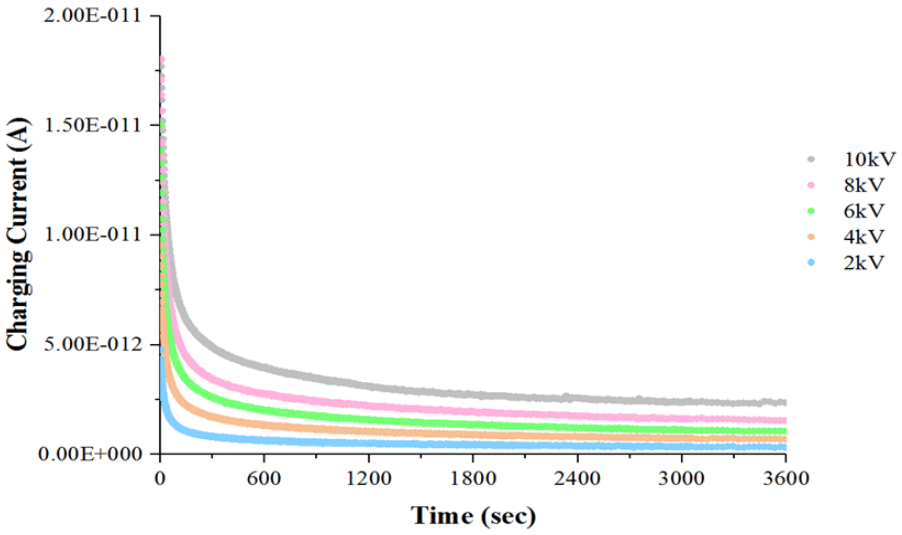

Figure 116: Charging transients for untreated thick PMMA.

It can be seen from figure 116 that the general shape of the transients follow the charging behaviour expected where an initial peak can be observed that is followed by a transient decay process which slows down significantly moving towards a steady DC value. Fittings for the transient behaviour were performed using data analysis and graphing software called OriginPro. Attempts were made to fit the data to an expression of the form of equation 87.

$$\boldsymbol{I(t) = A_1 t^{-n} + I_o} \tag{87}$$

However, it was established that the best fitting for the transient behaviour was that of a 3 term exponential fit taking the form of equation 88.

$$\boldsymbol{I(t) = A_1 Exp\left(-\frac{t}{\tau 1}\right) + A_2 Exp\left(-\frac{t}{\tau 2}\right) + A_3 Exp\left(-\frac{t}{\tau 3}\right) + I_o} \tag{88}$$

Where,

$\boldsymbol{A_1}$, $\boldsymbol{A_2}$ and $\boldsymbol{A_3}$ = Pre-exponential terms associated with the fits across the short time, mid time and long time behaviour of the transients.

$\boldsymbol{\tau_1}$, $\boldsymbol{\tau_2}$ and $\boldsymbol{\tau_3}$ = The time constants associated with the fits across the short time, mid time and long time behaviour of the transients and,

$\boldsymbol{I_o}$ = The DC steady state current.

The possible mechanisms responsible for conduction at these time constants are discussed in section 6.5.1.5. Figure 117 shows a log/log plot of the charging transients fitted with the 3 term exponential fitting as in equation 88 and table 4 shows the parameter values for the fits.

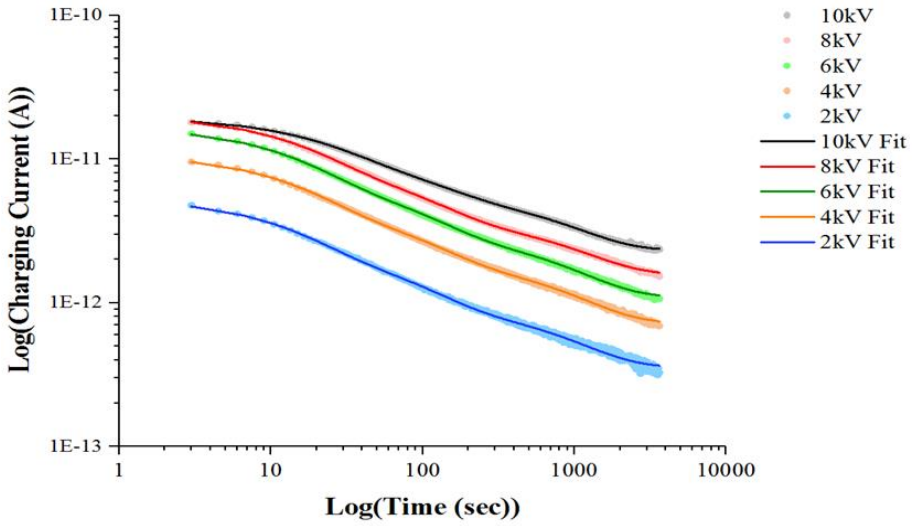

Figure 117: Log plot of charging transients in figure 116 fitted with relationship of equation 88.

Table 4: Parameters for the fittings applied to the charging transients.

Voltage (kV)	A_1 (pA)	A_2 (pA)	A_3 (pA)	τ_1 (sec)	τ_2 (sec)	τ_3 (sec)	I_o (pA)	R^2
2.0	2.98	1.39	0.59	13.4	81.8	850	0.36	0.99
4.0	6.08	2.70	1.24	14.7	88	871	0.73	0.99
6.0	9.53	4.23	1.89	14.5	86.9	856	1.10	0.99
8.0	10.90	5.36	2.26	15.9	89.9	938	1.58	0.99
10.0	8.62	5.20	3.33	22.1	95	833	2.33	0.99

From table 4 it can be seen that the pre-exponential terms i.e. peak currents in the short time, mid time and long time section of the transient behaviour show a general rising trend up to 8kV. Figure 118 shows the behaviour of the pre-exponential terms against supply voltage where a general rising trend against supply voltage can be observed.

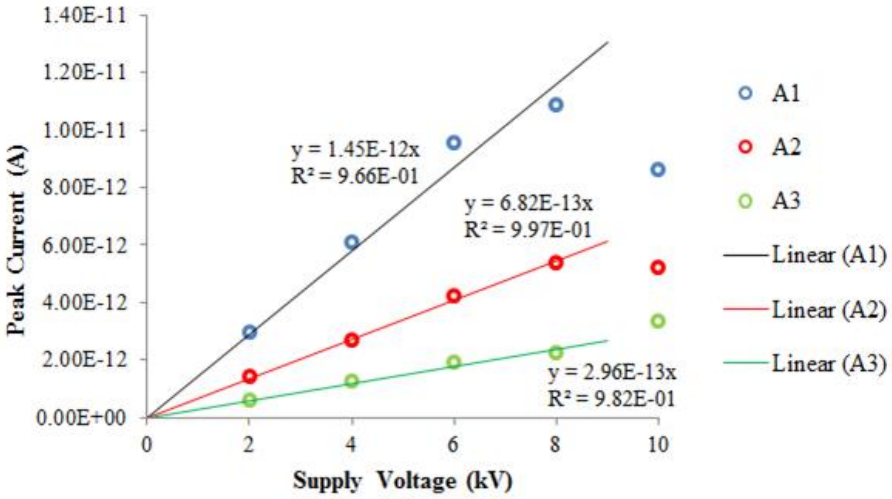

Figure 118: Peak currents against supply voltage for untreated thick PMMA.

Figure 119 shows the behaviour of the log of time constants against supply voltage. It can be seen that the time constants are reasonably constant across the supply voltages. The average values of the time constants being ~ 16.13 ± 3.45 secs, ~ 88.33 ± 4.80 secs and ~ 869.58 ± 40.88 secs.

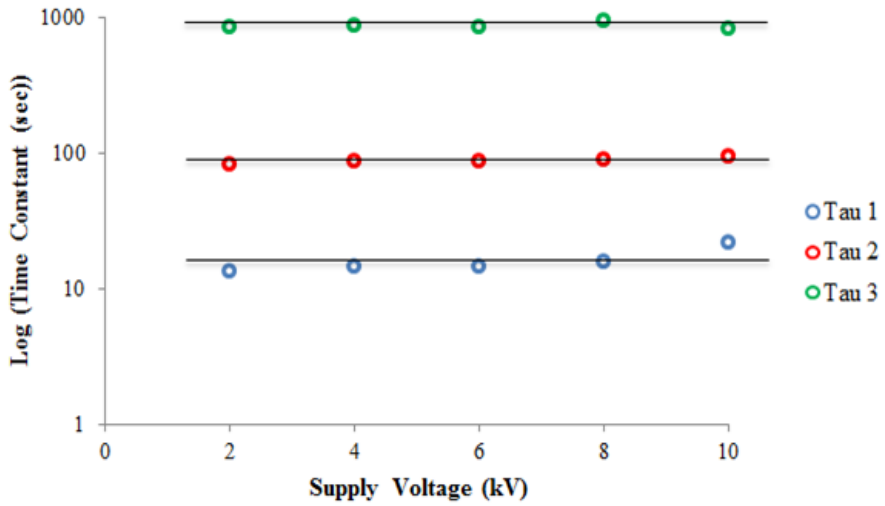

Figure 119: Log of time constants (Tau 1, Tau 2, Tau 3) against supply voltage.

Figure 120 shows a plot of the current transient at 6 kV supply voltage that illustrates the influence of the transient decay (A) against the log of time (sec) in the short time, mid time and long time sections.

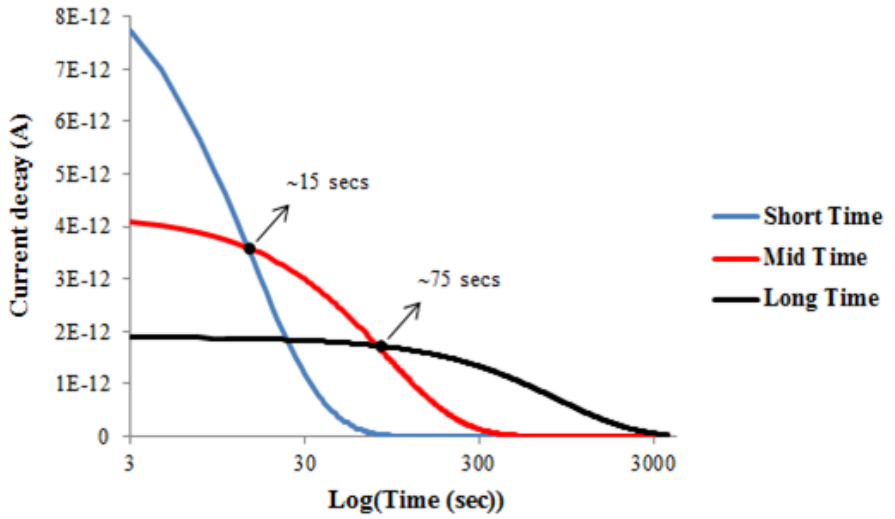

Figure 120: Current decay (A) against log of time (sec) showing the time zones where the current decay is dominated by the short time, mid time and long time exponential behaviours.

It can be seen from figure 120 that the transient decay process is initially dominated by the short time constant exponential, between 15 and 75 secs the behaviour is controlled by the medium time constant exponential and the transient behaviour at longer times is dominated by the long time constant exponential.

Figure 121 shows the process of establishing a fitting across the charging transient at 6 kV supply voltage in different stages. The influence of each exponential term of the 3 term fitting relationship, the combined sum of the 3 exponentials and the complete fit consisting of the sum of the 3 exponentials and the approximate DC current $\boldsymbol{I_{3300}}$ is also shown.

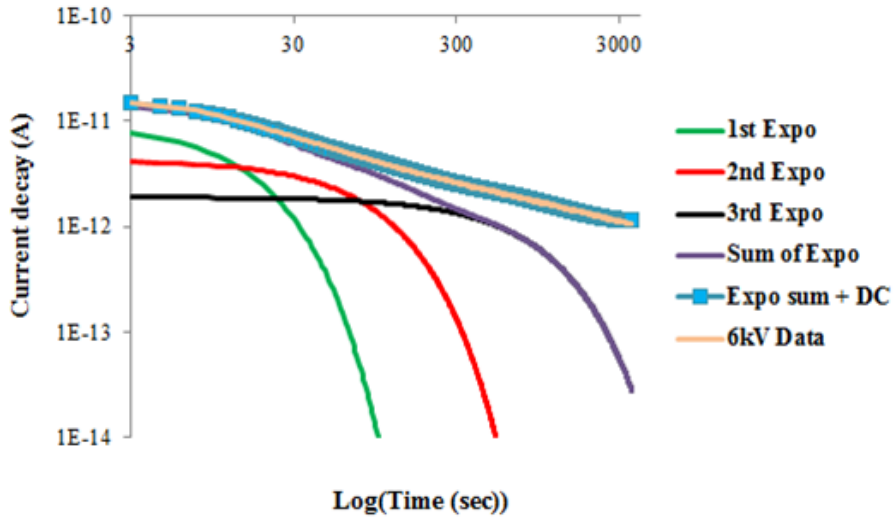

Figure 121: Fitting process of the charging transient at 6kV supply voltage.

The average current $\boldsymbol{I_{3300}}$ in the last 10 mins of the data was an approximate DC current as at this time the decay process had slowed down significantly. However, the actual DC current maybe be different to this approximation as later analysis on the discharging transients showed that a further much slower decay process may be taking place beyond the measurement time of 1 hour made for the charging transients. This method was used to obtain an approximate DC current throughout the experimental observations for both experimental conditions. This way an isochronal comparison of the average currents $\boldsymbol{I_{3300}}$ can be made for the observed transient behaviours. Figure 122 shows a plot of $\boldsymbol{I_{3300}}$ against supply voltage for the untreated thick PMMA.

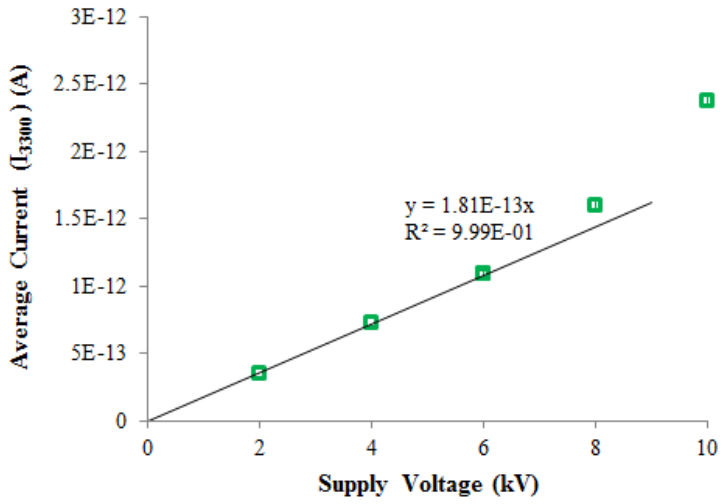

Figure 122: Average current (I_{3300}) □ against supply voltage for untreated thick PMMA.

Figure 122 shows that the approximate DC currents $\boldsymbol{I_{3300}}$ follow a linear relationship of the form of equation 89 up to a supply voltage of ~ 6 kV after which a rapid increase is observed.

$$\boldsymbol{I = m \cdot V} \tag{89}$$

The behaviour of $\boldsymbol{I_{3300}}$ at higher voltages shows a deviation from the linear relationship and it was important to explore the potential conduction mechanism responsible for this behaviour. The behaviour of $\boldsymbol{I_{3300}}$ was examined against a range of different conduction mechanisms: Space charge limited conduction (SCLC), Poole-Frenkel mechanism, Schottky type conduction and Hopping conduction.

- ***Space charge limited conduction (SCLC)***

For the SCLC using equation 27 it can be determined that at higher fields, $\boldsymbol{I \propto V^2}$. So, a slope of 2 is expected between a graph of $\boldsymbol{ln\, I}$ against $\boldsymbol{ln\, V}$. The low field current is expected

to be Ohmic which would lead to a gradient of 1 on the $\boldsymbol{ln\, I}$ against $\boldsymbol{ln\, V}$ plot. Therefore, two linear sections would be expected on the plot. These can be seen in figure 123.

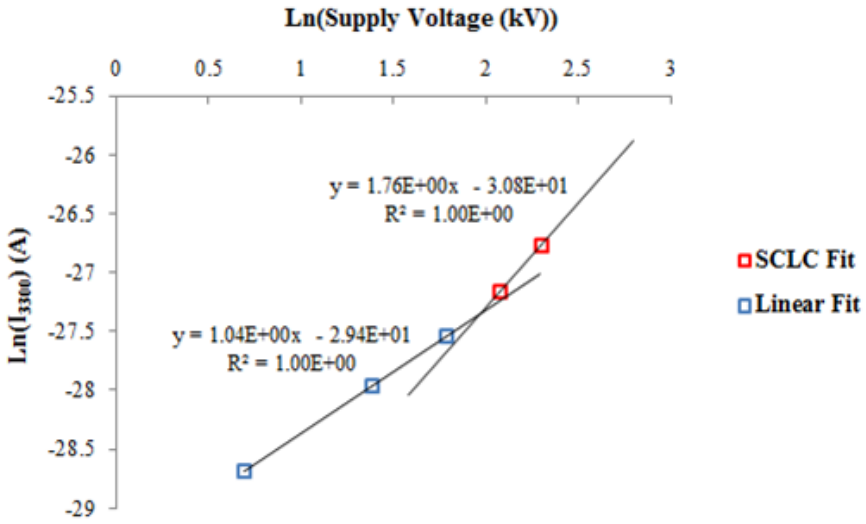

Figure 123: Ln(I_{3300}) (A) vs Ln(Supply Voltage) (kV) for examining SCLC behaviour.

The gradient in the low field region is ~ 1 corresponding to Ohmic behaviour. However the gradient of the high field region is ~ 1.76 rather than 2. This indicates that the observed change in current behaviour is not as a result of the onset of SCLC.

- ***Poole-Frenkel mechanism***

For the DC behaviour to follow the Poole-Frenkel mechanism, it is expected that a straight line plot would be observed for $\boldsymbol{ln}(\boldsymbol{I}/\boldsymbol{V})$ against $\boldsymbol{V^{1/2}}$ as from equation 39, $\boldsymbol{ln}(\boldsymbol{I}/\boldsymbol{V}) \propto \boldsymbol{V^{1/2}}$. Figure 124 shows this observation.

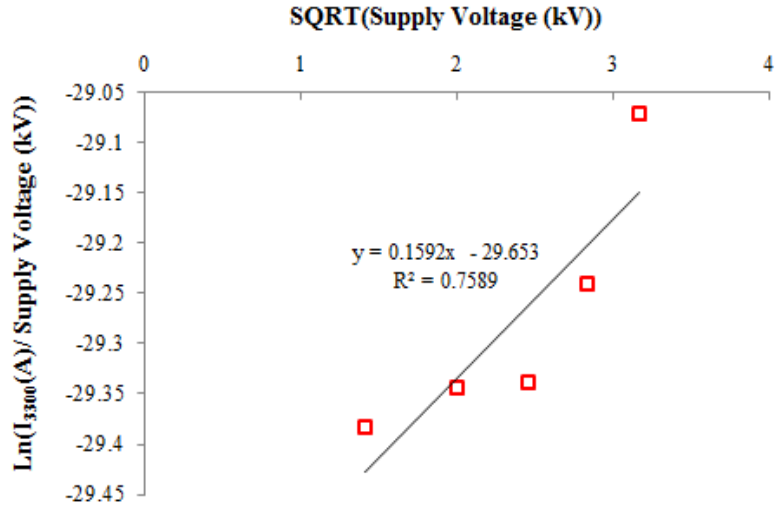

Figure 124: Fit to establish if the behaviour of I_{3300} agrees with the Poole-Frenkel mechanism.

From figure 124 it can be seen that the fitting does not correspond to that expected for the Poole-Frenkel mechanism.

- ***Schottky type conduction***

For I_{3300} to be considered to follow the Schottky mechanism, it is expected that a straight line plot would be achieved for $\ln I$ against $V^{1/2}$ as from equation 8: $\ln I \propto V^{1/2}$. Figure 125 shows this observation.

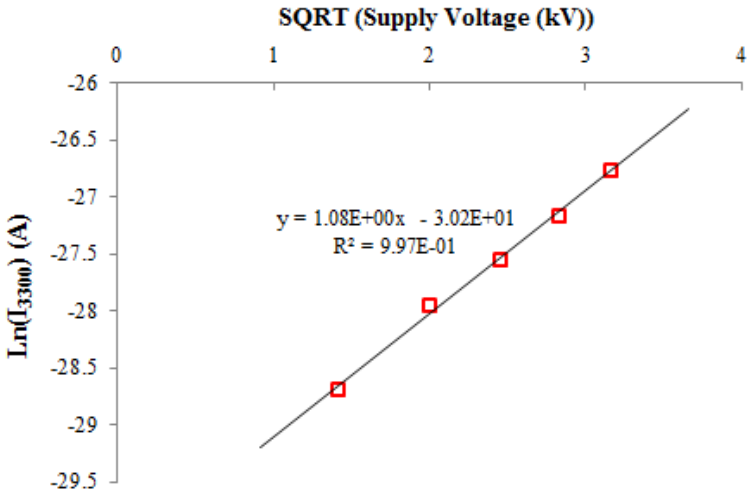

Figure 125: Fit to establish if the behaviour of I_{3300} agrees with the Schottky mechanism.

It can be seen that a good fit is established corresponding to the Schottky type behaviour. This is further illustrated in figure 126 where a plot of the I_{3300} is fitted against the calculated Schottky currents across the supply voltages.

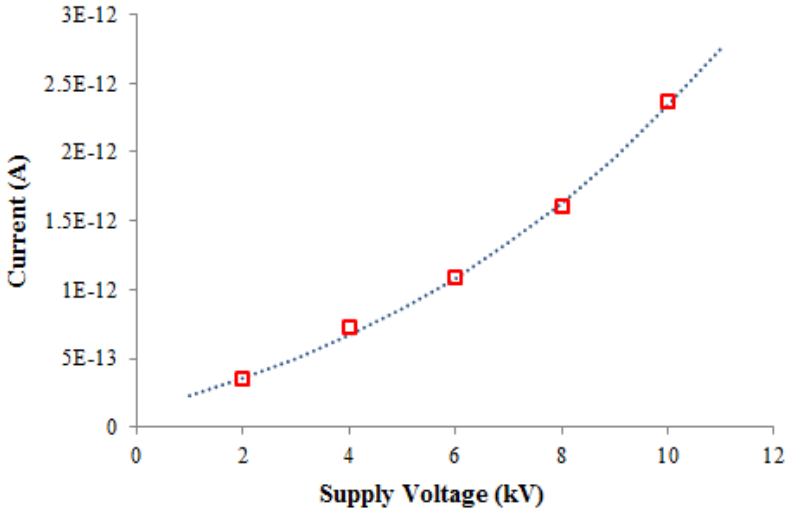

Figure 126: I_{3300} fitted against calculated Schottky currents.

- ***Hopping type conduction***

From equation 40 the current as a result of a Hopping conductivity model is expected to take the form:

$$I(E) = A\,sinh(BE) \tag{90}$$

Figure 127 shows a plot of I_{3300} fitted against the calculated Hopping currents across the supply voltages. A good fit is established against the expected Hopping type behaviour.

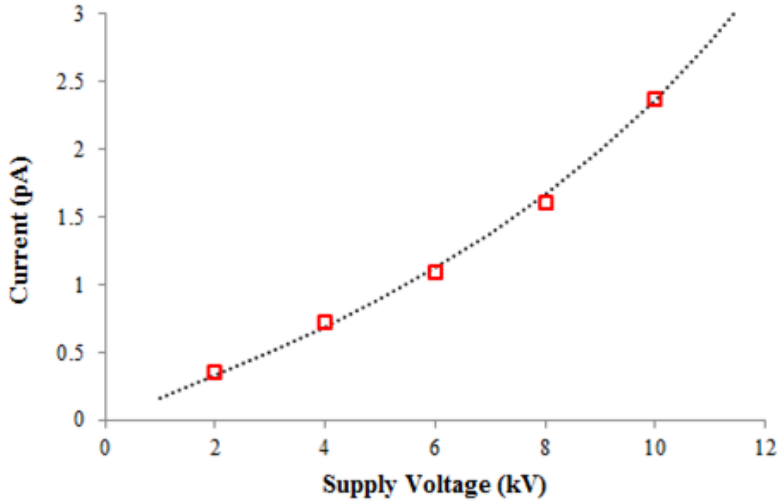

Figure 127: I_{3300} fitted against calculated Hopping currents.

From the observed behaviour of the transients over a range of 0 to 10 kV it is unclear whether the behaviour of I_{3300} is a result of Schottky-type conduction or the Hopping mechanism.

6.5.1.2. Corona Treated Thick PMMA: Charging Transients

Figure 128 shows the averaged surface charging transients observed across the corona treated thick PMMA samples using a grid voltage of 500V. The observed current behaviour shows a transient response similar to that of the untreated thick PMMA. It can be seen that the transient currents are larger than those observed for the untreated thick PMMA.

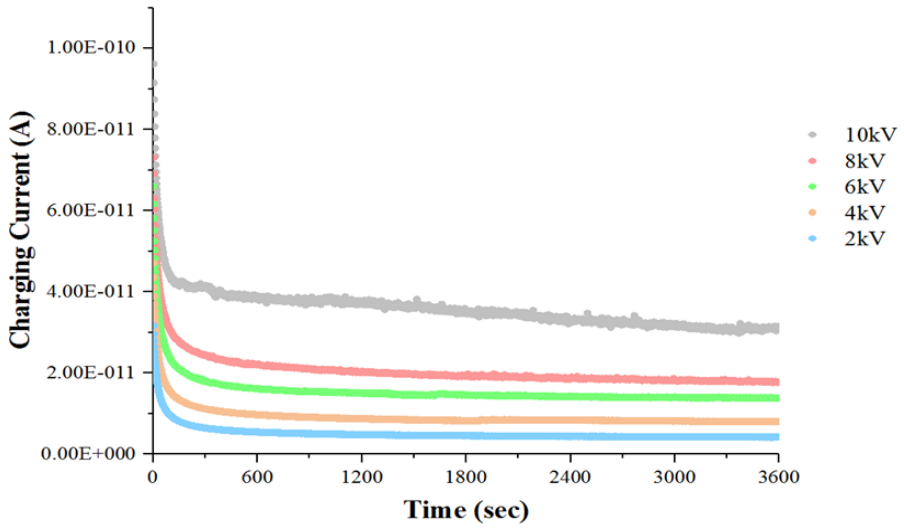

Figure 128: Charging transients for corona treated thick PMMA.

Figure 129 shows the log/log plot of the charging transients plotted against time (sec) fitted with the 3 term exponential fit taking the form of equation 88 and table 5 shows the parameter values for the fits established across the charging transients.

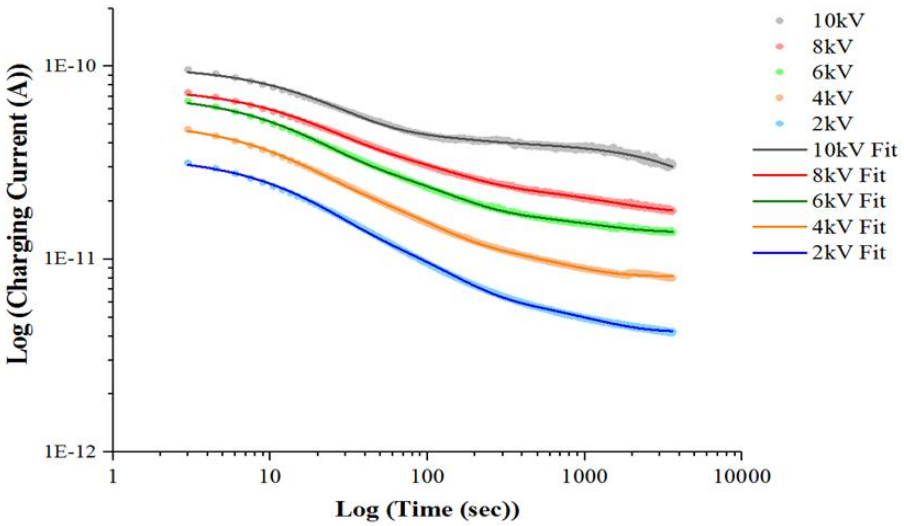

Figure 129: Log/Log plot of charging transients for corona treated thick PMMA.

Table 5: Parameters for the fittings applied to the charging transients.

Voltage (kV)	A_1(pA)	A_2(pA)	A_3(pA)	τ_1 (sec)	τ_2 (sec)	τ_3 (sec)	I_o (pA)	R^2
2.0	18.30	9.40	2.55	15.2	91.4	853.4	4.20	0.99
4.0	27.90	11.60	3.07	15.9	112.4	900	8.03	0.99
6.0	36.90	17.10	4.39	14.1	96.4	962.5	13.80	0.99
8.0	39	17.60	8.35	13.4	82.8	865.6	17.60	0.99
10.0	41.70	18	8.62	16.2	49	1002.1	34	0.99

From table 5 it can be seen that the pre-exponential terms show a general rising trend with applied voltage. They are also significantly larger than those observed for the untreated thick PMMA. The time constants are reasonably constant over the range of supply voltages, the average values being ~ 15 ± 1.18 secs, ~ 86.40 ± 23.51 secs and ~ 917 ± 63.80 secs. The time constants are relatively similar in value to those observed for the untreated thick PMMA. Figure 130 shows a plot of the I_{3300} against supply voltage for corona treated thick PMMA with a grid voltage of 500 V.

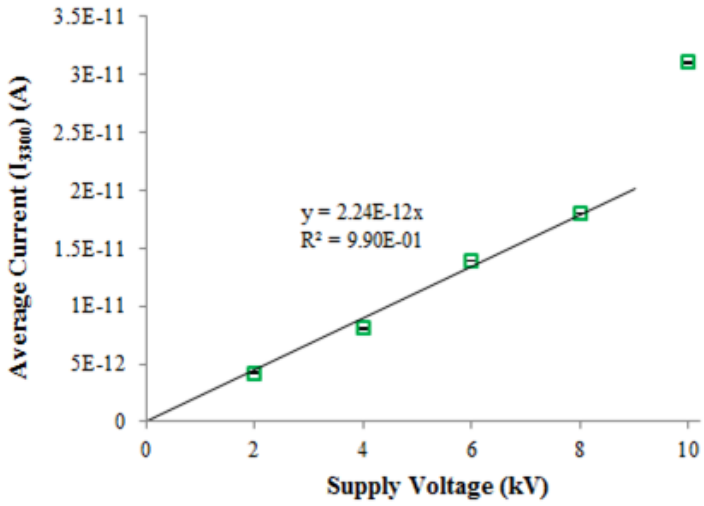

Figure 130: I_{3300} against supply voltage for corona treated thick PMMA.

From figure 130 it can be seen that I_{3300} follows a linear relationship of the form of equation 89 up to ~ 8 kV after which a rapid increase is observed. This behaviour is similar to that observed for the untreated thick PMMA samples.

When analysed against a range of conduction mechanisms it was observed that the SCLC and the Poole-Frenkel mechanism did not provide reliable fits to be considered responsible for this behaviour. A good fit for the behaviour of I_{3300} was established against the expected Schottky and Hopping currents. This is similar to the observations made for the untreated thick PMMA samples. Figure 131 shows this observation.

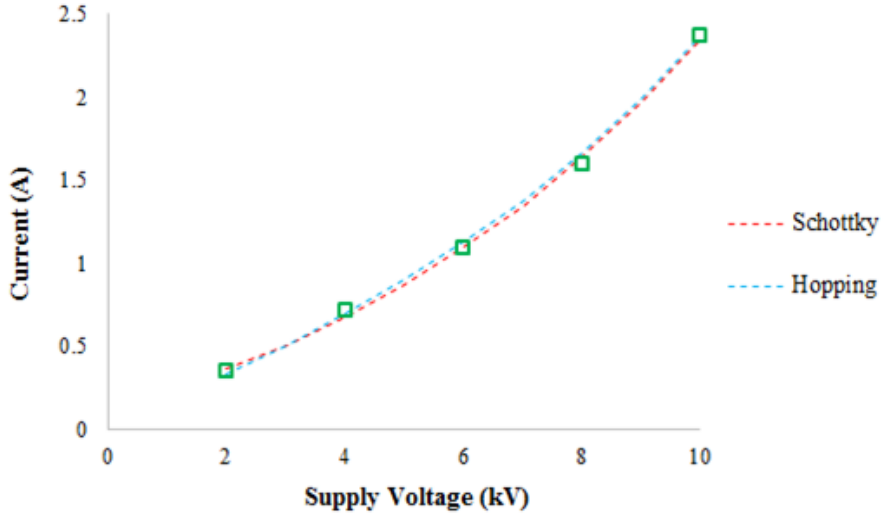

Figure 131: I_{3300} □ fitted against calculated Schottky and Hopping currents.

After conducting the tests on corona treated thick samples using a grid voltage of 500 V, measurements were made to observe the effect of pre-charging the sample with a higher grid voltage of 1 kV. Measurements for charging transients were made for supply voltages of 4 kV and 8 kV. Figure 132 shows the observed charging transients.

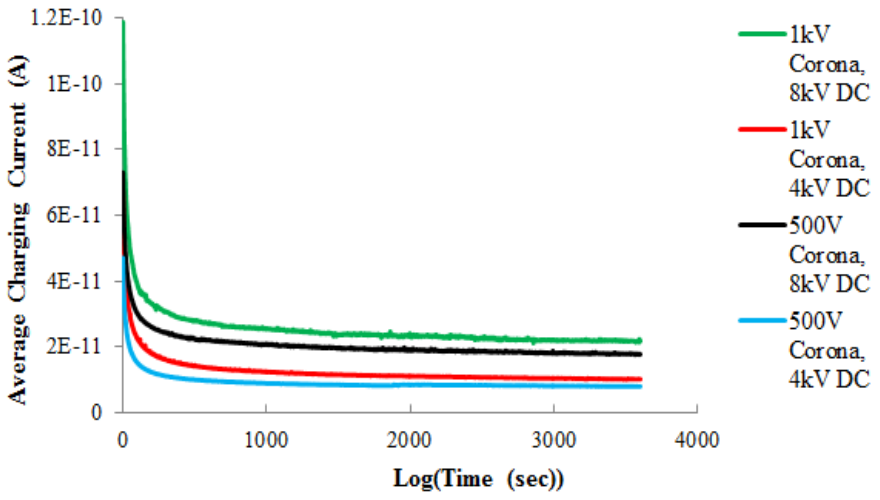

Figure 132: Charging transients observed across corona treated thick PMMA using grid voltages of 500 V and 1 kV.

Figure 132 shows that corona charged samples with higher grid voltages exhibit higher transient currents. Values of I_{3300} for supply voltages of 4kV for thick corona charged samples with grid voltage of 500 V and 1 kV were 8.07 ± 0.0534 pA and 10.32 ± 0.0859 pA and I_{3300} values for 8 kV supply voltage were 18.00 ± 0.141 pA and 21.93 ± 0.137 pA. Figure 133 shows the I_{3300} data for untreated and corona treated thick PMMA.

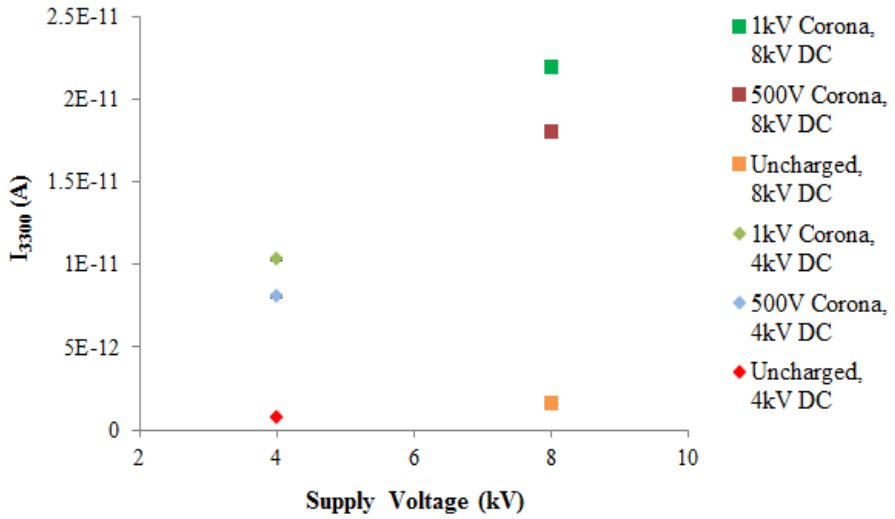

Figure 133: I_{3300} observed for DC voltages of 4 kV and 8 kV across uncharged and corona treated thick PMMA with grid voltages of 500 V and 1 kV.

It can be observed that the corona treated samples exhibit a significantly higher I_{3300}.

6.5.1.3. Untreated Thin PMMA: Charging Transients

Figure 134 shows the averaged charging transients for the untreated thin PMMA samples.

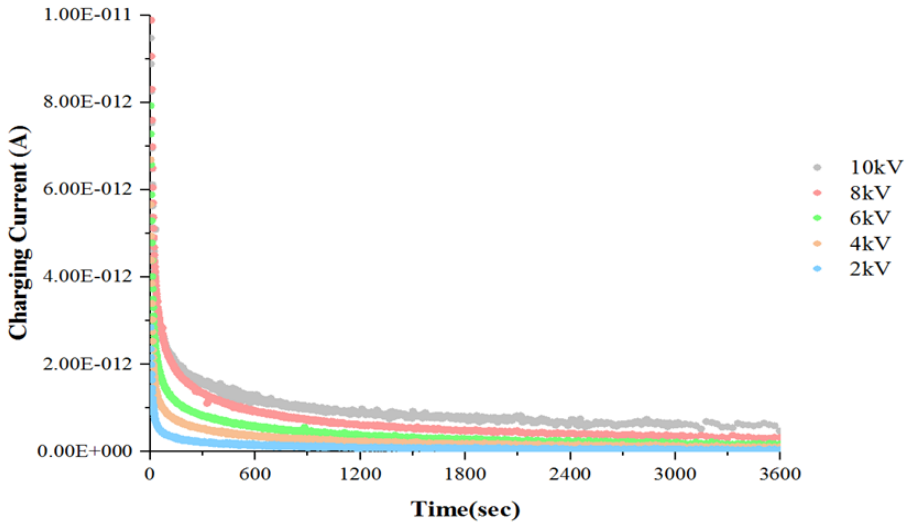

Figure 134: Charging transients for untreated thin PMMA samples.

The charging transients were fitted with the 3 term exponential fit taking the form of equation 88. Figure 135 shows the log/log plot of the averaged charging currents (A) plotted against time (sec) and table 6 shows the parameter values for the fits established across the charging transients.

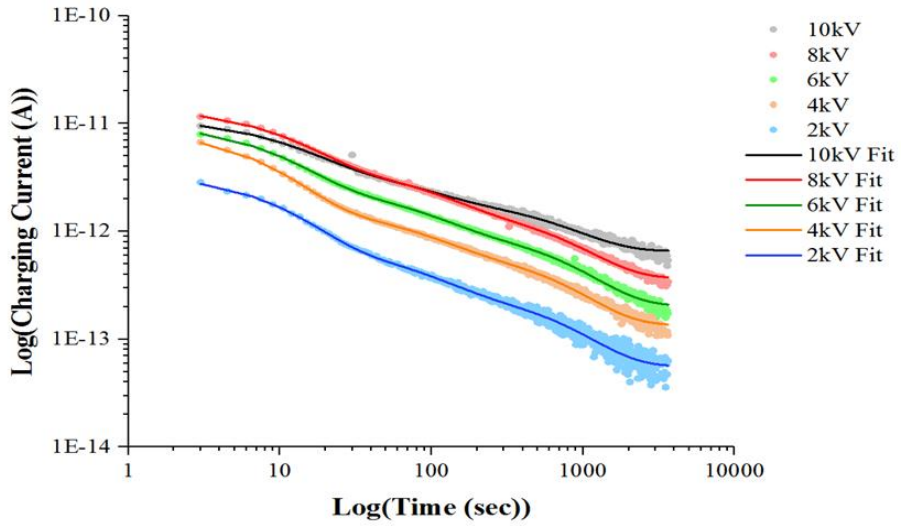

Figure 135: Log plot of charging transients in figure 134 fitted with relationship of equation 88.

Table 6: Parameters for the fittings applied to the charging transients.

Voltage (kV)	A_1 (pA)	A_2 (pA)	A_3 (pA)	τ_1 (sec)	τ_2 (sec)	τ_3 (sec)	I_o (pA)	R^2
2.0	2.77	0.47	0.24	9.5	72.9	675	0.060	0.99
4.0	7.38	0.99	0.58	7.6	71.8	646	0.14	0.99
6.0	7.60	1.62	0.89	8.9	73.4	710	0.20	0.99
8.0	10.20	2.47	1.36	10.4	83.5	693	0.37	0.99
10.0	7.12	2.18	1.44	10.6	63.3	642	0.65	0.99

From table 6 it can be seen that the pre-exponential terms show a general rising trend up to 8 kV. It can also be seen that the time constants are reasonably constant across the supply voltages, the average values being ~ 9.37 ± 1.22 secs, ~ 73.00 ± 7.19 secs and ~ 673.00 ± 29.46 secs. Figure 136 shows a plot of I_{3300} against supply voltage for the untreated thin PMMA.

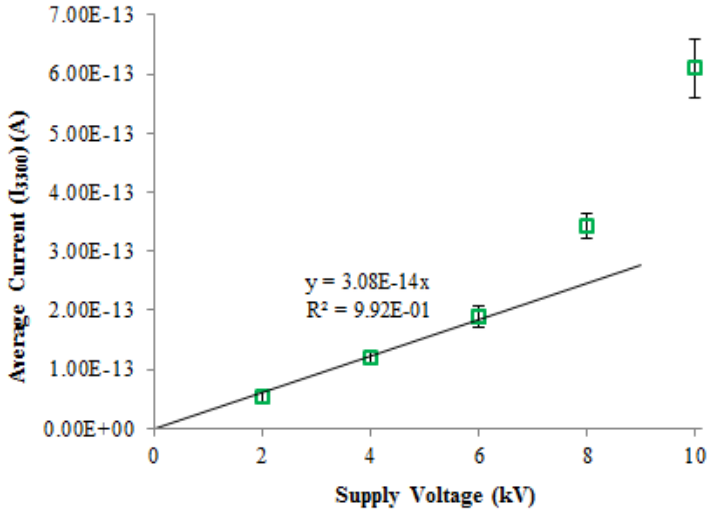

Figure 136: I_{3300} against supply voltage for untreated thin PMMA.

From figure 136 it can be seen that $\boldsymbol{I_{3300}}$ follows a linear relationship of the form of equation 89 up to ~ 6 kV after which a rapid increase in the current is observed. This behaviour is similar to that observed in the case of the thick PMMA. When analysed against a range of conductivity mechanisms it was observed that the SCLC and the Poole-Frenkel mechanism did not provide reliable fits to be considered responsible for this behaviour.

A good fit for the $\boldsymbol{I_{3300}}$ data was established against the expected Schottky and Hopping currents similar to the thick PMMA. Figure 137 shows the observation.

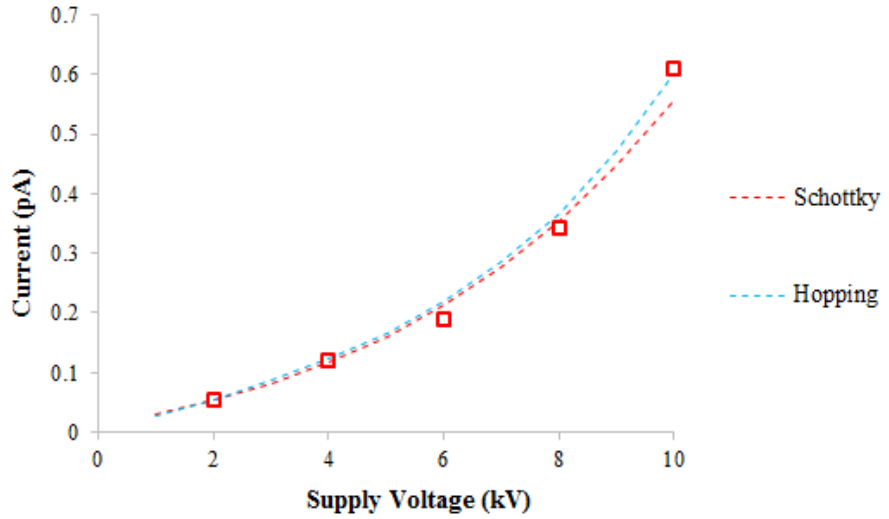

Figure 137: I_{3300} fitted against Schottky and Hopping currents for untreated thin PMMA.

6.5.1.4. Corona Treated Thin PMMA: Charging Transients

Figure 138 shows the log/log plot of the charging transients for corona treated thin PMMA using a grid voltage of 500 V. The transients were fitted with the 3 term exponential relationship taking the form of equation 88 and table 7 shows the parameter values for the fits established across the charging transients.

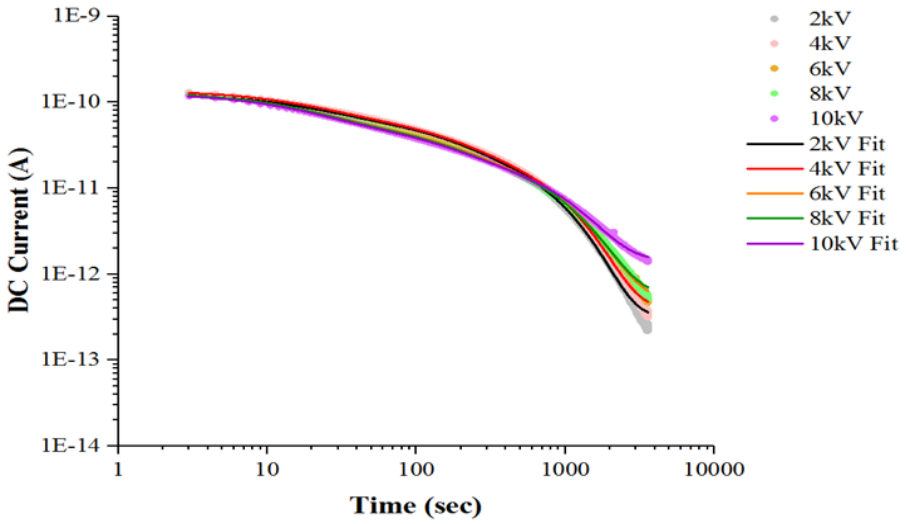

Figure 138: Log/Log plot of charging transients for corona treated thin PMMA.

Table 7: Parameters for the fittings applied to the charging transients.

Voltage (kV)	A_1 (pA)	A_2 (pA)	A_3 (pA)	τ_1 (sec)	τ_2 (sec)	τ_3 (sec)	I_{DC} (pA)	R^2
2.0	51.30	39.80	36.80	16.7	109.7	529.7	0.32	0.99
4.0	60	42.60	36.40	16.6	112.3	573.9	0.41	0.99
6.0	61.20	36.80	29.10	16.6	110.5	652.5	0.52	0.99
8.0	67.20	37.10	28.40	15.4	104.2	649.1	0.59	0.99
10.0	64.50	36.60	26.70	15.1	101.9	664.9	1.47	0.99

From table 7 it can be seen that the pre-exponential terms are significantly larger than those observed for untreated thin PMMA samples. The time constants are relatively constant over the range of supply voltages, the average values being ~ 16.1 ± 0.77 secs, ~ 108 ± 4.43 secs and ~ 614.0 ± 59.21 secs. Figure 139 shows a plot of I_{3300} against supply voltage for corona treated thin PMMA.

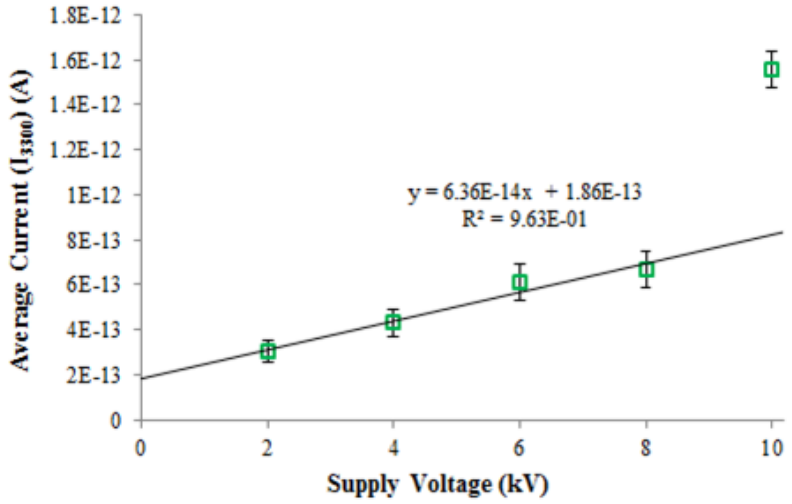

Figure 139: I_{3300} vs supply voltage for thin PMMA with prior corona charging.

From figure 139 it can be seen that $\boldsymbol{I_{3300}}$ follows a linear relationship with a constant (**C**) of the form of equation 91 up to 8 kV. After the linear regime a rapid increase is observed.

$$\boldsymbol{I = m * V + C} \tag{91}$$

The general behaviour of $\boldsymbol{I_{3300}}$ against supply voltage is again similar to the previous observations. It was again observed that the SCLC and the Poole-Frenkel mechanism did not provide reliable fits for this behaviour. When $\boldsymbol{I_{3300}}$, with the offsets removed, was plotted against the expected Schottky and Hopping currents, a good correlation was observed at supply voltage of 2 kV, 4 kV and 6 kV against these mechanisms. However at higher DC voltages the fitting was not good. Figure 140 shows this observation.

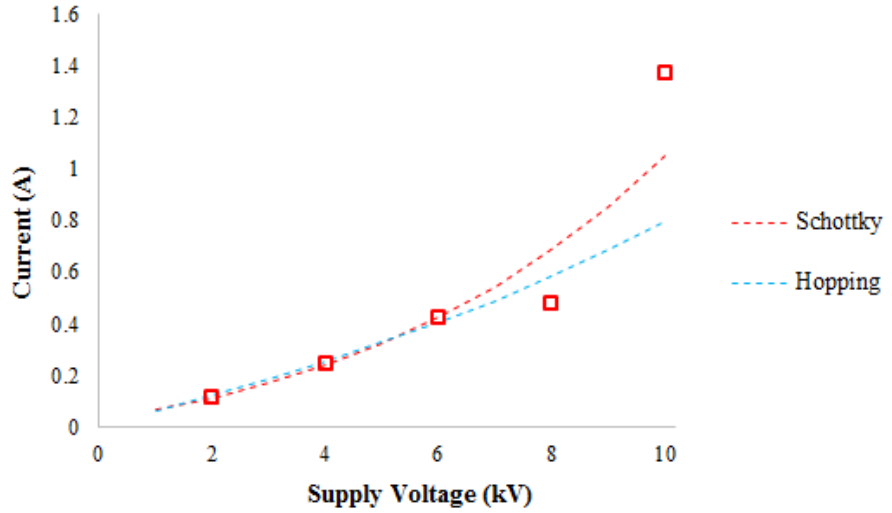

Figure 140: I_{3300} against Schottky and Hopping currents for corona treated thin PMMA.

Measurements were made to observe the effect of corona charging the sample with a higher grid voltage of 1 kV. Charging transient behaviour were observed for DC voltages of 4 kV and 8 kV. Figure 141 is a log/log plot showing a comparison of the observed charging transients for corona charged thin samples with a grid voltage of 500 V and 1 kV.

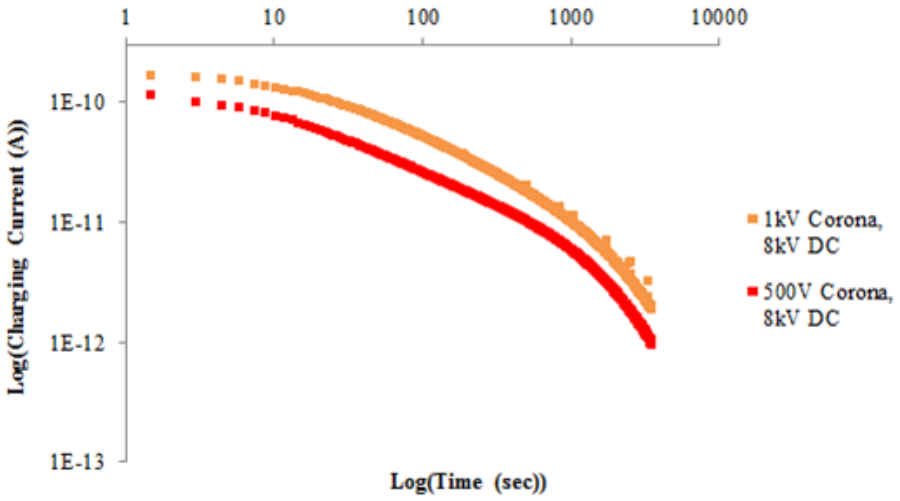

Figure 141: Charging transients for 8 kV supply voltage across corona treated thin PMMA.

It can be seen from figure 141 that again the transients for corona treated thin PMMA with higher grid voltage generally exhibit higher currents. The I_{3300} values for supply voltage of 4 kV for corona treated thin PMMA with grid voltages of 500 V and 1 kV were 0.431 ± 0.0626 pA and 1.15 ± 0.115 pA; and for supply voltage of 8 kV were 0.673 ± 0.0795 pA and 2.16 ± 0.206 pA . Figure 142 shows I_{3300} for untreated and corona treated thin PMMA.

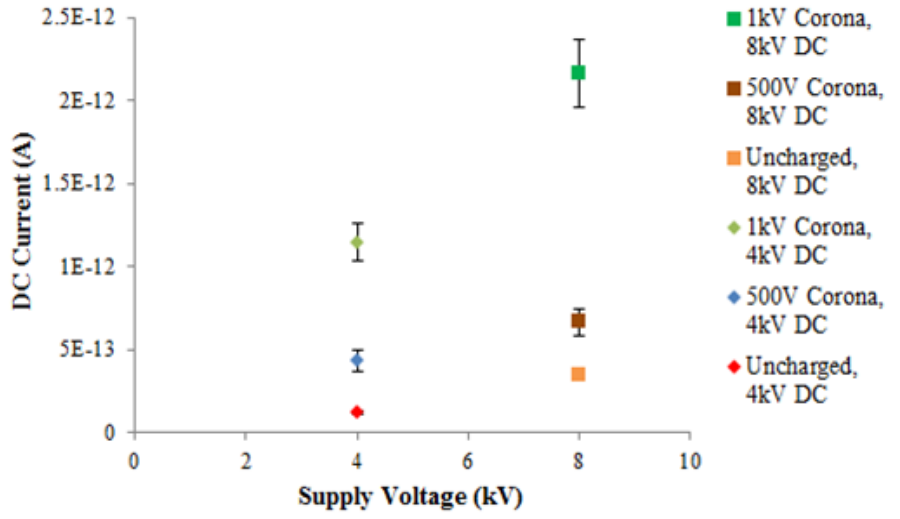

Figure 142: I_{3300} observed for supply voltages of 4 kV and 8 kV across untreated and corona treated thin PMMA with grid voltage of 500 V and 1 kV.

6.5.1.5. Discussion: Charging Transients

The discussion of the test results for charging transients is divided into two subsections. In the first (6.5.1.5.1), where the time constants obtained from the 3 term fittings without restraints are analysed and used to perform further fittings to derive meaningful conclusions. The effect of corona treatment and sample thickness on the charge decay behaviour is also analysed, along with the pre-exponential terms.

In the second (6.5.1.5.2), the approximate DC currents $\boldsymbol{I_{3300}}$ from the raw data are compared to the steady state currents $\boldsymbol{I_o}$ obtained from the new 3 term fittings applied in section 6.5.1.5.1. Comparisons are made between the steady state values for thick and thin PMMA samples under both experimental conditions. The steady state values are used to calculate the resultant surface conductivities and the mechanisms responsible for the behaviour of the steady state currents with applied voltage are further analysed.

6.5.1.5.1. Charging Transients: Transient Decay and Pre-Exponential Terms

When fitting the transients with the 3 term exponential relationship with no restrictions on the fitting parameters in subsections 6.5.1.1 to 6.5.1.4, it was observed that the time constants ($\boldsymbol{\tau_1}$, $\boldsymbol{\tau_2}$ and $\boldsymbol{\tau_3}$) for a particular sample remained reasonably constant across the supply voltage range. This was the case for both experimental conditions. As a result of this observation the time constants for each term of the exponential fitting could be presented as an averaged value across the supply voltages for a given sample under the particular test condition. Table 8 shows the averaged time constants ($\boldsymbol{\tau_1}$, $\boldsymbol{\tau_2}$ and $\boldsymbol{\tau_3}$) for thick and thin PMMA samples under the two experimental conditions.

Table 8: Averaged time constants across the voltage range for thick and thin samples under both experimental conditions.

Time Constants	Untreated Thin	Untreated Thick	Corona Treated Thin	Corona Treated Thick
$\boldsymbol{\tau_1}$	9.4 ± 1.2	16.1 ± 3.5	16.1 ± 0.8	15 ± 1.2
$\boldsymbol{\tau_2}$	73 ± 7.2	88.3 ± 4.8	108 ± 4.4	95.7 ± 12
$\boldsymbol{\tau_3}$	673 ± 29.5	869.6 ± 40.9	614 ± 59.2	916.7 ± 63.8

It can be seen that the values for $\boldsymbol{\tau_1}$ and $\boldsymbol{\tau_2}$ for untreated and corona treated PMMA are not significantly different and it is not possible to conclude if the sample thickness or the corona treatment had an impact on the decay process in the short-term and mid-term region of the transients. It can be seen that the values of $\boldsymbol{\tau_3}$ for untreated thin and corona treated thin

samples are reasonably close but significantly different from the corresponding values of the untreated thick and corona treated thick PMMA. The same observations of τ_3 are applicable for the thick PMMA.

From these observations it is proposed that τ_1 and τ_2 are constant for both samples and are not influenced by the sample thickness or the pre-existence of charge on the sample surface. Whereas, τ_3 is not influenced by the corona charging of the sample surface but is rather changed due to the sample thickness.

To validate this proposition the charging transients were fitted with the 3 term exponential fitting with common time constant values. Average values for τ_1 and τ_2 were calculated from table 8 which were used for all the fits. The value of τ_3 used for fitting the transients for untreated and corona treated thin samples was calculated by averaging the τ_3 values for the untreated and corona treated thin samples from table 8. The value of τ_3 used for fitting the transients for untreated and corona treated thick samples was calculated by averaging the τ_3 values for the untreated and corona treated thick samples from table 8. Table 9 shows the time constants used to fit the charging transients.

Table 9: Fixed time constants for the 3 term exponential fits to the charging transients.

Sample	τ_1 (sec)	τ_2 (sec)	τ_3 (sec)
Thin	14.1	91.2	643
Thick	14.1	91.2	893

It was possible to obtain good fits across all charging transients by using the fixed time constants. This observation supports the proposition that common time constants exist for the current transients observed.

It is proposed that the shortest time constant τ_1 is associated with the development of an initial charge distribution close to the cathode. This is likely to be controlled by Schottky type emission of the electrons from the electrode into the surface of the samples. The rate at which this charge distribution changes and therefore the current changes, will be controlled by the local electric field near the electrode, which is reduced as the charge is transferred to the polymer sample.

The time constant τ_2, is associated with the motion of the charge across the surface of the polymer, probably associated with the hopping mechanism. This transient is associated with the time for charge carriers originating from the cathode to reach the anode. The motion of

these charge carriers will occur in a region of relatively high electric field, as the negatively charged electrons approach the anode.

Once the charge carriers have reached the anode, there will be no regions of significantly higher electric field, though a field profile will exist across the sample surface. At equilibrium at the end of the transient process, the gradient of the current density must be zero ($\boldsymbol{\nabla J = 0}$). The conductivity or the mobility of the carriers will be field dependent. The motion of the carriers in the final transient process is thought to be due to the hopping mechanism. The time constant $\boldsymbol{\tau_3}$, reflects the establishment of an equilibrium charge distribution to satisfy the condition where the gradient of the current density is equal to zero.

The fits for untreated thin PMMA are shown in figure 143 and table 10 shows the pre-exponential currents, the DC steady state currents $\boldsymbol{I_o}$ and the coefficient of determination $\boldsymbol{R^2}$ obtained from these fits.

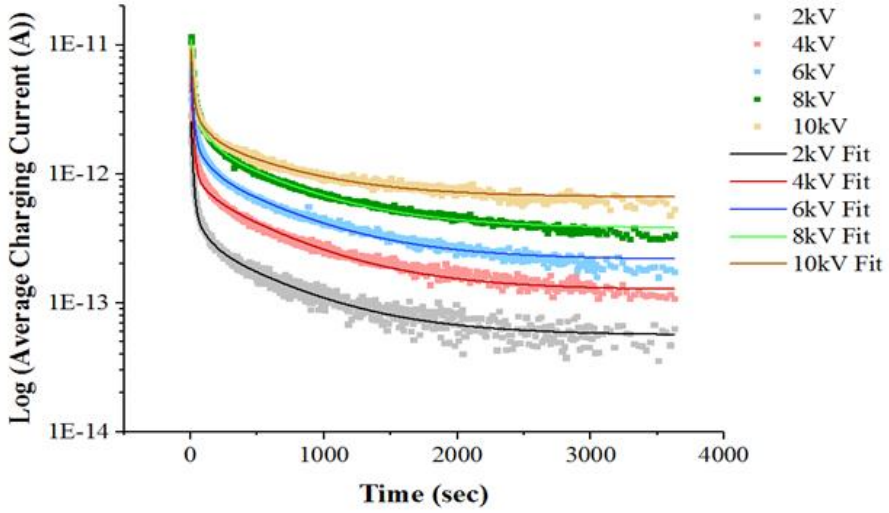

Figure 143: Log (Average Charging Current (A)) against Time (sec) plot of 3 term fitting applied to charging transients for untreated thin PMMA with fixed time constants.

Table 10: Pre-exponential, DC current and R^2 values from the 3 term fittings with fixed time constants across charging transients for untreated thin PMMA.

Voltage (kV)	A_1 (A)	A_2 (A)	A_3 (A)	I_o (A)	R^2
2.0	2.44E-12	2.41E-13	2.52E-13	5.62E-14	0.99
4.0	5.57E-12	3.55E-13	6.32E-13	1.26E-13	0.98
6.0	6.53E-12	8.83E-13	9.40E-13	2.17E-13	0.99
8.0	9.26E-12	1.77E-12	1.43E-12	3.79E-13	0.99
10.0	7.16E-12	1.40E-12	1.38E-12	6.61E-13	0.99

The pre-exponential terms from table 10 show a general rising trend up to 8 kV. Figure 144 shows the fits across the corona treated thin PMMA using fixed time constants and table 11 shows the pre-exponential currents, the DC current I_o and the coefficient of determination R^2 obtained from these fits.

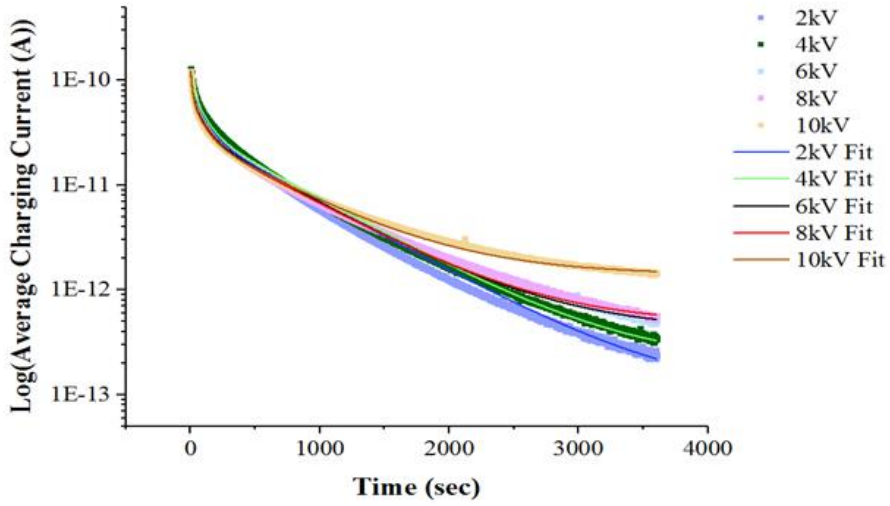

Figure 144: Log (Average Charging Current (A)) against Time (sec) plot of 3 term fitting applied to charging transients for corona treated thin PMMA with fixed time constants.

Table 11: Pre-exponential, DC current and R^2 values from the 3 term fittings with fixed time constants across charging transients for corona treated thin PMMA.

Voltage (kV)	A_1	A_2	A_3	I_o	R^2
2.0	3.83E-11	5.53E-11	3.25E-11	1E-13	0.99
4.0	4.91E-11	5.47E-11	3.47E-11	2E-13	0.99
6.0	5.72E-11	4.15E-11	3.06E-11	4.10E-13	0.99
8.0	6.43E-11	4E-11	2.96E-11	4.70E-13	0.99
10.0	6.30E-11	3.79E-11	2.80E-11	1.40E-12	0.99

The pre-exponential term A_1 follows the rising trend observed for the untreated thin PMMA up to a supply voltage of 8 kV. However, pre-exponentials A_2 and A_3 associated with the mid-term and the long-term behaviour for the corona treated thin PMMA do not follow this rising trend and exhibit a somewhat decreasing trend. This is also reflected by the noticeable change in the transient behaviour of the corona treated thin PMMA from 200 sec through to the end of the transient.

It is also clear that the pre-exponentials for corona treated thin PMMA are significantly larger than the untreated thin PMMA. This is expected as the availability of the excess charge carriers on the surface of the polymer would lead to higher currents which is evident by observing the resultant DC values. The DC current components are higher for the corona treated thin PMMA compared to the untreated thin PMMA.

Figure 145 shows the fits for the untreated thick PMMA using fixed time constants and table 12 shows the pre-exponential currents, the DC current I_o and the coefficient of determination R^2 obtained from these fits.

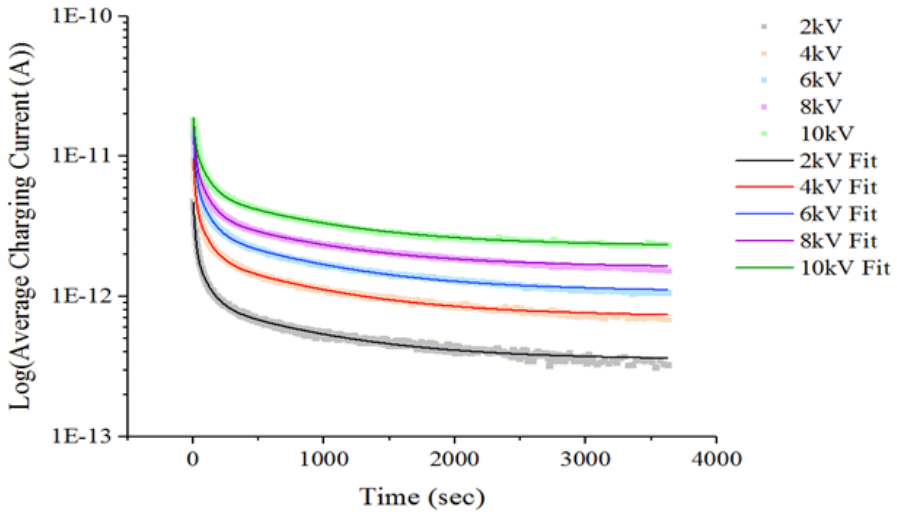

Figure 145: Log (Average Charging Current (A)) against Time (sec) plot of 3 term fitting applied to charging transients for untreated thick PMMA with fixed time constants.

Table 12: Pre-exponential, DC current and R^2 values from the 3 term fittings with fixed time constants across charging transients for untreated thick PMMA.

Voltage (kV)	A_1	A_2	A_3	I_o	R^2
2.0	3.08E-12	1.30E-12	5.64E-13	3.55E-13	0.99
4.0	6.24E-12	2.72E-12	1.22E-12	7.23E-13	0.99
6.0	9.76E-12	4.22E-12	1.84E-12	1.09E-12	0.99
8.0	1.13E-11	5.54E-12	2.21E-12	1.62E-12	0.99
10.0	8.70E-12	6.65E-12	3.19E-12	2.30E-12	0.99

The pre-exponential terms from table 12 show a general rising trend. A_1 exhibits a rising trend up to 8 kV, whereas, A_2 and A_3 follow a rising trend up to 10 kV.

Figure 146 shows the fits across the corona treated thick PMMA using fixed time constants and table 13 shows the pre-exponential currents, the DC current I_o and the coefficient of determination R^2 obtained from these fits.

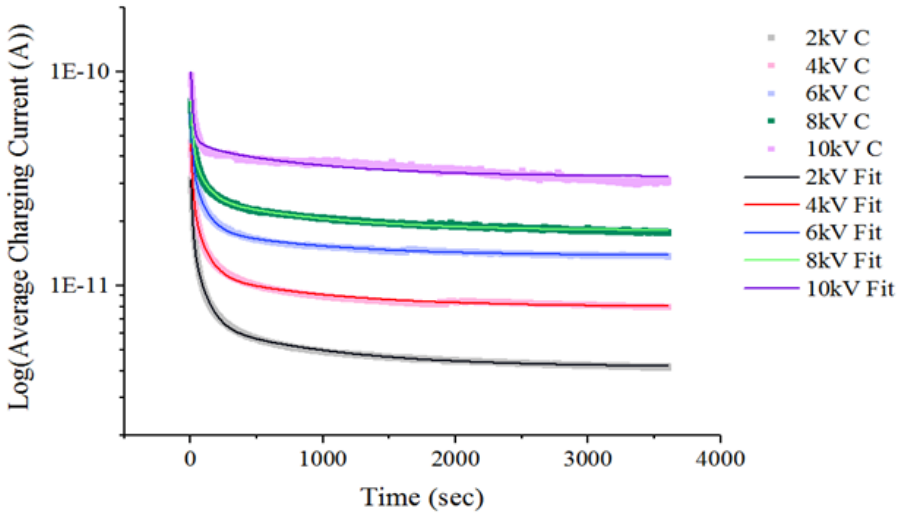

Figure 146: Log (Average Charging Current (A)) against Time (sec) plot of 3 term fitting applied to charging transients for corona treated thick PMMA with fixed time constants.

Table 13: Pre-exponential, DC current and R^2 values from the 3 term fittings with fixed time constants across charging transients for corona treated thick PMMA.

Voltage (kV)	A_1	A_2	A_3	I_o	R^2
2.0	1.86E-11	9.80E-12	2.49E-12	4.19E-12	0.99932
4.0	2.62E-11	1.35E-11	3.38E-12	7.99E-12	0.99765
6.0	3.60E-11	1.73E-11	4.61E-12	1.38E-11	0.99888
8.0	3.66E-11	1.76E-11	7.77E-12	1.81E-11	0.99758
10.0	6.10E-11	5.14E-12	1.28E-11	3.23E-11	0.93753

It was again evident that the pre-exponential terms exhibit a general rising trend. Also again visible is that the pre-exponentials for corona treated thick PMMA are significantly larger than the untreated thick PMMA. The DC current components were also again observed to be higher for the corona treated thick PMMA compared to the untreated thick PMMA.

It was observed that the pre-exponential terms for the untreated thick PMMA were larger than the untreated thin PMMA. This was also reflected by the larger values observed for the DC currents I_o for the untreated thick PMMA compared to the untreated thin PMMA. However, on the contrary, the pre-exponential terms for the corona treated thin PMMA were observed to be larger than those for the corona treated thick PMMA.

6.5.1.5.2. Charging Transients: DC Currents and Surface Conductivities

The predicted DC currents I_o from the fittings with fixed time constants were compared to the I_{3300} from the raw data. I_{3300} was reasonably similar to I_o. Figure 147 shows a comparison of I_o and I_{3300} for untreated thin PMMA and table 14 show the comparison of I_{3300} and I_o for the untreated and corona treated thin and thick PMMA.

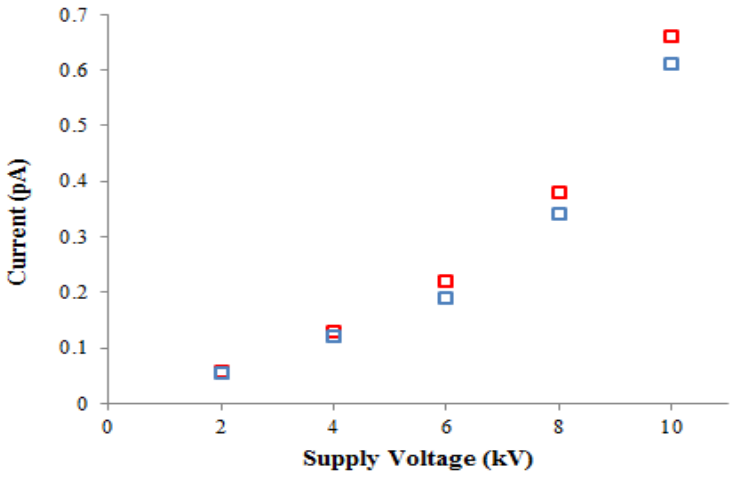

Figure 147: Comparison of I_{3300} □ and I_o □ for untreated thin PMMA.

Table 14: I_{3300} and I_o for untreated and corona treated PMMA samples.

Supply Voltage (kV)	Untreated Thin (pA)		Untreated Thick (pA)		Corona Treated Thin (pA)		Corona Treated Thick (pA)	
	I_{3300}	I_o	I_{3300}	I_o	I_{3300}	I_o	I_{3300}	I_o
2.0	0.055 ± 0.0093	0.056	0.35 ± 0.017	0.36	0.12 ± 0.046	0.10	4.23 ± 0.029	4.20
4.0	0.12 ± 0.0090	0.13	0.72 ± 0.019	0.72	0.25 ± 0.063	0.20	8.07 ± 0.053	8
6.0	0.19 ± 0.017	0.22	1.10 ± 0.020	1.09	0.43 ± 0.081	0.41	14 ± 0.056	13.8
8.0	0.34 ± 0.021	0.38	1.60 ± 0.034	1.62	0.48 ± 0.080	0.47	18 ± 0.14	18.1
10.0	0.61 ± 0.049	0.66	2.37 ± 0.035	2.30	1.37 ± 0.081	1.40	31 ± 0.42	32.3

The behaviours of I_{3300} and I_o for both thick and thin PMMA samples were similar and, as I_{3300} and I_o were reasonably similar, it was deemed reasonable to compare the DC behaviours for thick and thin samples using plots of I_{3300}.

As stated in subsection 6.5.1.1, it was observed that the DC currents across corona treated thin and thick samples were higher than those for the untreated thin and thick samples. It was observed that the DC currents across the corona treated thin samples were ~ 2 times higher than for the untreated thin samples and the DC currents across the corona treated thick samples were ~ 12 times higher than for the untreated thick samples.

The increase in the measured DC currents after treating the samples with corona is thought to be as a result of excess of charge carriers being present on the surface of the polymers due to corona charging. The excess charge carriers will contribute to the current being measured, and it is expected that if the charging transients were measured for longer periods of time, then the excess charge would decay away and the measured DC currents would be similar to those for untreated samples. As repeated measurements were performed and the resulting transient behaviours were observed to be similar for each repeated measurement for corona treated samples, it is assumed that the corona charging of the materials does not change the surface properties of the samples, and this supports the suggestion that the increase in the DC currents is not due to a change in mobility of the carriers but rather due to the presence of excess charge on the surface.

Figure 148 shows the observed DC currents across the untreated and corona treated thin samples and figure 149 shows the observed DC currents across the untreated and corona treated thick samples.

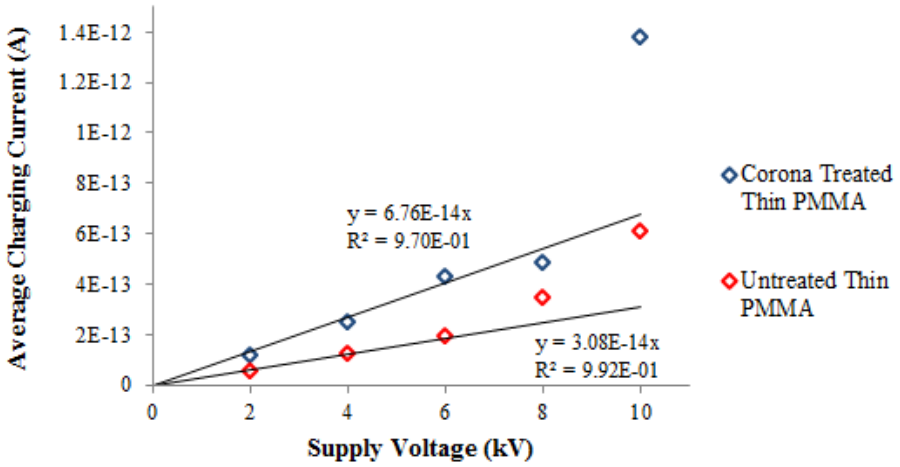

Figure 148: I_{3300} across untreated and corona treated thin PMMA against supply voltage.

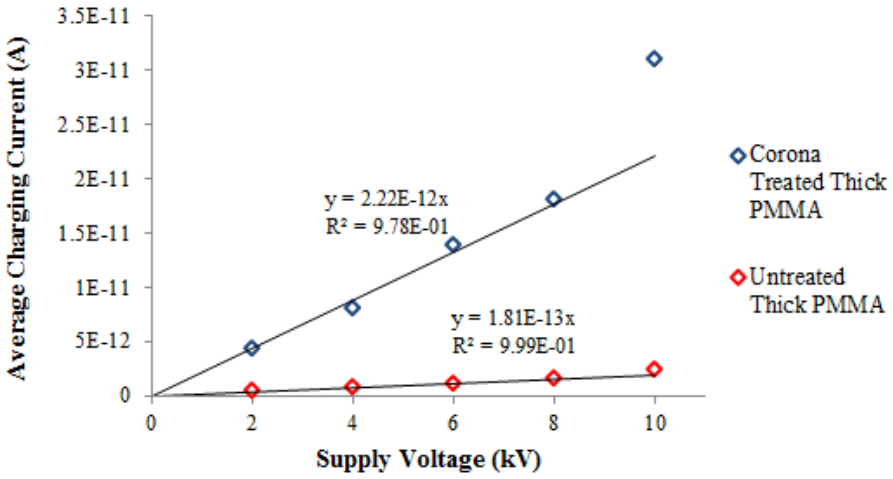

Figure 149: I_{3300} across untreated and corona treated thick PMMA against supply voltage.

When comparing $\boldsymbol{I_{3300}}$ for untreated thick and thin PMMA, similar behaviours were observed for both sample types, where the currents increased linearly with supply voltage following the relationship of equation 89 up to ~ 6 kV, which was followed by a rapid increase in the current. It was also observed that $\boldsymbol{I_{3300}}$ was on average ~ 6 times greater for untreated thick PMMA compared to the untreated thin PMMA across the range of supply voltages. $\boldsymbol{I_{3300}}$ for untreated thick and thin PMMA are shown in figure 150.

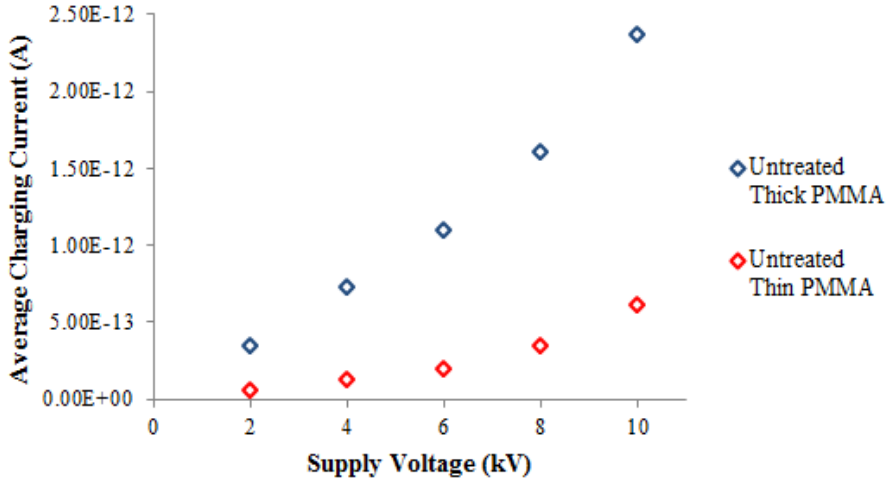

Figure 150: I_{3300} across untreated thick and thin PMMA with supply voltage.

Similar behaviours of DC currents were observed for the corona treated thick and thin PMMA. The currents increased linearly with supply voltage following the relationship of equation 89 up to ~ 8 kV which was followed by a rapid increase in the current. In this case a

more significant increase in the DC current was observed across the corona charged thick PMMA. I_{3300} was on average ~ 30 times greater for corona treated thick PMMA compared to the corona treated thin PMMA. I_{3300} for corona treated thick and thin PMMA are shown in figure 151.

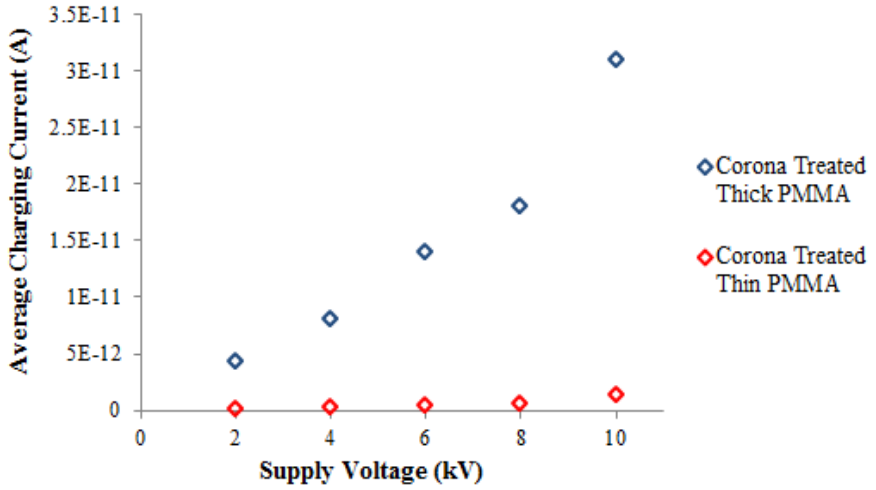

Figure 151: I_{3300}across untreated thick and thin PMMA with supply voltage.

The resultant surface conductivities are calculated using the I_{3300} values from table 14. It is observed that the surface conductivities tend to follow the behaviour of the DC currents and that in general the surface conductivity of the samples is enhanced by corona treatment of the samples. As in the case of the DC current behaviour it was observed that the surface conductivities for the untreated and corona treated thick PMMA were greater than the untreated and corona treated thin PMMA. Table 15 shows the surface conductivities.

Table 15: Resultant surface conductivities calculated from the I_{3300} values from table 14.

Supply Voltage (kV)	Untreated Thin PMMA Surface Conductivity (S)	Untreated Thick PMMA Surface Conductivity (S)	Corona Treated Thin PMMA Surface Conductivity (S)	Corona Treated Thick PMMA Surface Conductivity (S)
2.0	3.85E-18	2.43E-17	8.27E-18	2.96E-16
4.0	4.22E-18	2.53E-17	8.59E-18	2.83E-16
6.0	4.41E-18	2.54E-17	1E-17	3.25E-16
8.0	6.01E-18	2.81E-17	8.43E-18	3.16E-16
10.0	8.54E-18	3.32E-17	1.93E-17	4.35E-16

Figure 152 and 153 show the surface conductivity behaviours for untreated thick and thin samples and the corona treated thick and thin samples.

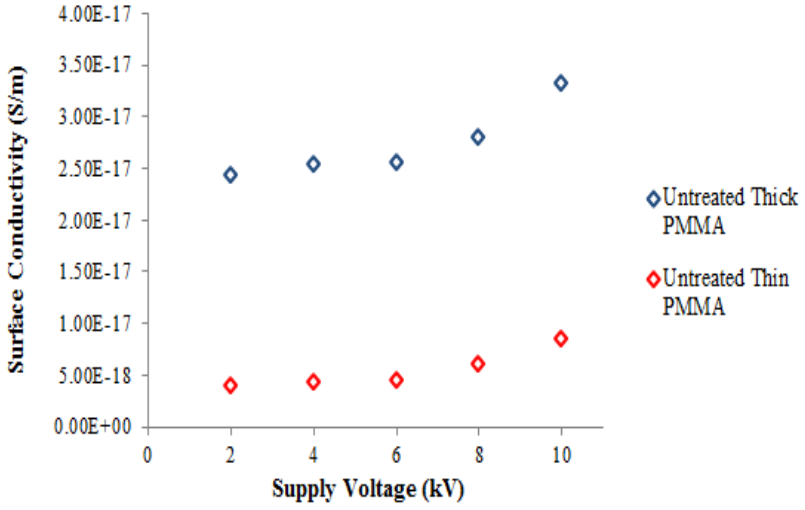

Figure 152: Surface conductivities calculated from the I_{3300} values for untreated thick and thin PMMA samples.

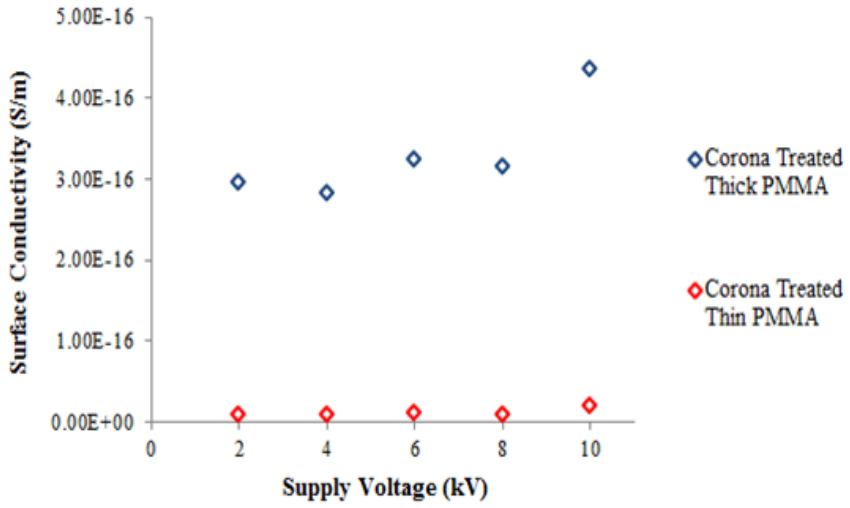

Figure 153: Surface conductivities calculated from the I_{3300} values for corona treated thick and thin PMMA samples.

In sections 6.5.1.1-6.5.1.4, the behaviour of the DC currents for both samples was analysed against 4 different conduction mechanisms. It was established that the SCLC and the Poole-Frenkel mechanism were not responsible for the behaviour of the DC currents. The behaviour fitted well with the expected Schottky and Hopping currents.

As both these conduction mechanisms provided respectable fits for the DC behaviour, it was not possible to highlight one particular conduction mechanism that was responsible for the behaviour within the supply voltage range of the measurements. However, if transient measurements were made over a broader supply voltage range it would be possible to distinguish between the mechanisms as at higher voltages a clear deviation is observed between the predicted Schottky and Hopping currents. Figure 154 provides an example where DC currents $\boldsymbol{I_{3300}}$ across corona treated thick PMMA are plotted against the expected Schottky and Hopping currents between an extended supply voltage range of 1 kV to 20 kV.

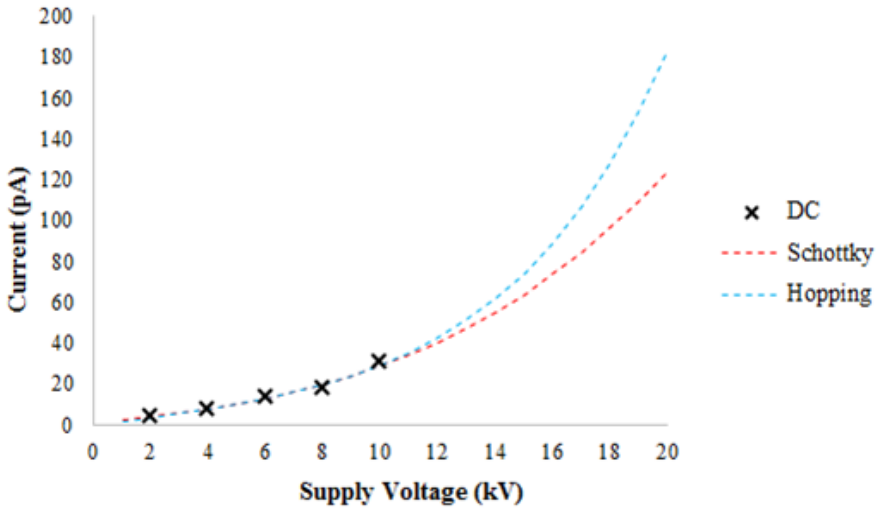

Figure 154: Example showing deviation between Hopping and Schottky currents.

Figure 154 shows a clear separation between the calculated currents from Schottky and Hopping mechanisms at higher voltages > 10 kV. However, measurements are made only up to 10 kV in this project which limits the ability to identify a particular charging mechanism.

Table 16 shows the parameters used to calculate the expected Schottky and Hopping currents for the untreated and corona treated, thin and thick PMMA.

Table 16: Parameters used to calculate Schottky and Hopping currents across untreated and corona treated thin and thick samples.

Sample Condition	α	β	A	B
Untreated Thin	-4.843	1.347	0.110	0.240
Untreated Thick	-2.533	1.070	1.050	0.155
Corona treated Thin	-3.985	1.275	0.470	0.130
Corona treated Thick	-0.122	1.105	10.0	0.180

The parameters **α** and **β** come from the Schottky relationship in equation 92.

$$I_{Schottky} = \alpha * exp(\beta V^{\frac{1}{2}}) \quad (92)$$

The parameters **A** and **B** come from the Hopping relationship in equation 93.

$$I_{Hopping} = A * sinh(BV) \quad (93)$$

6.5.2. Discharging Transient: Results and Analysis

The discharging transient test results and the analysis for tests conducted under both experimental conditions are presented below.

6.5.2.1. Untreated Thick PMMA: Discharging Transients

For the discharging transients it is expected that at longer times the currents decay to zero. The transients were initially fitted with a 3 term exponential expression with the assumption that the current at long times was zero. It was apparent, however, that there was an additional transient process occurring at longer times. As with the charging transients, a fit of the form of $\boldsymbol{At^{-n}}$ was also attempted but the quality of the fit was poor. An additional exponential term was therefore added to the fit, equation 94.

$$\boldsymbol{I(t) = A_1 Exp\left(-\frac{t}{\tau 1}\right) + A_2 Exp\left(-\frac{t}{\tau 2}\right) + A_3 Exp\left(-\frac{t}{\tau 3}\right) + A_4 Exp\left(-\frac{t}{\tau 4}\right)} \quad (94)$$

Figure 155 shows the discharging transients for the untreated thick PMMA fitted to the 4 term exponential function with no restrictions to the fitting parameters and table 17 shows the parameter values for the fits.

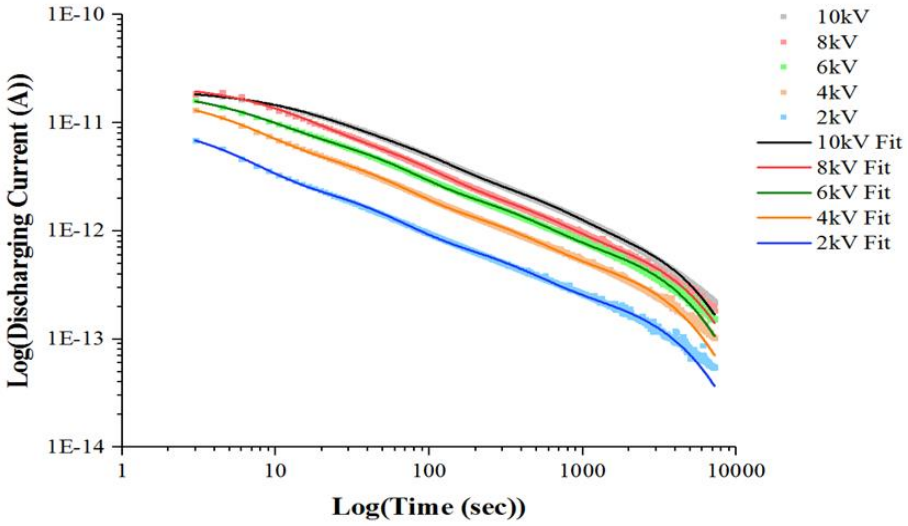

Figure 155: Discharging transients for untreated thick PMMA fitted to 4 term exponential.

Table 17: Parameters for 4 term exponential fitting to discharging transients for untreated thick PMMA.

Voltage (kV)	A_1 (pA)	A_2 (pA)	A_3 (pA)	A_4 (pA)	τ_1 (sec)	τ_2 (sec)	τ_3 (sec)	τ_4 (sec)	R^2
2.0	7.90	2.26	0.68	0.32	4.1	35.8	278	3340	0.99
4.0	12.8	4.58	1.38	0.66	4.8	38.3	286	3240	0.99
6.0	11.9	6.26	1.95	0.95	5.9	42	304	3290	0.99
8.0	14	6.42	2.01	1.04	10	59.9	385	3600	0.99
10.0	9.68	6.96	2.50	1.34	14.1	69.7	436	3470	0.99

It can be seen from figure 155 that at very long times i.e. beyond 3500 secs, the fitting falls below the transient. This indicates that a further much slower decay process might be taking place. However, the time over which the data was recorded is too short to allow this behaviour to be fitted.

Figure 156 shows the predicted current decay (A) for each of the 4 exponential terms of the fitting relationship for a discharge transient at 6 kV. It can be seen that the slowest transient decay process is still leading to changes in the current which prevents data on any longer processes from being extracted.

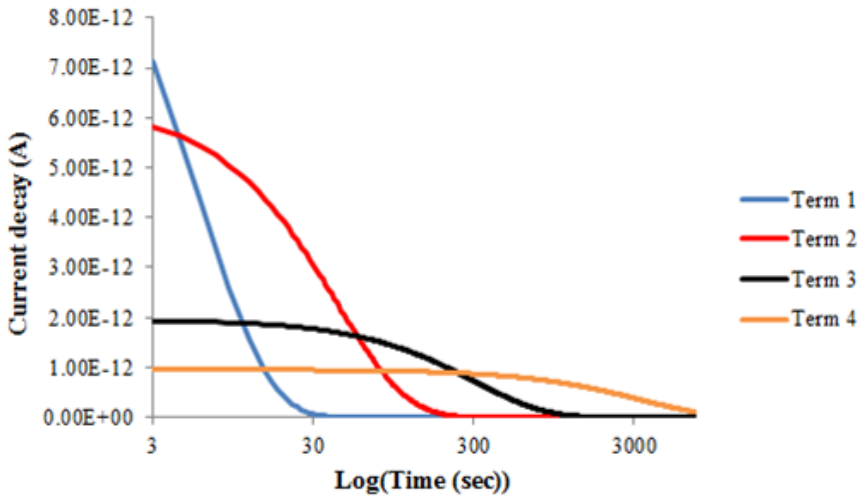

Figure 156: Current decay (A) against log of time (sec) for discharging transients for untreated thick PMMA across the 4 exponential terms.

For the response of the system to be considered linear it is expected that the time constants associated with the discharging transients would be similar to the charging transients. To

compare the time constants of the discharging transients impartially against the charging transients, the discharging transients were fitted with a 3 term exponential fitting function as that used for the charging transients taking the form of equation 88 for the first 1 hour of measurement. It was assumed that any changes in the current at long times due to the slower processes could be reasonably modelled by a DC component over this time period. The parameters of the fitting function were kept floating and not set to any value.

Figure 157 shows the discharging transients fitted with the 3 term exponential function and table 18 shows the parameter values for the fits.

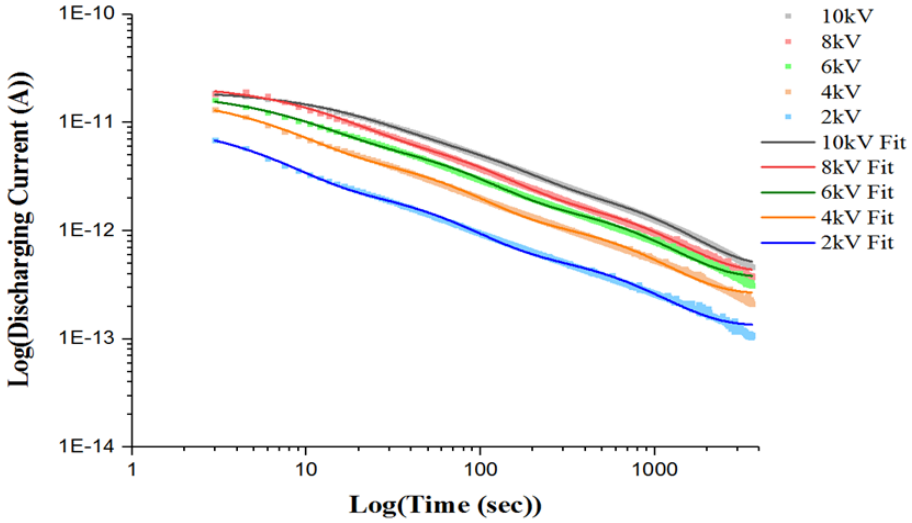

Figure 157: Discharging transients for untreated thick PMMA fitted to a 3 term exponential.

Table 18: Parameters for the 3 term exponential fitting applied to untreated thick PMMA.

Voltage (kV)	A_1 (pA)	A_2 (pA)	A_3 (pA)	τ_1 (sec)	τ_2 (sec)	τ_3 (sec)	I_o (pA)	R^2
2.0	7.65	2.09	0.57	4.9	52.6	669	0.13	0.99
4.0	12.60	4.18	1.17	5.8	56.8	695	0.26	0.99
6.0	12.10	5.47	1.66	7.9	65.5	750	0.37	0.99
8.0	14.70	6.06	1.89	11.2	80.1	817	0.41	0.99
10.0	11	6.10	2.42	17.5	102	930	0.47	0.99

In figure 158 the time constants τ_1, τ_2 and τ_3 observed from the 3 term fittings across the charging transients for the untreated thick PMMA are compared with the time constants τ_1, τ_2 and τ_3 observed from the 3 term fitting applied across the first hour of the discharge measurement data for the untreated thick PMMA and the time constants τ_1, τ_2 and τ_3

observed for the 4 term fitting applied to the complete 2 hours of the discharge measurement data for the untreated thick PMMA.

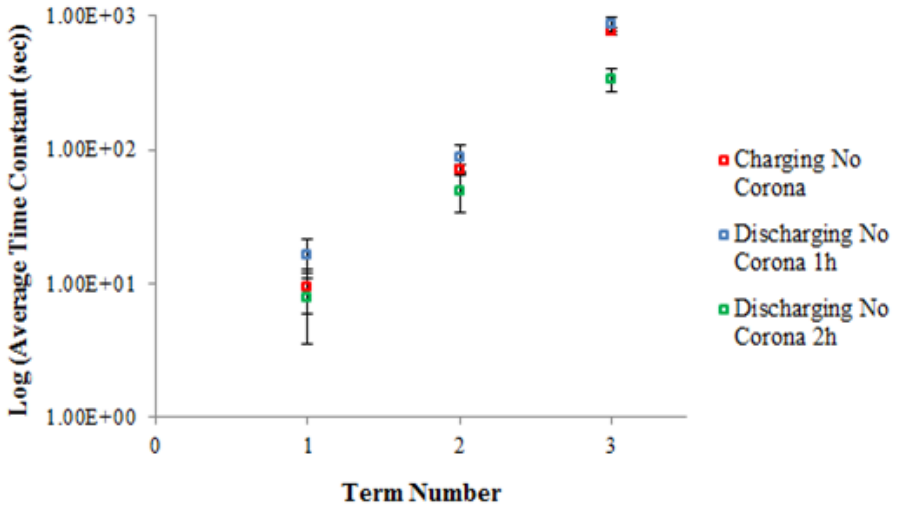

Figure 158: Log of average time constant for charging transients fitted to 3 term exponential and discharging transients fitted to 3 term and 4 term exponential fits for untreated thick PMMA.

It can be seen from figure 158 that the time constants for the discharging transients fitted with the 3 term exponential function for the first hour of the measurement are reasonably comparable to the time constants measured for charging transients. However, a more noticeable separation in the time constants between the charging transients and the discharging transients fitted with a 4 term exponential over 2 hours can be observed.

6.5.2.2. Corona Treated Thick PMMA: Discharging Transients

Figure 159 shows the discharging transients for the corona treated thick PMMA fitted to the 4 term exponential function with no restrictions to the fitting parameters and table 19 shows the parameter values for the fits.

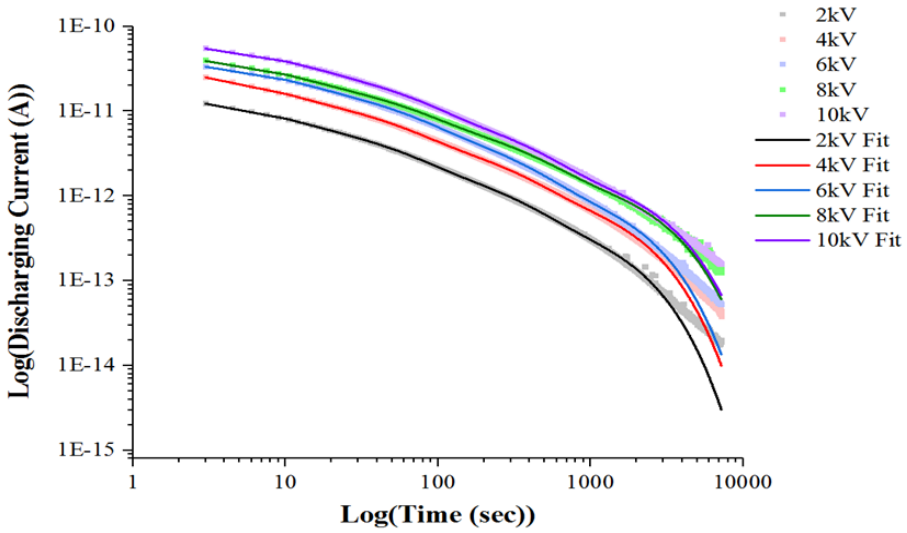

Figure 159: Discharging transients for corona treated thick PMMA fitted to a 4 term exponential function.

Table 19: Parameters for 4 term exponential fitting to discharging transients for corona treated thick PMMA using a grid voltage of 500V.

Voltage (kV)	A_1 (pA)	A_2 (pA)	A_3 (pA)	A_4 (pA)	τ_1 (sec)	τ_2 (sec)	τ_3 (sec)	τ_4 (sec)	R^2
2.0	7.74	5.31	1.93	0.59	6.4	39.4	219	1360	0.99
4.0	17.3	10.5	3.89	1.22	5.7	38.1	220	1500	0.99
6.0	19.5	14.3	5.48	1.48	7.7	44.5	235	1530	0.99
8.0	24.2	16.9	6.26	1.97	7.4	46.2	273	2070	0.99
10.0	32.0	23.3	8.20	2.17	8.4	48.4	275	2080	0.99

As with the untreated thick PMMA it can be seen from figure 159 that again at long times, further slower decay processes may be taking place. Figure 160 shows the discharging transients fitted with the 3 term exponential of the form of equation 88 for the first hour of measurement and table 20 shows the parameter values for the fits.

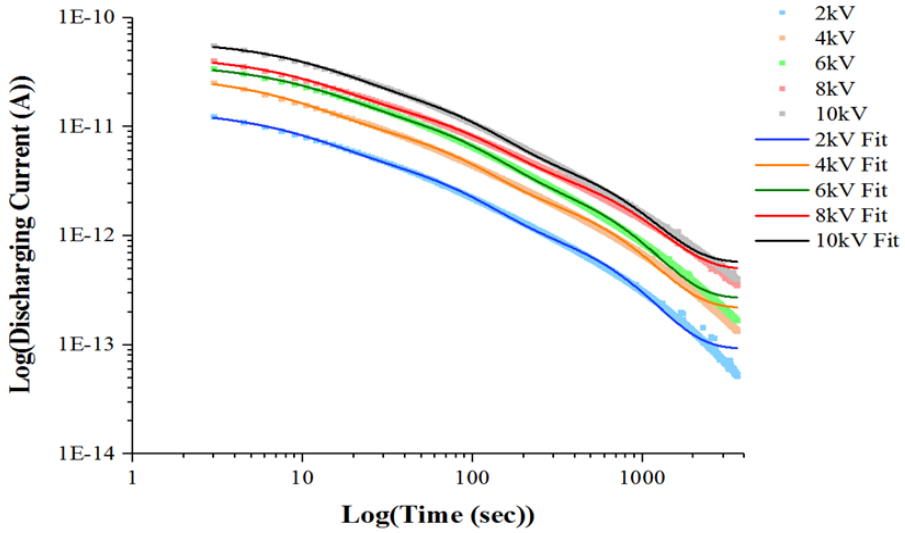

Figure 160: Log plot of discharging transients for corona treated thick PMMA fitted to a 3 term exponential function.

Table 20: Parameters for 3 term exponential fitting to discharging transients for corona treated thick PMMA.

Voltage (kV)	A_1(pA)	A_2(pA)	A_3(pA)	τ_1(sec)	τ_2(sec)	τ_3(sec)	I_o(pA)	R^2
2.0	8.40	4.80	1.41	9	63.8	528	0.090	0.99
4.0	18.10	9.50	2.82	8.1	63	546	0.22	0.99
6.0	22	13.10	3.83	10.6	71.3	538	0.27	0.99
8.0	26.30	14.30	4.70	10.2	75.4	621	0.49	0.99
10.0	35.40	21.10	6.07	11.1	72.6	566	0.57	0.99

In figure 161 the time constants τ_1, τ_2 and τ_3 observed from the 3 term fittings across the charging transients for the corona treated thick PMMA are compared with the time constants τ_1, τ_2 and τ_3 observed from the 3 term fitting applied across the first hour of the discharge measurement data for the corona treated thick PMMA and the time constants τ_1, τ_2 and τ_3 observed for the 4 term fitting applied to the complete 2 hours of the discharge measurement data for the corona treated thick PMMA. It can be seen that the time constants for the discharging transients with the 3 term exponential fitting are comparable to the time constants measured for charging transients. However, a more noticeable separation in the time constants between the charging transients and the discharging transients fitted with a 4 term exponential over 2 hours can be observed.

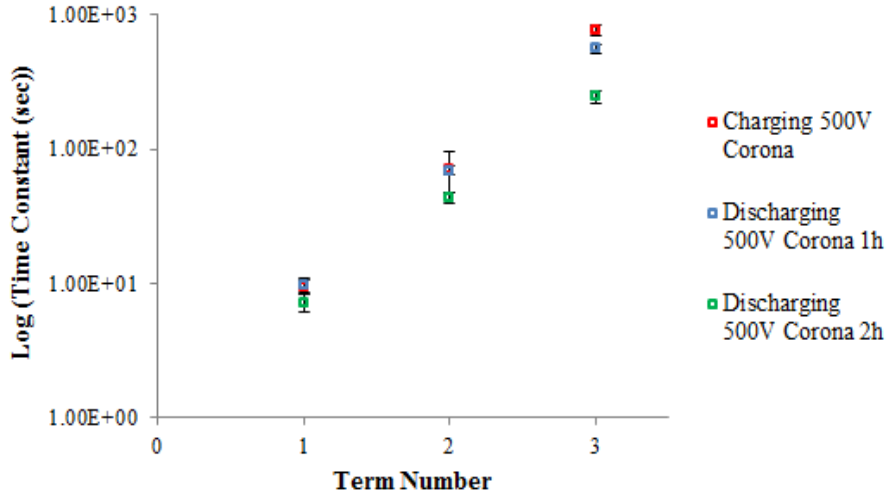

Figure 161: Log of average time constant for charging and discharging transients.

6.5.2.3. Untreated Thin PMMA: Discharging Transients

Figure 162 shows the discharging transients for untreated thin PMMA fitted to the 4 term exponential function and table 21 shows the parameter values for the fits.

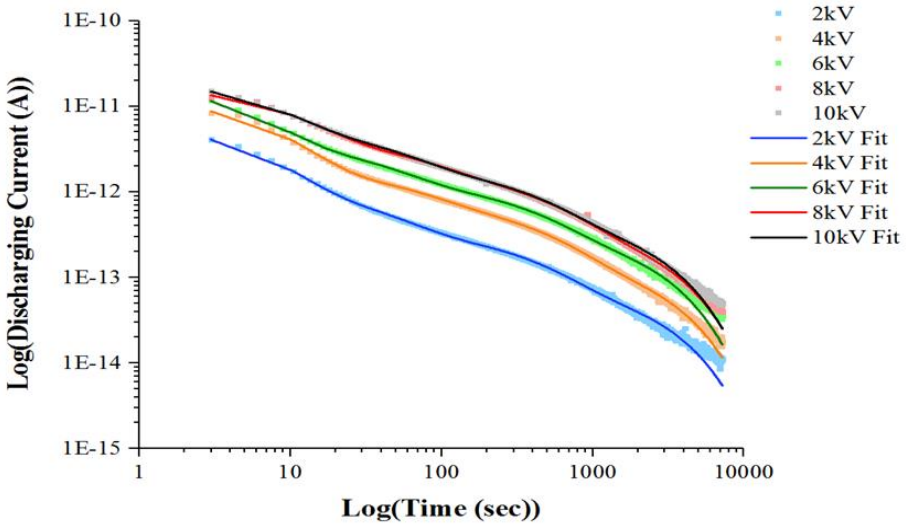

Figure 162: Discharging transients for untreated thin PMMA fitted to a 4 term exponential.

Table 21: Parameters for 4 term exponential fitting to discharging transients for untreated thin PMMA.

Voltage (kV)	A_1 (pA)	A_2 (pA)	A_3 (pA)	A_4 (pA)	τ_1 (sec)	τ_2 (sec)	τ_3 (sec)	τ_4 (sec)	R^2
2.0	5.09	0.79	0.27	0.080	5.7	35.2	353	2674	0.99
4.0	10.90	1.12	0.60	0.17	6.7	55.6	402	2672	0.99
6.0	14.90	2.58	0.96	0.34	4.7	35.6	336	2371	0.99
8.0	13.20	2.46	1.34	0.42	8.7	63.6	418	2570	0.99
10.0	15.10	3.84	1.47	0.51	6.2	41.7	350	2397	0.99

As with the thick PMMA it can be seen from figure 162 that again at long times, further slower decay processes may be taking place.

Figure 163 shows the discharging transients fitted with the 3 term exponential of the form of equation 88 for the first hour of measurement and table 22 shows the parameter values for the fits.

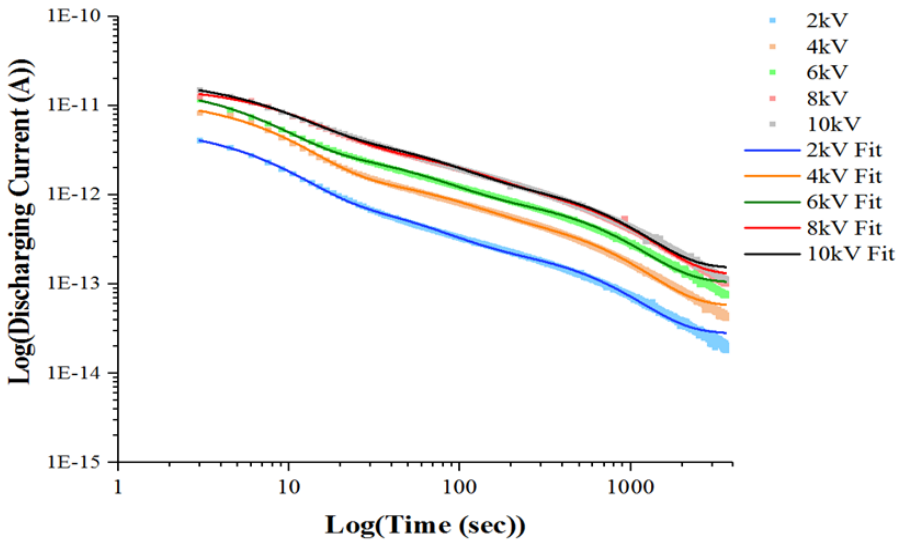

Figure 163: Discharging transients for untreated thin PMMA fitted to 3 term exponential.

Table 22: Parameters for the 3 term exponential fitting to the discharging transients for thin PMMA.

Voltage (kV)	A_1(pA)	A_2(pA)	A_3(pA)	τ_1(sec)	τ_2(sec)	τ_3(sec)	I_o(pA)	R^2
2.0	5.13	0.71	0.26	6	46.6	565	0.03	0.99
4.0	10.90	1.13	0.60	6.8	69.5	606	0.06	0.99
6.0	14.80	2.34	0.95	5.1	49.5	591	0.10	0.99
8.0	13.40	2.49	1.32	9.1	81.7	661	0.13	0.99
10.0	15.30	3.49	1.43	6.9	57.8	611	0.15	0.99

In figure 164 the time constants τ_1, τ_2 and τ_3 observed from the 3 term fittings across the charging transients for the untreated thin PMMA are compared with the time constants τ_1, τ_2 and τ_3 observed from the 3 term fitting applied across the first hour of the discharge measurement data for the untreated thin PMMA and the time constants τ_1, τ_2 and τ_3 observed for the 4 term fitting applied to the complete 2 hours of the discharge measurement data for the untreated thin PMMA. It can be seen that the time constants for the discharging transients with the 3 term exponential fitting are comparable to the time constants measured for charging transients. However, a more noticeable separation in the time constants between the charging transients and the discharging transients fitted with a 4 term exponential over 2 hours can be observed.

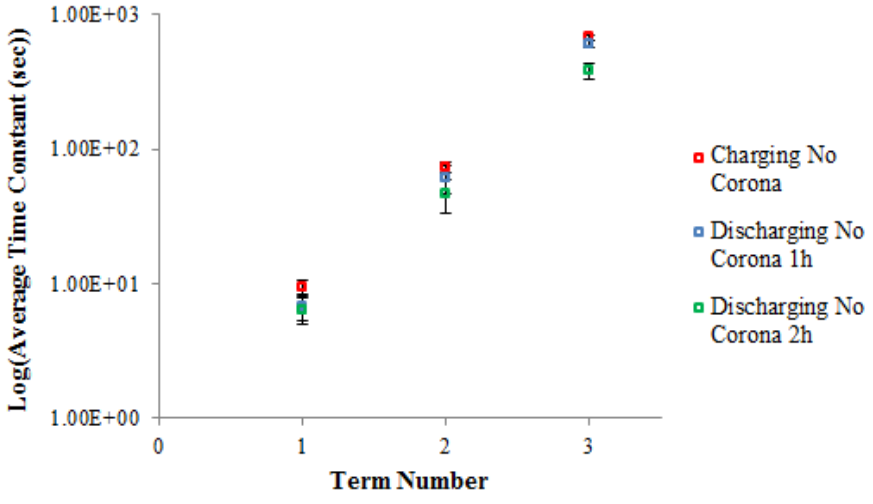

Figure 164: Log of average time constant for charging transients and discharging transients.

6.5.2.4. Corona Treated Thin PMMA: Discharging Transients

Figure 165 shows the discharging transients for corona treated thin PMMA fitted to the 4 term exponential function and table 23 shows the parameter values for the fits.

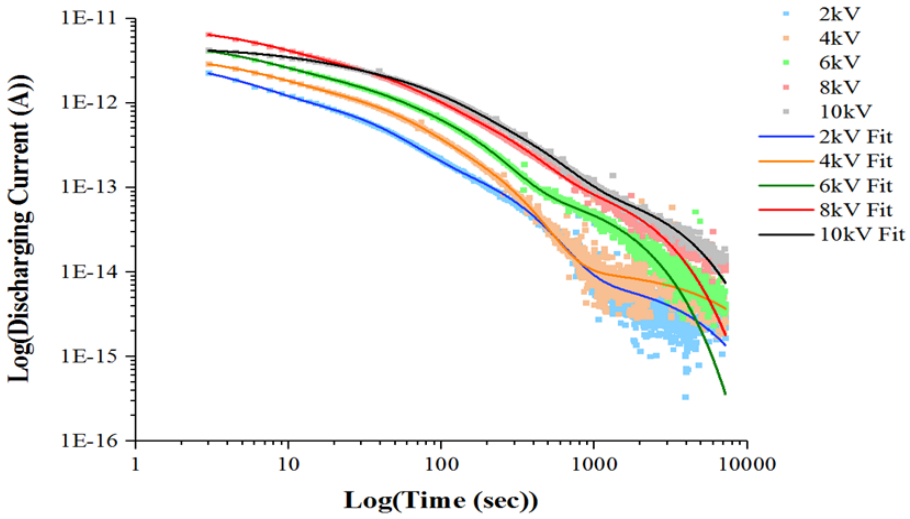

Figure 165: Discharging transients for corona treated thin PMMA fitted to 4 term exponential.

Table 23: Parameters of 4 term exponential to discharging transients.

Voltage (kV)	A_1 (pA)	A_2 (pA)	A_3 (pA)	A_4 (pA)	τ_1 (sec)	τ_2 (sec)	τ_3 (sec)	τ_4 (sec)	R^2
2.0	2.14	1.14	0.25	0.0090	3.7	29.9	213	3820	0.99
4.0	1.98	1.35	0.51	0.011	5.3	36.6	159	6580	0.99
6.0	2.74	1.48	1.24	0.10	4.8	26.4	110	1280	0.99
8.0	4.25	2.81	1.11	0.14	5.9	40.2	187	1650	0.99
10.0	1.43	2.11	0.924	0.12	12.6	67	273	2630	0.99

It can be seen from figure 165 that at long times ~ 1000 secs, the measured currents are scattered and close to the theoretical limit of the measurement range of the electrometer of 1 fA. Although the 4 term fitting was applied, it is possible that again further decay processes might be taking place.

Figure 166 shows the discharging transients fitted with the 3 term exponential of the form of equation 88 for the first hour of measurement and table 24 shows the parameter values for the fits.

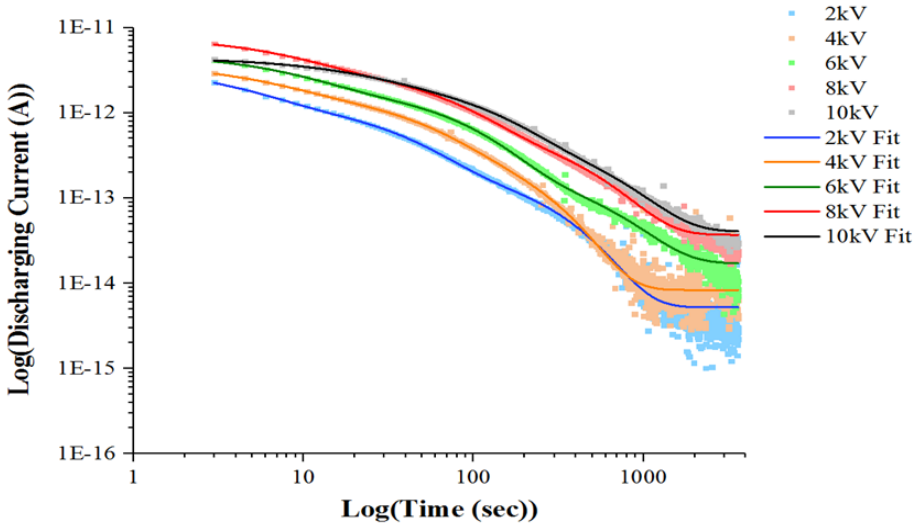

Figure 166: Discharging transients for corona treated thin PMMA fitted to a 3 term exponential function.

From figure 166 it can be seen that at lower voltage levels of 2 kV and 4 kV the data beyond times of ~ 1000 secs is close to the theoretical limit of the measurement range of the electrometer. Table 24 shows the parameter values for the 3 term exponential fittings.

Table 24: Parameters for 3 term exponential to discharging transients for corona treated thin PMMA.

Voltage (kV)	A_1(pA)	A_2(pA)	A_3(pA)	τ_1(sec)	τ_2(sec)	τ_3(sec)	I_o(pA)	R^2
2.0	2.13	1.13	0.24	3.8	30.8	229.4	0.0052	0.99
4.0	1.99	1.36	0.49	5.4	37.8	167	0.0083	0.99
6.0	2.98	1.82	0.22	7.9	71.7	464.8	0.017	0.99
8.0	4.40	2.82	0.67	7.5	57.4	348.6	0.037	0.99
10.0	1.78	2.09	0.54	18.2	96.7	474.5	0.041	0.99

In figure 167 the time constants τ_1, τ_2 and τ_3 observed from the 3 term fittings across the charging transients for the corona treated thin PMMA are compared with the time constants τ_1, τ_2 and τ_3 observed from the 3 term fitting applied across the first hour of the discharge measurement data for the corona treated thin PMMA and the time constants τ_1, τ_2 and τ_3 observed for the 4 term fitting applied to the complete 2 hours of the discharge measurement data for the corona treated thin PMMA. It can be seen that the time constants for the discharging transients with the 3 term exponential fitting are closer to the time constants

measured for charging transients. However, a more noticeable separation in the time constants between the charging transients and the discharging transients fitted with a 4 term exponential over 2 hours can be observed.

.

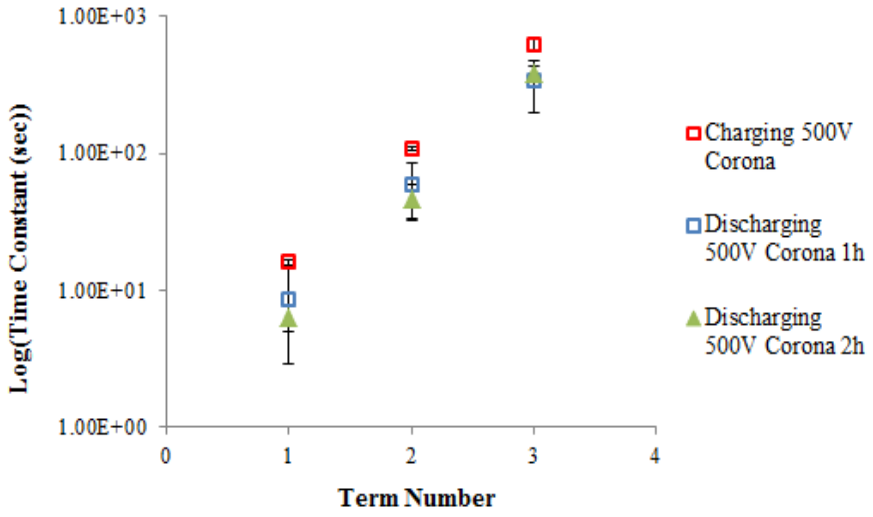

Figure 167: Log of average time constant for charging transients fitted to 3 term and discharging transients fitted to 3 term and 4 term exponential for corona treated thin PMMA.

6.5.2.5. Discussion: Discharging Transients

When the average time constants across the supply voltage range were compared for charging transients to the discharging transients it was observed that the time constants for the discharging transients over the first hour of measurements were close to the time constants of the charging transients. In an ideal system it is expected that the time constants for the charging transients would be similar to those of the discharging transients.

From the analysis of the charging transients it was established that in the 1 hour measurement period, the time constants τ_1 and τ_2 remained constant regardless of sample thickness or corona treatment, whereas, τ_3 was not influenced by corona treatment but was rather effected due to the sample thickness. Initial 3 term exponential fits taking the form of equation 88 were made to the discharging transients using the fixed time constants used for the charging transients from table 9 and good fits were established which showed that the decay behaviour of the charging and discharging transients was similar up to 1 hour.

In order to investigate the discharge behaviour over the complete measurement time of 2 hours the transient was fitted with the 4 term exponential with inclusion of a DC offset component taking the form of equation 95.

$$I(t) = A_1 Exp\left(-\frac{t}{\tau 1}\right) + A_2 Exp\left(-\frac{t}{\tau 2}\right) + A_3 Exp\left(-\frac{t}{\tau 3}\right) + A_4 Exp\left(-\frac{t}{\tau 4}\right) + I_o \quad (95)$$

The DC component was added because fitting the discharging transients over the 2 hour measurement period with the assumption that the currents at longer time periods decay to zero in subsection 6.5.2.1-6.5.2.4 showed that there were further slower decay processes taking place. It was assumed that any changes in the current at long times due to the slower processes could be reasonably modelled by a DC offset component.

The fittings were performed by using the fixed time constants τ_1, τ_2 and τ_3 used for fitting the charging and discharging transients in the first hour of measurement. τ_4 was left free. Good fits were obtained for both untreated thin and thick samples using these fixed time constants. A common value of τ_4 existed for the untreated thin and thick PMMA suggesting that the sample thickness or corona treatment did not influence the decay behaviour of the untreated PMMA at very long times. Table 25 shows the time constants.

Table 25: Time constants for 4 term exponential fits across untreated thick and thin PMMA.

Sample	τ_1	τ_2	τ_3	τ_4
Thin	14.1	91.2	643	5500
Thick	14.1	91.2	893	5500

Figures 168 and 169 show the discharge transient fittings for untreated thin and thick PMMA and tables 26 and 27 show the parameters values for the fits.

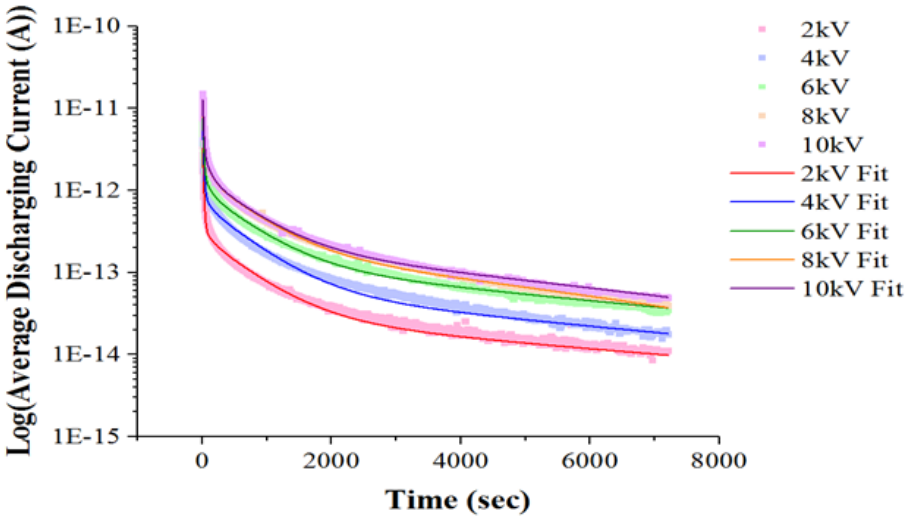

Figure 168: 4 term exponential fittings to untreated thin PMMA with fixed time constants.

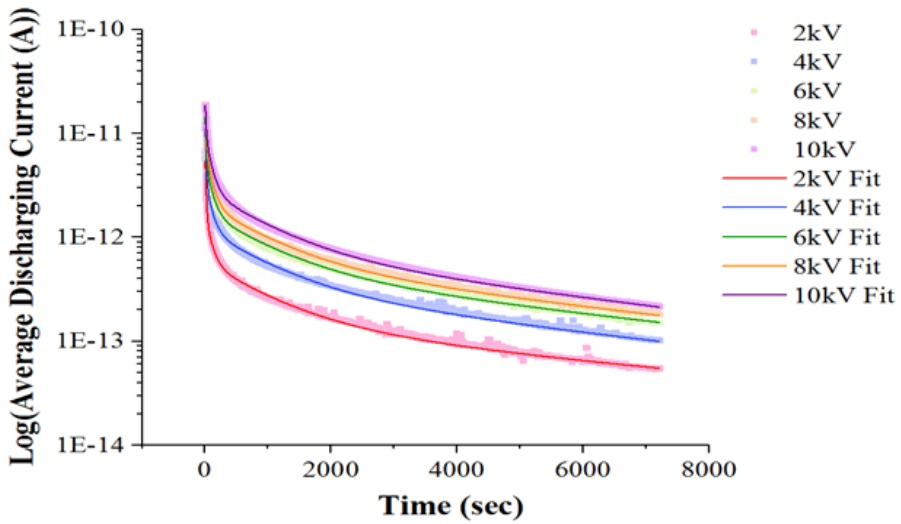

Figure 169: 4 term exponential fittings to untreated thick PMMA with fixed time constants.

Table 26: Parameters for the 4 term exponential fittings to untreated thin PMMA with fixed time constants.

Supply Voltage (kV)	A_1 (pA)	A_2 (pA)	A_3 (pA)	A_4 (pA)	I_o (A)	R^2
2.0	3.48	0.11	0.24	0.030	2E-15	0.97
4.0	7.48	0.28	0.61	0.063	1e-15	0.97
6.0	8.74	0.66	0.87	0.13	2e-15	0.97
8.0	11.12	1.60	1.30	0.21	-2e-14	0.99
10.0	11.17	1.64	1.27	0.22	-1e-14	0.99

Table 27: Parameters for the 4 term exponential fittings to untreated thick PMMA with fixed time constants.

Supply Voltage (kV)	A_1 (pA)	A_2 (pA)	A_3 (pA)	A_4 (pA)	I_o (A)	R^2
2.0	4.71	1.09	0.42	0.15	1E-15	0.98
4.0	9.05	2.47	0.85	0.33	1E-14	0.99
6.0	10.61	3.97	1.24	0.49	2E-14	0.99
8.0	14	5.39	1.51	0.58	2E-14	0.99
10.0	10.70	7.20	2.10	0.75	1E-14	0.99

From tables 26 and 27 it can be seen that the pre-exponential terms for the untreated thick samples are larger in value than the untreated thin samples. It is also observed that the pre-exponential terms generally exhibit a growing trend with supply voltage.

For the discharging transients of the corona treated thin and thick samples, attempts were made to fit the transients with the fixed time constants as used for the untreated samples in table 25. However, good fits could not be established at longer times. It was possible to fit the transients with fixed time constants τ_1 and τ_2 at shorter times having the same value as that used for the untreated samples.

Time constants τ_3 and τ_4 were different to those for untreated samples which suggested that at longer times corona treatment influences the decay behaviour of the discharging transients. As in the case of the untreated samples, the value for τ_3 was not common for the corona treated thin and thick samples. However, a common value for τ_4 existed for the samples. This suggests that at very long times the decay behaviour of the corona charged thin and thick samples was comparable.

Table 28 shows the time constants used to fit the discharging transients for the corona treated thin and thick PMMA to the 4 term exponential.

Table 28: Time constants for 4 term exponential fits across discharging transients for corona treated thick and thin PMMA.

Sample	τ_1	τ_2	τ_3	τ_4
Thin	14.1	91.2	450	3500
Thick	14.1	91.2	650	3500

Figures 170 and 171 show the discharge transient fittings for the corona treated thin and thick PMMA and tables 29 and 30 show the parameters values for the fits.

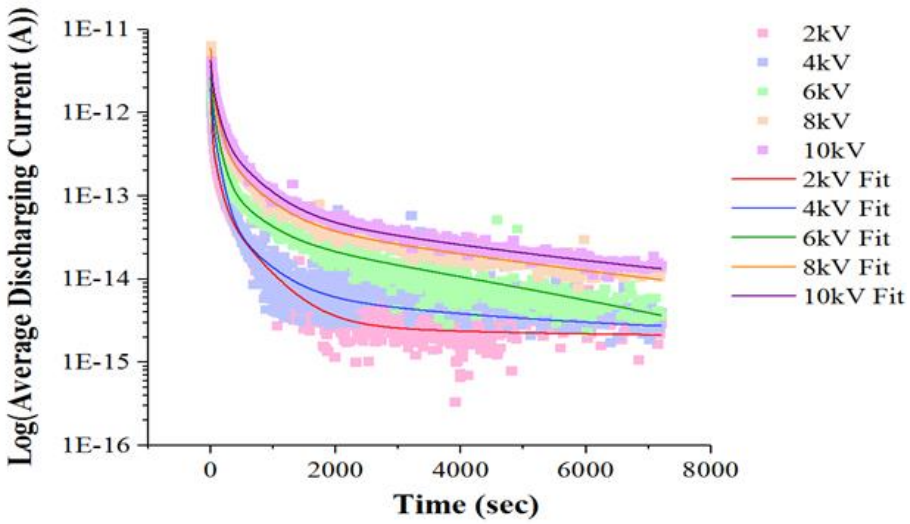

Figure 170: 4 term exponential fittings to corona treated thin PMMA with fixed time constants.

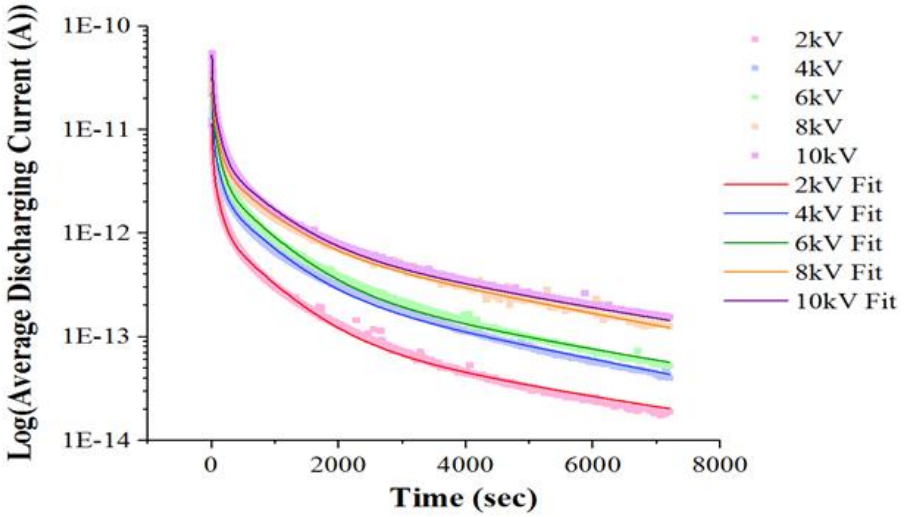

Figure 171: 4 term exponential fittings to corona treated thick PMMA with fixed time constants.

Table 29: Parameters for the 4 term exponential fittings to corona treated thin PMMA with fixed time constants.

Supply Voltage (kV)	A_1 (pA)	A_2 (pA)	A_3 (pA)	A_4 (pA)	I_o (A)	R^2
2.0	1.74	0.44	0.082	0.0011	2E-15	0.99
4.0	1.98	0.97	0.069	0.0058	2E-15	0.99
6.0	2.64	1.41	0.15	0.036	-1E-15	0.99
8.0	4.28	2.04	0.38	0.054	3E-15	0.99
10.0	1.74	2.27	0.52	0.065	5E-15	0.99

Table 30: Parameters for the 4 term exponential fittings to corona treated thick PMMA with fixed time constants.

Supply Voltage (kV)	A_1 (pA)	A_2 (pA)	A_3 (pA)	A_4 (pA)	I_o (A)	R^2
2.0	8.28	3.65	1.06	0.12	5E-15	0.99
4.0	16.80	6.92	2.12	0.31	1E-15	0.99
6.0	21.91	11.20	2.94	0.37	1E-14	0.99
8.0	25.23	12.18	3.76	0.88	1E-14	0.99
10.0	36.17	18.26	4.59	0.89	3E-14	0.99

From tables 29 and 30 it can be seen that the pre-exponential terms for the corona treated thick sample are significantly larger in value than the thin sample. It can also be seen that the pre-exponentials exhibit a general growing trend with supply voltage.

6.6. Chapter 6: Summary

This chapter reported on the surface transient measurement experiments conducted on the PMMA samples. The process of sample selection and preparation before conducting practical experiments was described. This was followed by an explanation of the experimental setup and the test conditions. The charging and discharging measurements were made on thick (2 mm) and thin (0.25 mm) PMMA samples. For each sample type there were two sets of measurement conditions. The first stage of transient measurements were performed on untreated thick and thin samples. The second stage of measurements were performed on corona treated samples.

Repeated transient measurements were performed at supply voltages ranging from 2 kV to 10 kV. Good repeatability was observed in the transient behaviour at each supply voltage and the measurements at each supply voltage were therefore presented as an average.

It was established that the best fitting for the charging transients was a 3 term exponential taking the form of equation 88. This fitting function was applied to both untreated and corona treated samples. Initial fits were performed by leaving the fitting parameters free. When fitting the transients it was observed that the higher values of current at shorter times have a bigger influence on the fitting process than the lower values at longer times which can lead to some problems with the fits at longer times. It was observed that the time constants remained reasonably constant across the supply voltage range for the three exponential terms. It was also observed that the time constants τ_1 and τ_2 for the thin and thick samples were similar for untreated and corona treated samples. However, τ_3, the time constant for the slowest process, for the thin PMMA was significantly smaller than for the thick PMMA.

It was proposed that the change in τ_3 was caused due to the sample thickness and not as a result of corona treatment. To validate this proposition, charging transients were fitted again with the 3 term exponential function using common time constant values for τ_1 and τ_2 for untreated and corona treated thin and thick samples. The value for τ_3 was also fixed but different for the thin and thick samples. Good fits were established across the charging transients with these fixed time constants. This validates the proposition that the corona treatment did not influence the decay behaviour for charging transients within the measurement time of 1 hour, and that the change in time constant τ_3 was due to the sample thickness.

Initial fits of the measured discharge transients were performed with a 4 term exponential fitting with free time constants and the assumption that the currents at very long times become zero. The 4 term exponential function took the form of equation 94. The initial 4 term fittings did not provide good fits at long times > 3500 secs, with fitting curves tending to fall off faster than the transients. This suggested that a further, slower, decay process might be taking place beyond the measurement time.

The discharging transients over the first hour of measurement were fitted with the 3 term exponential including a DC offset component. It was assumed that any changes in the current at longer times could be approximated by the DC component. The time constants from the 3 term fits to the discharging transients were compared to the charging transients and it was observed that the time constants were close in value. To establish if common time constants existed between the charging and discharging transients the discharging transients over the 2

hour period were fitted with a 4 term exponential including the DC offset component. The fitting function took the form of equation 95.

Attempts were made to fit the discharging transients to the common time constants used in fitting the charging transients with τ_4 left free. It was possible to obtain good fits for the untreated samples for common values of time constants. For the corona treated thin and thick samples the time constants τ_1 and τ_2 were similar to those for the untreated samples however, the values of the time constants τ_3 and τ_4 were different from those for the untreated samples. As in the case of the untreated samples τ_3 was different for the thin and thick samples. A common value for τ_4 existed for the corona treated samples. This suggested that at longer times the corona treatment has an influence on the discharge behaviour.

The corona treatment of the surface of the samples leads to an increase in the values of the pre-exponential terms in both thick and thin samples during charging measurements. The relative increase for the thin samples is more significant than for thick samples. On discharging, again the corona treatment of the surface leads to an increase in the pre-exponential terms. This is not observed in the thin samples. The larger pre-exponential terms and the smaller value of the time constant for the slower decay process indicate that significantly more charge may have been removed from the surface of the thin samples during the measurement of the charging transients. This is supported by the smaller values of I_o obtained for the thin samples. This would result in significantly less charge present on the surface of the thin samples at the start of the discharging measurements leading to the smaller values of the pre-exponential terms.

The observed DC currents from the charging transients showed that the DC currents for the thick samples remained higher than for the thin samples. It was also observed that the samples subjected to corona treatment exhibited higher DC currents than the untreated samples. The general behaviour of the DC current against supply voltage for both untreated and corona treated samples showed similar behaviours, where a linear regime at lower voltages is followed by a sharp rise in the currents. Further analysis of the DC currents showed that Hopping or Schottky conduction mechanisms could be responsible for the DC behaviour. Measurements at higher (> 10 kV) supply voltages would be needed to make it possible to differentiate between the mechanism responsible for the DC behaviour.

7. Surface Charge Decay behaviour of Polymeric Insulators

7.1. Chapter 7: Overview

This chapter presents the test results and analyses of the experimental data collected by using the varactor probe measurement system developed in chapters 3 and 4 for measurements of surface potentials. The surface potentials are used to evaluate the surface charge density and the decay behaviour for the thick and thin PMMA samples. The tests were carried out under two conditions.

In the first, the measurements for surface potentials were performed on uncoated PMMA samples. The test was designed to investigate the charge decay behaviour that would generally be as a result of the neutralisation of charge through the surrounding gas medium.

In the second, surface potential measurements were performed across coated PMMA samples. The test was designed to investigate the charge decay behaviour that would generally be as a result of the neutralisation of charge through surface conduction.

The initial part of the chapter contains details on the experimental setup and test methods for the two test conditions. This is followed by results for the calibration of the measurement system at a fixed gap separation of 9 mm between the sample surface and the probe sensor. This distance was selected as it was the shortest gap separation where breakdown from the surface would be avoided, based upon trials with a metal plate. As the output of the probe showed a $1/D$ dependence on separation, this led to a significant increase in the probe output. The derived $\boldsymbol{\Phi}$-Matrices for the two experimental conditions are also presented.

The measured surface potentials at various times after the surface was charged are presented. They are used along with the derived $\boldsymbol{\Phi}$-Matrix to evaluate the charge densities across the sample surfaces. These charge densities have been analysed and were used to calculate the total charge across the sample surfaces at the different measurement times. The effect of the thickness of the sample and the amount of corona deposition on the charge decay behaviour is discussed.

These results will help to provide knowledge which will aid in better understanding the charge decay behaviour of thin and thick polymeric insulators under these conditions.

7.2. Experimental Setup and Test Conditions

7.2.1. Condition 1: Uncoated Samples

The probable conduction paths for charge decay in the test setup for uncoated samples are shown in figure 172 and it is expected that most of the charge will decay due to the mechanism of neutralisation via the surrounding gas medium.

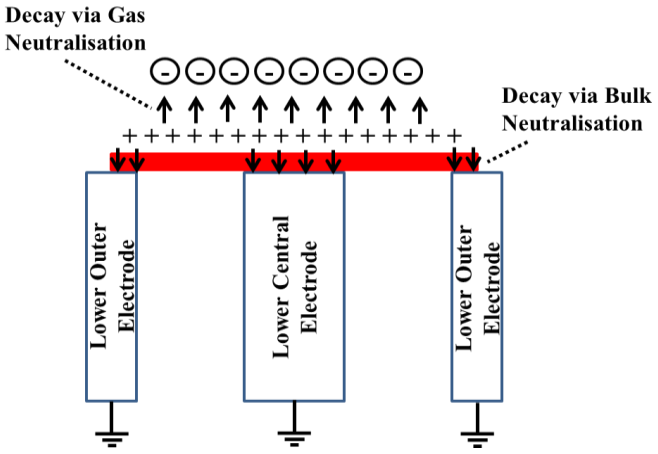

Figure 172: Charge decay path for uncoated samples.

The mechanism of charge decay through bulk neutralisation is expected to play a lesser role in this condition, due to the coaxial arrangement of the geometry in this project. The arrangement used here does not allow for characterisation of the charge distribution on the bottom of the samples. An equal and opposite distribution of charge is normally present at the bottom of the samples while having the samples placed on top of a grounded base plate, which is the traditional configuration to measure charge decay on insulating samples. With the inclusion of a base plate, charge decay through the bulk has been reported to be the prominent decay mechanism by many researchers [27, 45, 66], due to the well-defined normal field component on the surface.

The setup of the system to deposit corona charge on the PMMA samples has been described in section 5.2.1. In section 5.2.2, the results of initial surface potential measurements were reported for the uncoated samples. The experimental arrangement for conducting the surface potential measurements on uncoated samples reported in this chapter is similar to that in section 5.2.2. The process of measuring the surface potential on the uncoated samples and the schematic and actual image of the experimental setup are also shown in section 5.2.2.

In section 5.2.4, the process of obtaining a realistic set of values for the surface charge distribution was established. It was realised that the charge on the sample surface directly above the central and outer electrodes had to be considered to obtain realistic results. This required the extrapolation of an additional two measurement points from the existing surface potential values to avoid the requirement to repeat the entire measurement sequence.

In the present experiments, complete scans including these additional measurement points were performed. The probe's initial scanning position was now offset by 2.05 mm towards the central electrode, causing the first measurement to be made over the central electrode. A total of 22 measurements were made at equal separations of 2.05 mm, causing the last measurement to be made 2.05 mm above the sample surface over the outer electrode. This way the required 22 element vector was obtained.

Measurements for the surface potential of the thick and thin samples were made at times of 5 min, 60 min, 120 min, 240 min and 360 min after surface charging. The measurements were made for the surfaces charged with grid voltages of 1 kV and 2 kV. The voltage of the needle electrodes was set at 14 kV and 15 kV for these two grid voltages. The corona charging time was set at 5 mins. Each scan of the surface took ~ 10 min. A total of 3 scans were taken for each sample charged with 1 kV and 2 kV grid voltage. After each scan was complete the sample was removed from the system and wrapped in aluminium foil which was grounded through a copper wire connection to the earth point in the lab. The method was similar to that discussed in section 6.3 and shown in figure 111. The results for the surface potentials for the samples charged with grid voltages of 1 kV and 2 kV were presented as an average of the 3 scans for each measurement time.

A 22 by 22 $\boldsymbol{\Phi}$-Matrix appropriate for the measuring positions was obtained using Comsol including the central disk element and the outer ring element in the matrix. The process to obtain the $\boldsymbol{\Phi}$-Matrix is discussed in section 5.2.3. This means that these elements that were previously fixed with a zero charge density were also assigned a defined charge density (1 C/m^2). This was done to include the influence of the charge on these areas of the samples on the induced potential on the probe sensor. Figure 173 shows the induced surface potential vectors of the $\boldsymbol{\Phi}$-Matrix for defined charge densities assigned to the 1^{st}, 10^{th}, 11^{th} and the 22^{nd} element of the sample surface for the uncoated samples at a probe sensor to sample surface gap of 9 mm.

Once the surface potentials and the complete $\boldsymbol{\Phi}$-Matrix were obtained, the charge distributions across the sample surface were evaluated using the process described in section 5.2.4, with the surface potentials passed through a digital filtering process to minimise the

effect of noise in the measured potentials. These filtered potentials were then used along with the Φ-Matrix to evaluate the resultant surface charge distributions in MATLAB, using equation 20.

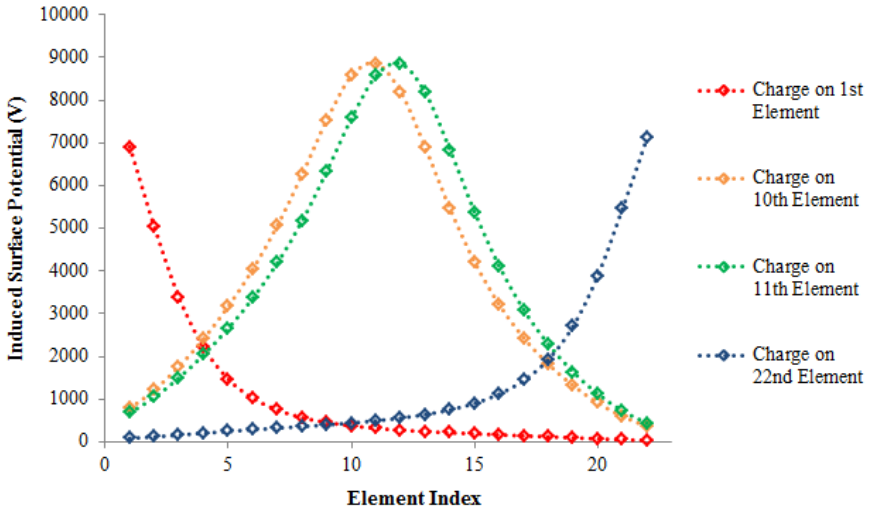

Figure 173: Induced surface potentials for defined charge density assigned to the 1st, 10th, 11th and 22nd element of the uncoated samples.

7.2.2. Condition 2: Coated Samples

The probable conduction paths for charge decay in the test setup for coated samples are shown in figure 174 and it is expected that most of the charge will decay due to the mechanism of neutralisation via surface conduction.

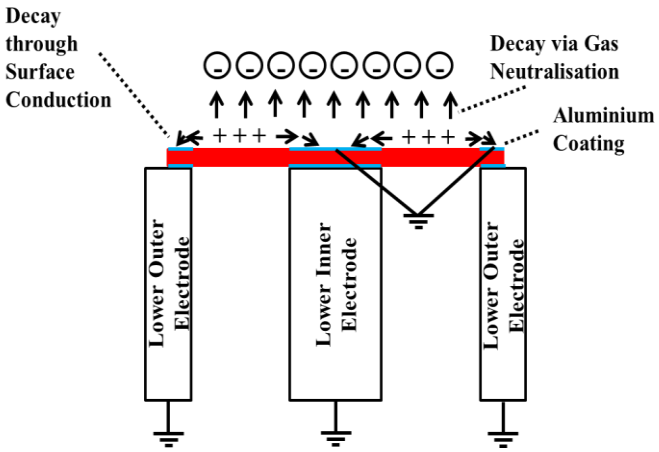

Figure 174: Charge decay path for coated samples.

The experimental setup for measurements of surface charge decay on coated samples was similar to that of the initial experiment in 5.2.2. After the corona charging of the coated

samples was completed, a metallic earth connection was established between the central disk and outer ring of the sample surface. These parts of the sample were acting as electrodes, as they had been coated with a thin aluminium layer. This connection was established approximately 30 secs after the charging process had been completed.

The purpose of grounding the coated sections of the samples was to remove any charge that existed in these regions and also to develop a situation by which, the charge present in the scanning area between the central and outer electrodes of the system could be encouraged to decay through surface conduction, by moving towards these grounded electrodes. As the charge above the central and outer electrodes was removed, the 2 extra measurements that were made for uncoated samples were not required, and surface potential measurements were only made on the sample surface laying between the central and outer electrodes of the system. A 20 element vector for surface potentials was obtained.

After establishing the earth connection for the coated regions of the sample surface, the process of surface potential measurements was carried out similarly to that discussed in section 5.2.2. The first measurement was made 5mins after corona charging of the surface was completed. Surface potential scans were made at time intervals of 5 min, 60 min, 120 min, 240 min and 360 min for corona charged thick samples and 5 min, 60 min, 120 min, 240 min and 1200 min for corona charged thin samples.

As in the case of the uncoated samples, the potential measurements were made for the surfaces charged with grid voltages of 1 kV and 2 kV. The voltage of the needle electrodes was set at 14 kV and 15 kV for these two grid voltages. A total of 3 scans were taken for each sample charged with 1 kV and 2 kV grid voltage. Again after each scan was complete the sample was removed from the system and wrapped in aluminium foil which was grounded through a copper wire connection to the earth point in the lab. The results for the surface potentials for the samples charged with grid voltages of 1 kV and 2 kV were presented as an average of the 3 scans at each measurement time.

A 20 by 20 $\boldsymbol{\Phi}$-Matrix was obtained using Comsol. The process to obtain the $\boldsymbol{\Phi}$-Matrix was similar to that discussed in section 5.2.3, the only difference being that the sample was modelled as a coated sample with the coated sections of the samples having a fixed potential of 0 V. This was identical to the condition of the practical experiments. Figure 175 shows the induced surface potential on the probe sensor with defined charge densities (1 C/m^2) assigned to the 1^{st}, 10^{th}, 11^{th} and the 20^{th} element of the sample surface of the coated samples at a probe sensor to sample surface gap of 9 mm.

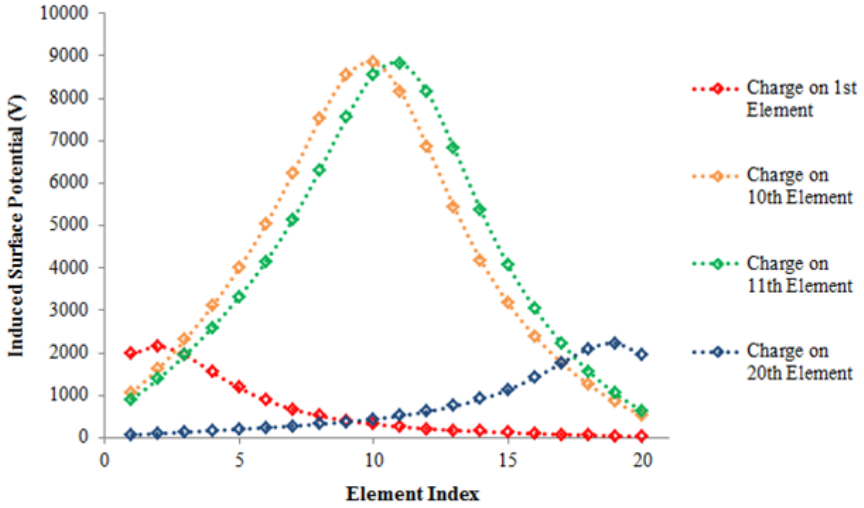

Figure 175: Induced surface potentials for defined charge density assigned to the 1st, 10th, 11th and 20th element of the coated samples.

Once the surface potentials and the $\boldsymbol{\Phi}$-Matrix were obtained, the charge distributions across the sample surface were evaluated using the process described in section 5.2.4, with the surface potentials passed through a digital filtering process to minimise the effect of noise on the measured potentials. These filtered potentials were then used along with the $\boldsymbol{\Phi}$-Matrix to evaluate the resultant surface charge distributions in MATLAB by using equation 20.

7.3. Calibration of the Probe and Offset Evaluation

Before any experiments on the samples were performed, the measurement system was calibrated at the fixed gap of 9mm between the test surface and probe sensor. The test was performed similarly to that of section 4.4, where a circular metal plate was used as the test sample. The probe was placed centrally above the test surface. Measurements of the induced potential on the probe sensor were made for the metal plate charged with voltages up to 2 kV. The 2 kV limit for the system calibration was selected because it was planned that in the practical experiments with PMMA, the samples would be charged with a maximum grid voltage of 2 kV. The probe response for this experiment can be seen in figure 176.

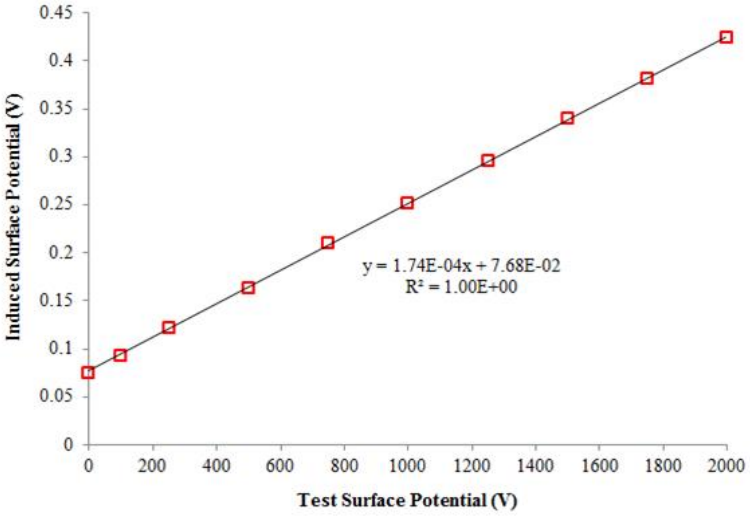

Figure 176: Probe response to charged metal plate at a separation of 9 mm.

A linear probe response was observed with an offset of ~ 0.077 V. After observing the probe response for the condition where the probe was located at a fixed position, measurements to establish a degree of certainty in the value of the offset were performed. These measurements were made to mimic the practical experiments that were to follow on the PMMA samples, where the probe was set up to scan the surface of the samples between the inner and outer electrodes of the system on which the sample lay. The metal test plate was grounded and measurements of the surface potential were made across the scanning area of the test sample. The resultant probe response across the scanning area, divided into 20 equally spaced ring elements of 2.05 mm width, is shown in figure 177.

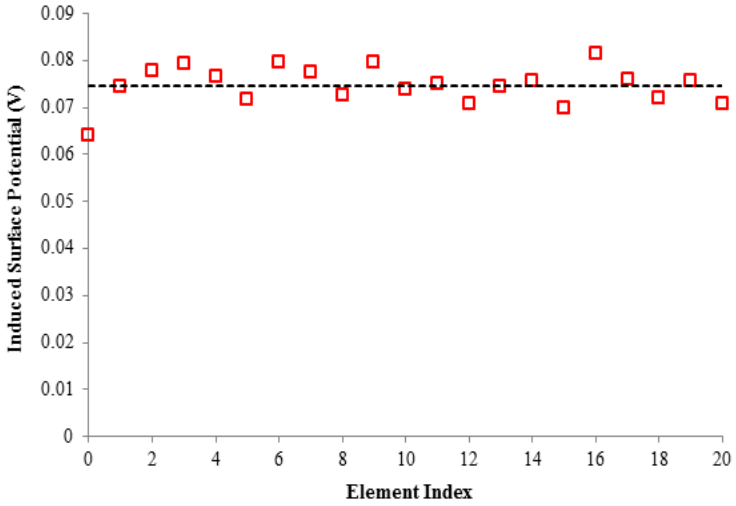

Figure 177: Probe response for a scan across a grounded test plate at a separation of 9 mm.

A mean offset of ~ 0.075 V was observed from figure 177. When compared to the offset value of 0.077 V from figure 176, it is reasonable to conclude that the offset value remains constant. From this observation, it was established that the fixed offset value of 0.075 V would be subtracted from the surface potentials measured across the PMMA samples. The resulting surface potentials would be calibrated against figure 178, which is a representation of the linear response observed in figure 176, but after removing the offset.

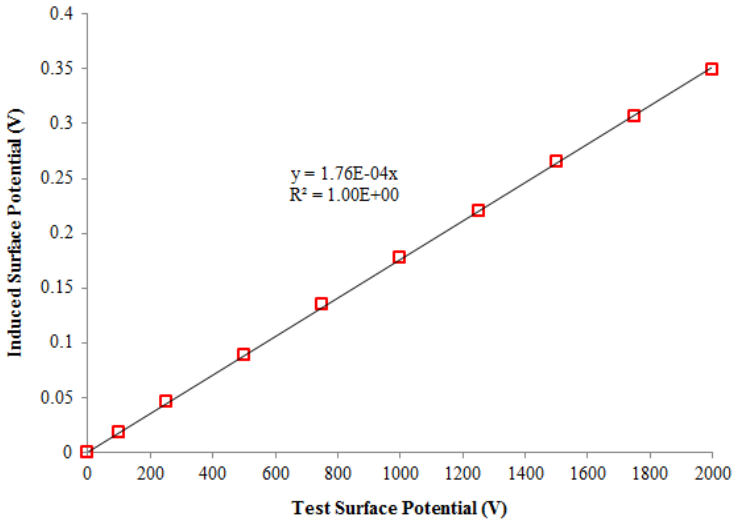

Figure 178: Linear response of figure 176 without the offset.

7.4. Results: Surface Potential

7.4.1. Uncoated Samples: Surface Potential

The measured surface potentials across the thin and thick uncoated samples for a grid voltage of 1 kV are presented as figures 179 and 180.

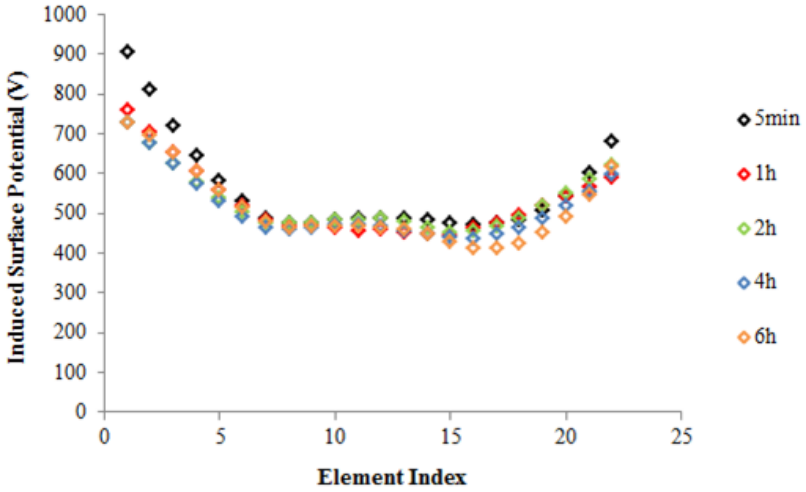

Figure 179: Induced surface potential for uncoated thin PMMA charged with 1 kV grid voltage.

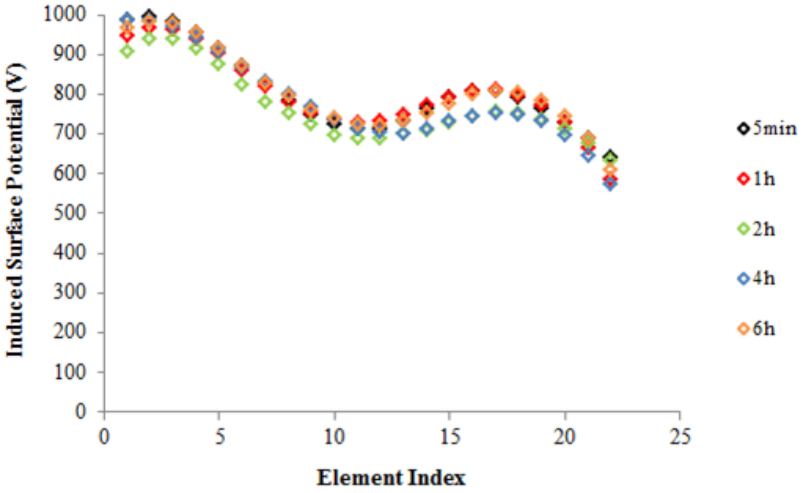

Figure 180: Induced surface potential for uncoated thick PMMA charged with 1 kV grid voltage.

When the average surface potentials of the 3 repeated measurements for the thin PMMA are compared to the average surface potentials of the 3 repeated measurements for the thick PMMA for samples charged at a grid voltage of 1 kV, it is observed that the surface of the thicker sample has a greater overall potential, which suggests that the thicker samples have a higher amount of charge present on the surface. Figure 181 shows this observation.

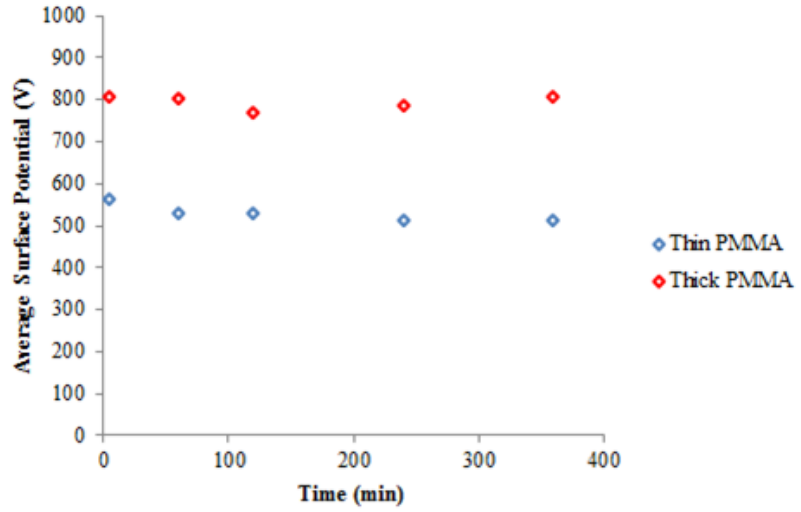

Figure 181: Average surface potential across uncoated thin and thick samples charged with a grid voltage of 1 kV.

The measured surface potentials across the uncoated thin and thick samples for a grid voltage of 2 kV are presented as figure 182 and 183.

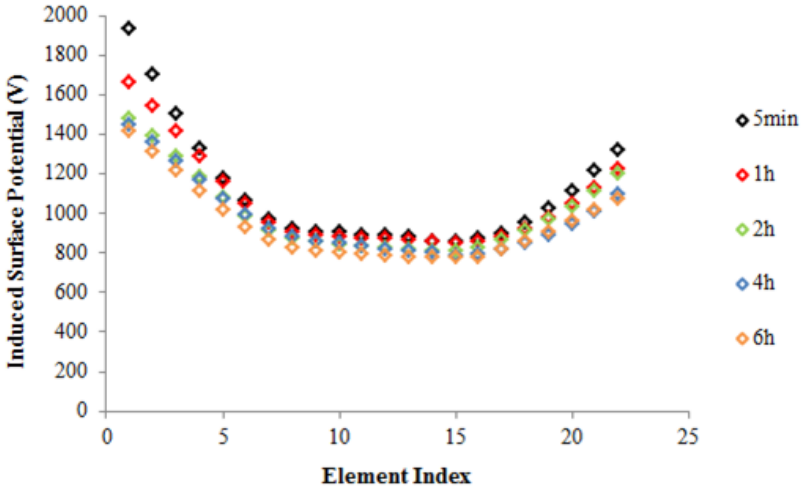

Figure 182: Induced surface potential for uncoated thin PMMA charged with 2kV grid voltage.

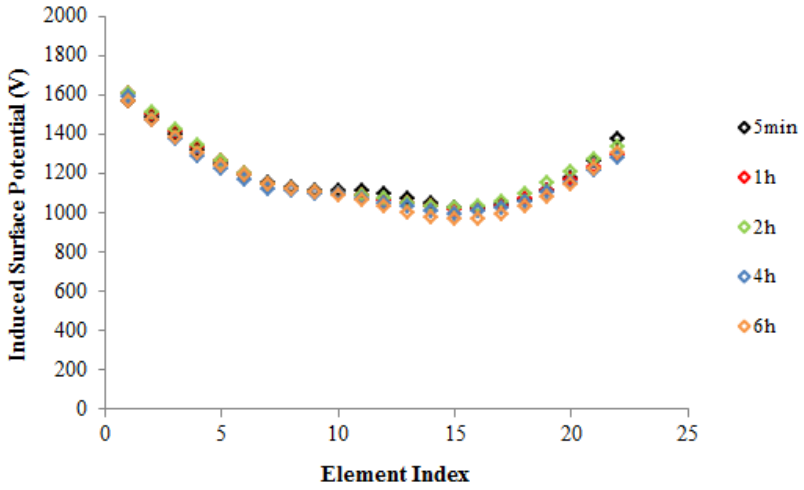

Figure 183: Induced surface potential for uncoated thick PMMA charged with 2kV grid voltage.

When the average surface potential of the thin PMMA is compared to the thick PMMA for samples charged at a grid voltage of 2 kV, it is again observed that the surface of the thicker sample has a greater overall potential. Figure 184 shows this observation.

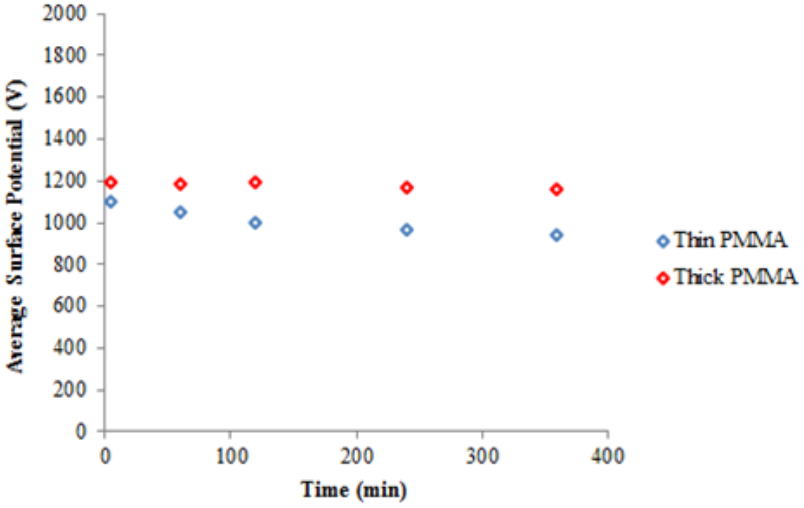

Figure 184: Average surface potential across uncoated thin and thick samples charged with a grid voltage of 2 kV.

When analysing the data for the surface potential measurements, it was observed that the shape of the surface potential plots for the thick PMMA charged with a grid voltage of 1 kV were not consistent with those of the other measurements performed on the uncoated samples. These plots did not exhibit the peak surface potentials in the region of the electrodes observed for the other surface potential measurements performed on uncoated

samples. The peaks in the regions of the electrodes suggest that the majority of the charge was concentrated in this area. It is possible that image charges on the electrodes cause the charge to get trapped in these regions.

The difference in the measured surface potential behaviour for the thick PMMA charged with a grid voltage of 1 kV is not clear, as all experiments were carried out in an identical manner. The charging of the sample was performed with the same voltage and time. The discharging of the sample was performed in an identical manner and time. The samples were handled with care and repeated measurements were performed. The behaviour may be an inherent characteristic of the sample for a charging voltage of 1 kV. This is proposed as the surface potential measurements on thick PMMA with a grid voltage 2 kV show similar behaviours to the rest of the experiments in this section.

7.4.2. Coated Samples: Surface Potential

The measured surface potentials across the thin and thick coated samples for a grid voltage of 1 kV are presented as figures 185 and 186.

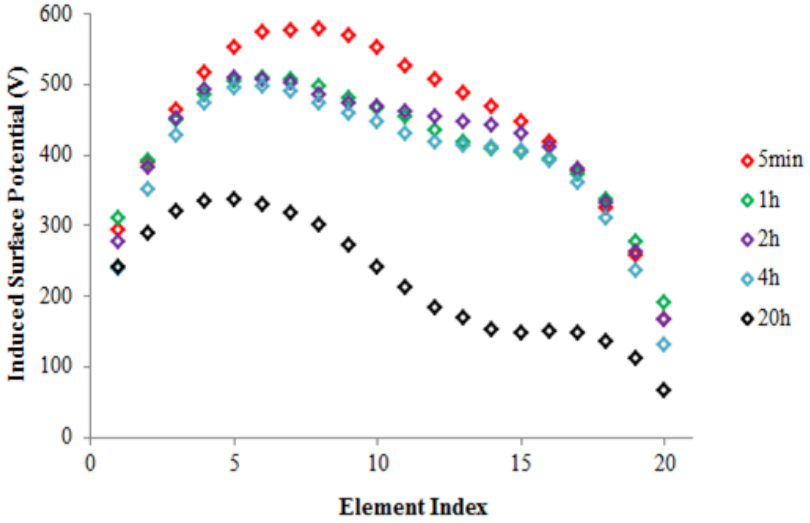

Figure 185: Induced surface potential for coated thin PMMA charged with 1 kV grid voltage.

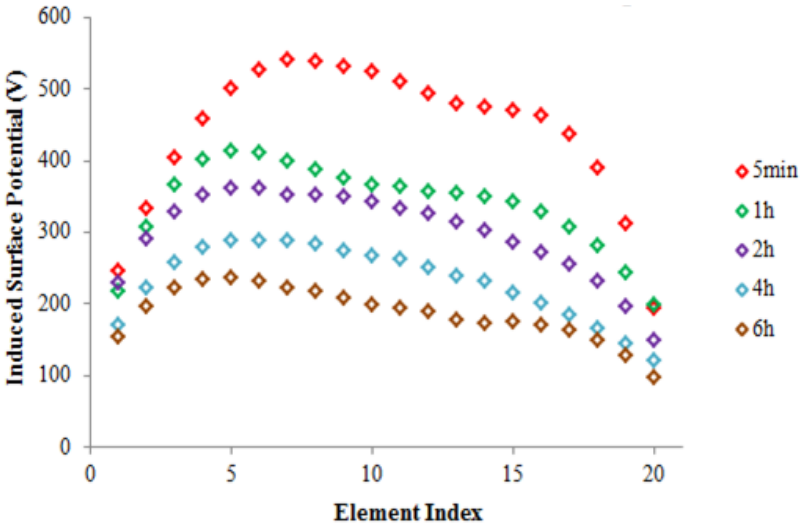

Figure 186: Induced surface potential for coated thick PMMA charged with 1 kV grid voltage.

When the average surface potential of the thin PMMA is compared to the thick PMMA for samples charged at a grid voltage of 1 kV, it is observed that in this case, the surface of the thin sample has a greater overall potential than the thick samples. This behaviour is not consistent with that observed for the uncoated samples and suggests that more charge may be present on the surface of the thin sample. Figure 187 shows the plot of the average surface potential against time for coated samples charged with a grid voltage of 1 kV.

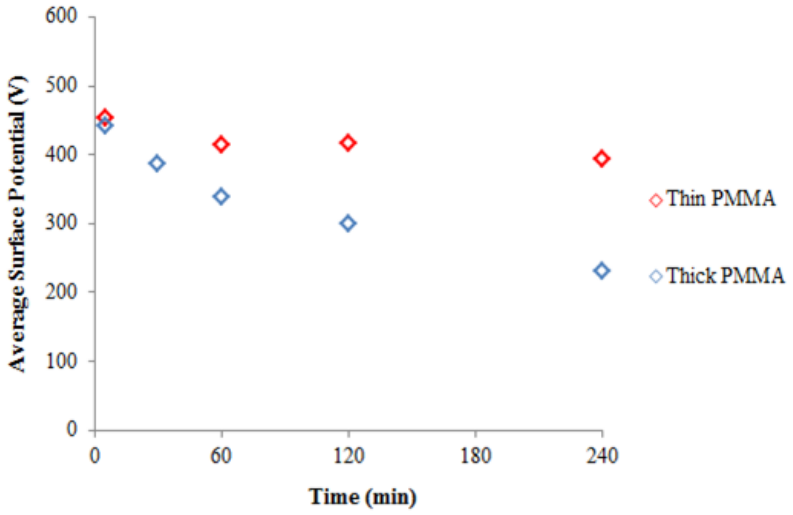

Figure 187: Average surface potential across coated thin and thick samples charged with a grid voltage of 1 kV.

The measured surface potentials across the thin and thick samples for a grid voltage of 2 kV are presented as figures 188 and 189.

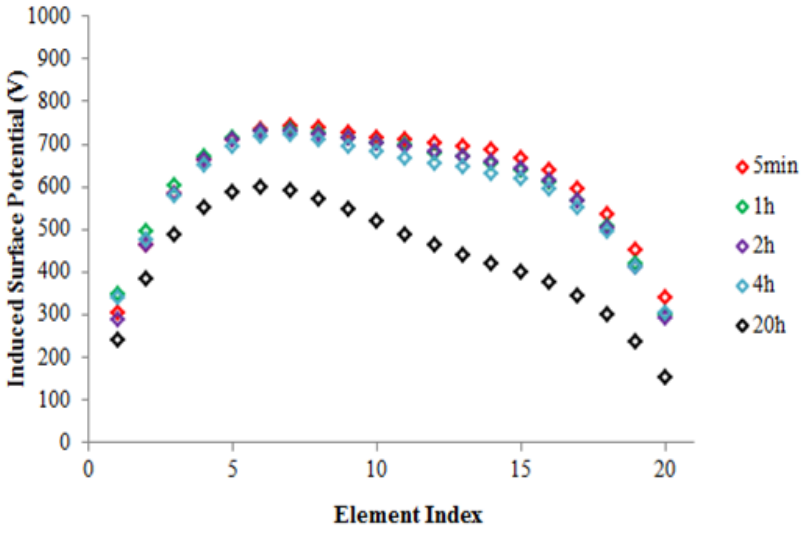

Figure 188: Induced surface potential for coated thin PMMA charged with 2 kV grid voltage.

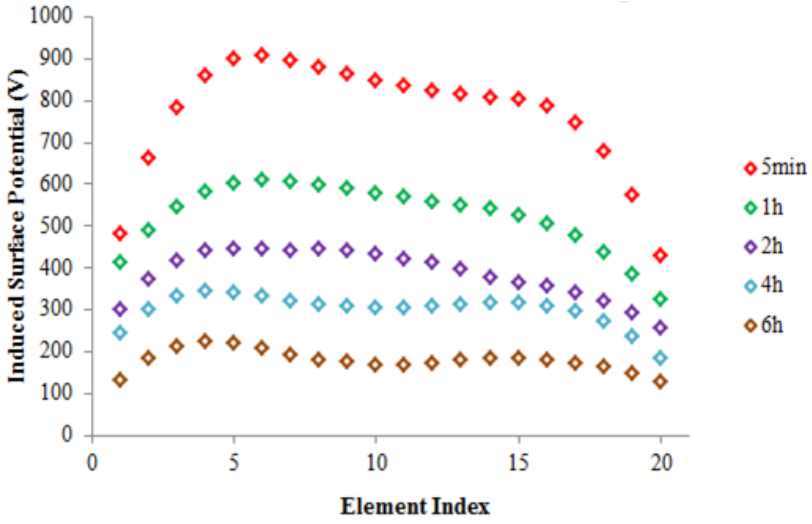

Figure 189: Induced surface potential for coated thick PMMA charged with 2 kV grid voltage.

When the average surface potential of the coated thin PMMA is compared to the thick PMMA for samples charged at a grid voltage of 2 kV, it is again observed that the thin sample has a greater overall potential than the thick samples. A more noticeable decay in the potential of thick samples with time is also observed. Figure 190 shows the plot of the average surface potential against time for coated samples charged with a grid voltage of 2 kV.

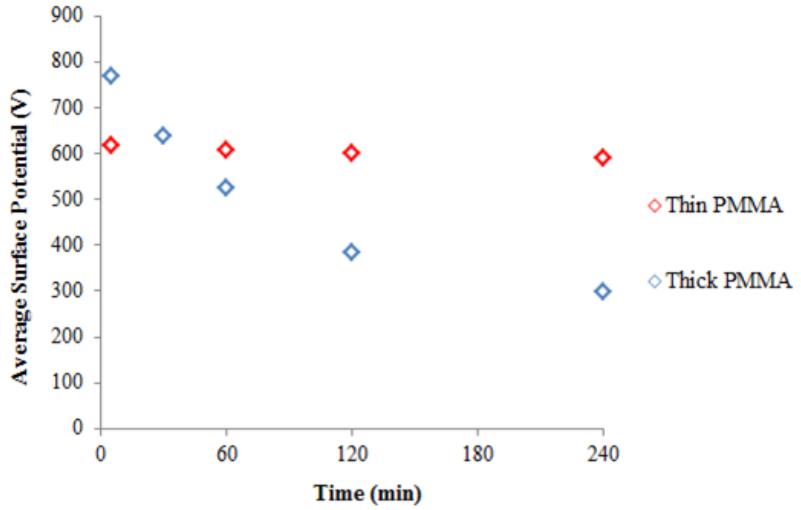

Figure 190: Average surface potential across coated thin and thick samples charged with a grid voltage of 2 kV.

7.5. Results: Charge Densities

7.5.1. Uncoated Samples: Charge Density Distribution

The calculated charge densities from Matlab for uncoated thin PMMA samples, corona charged with grid voltages of 1 kV and 2 kV are shown in figures 191 and 192 and those for uncoated thick PMMA samples, corona charged with grid voltages of 1 kV and 2 kV are shown in figures 193 and 194.

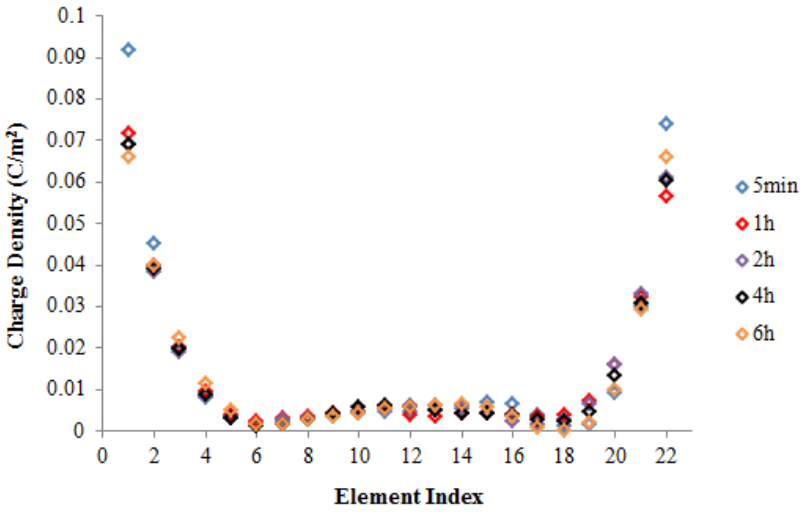

Figure 191: Charge densities for uncoated thin PMMA charged with a grid voltage of 1 kV.

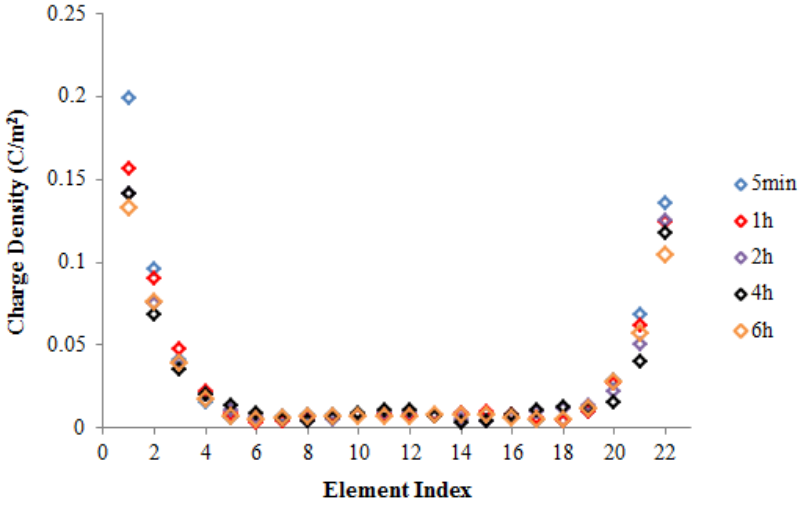

Figure 192: Charge densities for uncoated thin PMMA charged with a grid voltage of 2 kV.

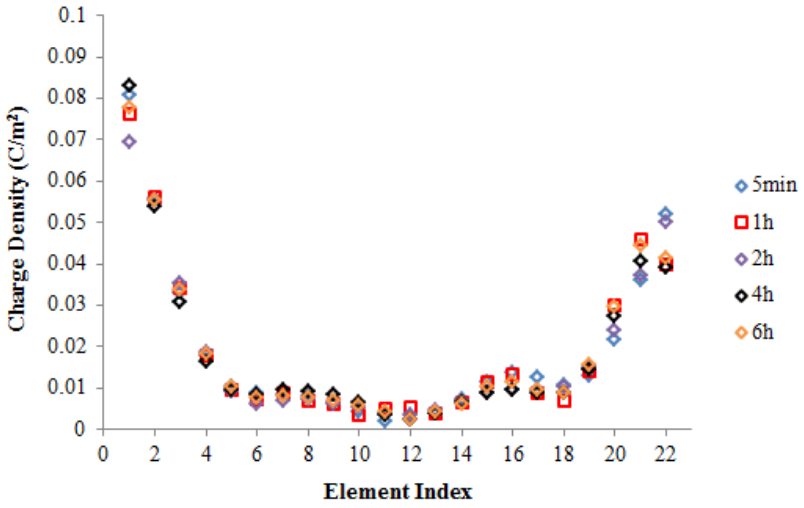

Figure 193: Charge densities for uncoated thick PMMA charged with a grid voltage of 1 kV.

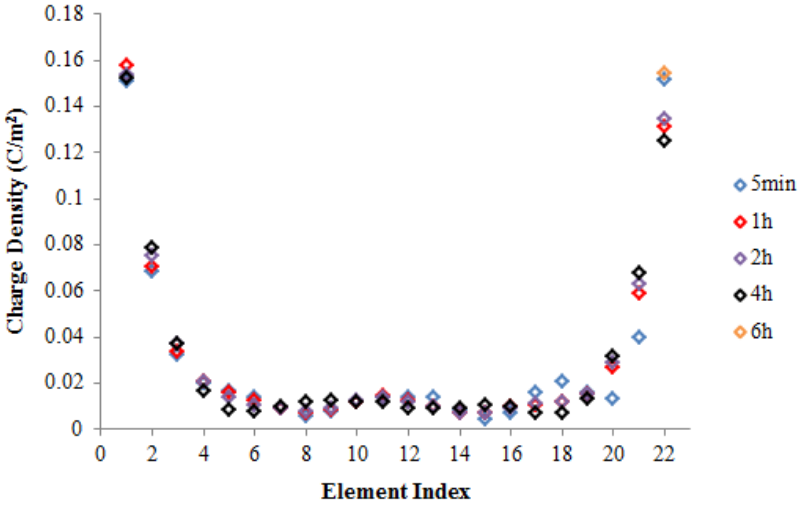

Figure 194: Charge densities for uncoated thick PMMA charged with a grid voltage of 2 kV.

From the plots of the charge densities for both thin and thick samples, it can be seen that the majority of the charge is concentrated in the regions close to the central and outer electrodes of the system. It is proposed that the concentration of the charge in these areas of the sample is a result of image charges being formed on the electrode surfaces, causing most of the charge on the surface to migrate towards these regions.

The observed charge density plots were divided into three regions to simplify the analysis of the data. The first section of the plot represents the charge density associated with regions close to the inner electrode. The second section of the plot represents the relatively flat charge density distribution observed between the regions influenced by the electrodes, i.e. the central part of the sample, and the third section of the plot represents the charge density associated with regions close to the outer electrode.

The charge densities in the regions close to the electrodes are presented as an average of the measurements performed at the 5 positions closest to the electrodes. This was done as it was observed that the peaks in the charge distribution plots are generally associated with the 5 measurements closest to the electrodes. The flat part of the charge density distribution is presented as an average of the remaining measurements in the central region of the sample.

Figures 195 and 196 show plots of the average charge densities in the three sections of the samples measured over a 6 hour period. The plots show the average charge densities associated with the regions close to the central electrode, close to the outer electrode, and in the central region of the thin and thick samples corona charged with a grid voltage of 1 kV.

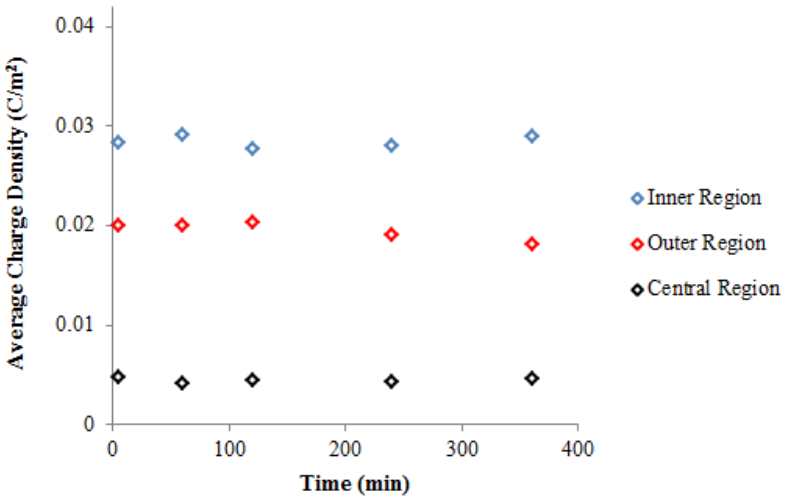

Figure 195: Average charge densities in the central region of the uncoated thin sample and regions close to the inner and outer electrodes for corona charging with a grid voltage of 1 kV.

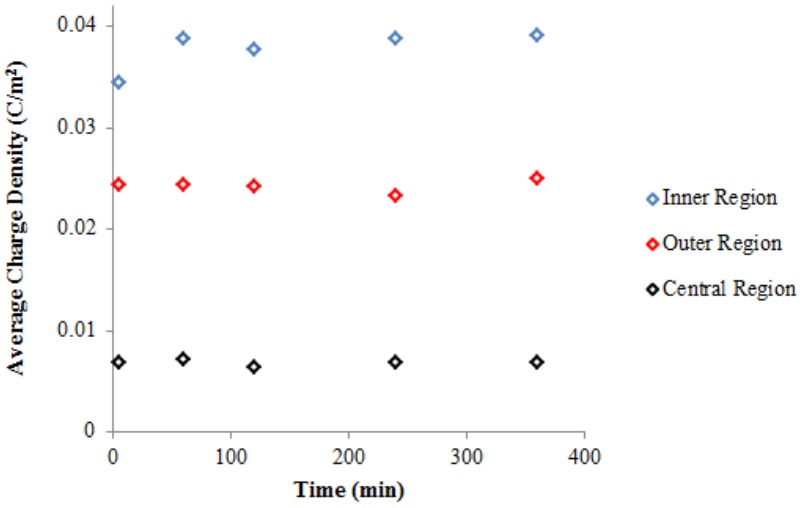

Figure 196: Average charge densities in the central region of the uncoated thick sample and regions close to the inner and outer electrodes for corona charging with a grid voltage of 1 kV.

From figures 195 and 196, it can be seen that for both the thin and thick PMMA samples, the largest amount of charge is concentrated in the regions associated with the inner electrode. This is followed by the regions associated with the outer electrode and the least amount of charge is present in the central part of the sample. Similar observations were made for both the samples corona charged with a grid voltage of 2 kV. It is also observed that the charge densities across all three regions of the thick sample are larger than for the thin sample. This suggests that more charge is present on the thick sample as compared to the thin sample.

Figures 197 and 198 show a comparison of the average charge density across the sample surface for both the uncoated thin and thick PMMA samples, corona charged with grid voltages of 1 kV and 2 kV.

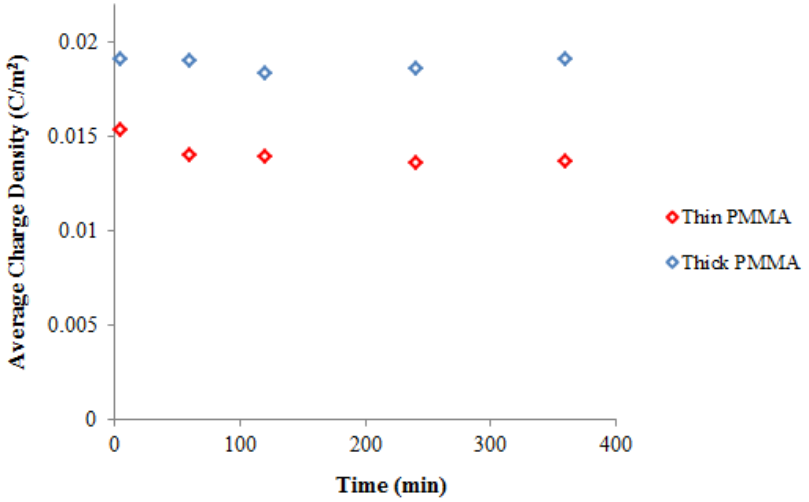

Figure 197: Average charge densities across the uncoated thin and thick PMMA corona charged with a grid voltage of 1 kV.

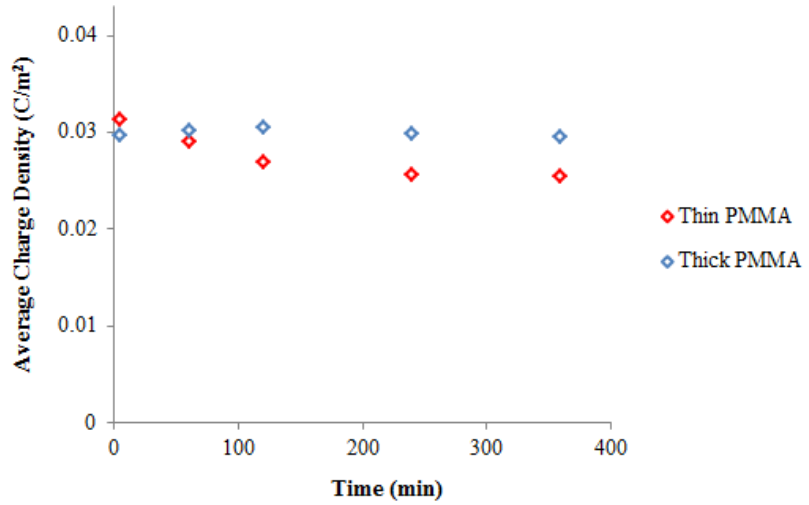

Figure 198: Average charge densities across the uncoated thin and thick PMMA, corona charged with a grid voltage of 2 kV.

From figures 197 and 198, it can be seen that the average charge density across the thick PMMA is larger than that for the thin PMMA, for samples charged with 1 kV. At 2 kV the difference between the charge densities is much smaller, but at longer times the charge density on the thick sample is higher. It can be seen that the average charge densities for the thin sample charged with a grid voltage of 2kV are ~ 2 times greater than those for the thin

PMMA charged with a grid voltage of 1 kV. The average charge densities for the thick sample charged with a grid voltage of 2 kV are ~ 1.5 times greater compared to the thick PMMA charged with a grid voltage of 1 kV. It is also noticeable that, for the thick PMMA samples no significant charge decay occurs. For the thin samples a small decay may be occurring in the first 60 minutes after charging at 1 kV, and a more significant decay appears to occur over the first 2 hours of measurement after charging at 2 kV.

7.5.2. Coated Samples: Charge Density Distribution

The calculated charge densities from Matlab for the coated thin PMMA samples, corona charged with grid voltages of 1 kV and 2 kV are shown in figures 199 and 200, and those for the coated thick PMMA samples, corona charged with grid voltages of 1 kV and 2 kV are shown in figures 201 and 202.

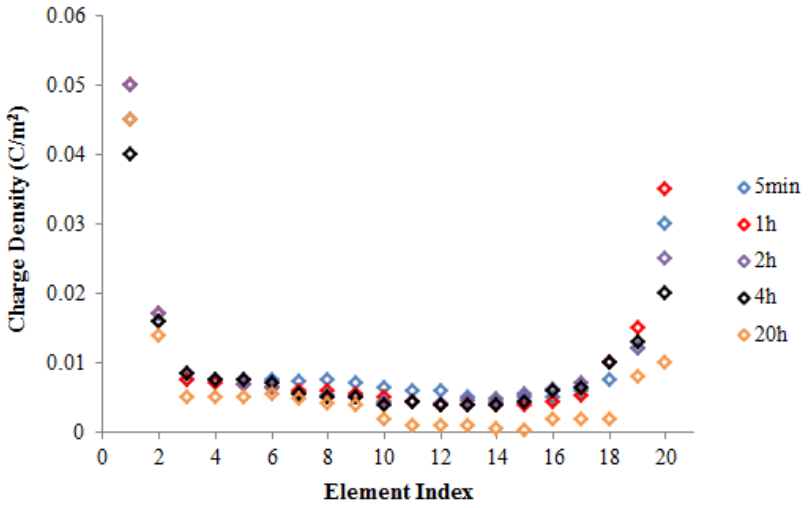

Figure 199: Charge densities for coated thin PMMA samples, corona charged with a grid voltage of 1 kV.

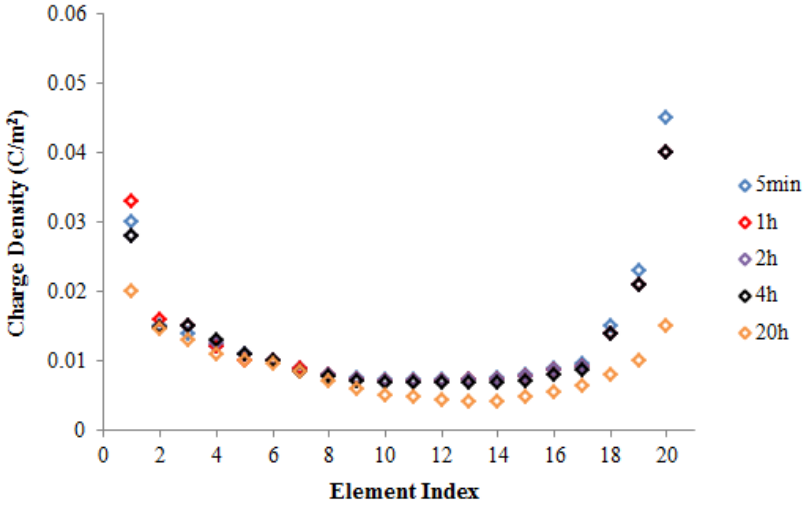

Figure 200: Charge densities for coated thin PMMA samples, corona charged with a grid voltage of 2 kV.

.

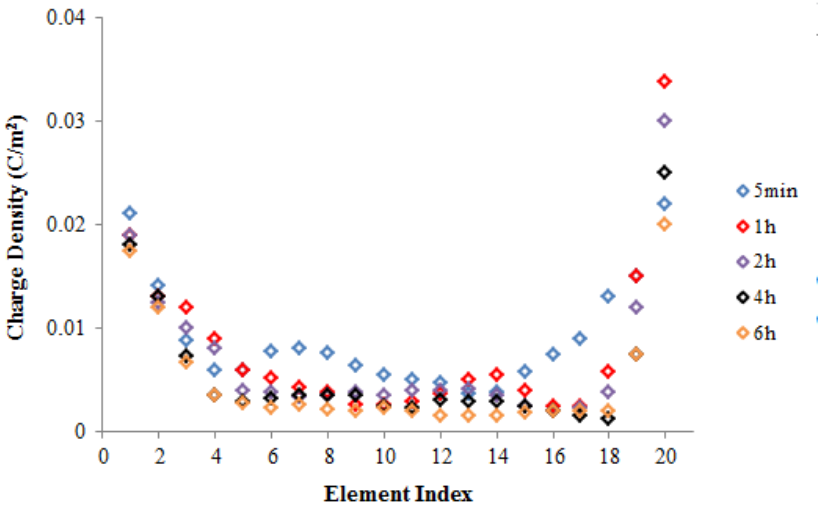

Figure 201: Charge densities for coated thick PMMA samples, corona charged with grid voltage of 1 kV.

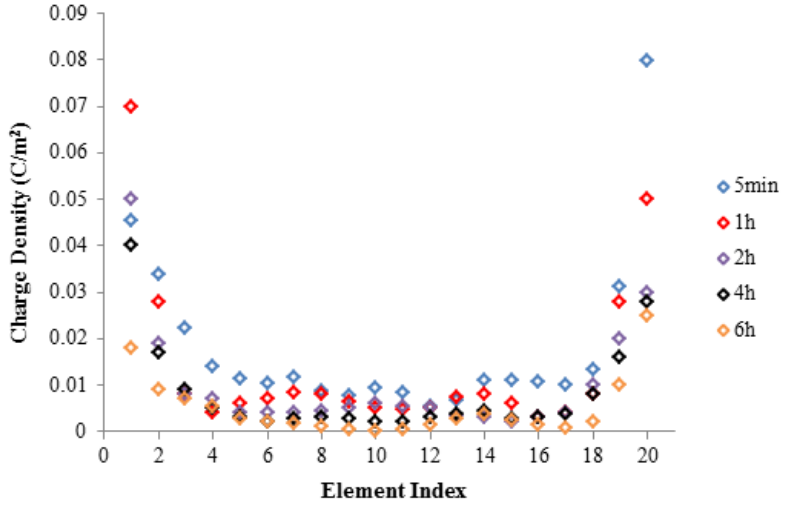

Figure 202: Charge densities for coated thick PMMA samples, corona charged with grid voltage of 2 kV.

From these plots of the charge densities, it can again be seen that the majority of the charge is concentrated in the regions close to the central and outer electrodes. The reason for this behaviour is not clear. It may be an inherent characteristic of the design of the experimental setup, or the migration of the charge to the grounded electrodes on the sample surface, causing more charge to be present closer to the surface electrodes. A more visible decay in the charge density distribution in the central part of the sample can be seen.

The charge density plots are divided into three regions similar to those of the uncoated samples. Figures 203 and 204 show plots of the average charge densities in the three discrete sections of the coated thin and thick samples, corona charged with a grid voltage of 1 kV.

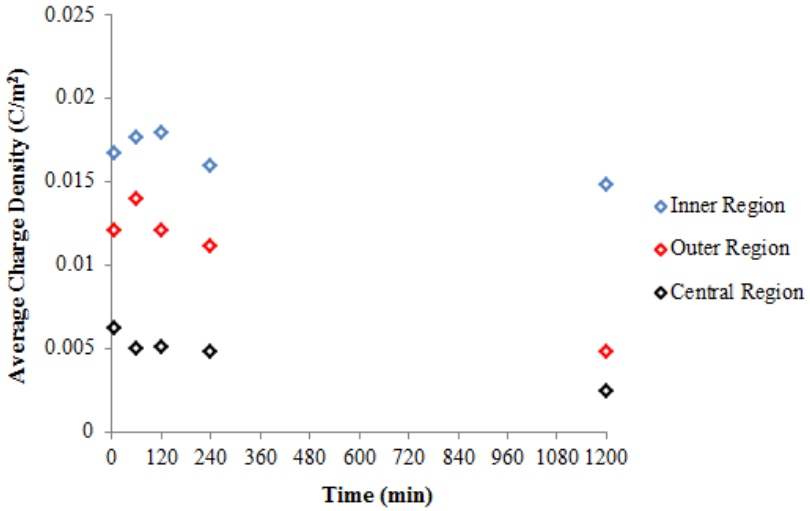

Figure 203: Charge densities in the 3 regions of the coated thin samples at 1 kV grid voltage.

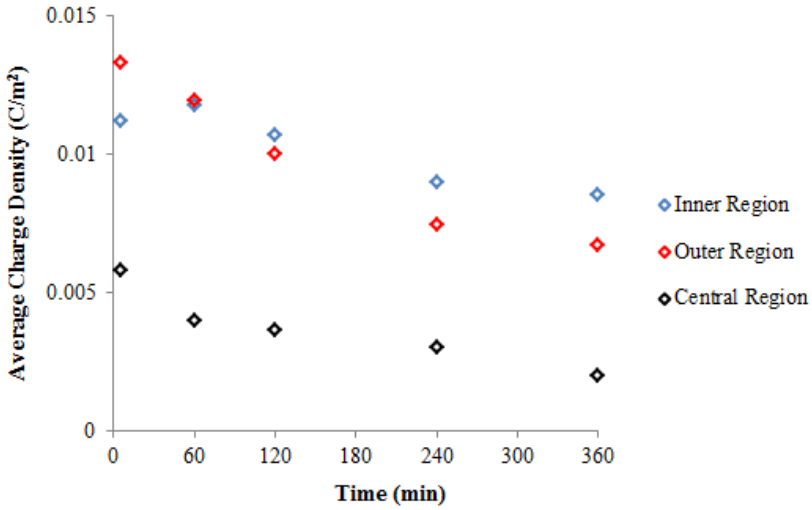

Figure 204: Charge densities in the 3 regions of the coated thick samples at 1 kV grid voltage.

From figures 203 and 204 it can be seen that for both the thin and thick PMMA samples, corona charged with a grid voltage of 1 kV, the largest amount of charge is generally concentrated in the regions close to the inner electrode. This is followed by the regions associated with the outer electrode, and the least amount of charge is present across the central part of the sample.

Figures 205 and 206 show the average charge density plots along the 3 discrete regions of the thin and thick PMMA samples, corona charged with a grid voltage of 2 kV.

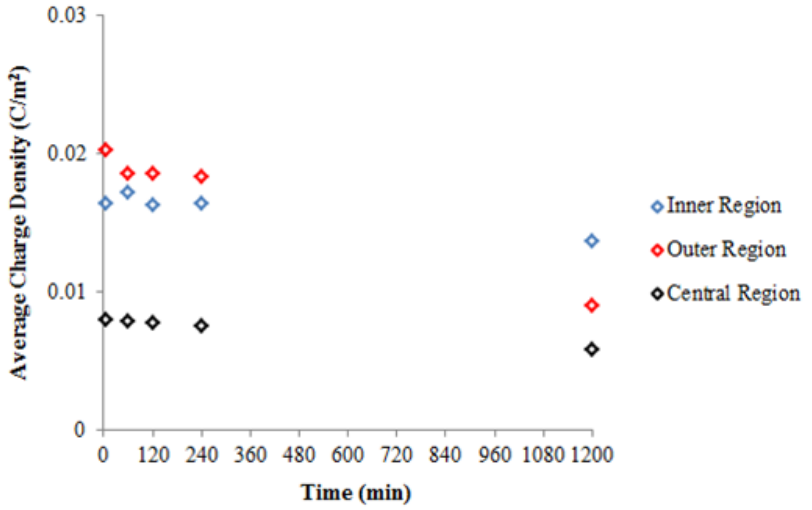

Figure 205: Charge densities in the 3 regions of the coated thin samples at 2 kV grid voltage.

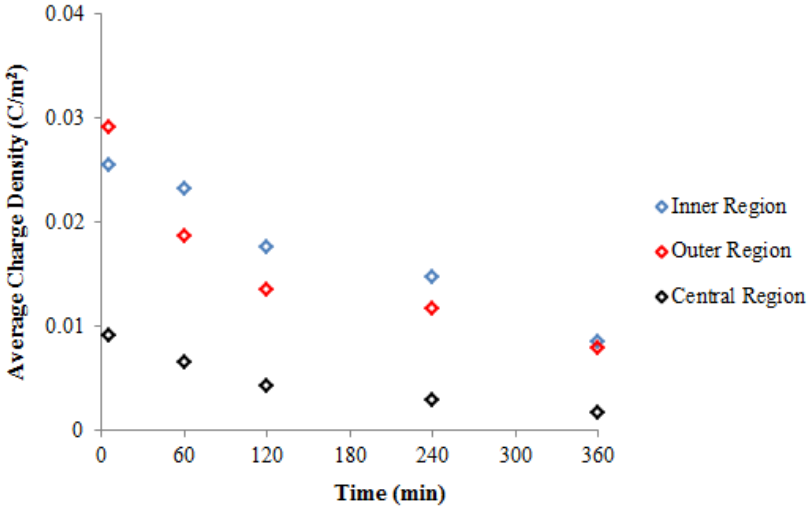

Figure 206: Charge densities in the 3 regions of the coated thick sample at 2 kV grid voltage.

From figures 205 and 206, it can be seen that for the thin PMMA samples charged at grid voltage of 2 kV the charge density is higher in the regions close to the outer electrode for the first 4 hours. Initially, the charge density close to the outer electrode is also higher for the thick samples. At longer times, the behaviour is similar to that seen for the uncoated samples, where the charge densities are larger in regions close to the inner electrodes, followed by the outer and the central regions of the samples.

It is also notable that, for the first 4 hours of the measurements, the charge densities present on the thin samples are generally larger than for the thick samples. This suggests that more charge remains on the surface of the thin samples as compared to the thick samples. The charge density plots also show that the decay of the charge densities on the thick PMMA samples is more significant than for the thin PMMA samples.

Figures 207 and 208 show a comparison of the average charge density across the sample surface for coated thin and thick PMMA, charged with grid voltages of 1 kV and 2 kV.

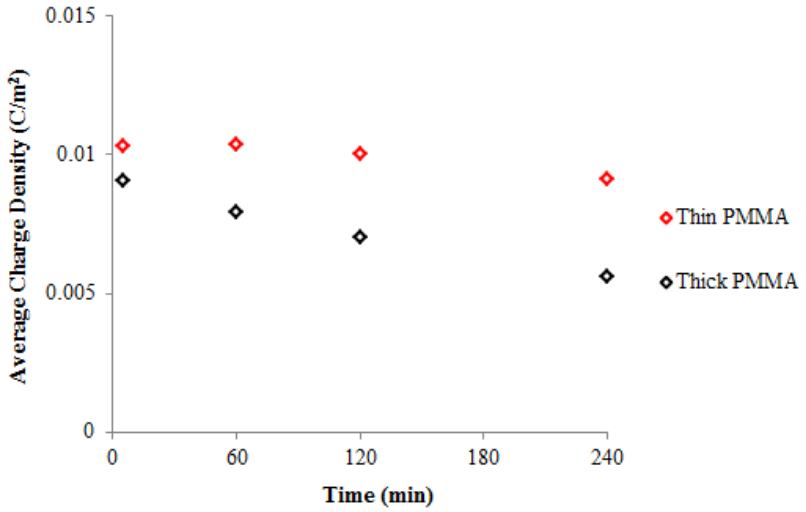

Figure 207: Charge densities across the coated thin and thick PMMA at 1 kV grid voltage.

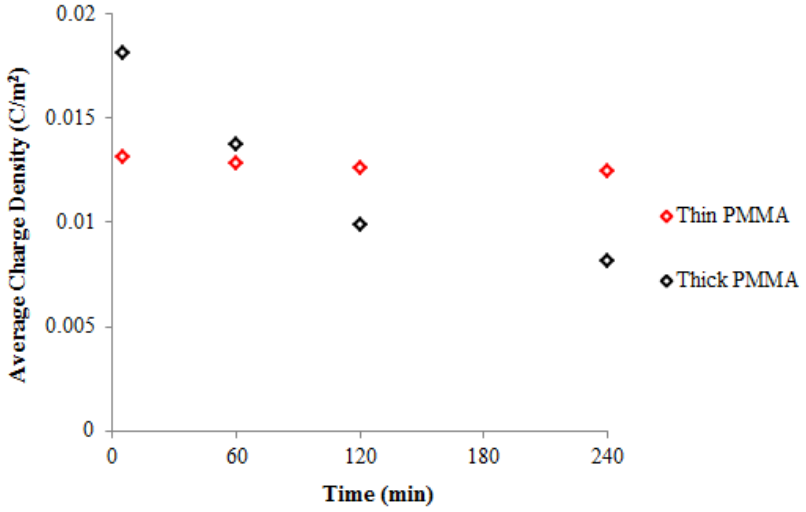

Figure 208: Charge densities across the coated thin and thick PMMA at 2 kV grid voltage.

From figures 207 and 208, it can be seen that the charge densities across the surface of the thin sample at longer times are larger than those for the thick sample. It is also observed that the charge density decays at a faster rate on the thick samples as compared to the thin samples. It is also notable that the average charge densities across the thin sample charged with a grid voltage of 2 kV are ~ 1.3 times greater compared to the thin PMMA charged with a grid voltage of 1 kV. The average charge densities initially across the thick sample charged with a grid voltage of 2 kV are ~ 2 times greater compared to the thick PMMA charged with a grid voltage of 1 kV. The average charge densities across the thick sample charged with a grid voltage of 2 kV are only ~ 1.4 times greater than that of thick sample charged with 1 kV

after 4 hours. This observation suggests that the charge density decays at a faster rate across the thick samples charged with higher grid voltages.

7.6. Discussion: Charge Decay Behaviour

7.6.1. Uncoated Samples

The charge density distributions observed across the uncoated PMMA samples indicated that the thick samples have a larger amount of charge on the surface as compared with the thin samples. It was also observed that, under the condition where the experiment is set up so that the principle mechanism of surface charge decay is through neutralisation by the surrounding gas environment, no significant charge density decay is observed. This suggests that charge remains on the surface of the sample for long periods of time. To verify this proposition, the total amount of charge on the surface of the samples was calculated using the derived charge density distributions. Figures 209 and 210 show the total surface charge across the thin and thick samples, corona charged with grid voltages of 1 kV and 2 kV.

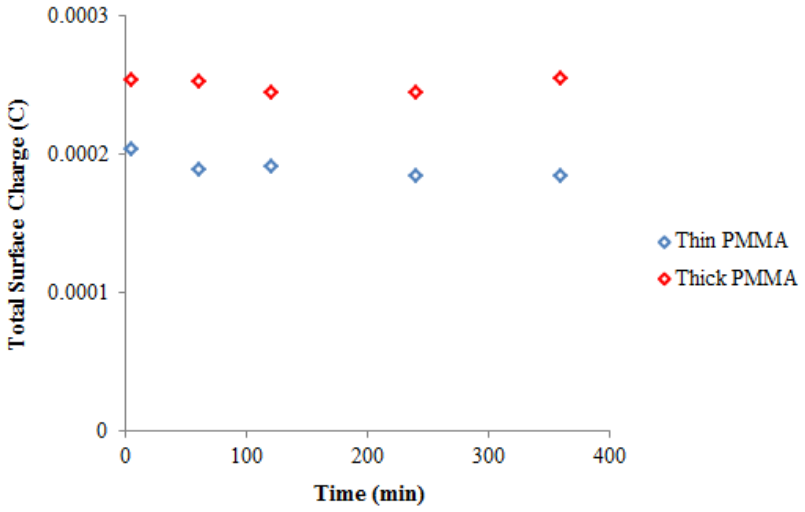

Figure 209: Total surface charge across uncoated thin and thick PMMA samples, corona charged with grid voltage of 1 kV.

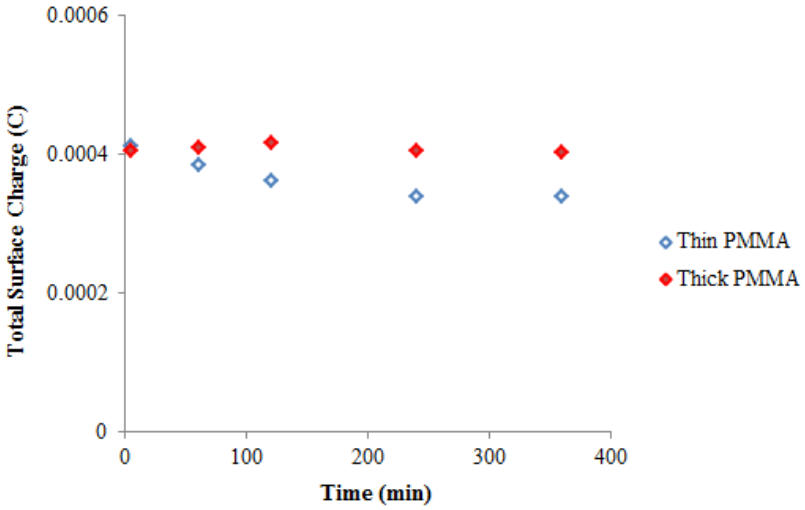

Figure 210: Total surface charge across uncoated thin and thick PMMA samples, corona charged with grid voltage of 2 kV.

The plots of the total charge across the surface of the thin and thick samples are consistent with the observations made from the results of the surface charge distributions. It can be seen that a significant charge decay is not evident for up to 6 hours after the charging of the samples for the thick PMMA. The thin PMMA charged with 2 kV grid voltage shows a more significant decay in the first 2 hours of measurement. It is also observed that larger amount of charge remains on the surface of the thick PMMA as compared to the thin PMMA. It is also notable that the total charge on the surface of the thin sample charged with grid voltage of 2 kV is ~ 2 times greater compared to the thin sample charged with grid voltage of 1 kV, whereas the total charge on the surface of the thick sample charged with grid voltage of 2 kV is ~ 1.6 times greater compared to the thick sample charged with grid voltage of 1 kV.

7.6.2. Coated Samples

The charge density distributions observed across the coated PMMA samples indicated that the thin samples have a larger amount of charge on the surface at longer times as compared to the thick samples. It was also observed that, under the condition where it is likely that the principle mechanism of surface charge decay is through surface conduction, charge density decay is more evident for both samples. A more significant charge density decay is observed for the thick PMMA.

The charge density distribution values were used to calculate the total charge across the surface of the thin and thick samples. An assumption was made that, at long times, the total charge on the surface of both the samples decays to a common value. From the experimental

data, this appeared to have a value of 4.0 × 10^{-5} C. Using this offset charge value $\boldsymbol{Q_o}$, the total surface charge for the thin and thick PMMA were plotted against time, and it was observed that charge decays exponentially, taking the form of equation 96.

$$\boldsymbol{Q(t) = Q_1 Exp\left(-\frac{t}{\tau 1}\right) + Q_o} \tag{96}$$

Figures 211 and 212 show plots of the total surface charge (C) against time (min) for thin and thick PMMA, charged with grid voltages of 1 kV and 2 kV and fitted with the relationship taking the form of equation 96. Table 31 shows the observed time constants and pre-exponential terms.

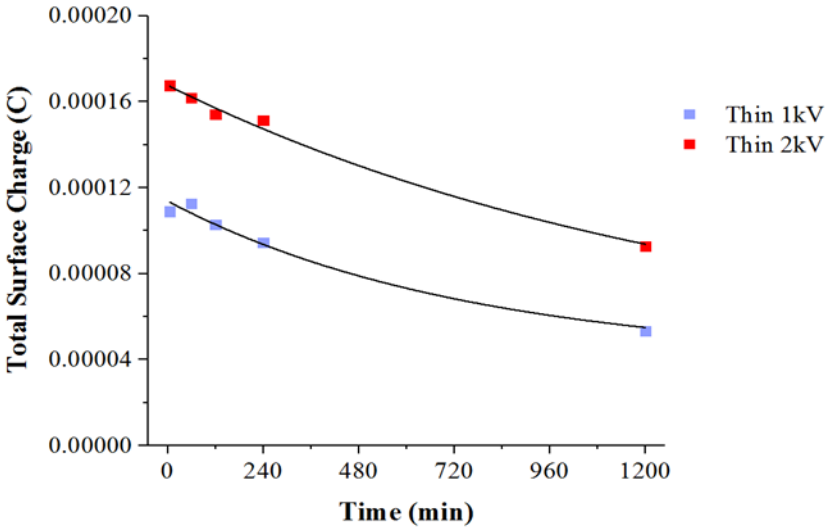

Figure 211: Total surface charge across coated thin PMMA for 1 kV and 2 kV grid voltages.

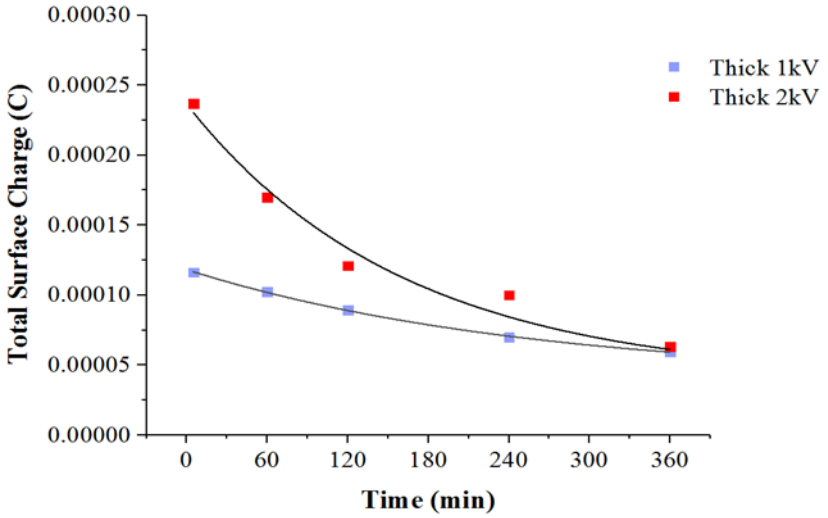

Figure 212: Total surface charge across coated thick PMMA for 1 kV and 2 kV grid voltages.

Table 31: Observed time constants and pre-exponential terms for the exponential fits applied to the total surface charge against time for thin and thick samples charged with grid voltages of 1 kV and 2 kV.

Sample	Grid Voltage (kV)	Time Constant (τ)	Pre-Exponential (Q_1)	R^2
Thin PMMA	1.0	752	7.40E-05	0.98
	2.0	1385	1.30E-04	0.99
Thick PMMA	1.0	257	7.82E-05	0.99
	2.0	162	1.96E-04	0.97

From figures 211 and 212, it can be seen that the total surface charge on the thin samples is generally greater than the thick samples over the period of 6 hours after charging the samples. It is also evident from figure 212 that, for thick PMMA charged with a 2 kV grid voltage, the charge decays at a faster rate than that for the thick sample charged with a 1 kV grid voltage. The thick sample charged with a grid voltage of 2 kV had an initial total surface charge that was ~ 2 times greater than the thick sample charged with a grid voltage of 1 kV. Further evidence of the faster decay rate of the thick sample charged with a 2 kV grid voltage can be seen from the measurement performed at 6 hours after charging the sample. It was observed that, at this measurement time the total charge across the thick sample charged with a higher grid voltage was approximately equal to that of the thick PMMA charged with the lower grid voltage.

These observations are reflected by the observed time constants in table 31, where it can be seen that the time constants for the thin PMMA are significantly longer than for the thick PMMA, indicating a slower decay rate. The time constant for the thick sample charged with the grid voltage of 2 kV is shorter than the time constant for the thick sample charged with the grid voltage of 1 kV, describing the differences observed in the charge decay rate for different grid voltages. The decay behaviour observed for the thick samples corresponds to the "crossover effect" which has been discussed in section 2.7. Many authors [41, 54, 55, 56] have reported seeing similar behaviours for charge decay, where samples charged with higher voltages tend to decay at faster rates than the samples charged with lower voltages. The time constants for the charge decay behaviours from table 31 were used to calculate the currents leaving the sample surface, shown in figures 213 and 214.

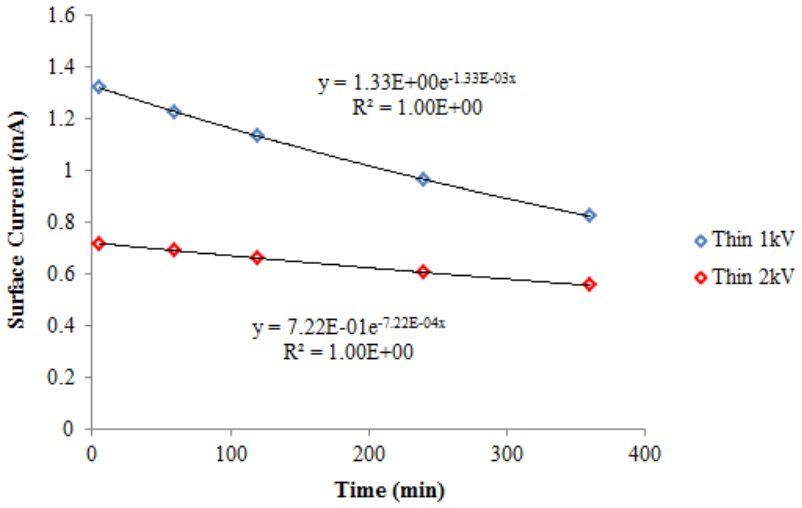

Figure 213: Currents across the surface of the thin PMMA.

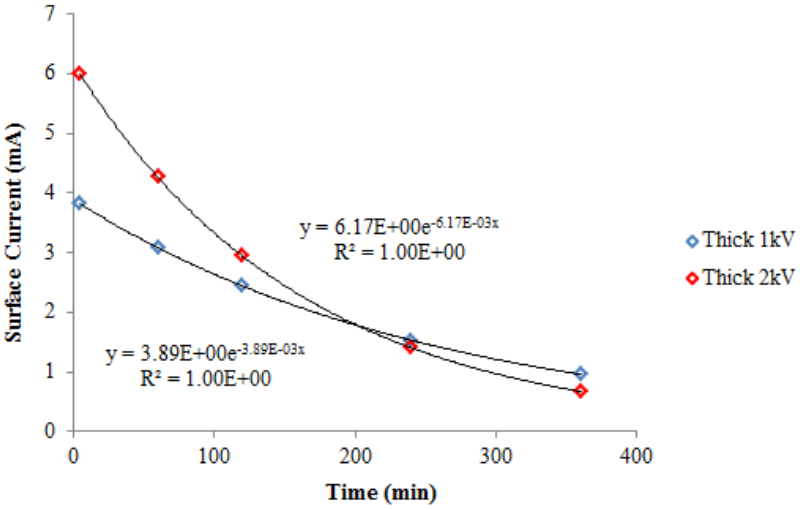

Figure 214: Currents across the surface of the thick PMMA.

From figure 213 and 214 it can be seen that the currents observed across the sample surface are of the order of milliamps. It can also be seen that the currents for the thin samples show a slower decay and are lower than for the thick samples. For the thick samples charged with a grid voltage of 2 kV, it can be seen that the currents across the surface of the sample decay at a faster rate and so much so that at ~ 200 mins a crossover (section 2.7) is observed, with the currents across the thick sample charged with a grid voltage of 1 kV. As the surface currents are calculated from the change in total surface charge with time, the crossover observed for the surface currents is supported by the crossover observed for the total surface charge. There is a monotonic dependence between the total surface charge and the surface current.

7.6.3. Correlations between Charge Decay Behaviours

In chapter 6, measurements were performed on the thin and thick PMMA samples to observe the charging and discharging transient behaviour for untreated and corona treated PMMA samples. During charging, an external electric field was applied across the surface of the samples. From these results, it was seen that the thin PMMA samples had a significantly shorter time constant than that of the thick samples. This suggested that charge was being removed much faster for the thin PMMA than for the thick PMMA with a field across the sample's surface. This was supported by the lower DC currents observed across the thin samples as compared to the thick samples.

The conclusion from chapter 6 is now compared to that of charge decay behaviours observed in the present experiments, where the decay was observed for conditions where no external field was applied across the sample surface. Under these conditions, the charge remained on the thin samples for much longer periods of time based on the observed time constants. These results suggest that there is a difference in the behaviour of the charge distribution with time when an external field is applied. It should also be noted that the measurements performed with corona treated samples in chapter 6 were made when charging the samples with a grid voltage of 0.5 kV compared to the 1 kV and 2 kV used for the grid voltage in the present experimental observations. Larger values of grid voltages were used in charge decay measurements to enhance the magnitude of signal that the varactor probe could measure. This would aid in increasing the accuracy of the measurements.

It is also observed that the currents flowing across the surface of the sample in chapter 6 were of the order of picoAmps, whereas the currents leaving the sample surface in the present experiment, calculated from the measured changes in surface charge with time, were of the order of miliAmps. The larger change in current for the present experiments is a result of the charge leaving the surface of the sample through paths on both the inner and outer electrodes. The lower currents observed in chapter 6 may be the result of the measured current being the difference of these two currents.

The charge decay behaviour in the present observations are in good correlation with the surface conductivities observed for observations made on corona treated samples in chapter 6. The surface conductivity for the thin samples was observed to be significantly lower than that for the thick samples and, based on this observation, it is expected that charge will remain on the thin samples for longer periods of time. Although the lower surface conductivity of the thin samples suggests that they are better insulators than the thick

samples, the higher amount of charge remaining on the surface of the thin samples is a problem, as this can promote flashover. This finding suggests that more research is required towards improving the electrical properties of insulators under high electric fields, as ideally an insulator would be required to have low surface conductivity and to not retain charge on its surface for long periods of time. Mohamad and Chen [146] performed chemical treatment on the surface of polymer samples (Bisphenol-A type epoxy resin) with the intention of modifying the charge transport characteristics of the subjected material via a fluorination process. The samples were subjected to different fluorination times. The resultant surface conductivities were measured by use of a test cell specifically developed to conduct surface conductivity measurements, based on the ASTM-D257 standard. The charge decay behaviours were measured using a JCI 140 static monitor over a 40 minute period. It was observed that the fluorination time of the samples slightly improved the surface conductivity of the materials, but also resulted in an increase of charge decay.

7.7. Chapter 7: Summary

In this chapter, measurements were performed to observe the charge decay behaviour along the surface of thin and thick PMMA samples using the varactor probe system constructed in chapters 3 and 4. The probe was calibrated against a metal test plate at the fixed gap separation for which the measurements were intended to be performed. The PMMA samples were corona charged by grid voltages of 1 kV and 2 kV. The probe was used to measure surface potentials across the sample surface at fixed positions covering the whole scanning region. Once the potentials were obtained, they were used in conjunction with the $\boldsymbol{\Phi}$-Matrix that was calculated via COMSOL to evaluate the charge densities across the sample surface using MATLAB. These charge densities were further analysed and data on the total charge across the sample surface was obtained and analysed.

The tests were performed under two decay conditions. In the first condition, measurements of the charge decay were conducted on uncoated samples to establish a condition where the most probable charge decay mechanism would be through neutralisation by the surrounding gas environment. In the second condition, the measurements were performed on coated samples. The coated parts of the samples were grounded while performing the measurements in an attempt to establish a condition where the most probable decay route was via surface conduction.

The charge densities observed for both test conditions across the surface of the thin and thick samples, charged with grid voltages of 1 kV and 2 kV showed a distribution where higher

amounts of charge were concentrated close to the inner and outer electrodes of the system on which the samples lay. The charge density distributions in the central region of the samples were fairly flat.

For the first condition, where charge is expected to decay through gas neutralisation mechanism, it was proposed that image charges on the inner and outer electrodes may have caused the charge build up in these areas resulting in noticeable peaks in the charge distribution plots. For the second condition, where charge is expected to decay through surface conduction, the charge density peaks in the region of the electrodes was not clear, however, it was proposed that this behaviour was either an inherent characteristic of the test set up or due to the migration of the charge towards the grounded surface electrodes on the samples, causing charge build up in these regions.

The charge density distributions were split into three sections to simplify the analysis. For the uncoated samples, it was observed that the largest amount of charge was concentrated near the inner electrode, this was followed by the region close to the outer electrode and then the central region of the sample. It was observed that the average charge densities across the thick samples were larger than those for the thin samples and no significant decay in the charge density was observed for the thick samples. However, for the thin samples, it was observed that a small decay may be occurring in the first 60 minutes after charging at 1 kV and a more significant decay appeared to occur over the first 2 hours of measurement after charging at 2 kV.

For the coated thick samples, the largest amount of charge was seen to be generally concentrated in the regions close to the inner electrode. This was followed by the regions associated with the outer electrode and the least amount of charge was observed to be present across the central part of the sample. For the thin PMMA samples charged at grid voltage of 2 kV, the charge density was higher in the regions close to the outer electrode for the first 4 hours. At longer times, the behaviour was similar to that seen for the uncoated samples. The average charge densities across the surfaces of the thin samples at longer times were larger than those for the thick samples and the charge density decays at a faster rate on the thick samples as compared to the thin samples.

Observations made for the total surface charge across the uncoated thick samples showed no significant charge decay for up to 6 hours after the charging. The uncoated thin PMMA charged with 2 kV grid voltage showed a more significant decay in the first 2 hours of measurement. It was also observed that a larger amount of charge remained on the surface of the uncoated thick PMMA samples as compared to the uncoated thin PMMA samples.

For the coated samples, a more noticeable decay in charge was observed. The total surface charge against time could be fitted with an exponential decay function, assuming that the charge on both the coated thin and thick samples decayed to a common value. In this case the total surface charge on the coated thin sample was observed to be generally greater than that for the coated thick sample. Analysis of the time constants supported the initial conclusions that the charge was decaying at a faster rate for coated thick samples charged at higher voltages as compared to those charged at lower voltages matching the "crossover" behaviour discussed in section 2.7.

In general, it can be concluded that significantly higher decay in charge is evident for the condition where the charge decays through surface conduction and no significant decay in the surface charge is observed for the condition where the charge decays through gas neutralisation mechanisms.

8. Conclusions and Future Work

This chapter summarises the achievements and conclusions drawn from the project and discusses the possible extensions of the research.

8.1. Achievements and Conclusions

The aim of this project was to enhance knowledge of the effect of accumulated charge on the surface conductivity, the surface charging/discharging behaviour and the surface charge decay behaviour of polymeric insulators. The project was carried out in 2 stages. In the first stage, experiments were conducted to observe surface charging/discharging transient currents for uncharged samples and samples charged by exposure to corona. In the second stage of the project, charge decay measurements were performed on uncoated and coated thick and thin samples subjected to corona charging with grid voltages of 1 kV and 2 kV. The experiments in this stage were carried out to mimic conditions where the majority of charge decay was expected to occur due to the mechanisms of neutralisation through the surrounding gas or through surface conduction.

During the course of this project the following achievements were made:

- A concentric cylindrical system was developed to allow the surface conduction processes on an insulator to be measured. The system had an added advantage of being able to be used for measurement of bulk conductivity of an insulator by adjusting the configuration of the electrodes. The system was tested for supply voltages of up to 10 kV and was able to resolve currents consistently with noise levels of the order of 10^{-2} pA.
- A varactor based surface potential measurement system has been developed and calibrated for sample surface voltages of up to 10 kV. The system was shown to be linear over this range of surface potentials. This is a novel approach to the measurement of surface charge on polymer surfaces.
- A simple test rig to allow surface charge to be deposited in a controlled manner was also developed. The system has been tested for grid voltages of up to 2 kV and needle voltages of up to 15 kV.
- Measurements of surface charging/discharging transients were conducted with good repeatability using the concentric cylindrical system. The transient currents were measured arising due to the application and removal of an electric field across the surface for applied voltages of up to 10 kV approximating to an average field of 2.5

$kVcm^{-1}$. Using these measurements, the behaviour of the observed transient currents was analysed and possible mechanisms for surface conductivity were identified.

- Surface potential measurements for the PMMA samples were conducted with good repeatability using the Varactor probe charge measurement system. A process was developed to use the measured potentials in conjunction with the evaluated $\boldsymbol{\Phi}$-matrix from COMSOL to calculate realistic surface charge distributions across the samples.
- The data obtained from the charge decay experiments was analysed and correlations of the results were made with those obtained from the transient current measurements made in the first part of the project.

The observations from the test results and the resulting conclusions drawn from these observations throughout the project are as follows:

- From the results of the charging transient current measurements where an electric field was applied across the surface of the thick and thin PMMA samples using the concentric cylindrical arrangement, it was observed that the time dependence of these transients is complex and can be modelled using a combination of three exponential processes. There are suggestions that there is a 4^{th} decay process present but the magnitude of the observed currents < 0.1 pA make this difficult to resolve using the present system.
- After fitting the charging transient data with the 3 term exponential function it was observed that the values of the time constants τ_1 and τ_2 associated with faster processes, for untreated and corona treated PMMA were common and were not influenced by the sample thickness or the pre-existence of charge on the sample surface. The time constant at longer times τ_3, had a common value for thin samples, independent of whether the surface had been charged. This time constant was significantly shorter than the values obtained for thick samples where τ_3 was again independent of the charging of the surface.
- When analysing the DC current behaviour, it was observed that the DC currents across the surface of thin PMMA samples were significantly lower than those for the thick PMMA samples.
- The DC current observations showed higher current magnitudes for corona charged samples as compared to the uncharged samples, suggesting that the presence of surface charge enhances the conductivity of the samples. A more significant increase in the DC current across the thick PMMA samples was observed.
- When analysed against supply voltage, the behaviour of the DC current was observed to be linear up to voltages of ~ 6 kV, after which a rapid increase in the currents was observed. The behaviour was observed to follow the trend expected as a result of the

"Schottky" or "Hopping" conduction mechanisms. Data at higher voltage levels would be required to distinguish between these mechanisms.

- For the measurements conducted on the charge decay behaviour across the surface of the PMMA samples using the varactor probe system, it was observed from the evaluated charge distribution plots that the majority of the charge for both the uncoated and coated samples was concentrated near the electrodes. For the uncoated samples, it was proposed that the image charges on the inner and outer electrodes may have caused the charge build up in these areas resulting in noticeable peaks in the charge distribution plots. The reason for the charge density peaks in the region of the coated samples was not clear. It was proposed that this behaviour was an inherent characteristic of the test setup, or due to the migration of the charge towards the grounded surface electrodes on the samples.
- The total surface charge for the uncoated samples did not show a significant decay over the course of the measurement period. The total charge on the thick samples remained relatively constant, whereas the thin samples showed a more noticeable decay in the first 2 hours of measurement after charging at 2 kV. A larger amount of charge remained on the surface of the thick PMMA samples.
- For the coated samples, a more significant decay was observed in the total surface charge for both samples. The total surface charge on the coated thin samples was observed to be greater than that for the coated thick samples. It was observed that the charge was decaying at a faster rate for thick samples charged at higher voltages compared to the thick samples charged at lower voltages. The shorter time constant for the thick sample charged at higher voltage compared to the thick sample charged at lower voltage also showed that the decay rate of charge was dependent on the degree of surface charging. The observed behaviour tends to follow the "crossover" effect discussed in section 2.7. The behaviour of the total surface charge on the samples followed an exponential decay and the time constants for the thin samples were significantly longer than those for the thick samples suggesting that charge remained on the thin samples for longer periods of time.
- In general, it was concluded that a significantly higher decay in charge is evident for the condition where the charge decays through surface conduction and no significant decay in the surface charge is observed through gas neutralisation mechanisms.
- The charge decay behaviour for the condition where no electric field was applied across the sample surface is in good correlation with the surface conductivities observed for

observations made on corona treated samples in chapter 6, where the surface conductivity for the thin samples was observed to be significantly lower than for the thick samples.

- It was also observed that the currents flowing across the surface of the samples in chapter 6 under the influence of an external field were of the order of picoAmps, whereas the currents leaving the sample surface in the condition where no electric field is applied across the sample surface were of the order of milliAmps. The larger change in current is a result of the charge leaving the surface of the sample through paths on both the inner and outer electrodes. The lower currents observed in chapter 6 may be the result of the measured current being the difference of these two currents.
- The concentric measurement system developed in this project, can be particularly beneficial to researchers conducting surface transient current and surface conductivity measurements on thin and thick polymer samples. The developed system is able to resolve small currents consistently with noise levels of 10^{-2}pA and is proposed as an improvement on the standard ASTM-D257, as the effect of the bulk component on the measured surface currents is negligible.
- The developed varactor probe provides an alternative to researchers performing charge decay measurements on the surface of polymeric materials and to detect static electric fields. It is proposed as an improvement on the traditional capacitive probes and the measured signal is not limited due to the frequency of the mechanical vibrations of the sensor plate. The prototype developed in this project can be improved further to obtain a better resolution and sensitivity.

8.2. Future Work

There are several ways the work conducted in this project could be developed and taken forward:

- A system where the surface charge distribution could be consistently measured after an external field had been applied across the surface of the sample for a time period would allow a better comparison of the transient current and surface charge measurements. The design of such a system is not clear, as the insertion of a probe in the concentric cylindrical system could lead to noise being introduced in the measurements; also, a discharge between the high voltage electrode and the probe is likely, as the probe moves closer to the high voltage electrode while scanning the surface of the sample.

- To allow a better understanding of the non-linear behaviour observed in the DC currents at higher voltage levels, surface transient current measurements should be carried out over a larger range of supply voltages.
- The development of a system to allow the transient currents at very long times to be measured would help in evaluating further decay processes that maybe happening at longer times, although the fundamental resolution of the electrometer may limit this. Conducting the experiments in an environment where the temperature and humidity were controlled more strictly would also be required.
- The varactor probe worked well, however it was a prototype and its design and manufacture could be significantly improved as could the control of probe position and processing of data.
- In this project, the conductivity measurement system was initially developed to perform both surface and bulk conductivity measurements. Due to the time spent on the development and calibration of the conductivity measurement system and the varactor probe system, it was not possible to conduct bulk current measurements. In the future, measurements of the transient current behaviours through the bulk of the samples can be conducted by using this test cell in bulk measurement mode as described in section 5. The current transient behaviours through the bulk of the material can then be compared to the surface current behaviours observed in this project.
- Investigate other polymer materials.

References

[1] Y. Ohki, N. Fuse and T. Arai, “Band Gap Energies and Localized States in Several Insulating Polymers Estimated by Optical Measurements,” in *Annual Report Conference on Electrical Insulation and Dielectric Phenomena*, West Lafayette, USA, 2010.

[2] L. Dissado and J. Fothergill, Electrical Degradation and breakdown in Polymers, London, UK: Peter Peregrinus Ltd., 1992.

[3] K. Kao, “Electrical Conduction and Breakdown in Insulating Polymers,” in *6th International Conference on Properties and Applications of Dielectric Materials*, Xi’an, June 2000.

[4] M. Ieda, “Dielectric Breakdown Process of Polymers,” *IEEE Transactions on Electrical Insulation,* Vols. E1-15, no. 3, pp. 206-224, June 1980.

[5] I. Al-Bawy, Surface Charging and Impulse Flashover of Insulating Spacer in SF6, PhD Thesis, Glasgow, UK: University of Strathclyde, June 1990.

[6] M. Ieda, “Electrical Conduction and Carrier Traps in Polymeric Materials,” *IEEE Transactions on Electrical Insulation,* vol. 3, no. E1-19, pp. 1-19, 1984.

[7] H. von Seggern, “New Developments in Charging and Discharging of Polymers,” *IEEE Transactions on Electrical Insulation,* Vols. E1-21, no. 3, pp. 281-288, June 1986.

[8] J. Davidson, A Study of Surface Phenomena on Dielectrics in Pressurised Gasses, PhD Thesis, Glasgow, UK: University of Strathclyde, 1979.

[9] V. Bloshchitsyn, “A review of Surface Discharge experiments,” in *Plasma Physics,* St.-Petersburg State University, May 2010.

[10] R. Fouracre, E. Santos, I. Timoshkin, M. Given and S. Macgregor, “Surface Discharge Propagation: The Influence of Surface Charge,” *Twenty-Seventh International Power Modulator Symposium,Arlington, VA,* pp. 39-42, May 2006.

[11] F. Messerer, M. Finkel and W. Boeck, “Surface Charge Accumulation on HVDC-GIS-Spacer,” *8th International Symposium on Electrical Insulation,* pp. 421-425, April 2002.

[12] E. Kuffel, F. Wang, Q. Zhang and Y. Qiu, “Insulator Surface Charge Accumulation under DC Voltage,” *IEEE Transactions on Electrical Insulation,* pp. 426-429, April 2002.

[13] P. Connolly, Surface charging and Flashover on Insulators, PhD Thesis, Glasgow, UK: University of Strathclyde, 1984.

[14] L. Caliap, O. Lesaint, A. Denat and N. Bonifaci, “Influence of a metallic particle at a metal/insulator/gas triple junction in air and SF6,” *IEEE Conference on Electrical Insulation and Dielectric Phenomena,Virginia Beach, VA,* pp. 364-367, Oct 2009.

[15] A. Pederson, “On the electrical breakdown of gaseous dielectrics-an engineering approach,” *IEEE Transactions on Electrical Insulation,* vol. 5, no. 5, pp. 721-739, Oct 1989.

[16] C. Tran Duy, N. Bonifaci and A. Denat, “Partial discharges at a triple junction metal/solid insulator/gas and simulation of inception voltage,” *Journal of Electrostatics,* vol. 66, no. 5-6, pp. 319-327, May 2008.

[17] J. Leghari and A. Qureshi, “Surface Flashover of Spacers in Compressed Gas Insulated Systems,” *IEEE Transactions on Electrical Insulation,* Vols. E1-16, no. 5, pp. 373-387, Oct 1981.

[18] C. Cooke, R. Wootton and A. Cookson, “Influence of particles on AC and DC electrical performance of gas insulated systems at extra-high-voltage,” *IEEE Transactions on Power Apparatus and Systems,* vol. 96, no. 5, pp. 768-777, May 1977.

[19] K. Srivastava and M. Morocos, “A Review of Some Critical Aspects of Insulation Design of GIS/GIL Systems,” *Transmission and Distribution Conference and Exposition, Atlanta, GA,* vol. 2, pp. 787-792, Nov 2001.

[20] C. Lederle and J. Kindersberger, “The influence of surface roughness and coating on the impulse breakdown voltage in SF6,” *Conference on Electrical Insulation and Dielectric Phenomena,* pp. 522-525, Oct 2004.

[21] Y. Yamano, S. Kobayashi and Y. Takahashi, “Reduction of Surface Charge Induced

Electric Field Enhancement and Increase in AC Surface Flashover Voltage," *IEEE Transactions on Electrical Insulation,* Vols. E1-20, pp. 529-536, June 1985.

[22] J. Deng, S. Matusuoka, A. Kumada and K. Hidaka, "The influence of residual charge on surface discharge propagation," *J. Phys. D: Appl. Phys.*, vol. 43, no. 49, Nov 2010.

[23] O. Farish, R. Fouracre and J. Al-Najmawi, "Charging mechanisms of polymer spacers electrically stressed in SF6 environment," *Conference on Electrical Insulation and Dielectric Phenomena,Victoria, BC,* pp. 166-171, Oct 1992.

[24] S. Okabe, "Phenomena and Mechanisms of Electric Charges on spacers in Gas Insulated Switchgears," *IEEE Transactions on Dielectrics and Electrical insulation,* vol. 14, no. 14, pp. 46-52, Feb 2007.

[25] Z. Fang, R. Fouracre and O. Farish, "Investigations of surface charging of DC insulator spacers," *Conference on Electrical Insulation and Dielectric Phenomena,* vol. 1, pp. 149-152, Oct 1996.

[26] D. Davies, "The examination of the electrical properties of insulators by surface charge measurement," *Journal of Science and Instrumentation,* vol. 44, pp. 521-524, 1967.

[27] D. Das-Gupta, "Surface Charge Decay on Insulating Films," *Second International Conference on Properties and Applications of Dielectric Materials, Beijing,* vol. 2, pp. 602-605, Sep 1988.

[28] R. Dougal and T. Sudarshan, "Mechanisms of Surface Flashover along Solid Dielectrics in Compressed Gases: A Review," *IEEE Transactions on Electrical Insulation,* Vols. EI-21, no. 5, pp. 727-745, Oct 1986.

[29] C. Mangelsdorf and C. Cooke, "Bulk Charging of Epoxy Insulation under DC Stress," *Proc. IEEE International Symposium on Electrical Insulation, Boston,* pp. 146-149, 1980.

[30] J. Cross and T. Sudharshan, "Effects of Oxide Coatings on Surface Flashover of Dielectric Spacers in Vacuum," *IEEE Transactions on Electrical Insulation,* no. 4, pp. 146-150, Dec 1974.

[31] J. Giacometti and O. Oliveira, "Corona Charging of Polymers," *IEEE Transactions on Electrical Insulation,* vol. 27, no. 5, pp. 924-943, Oct 1992.

[32] S. Kumara, Electrical Charges on Polymeric Insulator Surfaces and their Impact on Flashover Performance, PhD Thesis, Gothenburg, Sweden: Chalmers University of Technology, 2012.

[33] I. Campbell, P. David's and D. Smith, "The Schottky energy barrier dependence of charge injection in organic light-emitting diodes," *Applied Physics Letters: Semiconductors,* vol. 72, no. 15, pp. 1863-1865, 1998.

[34] H. Wintle, "Schottky Injection Currents in Insulators: The effect of Space Charge on time dependence," *IEEE Transactions on Electrical Insulation,* Vols. EI-12, no. 6, Dec 1997.

[35] F.C.Chiu, "A Review on Conduction Mechanisms in Dielectric Films," in *Advances in Materials Science and Engineering,* Article ID 578168, 2014.

[36] A. Imano, "Accumulation of surface charges on the particle contaminated spacer surface in compressed gas under impulse voltage stress," *Journal of Electrostatics,* vol. 61, no. 1, pp. 1-19, May 2004.

[37] O. Farish and P. Connolly, Surface Charge Measurement in Air and SF6, New York: pp. 405-413, Gaseous Dielectrics IV, Pergamon Press, 1984.

[38] K. Srivastra and J. Zhou, "Surface Charging and Flashover of Spacers in SF6 under Impulse Voltage," *IEEE Transactions on Electrical Insulation,* vol. 26, no. 3, pp. 428-442, 1991.

[39] F. Wang, Y. Qiu, W. Pfeiffer and E. Kuffel, "Insulator Surface Charge Accumulation under Impulse Voltage," *IEEE Transactions on Dielectrics and Electrical Insulation,* vol. 11, no. 5, pp. 847-854, Oct 2004.

[40] M. Ieda, G. Sawa and I. Shinohara, "A decay Process of Surface Electric Charges across Polyethylene Film," *Journal of Applied Physics,* vol. 6, p. 793–794, 1967.

[41] T. Mizutani, T. Oomura and M. Ieda, "Surface Potential Decay in Polyethylene," *Journal of Applied Physics,* vol. 20, p. 855–859, 1989.

[42] R. Coelho, "The electrostatic Characterization of Insulating Materials," *Journal of Electrostatics,* vol. 17, no. 1, pp. 13-27, 1985.

[43] H. Wintle, "Decay of Static Electrification by Conduction Processes in Polyethylene," *Journal of Applied Physics,* vol. 41, no. 10, p. 4004–4007, 1970.

[44] M. Debska, “Surface Potential Decay on Triglycine Sulfate Crystal,” *Journal of Electrostatics,* vol. 63, no. 11, p. 1017–1023, 2005.

[45] P. Llovera and P. Molinié, “New Methodology for Surface Potential Decay Measurements: Application to Study Charge Injection Dynamics on Polypropylene Films,” *IEEE Transactions on Dielectrics and Electrical Insulation,* vol. 11, no. 6, Dec 2004.

[46] G. Chen, Z. Xu and L. Zhang, “Measurement of the Surface Potential Decay of Corona-Charged Polymer Films Using the Pulsed Electroacoustic Method,” *Journal of Measurement Science and Technology,* vol. 18, no. 5, pp. 1453-1458, 2007.

[47] Z. Li, B. Du*, H. Xu, H. Du and Y. Gao, “Surface Charge Decay of Direct-fluorinated RTV Silicone Rubber/Si02 Nanocomposites,” *Conference Proceedings of ISEIM,* pp. 477-480, Aug 2004.

[48] S. Kumara and B. Ma, “Surface Charge Decay on HTV Silicone Rubber: Effect of Material Treatment by Corona Discharges,” *IEEE Transactions on Dielectrics and Electrical Insulation,* vol. 19, no. 6, Dec 2012.

[49] A. Neves and H. Martins, “Surface Charging and Charge Decay in Solid Dielectrics,” *IEEE International Symposium on Electrical Insulation,* pp. 782- 786, June 1996.

[50] P. Molinié, “Charge Injection in Corona-Charged Polymeric Films: Potential Decay and Current Measurements,” *Journal of Electrostatics,* vol. 45, no. 4, pp. 265-273, 1999.

[51] L. Trémas, B. Ohl and O. Lesaint, “Measurements of Surface Potential Decay on Polyphthalamide (PPA) Composite,” *IEEE International Conference on Dielectrics,* vol. 1, pp. 276- 279, 2016.

[52] L. Herous and M. Nemamcha, “Factors that influence the surface potential decay on a thin film of polyethylene terephtalate (PET),” *Journal of Electrostatics,* vol. 67, no. 2-3, pp. 198-202, 2009.

[53] M. Ieda, G. Sawa and I. Shinohara, “A decay Process of Surface Electric Charges across Polyethylene Film,” *Journal of Applied Physics,* vol. 6, pp. 793-794, 1967.

[54] H. Von Berlepsch, “Interpretation of surface potential kinetics in HDPE by a trapping model,” *Journal of Applied Physics,* vol. 18, pp. 1155- 1170, 1985.

[55] E. Neaqu, P. Pissis, L. Apekis and J. Ribelles, “Dielectric Relaxation Spectroscopy of Polyethylene Terephthalate (PET) Films,” *Journal of Applied Physics,* vol. 30, no. 11, p. 1551–1560, 1997.

[56] L. Herous, M. Remadnia*, M. Kachi and M. Nemamcha, “Decay of Electrical Charges on Polyethylene Terephthalate Surface,” *Journal of Engineering Science and Technology Review 2 (1),* pp. 87-90, 2009.

[57] P. Molinié, “Potential Decay Interpretation on Insulating Films: Necessity of Combining Charge Injection and Slow Volume Polarization Process,” *7th International Conference on Dielectric Materials, Measurements and Applications,* pp. 50-55, 1996.

[58] Z. Xu, L. Zhang and G. Chen, “Measurement and analysis of electric potential decay in corona charged low-density polyethylene films,” *International Conference on Solid Dielectrics,* pp. 454- 457, July 2007.

[59] E. Baum, T. Lewis and R. Toomer, “The Lateral Spreading of Charge on Thin Films of Polyethylene Terephthalate,” *Journal of Applied Physics,* vol. 11, pp. 963-977, 1978.

[60] T. Gaertner, T. Stoop, J. Tom, H. Verhaart and A. Verhage, “Decay of surface charges on insulators in SF6,” *IEEE International Conference on Electrical Insulation,* pp. 208-213, 1984.

[61] K. Nakanishi, A. Yoshioka, Y. Shibuya and T. Nitta, “Charge Accumulation on Spacer Surface at DC Stress in Compressed SF6 Gas,” *Gaseous Dielectrics III, Pergamon Press,* pp. 365-372, 1982.

[62] H. Hama, T. Hikosaka, S. Okabe and H. Okubo, “Cross-equipment Study on Charging Phenomena of Solid Insulators in High Voltage Equipment,” *IEEE Transactions on Dielectrics and Electrical Insulation,* vol. 14, no. 2, pp. 508- 519, 2007.

[63] S. Bektas, I. Somerville, O. Farish and I. Chalmers, “Measurement of the Temporal Decay of Charges on Insulator Surfaces,” *Gaseous Dielectrics V, Pergamon Press,* pp. 553-559, 1987.

[64] A. Kumada and S. Okabe, “Charge Distribution on a Truncated Cone Spacer under DC Voltage,” *IEEE Transactions on Dielectrics and Electrical Insulation,* vol. 11, no. 6,

pp. 929-938, 2004.

[65] I. McAllister, “Decay of Charge Deposited on the Wall of a Gaseous Void,” *IEEE Transactions on Electrical Insulation,* vol. 27, no. 6, pp. 1202-1207, 1992.

[66] L. Zang, G. Chen and Z. Xu, “Decay of Electric Charge on Corona Charged Polyethylene,” *Journal of Physics: Conference Series 142, ID: 012060,* 2008.

[67] J. Kindersberger and C. Linderle, “Surface Charge Decay on Insulators in Air and Sulfurhexafluorid – Part 2: Measurements,” *IEEE Transactions on Dielectrics and Electrical Insulation,* vol. 15, no. 4, pp. 949-957, Aug 2008.

[68] J. Kindersberger and C. Linderle, “Surface Charge Decay on Insulators in Air and Sulfurhexafluorid – Part I: Simulation,” *IEEE Transactions on Dielectrics and Electrical Insulation,* vol. 15, no. 4, pp. 941-948, Aug 2008.

[69] D. Das-Gupta, “Electrical properties of surface of polymeric insulators,” *IEEE Transactions on Dielectrics and Electrical Insulation,* vol. 27, no. 5, pp. 909-923, 1992.

[70] S. Kumara and Y. V. Serdyuk, “Surface Charge Decay on Polymeric Materials under Different Neutralization Modes in Air,” *IEEE Transactions on Dielectrics and Electrical Insulation,* vol. 18, no. 5, pp. 1779-1788, Oct 2011.

[71] P. Molinié and P. Llovera, “Surface potential measurement: implementation and interpretation,” *8th IEEE International Conference on Dielectric Materials, Measurement and Applications,* pp. 253-258, 2000.

[72] P. Molinié, “Measuring and Modelling Transient Insulator Response to Charging: the Contribution of Surface Potential Studies,” *IEEE Transactions on Dielectrics and Electrical Insulation,* vol. 12, no. 5, pp. 939-950, Oct 2005.

[73] R. Hill, “Relaxation of Surface Charge,” *Journal of Physics C: Solid State Physics,* vol. 8, no. 15, pp. 2488-2501, 1975.

[74] T. Sonnonstine and M. Perlman, “Surface potential decay in insulators with field dependent mobility and injection efficiency,” *Journal of Applied Physics,* vol. 46, pp. 3975-3981, 1975.

[75] S. Alam and Y. V. Serdyuk, “Contribution of Gas Neutralization to the Potential Decay on Silicon Rubber Surfaces at Different Ambient Pressures,” *IEEE*

International Conference on High Voltage Engineering and Application, Sep 2014.

[76] Y. Takahashi, "TWO HUNDRED YEARS OF LICHTENBURG FIGURES," *Journal of Electrostatics,* vol. 6, no. 1, pp. 1-13, Feb 1979.

[77] T. Kawasaki, Y. Arai and T. Takada, "Measurement of Electrical Surface Charge Distribution on Insulating Material by Electrooptic Pockels Cell," *IEEE Conference on Electrical Insulation and Dielectric Phenomena Annual Report.,* pp. 373-378, 1990.

[78] S. Yamaguchi, M. Noras and T. Williams, "New Surface Electrostatic Potential Measurement Technology," *ESD Forum, Munich,* 2007.

[79] G. Crichton and I. McAllister, "Surface Charge Measurement Using Electrostatic Probe," *IEE Colloquium on Surface Phenomena Affecting Insulator Performance,* pp. 7/1-7/4, Jan 1998.

[80] M. Noras, "Non- Contact Surface Charge/ Voltage Measurements: Capacitive Probe – Principle of Operation," *Trek Application Note, no. 3001,* 2002.

[81] M. Noras, "Non- Contact Surface Charge/ Voltage Measurements: Field meter and Voltmeter Methods," *Trek Application Note, no. 3002,* 2002.

[82] A. Pandey, J. Kieres and M. Noras, "Verification of non-contacting surface electric potential measurement model using contacting electrostatic voltmeter," *Journal of Electrostatics,* vol. 67, no. 2-3, pp. 453-456, 2009.

[83] M. Noras and A. Pandey, "Surface Charge Density Measurements: Uses and Limitations of Kelvin probe-based instruments," *IEEE Industry Applications Magazine,* pp. 41-47, 2010.

[84] T. Oda and K. Ueno, "Surface Charge Density Measurement of Dielectric Films Using Ultrasonic Vibrations," *IEEE Transactions on Electrical Insulation,* Vols. EI-21, pp. 375-381, June 1986.

[85] S. Kumara, I. Haq and S. Alam, "Surface Charges on Cylindrical Polymeric Insulators," *IEEE Transactions on Dielectrics and Electrical Insulation,* vol. 19, no. 3, pp. 1076-1083, June 2012.

[86] S. Miles, T. Bond and J. Meyer, "Report on Non-Contact DC Electric Field Sensors," *Lawrence Livermore National Laboratory, LLNL-TR-414129,* June 2009.

[87] Z. Zou, X. Cui and T. Lu, “Impact of Space Charges From Direct Current Corona Discharge on the Measurement by the Rotating Electric-Field Meter,” *IEEE Transactions on Power Delivery,* vol. 31, no. 4, pp. 1517 - 1523, AUG 2016.

[88] W. Pfeiffer, D. Schoen and C. Zender, “Advanced method of surface potential measurement with a field mill probe,” *IEEE Conference on Electrical Insulation and Dielectric Phenomena Annual Report.,* 1998.

[89] A. Fatihou, L. Dascalescu and N. Zouzou, “Interpretation of surface potential measurements performed with the vibrating capacitive probe of an electrostatic voltmeter,” *IEEE Industry Application Society Annual Meeting,* 2014.

[90] H. Herscovici, “Input Offset Voltage and Current in Varicap Diode Modulators,” *IEEE Transactions on Instrumentation and Measurement,* vol. 28, no. 1, pp. 36-41, 1979.

[91] M. Noras, “Electric Field Sensor Based on a Varactor Diode/MIS/MOS Structure,” *IEEE Industry Applications Society Annual Meeting (IAS),* pp. 1-3, 2010.

[92] M. Noras, S. Ramsey and B. Rhoades, “Projectile detection using quasi-electrostatic field sensor array,” *Journal of Electrostatics,* vol. 73, no. 3, pp. 220-223, June 2013.

[93] F. Johann and E. Soergel, “Quantitative measurement of the surface charge density,” *Appl. Phys. Lett. 95, 232906,* vol. 95, no. 23, 2009.

[94] M. Abdul-Hussain and K. Cornick, “Charge Storage on Insulation Surfaces in Air under Unidirectional Impulse Conditions,” *IEE Proceedings,* vol. 134, no. 9, pp. 731-740, Nov 1987.

[95] J. Davidson and A. Bailey, “Surface Charge Distribution Mapping of Insulating Materials,” *Institute of Physics, Electrostatics 1999 Conference Proceedings, Cambridge,* pp. 439-442, March 1999.

[96] T. Takuma, M. Yashima and T. Kawamoto, “Principle of Surface Charge Measurement for Thick Insulating Specimens,” *IEEE Transactions on Dielectrics and Electrical Insulation,* vol. 5, no. 4, pp. 497-504, Aug 1998.

[97] A. Pederson, “On the Electrostatics of Probe Measurements of Surface Charge Densities,” *Gaseous Dielectrics V, Pergamon Press,* pp. 235-240, 1987.

[98] T. Rerup, G. Crichton and I. McAllister, “Response of an electrostatic probe for a right cylindrical spacer,” *IEEE Conference on Electrical Insulation and Dielectric*

Phenomena, Arlington, USA, pp. 164-176, 1994.

[99] T. Rerup, G. Crichton and I. McAllister, "Using the λ Function to Evaluate Probe Measurements of Charged Dielectric Surfaces," *IEEE Transactions on Dielectrics and Electrical Insulation,* vol. 3, no. 6, pp. 770-777, Dec 1996.

[100] H. Ootera and K. Nakanishi, "Analytical method for evaluating surface charge distribution on a dielectric from capacitive probe measurement-application to a cone-type spacer in +or-500 kV DC-GIS," *IEEE Transactions on Power Delivery,* vol. 3, no. 1, pp. 165-172, 1988.

[101] E. Sudhakar and K. Srivastra, "Electric Field Computation from Probe Measurements of Charge on Spacers Subjected to Impulse Voltages," *5th International Symposium on High Voltage Engineering, Braunschweig, Germany,* 1987.

[102] S. Sato and W. Zaengl, "Effective 3-dimensional electric field calculation by surface charge simulation method," *IEE Proceedings A - Physical Science, Measurement and Instrumentation, Management and Education - Reviews,* vol. 133, no. 2, pp. 77-83, March 1996.

[103] D. Faircloth and N. Allen, "A System For Obtaining High Resolution Macroscopic Surface Charge Density Distributions On Contoured Axi-Symmetric Insulator Specimens," *IOP Electrostatics 1999: Proceedings of the 10th International Conference, Cambridge,* March 1999.

[104] D. Faircloth and N. Allen, "High Resolution Measurements of Surface Charge Densities on Insulator Surfaces," *IEEE Transactions on DieIechics and EIectrical Insulntion,* vol. 10, no. 2, pp. 285-290, April 2003.

[105] M. Ieda, T. Mizutani and S. Ikeda, "Electrical Conduction and Chemical Structure of Insulating Polymers," *IEEE Transactions on Electrical Insulation,* Vols. EI-21, no. 3, pp. 301-306, June 1986.

[106] T. Miyamoto and K. Shibayama, "Free-Volume Model for Ionic Conductivity in Polymers," *Journal of Applied Physics,* vol. 44, no. 12, pp. 5372-5376, Aug 1973.

[107] P. Pipinys, A. Rimeika and V. Lapeik, "DC conduction in polymers under high electric fields," *Journal of Applied Physics,* vol. 37, no. 6, pp. 828-831, 2004.

[108] V. Adamec and J. Calderwood, "Electrical Conduction at High Fields," *Journal of*

Applied Physics, vol. 8, no. 5, pp. 551-560, 1975.

[109] P. Yan, Y. Zhou and N. Yoshimura, "DC Conduction in Polyethylene Films under High Electric Field after Annealing," *Japanese Journal of Applied Physics,* vol. 39, no. 6A, 2000.

[110] R. Bahri and H. Singh, "DC Electrical Conduction in Solution-Grown in Thin Polyvinylchloride Films," *International Journal on the Science and Technology of Condensed Matter Films,* vol. 69, no. 3, pp. 281-288, July 1980.

[111] M. Ieda, M. Nagao and M. Hikita, "High-field Conduction and Breakdown in Insulating Polymers," *IEEE Transactions on Dielectrics and Electrical Insulation,* vol. 1, no. 5, pp. 934-945, Oct 1994.

[112] R. Fleming, "Space Charge in Polymers, Particularly Polyethylene," *Brazilian Journal of Physics,* vol. 29, no. 2, pp. 280-294, 1999.

[113] T. Mizutani, "Space Charge Distributions in Insulating Polymers," *8th International Symposium on Electrets, Paris,* pp. 163-169, Sep 1994.

[114] V. Mathur and R. Dahiya, "Space-charge-limited currents in insulators containing traps distributed in energy," *Solid-State Electronics: An International Journal, Pergamon Press,* vol. 17, pp. 61-70, 1974.

[115] S. Ganichev, E. Ziemann and W. Prettl, "Distinction between the Poole-Frenkel and tunnelling models of electric-field-stimulated carrier emission from deep levels in semiconductors," *The American Physical Society: Physical Review B,* vol. 61, no. 15, pp. 10361-10365, April 2000.

[116] D. Das Gupta and K. Joyner, "On the nature of absorption currents in polyethylene terephthalate (PET)," *Journal of Applied Physics. D,* vol. 9, pp. 829-840, 1976.

[117] J. Brunson, "Hopping Conductivity and Charge Transport in Low Density Polyethylene," Utah State University, 2010.

[118] "Volume and Surface Resistivity Measurements of Insulating Materials Using Model 6517A Electrometer/High Resistance Meter," Keithley Application Note Series, no. 314, 2010.

[119] A. Vlastos and J. Hutlen, "Insulator surface conduction state and surface flashover voltage," *IEEE Conference on Electrical Insulation and Dielectric Properties Annual*

Report., pp. 463- 466, 1995.

[120] "ASTM D257-14 Standard Test Methods for DC Resistance or Conductance of Insulating Materials," ASTM International, West Conshohocken, PA, 2014.

[121] W. Maryniak, T. Uehara and M. Noras, "Surface Resistivity and Surface Resistance Measurements: Using a Concentric Ring Probe Technique," *Trek Application Note, no. 1005,* 2013.

[122] "Surface & Volume Resistance/Resistivity Test Fixture: Operating Instructions," Model 853, electro-tech systems, Inc..

[123] J. Sang Sun, S. GokTurk and D. Kalyon, "Volume and surface resistivity of low-density polyethylene filled with stainless steel fibres," *Journal of Materials Science,* vol. 28, no. 2, pp. 364-366, 1993.

[124] R. Fouracre, G. Leonidopoulos and R. Frame, "Surface conductivity measurements on thin polymer films," *Journal of Physics E: Scientific Instruments,* vol. 19, no. 2, pp. 155-156, 1986.

[125] S. Bektas, O. Farish and M. Hizal, "Computation of the electric field at a solid/gas interface in the presence of surface and volume charges," *IEE Proceedings A - Physical Science, Measurement and Instrumentation, Management and Education - Reviews,* vol. 33, no. 9, pp. 577-586, 1985.

[126] G. Leonidopoulos, "Voltage Distribution of Two Thin Polymeric Film Surface Resistance Measurement Systems," *IEEE Transactions on Instrumentation and Measurement,* vol. 40, no. 3, pp. 635-639, 1991.

[127] G. Leonidopoulos, "Measurement and the Effect of Different Solvents on Thin Polymeric Film Surface Resistance," *IEEE Transactions on Instrumentation and Measurement,* vol. 38, no. 1, pp. 43-48, 1989.

[128] M. Given, R. Fouracre and I. Timoshkin, "Surface Conductivity Measurements on Large Polymer Samples," *IEEE Conference on Electrical Insulation and Dielectric Phenomena,* pp. 286-289, 2009.

[129] M. Noras, "Electric field detection using solid state variable capacitance," *Proceedings of the 2014 ESA Annual Meeting on Electrostatics,* June 2014.

[130] "1SV229," *TOSHIBA Variable Capacitance Diode, DataSheet,* March 2014.

[131] I. Poole, “Amplitude modulation AM demodulation,” *Resources and analysis for electronic engineers, Radio-Electronics.com.*

[132] “LT1016 UltraFast Precision 10ns Comparator,” *Data Sheet, Linear Technology*.

[133] “OPA678 Wideband Switched-Input OPERATIONAL AMPLIFIER,” *Data Sheet, BURR-BROWN, USA*, March 1998.

[134] “INA12x Precision, Low Power Instrumentation Amplifiers,” *Data Sheet, Texas Instruments,* Oct 2015.

[135] S. Bektas and O. Farish, “Surface Charging of Spacers under DC Stressing,” *9th International Conference on Gas Discharges and their Applications, Venice, Italy,* Sep 1988.

[136] “Teflon: PTFE, Properties Handbook,” R J Chase Company, Inc., [Online]. Available: http://www.rjchase.com/ptfe_handbook.pdf.

[137] “Technical Information - Polymethylmethacrylate,” Goodfellow, 27 Dec 2017. [Online]. Available: http://www.goodfellow.com.

[138] “hygrometers - 6100 & 6102 therma hygrometers with interchangeable probes,” Electronic Temperature Instruments Ltd, [Online]. Available: https://thermometer.co.uk/humidity-meters/917-therma-hygrometer-6100-hygrometer-thermometer.html.

[139] “EW Series Extended Current* 500 Watt Regulated High Voltage Power Supplies,” GLASSMAN HIGH VOLTAGE INC., 17 DEC 2003. [Online]. Available: http://www.glassmanhv.com/PDFs/EW_Series.pdf.

[140] “Model 617 Programmable Electrometer Instruction Manual,” Keithley Instruments Inc., 1984. [Online]. Available: http://www.univie.ac.at/photovoltaik/umwelt/ws2015/K617_original.pdf.

[141] “PROLOGIX GPIB-USB CONTROLLER, USER MANUAL,” PROLOGIX.BIZ, 14 May 2013. [Online]. Available: http://prologix.biz/downloads/PrologixGpibUsbManual-6.0.pdf.

[142] R. W. Schafer, “What is a SAVITZKY-GOLAY Filter?,” *IEEE SIGNAL PROCESSING MAGAZINE,* vol. 28, no. 4, pp. 111-117, July 2011.

[143] L. Ismail, “Effects of PMMA concentration on PMMA-based organic capacitor behavior,” in *10th IEEE International Conference on Semiconductor Electronics (ICSE)*, Kuala Lumpur, Malaysia, Sep 2012.

[144] M. Savage and B. Stotlzfus, “Performance of a radial vacuum insulator stack,” in *Pulsed Power Conference (PPC)*, Austin, TX, USA, 2015.

[145] S. Tehwari, R. Chandra and S. Sharma, “Surface potential decay of PMMA and POM in air,” *Materials Research Express*, vol. 2, no. 4, March 2015.

[146] G. Y. a. Z. A.Mohamad, “Surface Fluorinated Epoxy Resin for High Voltage DC Application,” *IEEE Transactions on Dielectrics and Electrical Insulation*, vol. 22, no. 1, pp. 101-108, Feb 2015.

Appendix A

1. Concentric Cylindrical Measurement System

1.1. Bottom Electrode Geometry Dimensions

Figure A 1, shows the dimensions of the electrode arrangement of the bottom half of the concentric cylindrical measurement system.

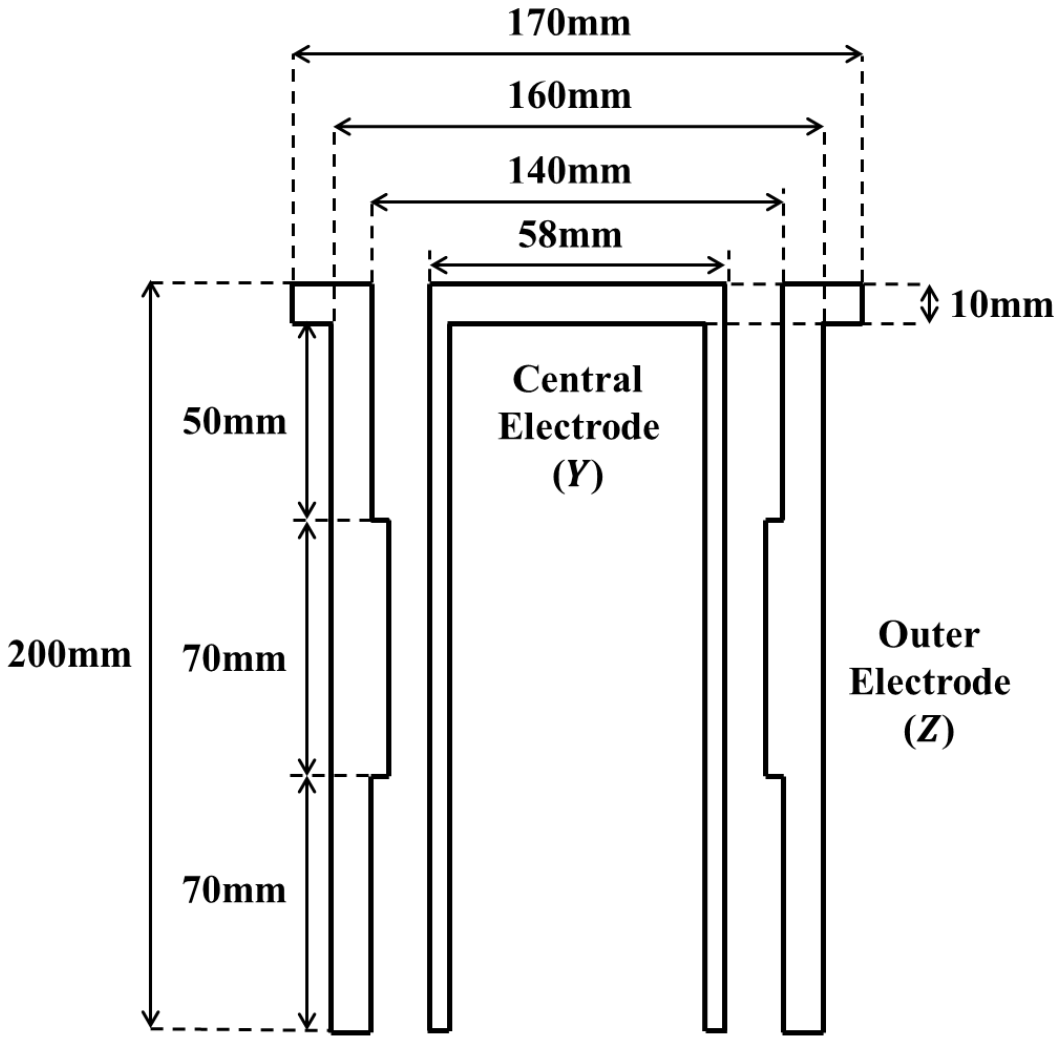

Figure A 1: Dimensions of the bottom half of the concentric cylindrical measurement geometry.

1.2. Upper Electrode Geometry Dimensions

Figure A 2, shows the general dimensions of the upper electrode geometry of the concentric measurement cylindrical system and figure A 3, shows the dimensions of the modified part of the inner electrode arrangement of the upper electrode geometry of the concentric cylindrical measurement system.

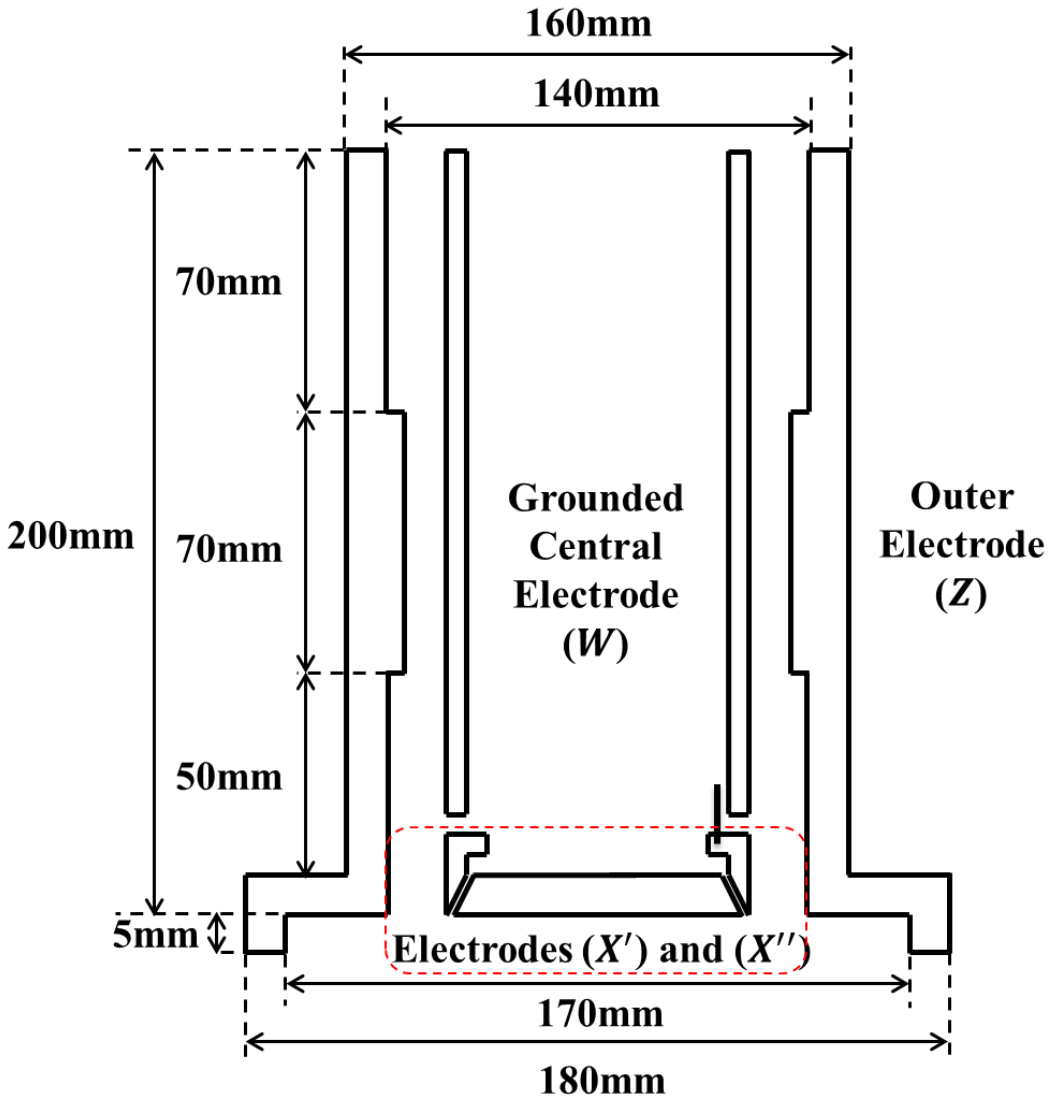

Figure A 2: Dimensions of the upper half of the concentric cylindrical measurement geometry.

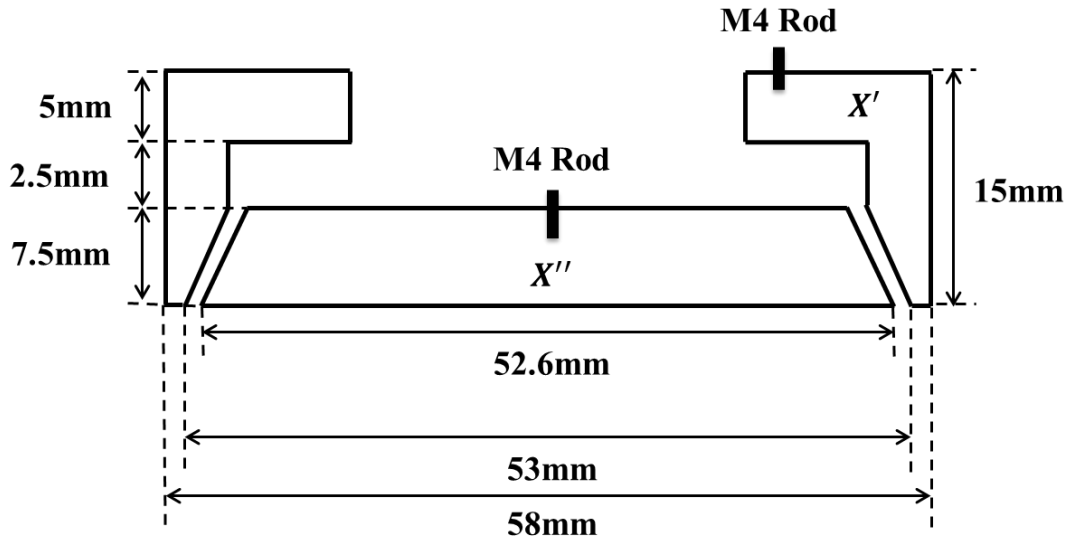

Figure A 3: Dimensions of the modified electrodes X' and X'' of the upper half of the concentric cylindrical measurement geometry.

Appendix B

1. *Grid System for Corona Deposition*

Figure B 1, shows the dimensions of the charge deposition system used to deposit corona onto the surface of the polymeric materials in a controlled manner and figure B 2, shows the schematic diagram of the aluminium ring with the positions of the needle electrodes.

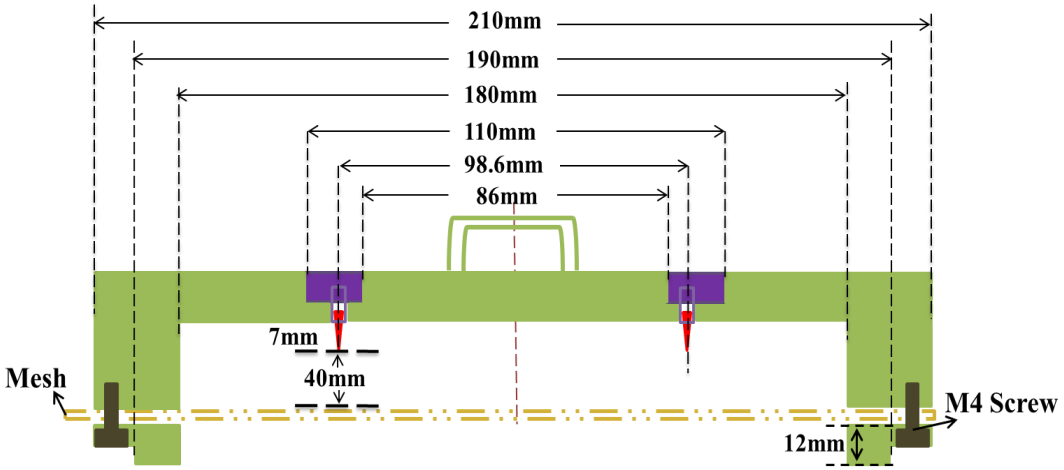

Figure B 1: Dimensions of the corona deposition system.

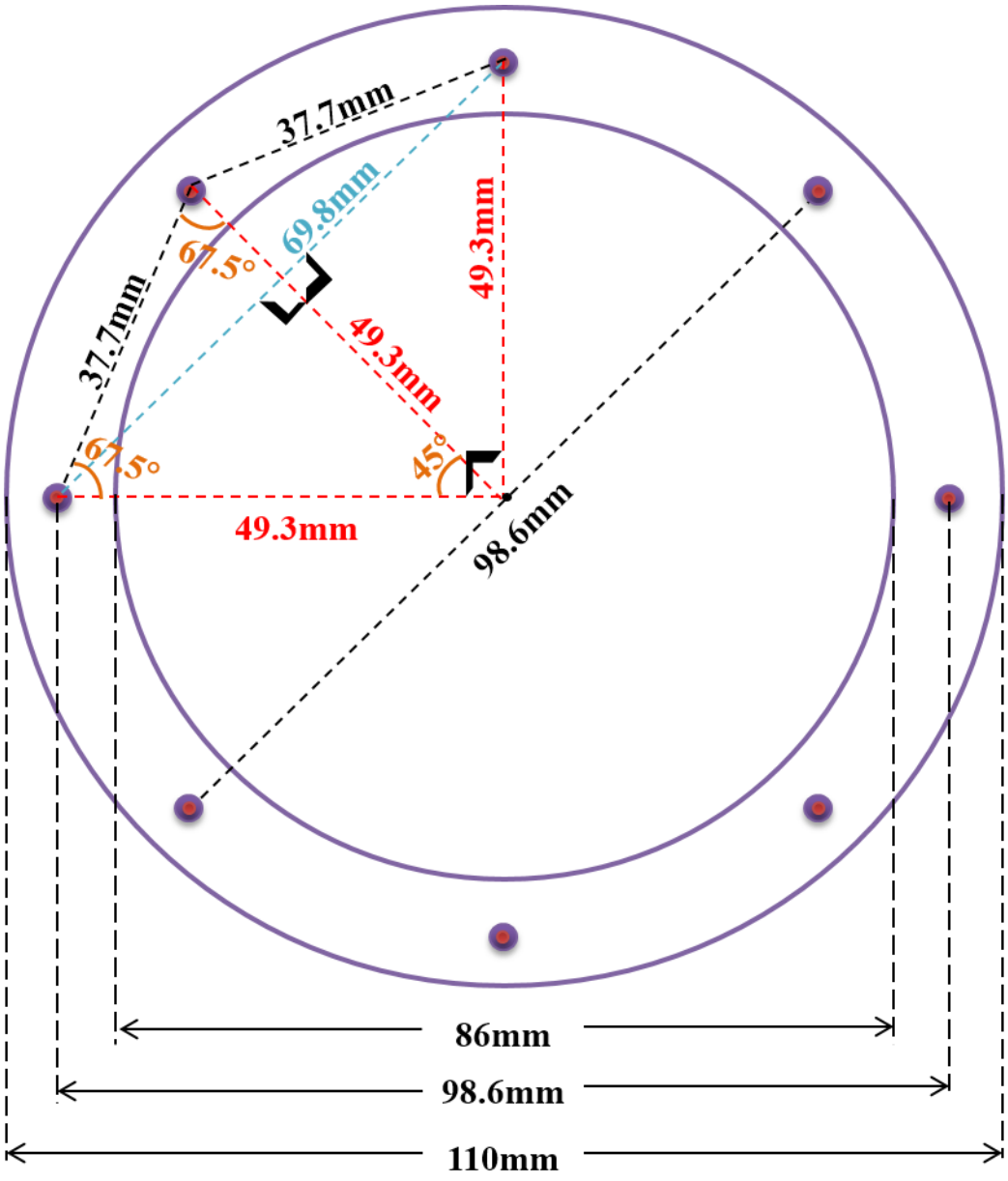

Figure B 2: Aluminium ring with the positions of the needle electrodes.